Contribution of type 1 interferon activated monocytes and macrophages to the immune pathology of idiopathic pulmonary fibrosis

Vishal Nathwani
St Hughes College
Nuffield Department of Clinical Medicine
University of Oxford



Submission for the degree of Doctor of Philosophy

Trinity Term 2026
Supervisor: Professor Ling-Pei Ho

Abstract

Idiopathic pulmonary fibrosis (IPF) is an age-related, progressive, and often fatal lung disease of unknown aetiology and median survival of 3-5 years. Current therapies target fibrotic pathways in established disease and primarily slow lung function decline, highlighting the need to better understand early pathophysiological processes.

IPF is characterised by repetitive injury to vulnerable type II alveolar epithelial (AT2) cells, leading to aberrant epithelial repair and persistent fibroblast activation. While these processes are well recognised, the contribution of immune pathways to these core pathological events remains incompletely understood. Monocytes and macrophages are increasingly implicated in disease progression; however, their functional heterogeneity and the factors that shape discrete cellular states in IPF are not clearly defined. Emerging evidence of increased type I interferon (type 1 IFN)-stimulated gene expression in circulating monocytes raises the possibility of coordinated immune activation across the circulation and lung. In parallel, specific intermediate epithelial cell states associated with injury and impaired repair have been described, suggesting that epithelial dysfunction may influence local immune responses.

I hypothesised that type 1 IFN signalling in circulating monocytes is associated with increased type 1 IFN activation in lung macrophages and linked to epithelial dysfunction in IPF. To address this, I examined type 1 IFN signalling across circulating immune cells and monocyte–macrophage populations in the lung using single-cell transcriptomic datasets from bronchoalveolar lavage and lung tissue. To complement this, I used single cell tissue mass cytometry to examine the contribution of the local tissue microenvironment to type 1 IFN activation in these myeloid cells. Finally, I examined my findings in a primary alveolar spheroid model co-cultured with a myeloid cell line.

My findings demonstrate that type 1 IFN–activated macrophages in IPF lung tissue are spatially restricted to the alveolar barrier and enriched in earlier stages of the disease process. These macrophages are selectively associated with intermediate epithelial states, including aberrant basaloid intermediates, transitional AT2, and inflammatory AT1 populations which exhibit features of cellular senescence and inflammation. In vitro studies indicate that these epithelial states can induce type 1 IFN responses in myeloid cells. Overall, the thesis supports a model in which epithelial dysfunction and aberrant repair define a local microenvironment associated with myeloid type 1 IFN activation at sites of epithelial injury, preceding established fibrosis. These findings suggest that targeting epithelial–myeloid interferon signalling may represent an opportunity to modulate early disease processes prior to irreversible fibrotic remodelling.

Acknowledgements

I would first like to thank my supervisor Professor Ling Pei Ho. She has been a truly remarkable mentor over the past 5 years both in clinical practice and in the laboratory. Ever since our first meeting just before the pandemic her enthusiasm for immunology has been apparent and at times infectious. Her patience and dedication to providing excellent training is matched only by her caring nature such that she is someone I can always turn to for sensible and pragmatic advise. She facilitated my transfer of clinical training to Oxford to be able to remain with my family for which I am forever grateful. Her support and confidence in my capability has certainly helped develop my current career trajectory and fuelled my desire to pursue a career as a clinician scientist and I look forward to continuing to work with her over the next few years.

Throughout my research degree she has guided me in acquiring technical skills, data analysis, comprehension and synthesis. She has been tireless in her pursuit to develop me as a clinician scientist and this study would not have been possible without her continual input.

I want to also highlight the contribution of the entire Ling Pei Ho group. Without their patient support, training and guidance I would not have been able to acquire the skills over the past few years. Whilst I contributed to every aspect of this study, its fullness would not have been possible without their input, specifically;

Dr Jeongmin Woo and Dr Agne Antanavicute who provided bioinformatic support and training in the single cell transcriptomic work presented here. In particular the data processing presented in part of Chapter 3 and 4.
Dr Leila Baghaarabini who provided continual bioinformatic support in adapting the SpOOX pipeline to my study design and technical guidance in troubleshooting issues with its implementation.
Dr Praveen Weeratunga who along with a wider group developed the SpOOx pipeline and provided input in navigating the statistical spatial analysis and input in the CyTOF study.
Dr Tian Hu, who at times, behaved as a supervisor in particular in the development of the alveolar spheroid model described in Chapter 6 where he provided mentorship in advanced techniques of cell culture and imaging
Chaitanya Vupusetty who has trained me in all the basic science lab skills performed in this study and with whom I performed the RNA work and CyTOF experiments.
Dr Laura Denney who performed all the processing of the bronchoalveolar lavage samples prior to sequencing in Chapter 4.
Harriet Parker who contributed to optimising and running of the CyTOF experiment.
Prof Jan Rehwinkel and Anne Bridgeman who provided the THP-1 cells used for optimisation of the imaging mass cytometry study and used in the coculture experiments

I would also like to thank all my collaborators, WiMM facilities and support staff for the input in this study.

Finally, I am eternally grateful to my wife Muriel who has supported this endeavour with incredible patience. She has always been there for me and made huge sacrifices to allow me to pursue this research study. She is a truly wonderful mother and at times over the last few years providing care to our children equivalent to both of us when I have been away. I would like to emphasise my love for my children Lila and Aaron who fill our home with joy and laughter and provide a welcome distraction after a difficult day.

I would also like to thank my parents without whose guidance over these many years I would not be the person I am today. They taught me dedication, hard work and self-sacrifice. I would also like to specifically thank my mother who is always on the end of the phone quietly allowing me to share my frustrations whilst offer worldly advise. Finally, a special mention to my sister who quietly keeps the whole family afloat works tirelessly in everything she does without asking for recognition or praise.

Table of Contents

Abstract ***2***

Acknowledgements ***3***

Abbreviations ***9***

Chapter 1 Introduction ***11***

1.1.1 Background and Epidemiology 11
1.1.2 Clinical Features 12
1.1.3 Diagnostic Criteria 12
1.1.4 Acute exacerbation of IPF 15
1.1.5 Management 16

1.2 Pathogenesis of IPF **17**
1.2.1 Susceptibility: Genetic, environmental and age-related factors 17
1.2.2 Alveolar epithelial cell injury and dysfunction 19
1.2.3 Epithelial – mesenchymal interactions 20
1.2.4 Fibroblast activation and extracellular matrix deposition 21
1.2.5 Contribution of immune cells 22

1.3 Monocytes and Macrophages **24**
1.3.1 Monocyte subsets and function 24
1.3.2 Lung macrophages in homeostasis 26
1.3.3 Lung macrophage ontogeny in ageing and following injury 27
1.3.4 Contribution of monocytes to IPF pathogenesis 28
1.3.5 Contribution of lung macrophages to IPF pathogenesis 30

1.4 Type 1 Interferon Signalling **32**
1.4.1 Overview of the type 1 IFN signalling pathway 32
1.4.2 Type 1 IFN signalling in myeloid cell function 34
1.4.3 Insights from type 1 IFN mediated diseases 35

1.5 Study Aims **37**

Chapter 2 Materials and methods ***39***

2.1 Experiential Methods **39**
2.1.1 Peripheral blood mononuclear cell (PBMC) isolation and cryopreservation 39
2.1.2 Antibody conjugation to metal isotypes for mass cytometry 39
2.1.3 PBMC IFN-β stimulation, antibody staining and CyTOF acquisition 40
2.1.4 Sample processing for droplet-based single-cell RNA sequencing 41
2.1.5 Immunofluorescence staining of formalin fixed paraffin embedded tissue sections 42
2.1.6 Haematoxylin and eosin staining of formalin fixed paraffin embedded tissue sections 42
2.1.7 IMC antibody selection, specificity testing and titration 43
2.1.8 Antibody staining of formalin fixed paraffin embedded tissue sections for imaging mass cytometry 44
2.1.9 Human lung tissue collection and processing 45
2.1.10 Magnetic bead activated cell sorting (MACS) 46
2.1.11 Fluorescent activated cell sorting (FACS) of AT2 cells 47
2.1.12 AT2 alveolar spheroid culture media 47
2.1.13 AT2 cell plating and long-term culture 49
2.1.14 Passaging of AT2 spheroids 49
2.1.15 Cell isolation, fixation, and staining for immunocytochemistry (ICC) 50
2.1.16 Paraffin embedding of intact AT2 spheroids 50
2.1.17 Bleomycin-induced injury of AT2 spheroids 51
2.1.18 RNA extraction and quantitative PCR 51
2.1.19 THP-1 cell culture and stimulation 52

2.1.20 Flow Cytometry 53
2.1.21 AT2–THP-1 co-culture experiments 53

Chapter 3 Type 1 IFN signalling in circulating immune cells in IPF 57

3.1 Introduction 57

3.2 Study Design and Methods 59
3.2.1 Overall Study Design 59
3.2.2 Patient selection 59
3.2.3 Suspension mass cytometry - IFN-β stimulation and antibody staining 65
3.2.4 Suspension mass cytometry - data processing and analysis 68
3.2.5 PBMC processing and droplet based single cell RNA sequencing 69
3.2.6 Processing, quality control and analysis of single cell RNA sequencing data 69

3.3 Results 73
3.3.1 High resolution single cell antibody-based (CyTOF) analysis of PBMCs reveals six monocyte subtypes 73
3.3.2 Composition analysis show increased TEMRA CD8+ T Cells and reduced CD56hi NK cells in IPF patients 77
3.3.3 Classical monocytes in IPF show a heightened response to IFN-β stimulation with increased canonical pSTAT expression 79
3.3.4 NK cells, effector memory $CD4^+$ T cells and naïve $CD8^+$ T cells display increased responses to IFN-β stimulation 82
3.3.5 pSTAT1:pSTAT3 expression is significantly higher in IPF cMonos following IFN-β stimulation 84
3.3.6 Baseline unphosphorylated STAT1 and STAT3 or membrane expression of IFNAR2 do not account for increased response to IFN-β in IPF. 85
3.3.7 Classical monocytes exhibit increased basal pNFkB in IPF 86
3.3.8 Single cell transcriptomic analysis of circulating PBMCs in IPF 89
3.3.9 Increased transcription factor activity related to type 1 IFN and inflammatory signalling in IPF circulating monocytes 94

3.4 Discussion 99

3.5 Conclusion 103

Chapter 4. Type 1 IFN signalling in lung monocytes and macrophages in IPF 104

4.1 Introduction 104

4.2 Study Design and Methods. 106
4.2.1 Overall Study Design 106
4.2.2 Patient Selection, patient and control demographic details 107
4.2.3 Analysis of single cell sequencing data 110

4.3 Results 112
4.3.1 scRNAseq reveals a macrophage landscape characterised by distinct homeostatic and pro-inflammatory transcriptomic states at the alveolar barrier 112
4.3.2 Increased inflammatory and type 1 I IFN signalling activities in AMs at the IPF alveolar barrier 121
4.3.3 Increased type 1 IFN regulatory network activity in alveolar barrier AMs from IPF lungs 126
4.3.4. Single-cell RNA sequencing of lung digest identifies several monocyte and tissue macrophage subsets in IPF lung 128
4.3.5 More advanced fibrotic states in IPF lung is associated with expansion of tissue macrophage subsets 132
4.3.6 - Advanced fibrosis is associated with activation of ECM remodelling and fibrotic pathways in macrophage subsets 134
4.3.7 Early disease is associated with increased interferon and cytokine signalling in lung monocytes and $CXCL10^+$ AMs 140
4.3.8 Circulating $CD14^+$ monocytes exhibit increased ISG expression in early disease 145

4.4 Discussion 146

4.5 Conclusion 149

Chapter 5 Spatial context of type 1 IFN–activated monocytes and macrophages in IPF lungs 150

5.1 Introduction 150

5.2 Study Design and Methods 152
5.2.1 IPF lung biopsy donor selection, clinical and radiological characteristics 152
5.2.2 Experimental workflow 152
5.2.3 Analysis of imaging mass cytometry data 154

5.3 Results 158
5.3.1 Histopathology analysis of IPF lung tissue and region of interest selection 158
5.3.2 Antibody panel validation 161
5.3.3 Characterisation of the cellular landscape of IPF lung tissue 163
5.3.4 Alveolar epithelial cell populations in IPF include aberrant basaloid and transitional states 166
5.3.5 Transitional and ABI cell states express markers associated with inflammation 170
5.3.6 Alveolar macrophage subtypes express highest levels of type 1 IFN activation markers 170
..... 175
5.3.7 Type 1 IFN-activated myeloid populations and type 1 IFN signalling are increased in early and intermediate stages of IPF 175
5.3.8 Spatial analysis reveals co-location between type 1 IFN-activated myeloid cells and ABIs, iAT1 and tAT2 epithelial cell populations 179
5.3.9 Type 1 IFN-activated AM populations form a cell network with ABIs, tAT2 and iAT1 182

5.4 Discussion 187

5.5 Conclusion 190

Chapter 6 Alveolar epithelial–myeloid interactions using an alveolar spheroid injury model 191

6.1 Introduction 191

6.2 Study Design and Methods 193
6.2.1 Overall Study Design 193
6.2.2 Lung Donor selection Criteria and type 2 alveolar epithelial cell isolation 193
6.2.3 Generation and characterisation of AT2 spheroids 194
6.2.4 Development of a lung injury model and co-culture with THP-1 cells 194

6.3 Results 196
6.3.1 Isolation of high purity primary human AT2 cells from donor lungs 196
6.3.2 Primary AT2 cells cultured in extra-cellular matrix (ECM) form 3D spheroid like structures and are capable of long-term expansion 198
6.3.3 Primary AT2-derived alveolar spheroids retain expression of canonical AT2 markers and apical–basal polarity 201
6.3.4 Single dose bleomycin induces injury and senescence transcriptional changes consistent with aberrant AEC responses in IPF 206
6.3.5 THP-1 cells retain cell surface expression and functional responses to LPS and IFN-β when co-cultured with AT2 cells in serum free AVOE media 210
6.3.6 Injured alveolar spheroids upregulate ISGs and TNF-α in THP-1 cells 213
6.3.7 THP-1 cells influence expression of injury -related transcripts in injured alveolar spheroids 218

6.4 Discussion 222

6.5 Conclusion 225

Chapter 7 - General Discussion and Future Directions 226

7.1 Discussion 226
7.2 Conclusion 231
Bibliography*..... *232

Abbreviations

ABIs – Aberrant Basaloid Intermediates
ACN / CCN – Adjacency Cell Network / Contacting Cell Network
AE-IPF – Acute Exacerbations Of Idiopathic Pulmonary Fibrosis
AEC – Alveolar Epithelial Cell
AMs – Alveolar Macrophages
AVOE – Alveolar Organoid Expansion Medium
αSMA – Alpha Smooth Muscle Actin
BAL – Bronchoalveolar Lavage
CCR2 – CC-Chemokine Receptor 2
CDGs – Cluster Defining Genes
CFE – Colony-Forming Efficiency
CSF1 – Colony Stimulating Factor 1
CSF2 – Colony Stimulating Factor 2
CT – Computed Tomography
CTGF – Connective Tissue Growth Factor
cGAS–STING – Cyclic GMP–AMP Synthase–Stimulator of Interferon Genes
DAMPs – Damage-Associated Molecular Patterns
DM – Dermatomyositis
DDR – DNA Damage Response
ER – Endoplasmic Reticulum
EQ – Equalisation Beads
ECM – Extracellular Matrix
FGF – Fibroblast Growth Factor
GRNs – Gene Regulatory Networks
GWAS – Genome-Wide Association Studies
H&E – Haematoxylin And Eosin
HRCT – High-Resolution Computed Tomography
iNOS – Inducible Nitric Oxide Synthase
iAT1 – Inflammatory Type I Alveolar Epithelial Cells
ILCs – Innate Lymphoid Cells
IFNAR – Interferon α/β Receptor
IRF3/7 – Interferon Regulatory Factors 3 And 7
ISGs – Interferon-Stimulated Genes
ISGF3 – Interferon Stimulated Gene Factor 3
ISRE – Interferon Stimulated Response Element
ILDs – Interstitial Lung Diseases
IMs – Interstitial Macrophages
i.p. – Intraperitoneal
LPS – Lipopolysaccharide

LRT – Likelihood Ratio Testing
LCMV – Lymphocytic Choriomeningitis Virus
MHC – Major Histocompatibility Complex
MMPs – Matrix Metalloproteinases
MDM – Monocyte-Derived Macrophages
NETs – Neutrophil Extracellular Traps
ncMono – Non-Classical Monocytes
ORB – Oxford Radcliffe Biobank
PAMPs – Pathogen-Associated Molecular Patterns
PRRs – Pattern Recognition Receptors
PEA – Pathway Enrichment Analysis
TAZ – PDZ-Binding Motif
PBMCs – Peripheral Blood Mononuclear Cells
PDGFR / FGFR / VEGFR – Platelet-Derived Growth Factor Receptor / Fibroblast Growth Factor Receptor / Vascular Endothelial Growth Factor Receptor
pDCs – Plasmacytoid Dendritic Cells
PET-CT – Positron Emission Tomography–Computed Tomography
PD-1 – Programmed Death-1
ROIs – Regions Of Interest
RSV – Respiratory Syncytial Virus
SATMs – Segregated Nucleus-Containing Atypical Monocytes
SASP – Senescence-Associated Secretory Phenotype
SCENIC – Single-Cell Regulatory Network Inference And Clustering
CyTOF – Single Cell Suspension Mass Cytometry
SFTPC – Surfactant Protein C
SLE – Systemic Lupus Erythematosus
SSc – Systemic Sclerosis
TSLP – Thymic Stromal Lymphopoietin
TRM – Tissue Resident Macrophages
TLR – Toll-Like Receptor
tAT2 – Transitional Type II Alveolar Epithelial Cells
TNF-α – Tumour Necrosis Factor α
AT1 – Type I Alveolar Epithelial Cells
AT2 – Type II Alveolar Epithelial Cells
UPR – Unfolded Protein Response
UIP – Usual Interstitial Pneumonia
YAP – Yes-Associated Protein

Chapter 1 Introduction

1.1 Idiopathic Pulmonary Fibrosis

1.1.1 Background and Epidemiology

Idiopathic Pulmonary Fibrosis (IPF) is an age-related, progressive, and often fatal lung condition of unknown aetiology, with a median prognosis of 3–5 years [1, 2]. IPF is the most common of the interstitial lung diseases (ILDs), a group of heterogeneous conditions characterised by pathology affecting the distal lung parenchyma [3].

IPF is characterised by progressive deposition of collagen-containing extracellular matrix within the distal lung, gradually replacing normal lung parenchyma and resulting in irreversible loss of lung function. Fibrosis restricts lung capacity and impairs gas exchange at the alveolar–capillary barrier, leading to exertional dyspnoea and progressive exercise limitation. With advancing disease, patients develop dyspnoea and hypoxia with minimal exertion, progressing to respiratory failure, pulmonary hypertension, and death.

Although uncommon, the incidence of IPF is rising in the United Kingdom[4, 5] and globally[6]. Incidence and prevalence vary depending on diagnostic criteria. In the UK, incidence increased from 3 to 6.1 (narrow criteria) and from 22.4 to 28.6 (broad criteria) per 100,000 population per year between 2008 and 2018[5]. Prevalence increased from 13.9 to 17.2 (narrow criteria) and from 73.7 to 97.8 (broad criteria) per 100,000 population[5]. These rates are comparable to those reported in the United States (93.7 per 100,000 population;)[7].

IPF is strongly age-associated, with prevalence increasing from 63.3 per 100,000 per year in individuals aged 66–69 to 129.8 per 100,000 per year in those aged over 80[1]. Males are approximately 1.3 times more likely to develop IPF than females, possibly reflecting greater exposure to environmental risk factors such as cigarette smoke and occupational dust[8].

Antifibrotic therapy is currently the only licensed disease-modifying treatment. While these agents slow disease progression, they are associated with significant adverse effects and discontinuation rates of up to 45%[9]. Despite treatment, 5-year survival remains below 45%[10].

1.1.2 Clinical Features

Patients typically present with gradually progressive exertional dyspnoea and a persistent dry cough developing over months to years. With disease progression, secondary pulmonary hypertension may occur, presenting with peripheral oedema and right heart dysfunction. Weight loss and anorexia are also common in advanced disease.

The insidious onset often leads to delayed diagnosis, with a median time to diagnosis of approximately 2.2 years from symptom onset[11, 12]. Increased availability of computed tomography (CT) imaging and the introduction of lung cancer screening programmes using low-dose CT, including in the UK[13] may reduce diagnostic delay.

Early UK screening data report detection of interstitial lung abnormalities in 1.34% of participants, although the proportion representing IPF is not yet defined[13] . Cohort studies suggest that 43–67% of such abnormalities progress radiologically, highlighting opportunities for earlier detection[14, 15].

Disease progression is heterogeneous. Some patients experience slow decline over years, whereas others deteriorate rapidly over months[8]. Alternatively, a stepwise pattern may occur, with periods of stability punctuated by acute deterioration.

Prognosis can be estimated using clinical variables such as age, sex, and baseline lung function[16, 17], although these do not reliably predict progression.

On examination, patients typically have bilateral basal inspiratory crackles. Finger clubbing is reported in 7–42% of cases[18].

Pulmonary function tests show a restrictive pattern with preserved or increased FEV1/FVC ratio (>0.7) and reduced total lung capacity. Diffusing capacity (TLCO) is reduced, reflecting impaired gas exchange. In patients with coexistent emphysema, spirometry may be preserved despite markedly reduced TLCO. Serial PFTs and six-minute walk testing are used to monitor disease progression.

1.1.3 Diagnostic Criteria

Diagnosis is guided by international clinical practice guidelines[19]. A confident diagnosis can be made based on characteristic radiological features of usual interstitial pneumonia (UIP) on high-resolution CT (HRCT) (Figure 1.1.1).

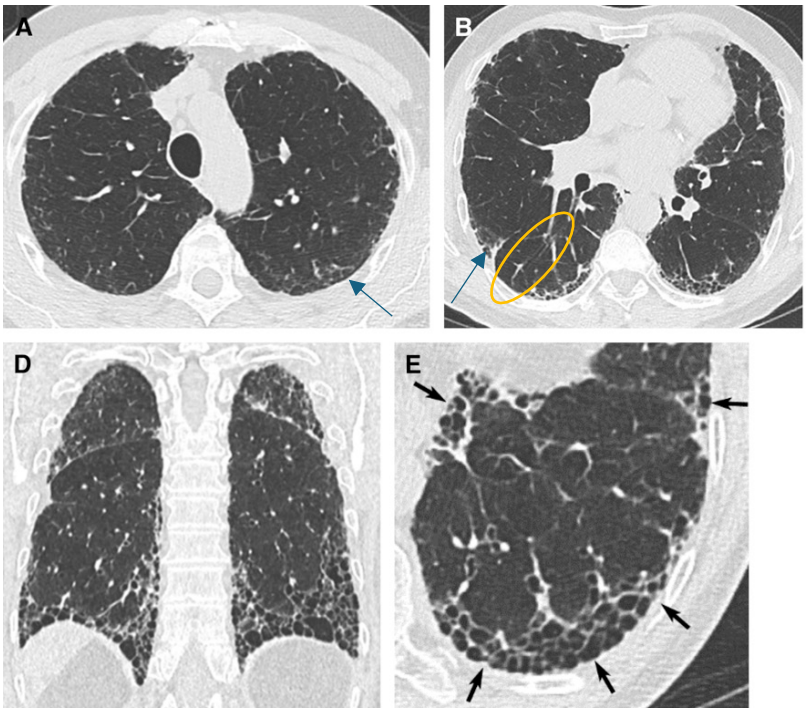


*Figure 1.1.**1 High resolution CT images depicting pulmonary fibrosis.*** *CT scans show typical subpleural and basal predominant change with honey comb cysts (black arrows, reticulation (blue arrows) and tractional bronchiolar dilatation (orange circles). Image adapted from Raghu et al 2018*[20]

Typical UIP features include basal and subpleural predominance, reticular abnormalities, and traction bronchiectasis. Honeycombing distinguishes definite from probable UIP (Table 1.1.1). Alternative imaging patterns suggest alternative diagnoses.

Table 4. High-Resolution Computed Tomography Scanning Patterns

UIP	Probable UIP	Indeterminate for UIP	Alternative Diagnosis
Subpleural and basal predominant; distribution is often heterogeneous*	Subpleural and basal predominant; distribution is often heterogeneous	Subpleural and basal predominant	Findings suggestive of another diagnosis, including: • CT features: ° Cysts ° Marked mosaic attenuation ° Predominant GGO ° Profuse micronodules ° Centrilobular nodules ° Nodules ° Consolidation • Predominant distribution: ° Peribronchovascular ° Perilymphatic ° Upper or mid-lung • Other: ° Pleural plaques (consider asbestosis) ° Dilated esophagus (consider CTD) ° Distal clavicular erosions (consider RA) ° Extensive lymph node enlargement (consider other etiologies) ° Pleural effusions, pleural thickening (consider CTD/drugs)
Honeycombing with or without peripheral traction bronchiectasis or bronchiolectasis†	Reticular pattern with peripheral traction bronchiectasis or bronchiolectasis May have mild GGO	Subtle reticulation; may have mild GGO or distortion ("early UIP pattern") CT features and/or distribution of lung fibrosis that do not suggest any specific etiology ("truly indeterminate for UIP")	

Table 1.1.1 Table summarising radiological criteria and definitions of radiological usual interstitial pneumonia. *adapted from Raghu et al 2018[20]. Abbreviations; CTD – connective tissue disease, GGO – ground glass opacification, RA – rheumatoid arthritis, UIP - usual interstitial pneumonia.*

As UIP is not specific to IPF, exclusion of known causes—including environmental exposure, connective tissue disease, and drug toxicity—is required.

Multidisciplinary discussion involving respiratory physicians and radiologists is recommended. Lung biopsy is reserved for atypical cases but remains the histological gold standard[20].

Histologically, UIP is characterised by spatial and temporal heterogeneity, with patchy fibrosis, architectural distortion, and fibroblastic foci representing active fibrogenesis (Figure 1.1.2). [20]

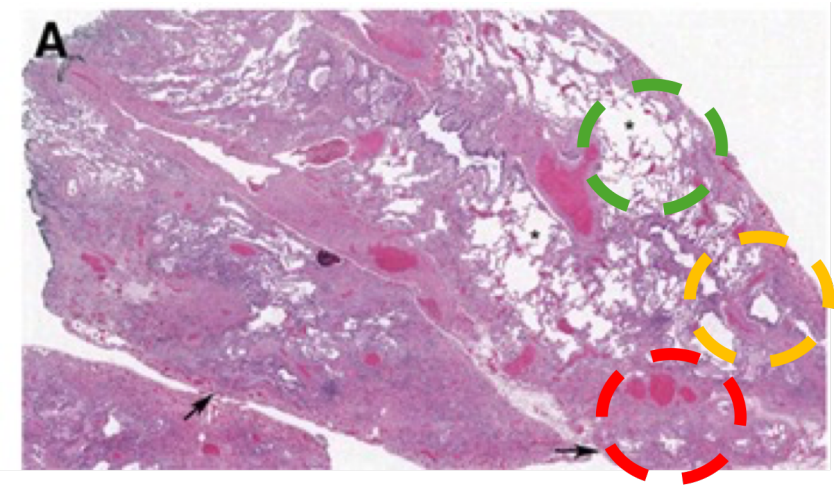


Figure 1.1.2 Haemoxylin and Eosin stained IPF tissue section. *Broken circles indicating areas of early disease (green) with alveolitis and septal thickening, fibroblastic foci (yellow) indicating emerging fibrosis and advanced disease (red) with architectural distortion and dense collagen deposition in close proximity, demonstrating temporal and spatial heterogeneity. Image adapted from Raghu et al 2018[20]*

1.1.4 Acute exacerbation of IPF

A subset of patients with IPF develop episodes characterised by a sudden and significant deterioration in symptoms over a period of less than 30 days, accompanied by new hypoxia and new diffuse airspace opacification on CT imaging[21]. These events are defined as acute exacerbations of IPF (AE-IPF), often necessitating hospital admission, and are associated with a poor prognosis, with approximately 50% mortality at 12 months.

The aetiology of acute exacerbations is not fully understood, although they are thought to represent responses to environmental triggers resulting in acute lung injury, diffuse inflammation, and acceleration of underlying fibrotic disease[22] [23]. Potential triggers

include viral or bacterial infection, aspiration, gastroesophageal reflux, lung surgery (including biopsy), and medications[24 25].

CT imaging typically demonstrates new diffuse inflammatory infiltrates, including ground-glass opacification and/or consolidation. Histologically, acute exacerbations are characterised by diffuse alveolar damage, with hyaline membrane formation and alveolar oedema, similar to acute lung injury from other causes[26].

Patients are often treated with high-dose corticosteroids to target presumed inflammation, although evidence supporting additional immunomodulatory therapies is limited[21]. Despite treatment, prognosis remains poor, with approximately 50% mortality at 3 months following AE-IPF.

1.1.5 Management

Management of IPF includes modification of risk factors, symptom control, and disease-targeted therapies.

Risk factor modification includes reduction of environmental exposures that may contribute to disease progression, particularly smoking cessation, pharmacological treatment of gastroesophageal reflux disease, and vaccination. Previous studies have investigated long-term antibiotic prophylaxis in IPF to reduce bacterial infection and exacerbations, and preclinical studies have suggested direct effects on fibrotic pathways with agents such as doxycycline[27] and azithromycin[28 29]. However, clinical studies have shown limited benefit, with meta-analyses demonstrating no significant improvement in mortality or lung function decline[30].

Symptom management includes pulmonary rehabilitation to maintain exercise capacity and oxygen therapy for patients with exertional or resting hypoxia. Symptomatic breathlessness and cough may be managed with low-dose opioids.

Two antifibrotic therapies—Pirfenidone and Nintedanib—have been shown to modify disease progression. Randomised controlled trials demonstrated that both agents reduce the rate of decline in lung function (FVC) and improve progression-free survival[31, 32]. Subsequent meta-analyses have demonstrated mortality benefit at 12–18 months for both Pirfenidone[33] and Nintedanib[34]. A pooled analysis has also demonstrated reduced risk of acute exacerbations[35].

More recently, real-world studies have confirmed improved survival with antifibrotic therapy compared with no treatment at 36 months, although long-term benefit appears

to attenuate over time[36]. Both medications are associated with significant adverse effects, with discontinuation rates of approximately 41% for Nintedanib and 24% for Pirfenidone at 12 months[37], particularly in older patients[38].

The mechanism of action of Pirfenidone remains unknown although in murine models has been shown to have a wide range of effects[39]. The main mechanism of action is proposed to be mediated via suppression of TGF-β signalling limiting fibroblast proliferation, myofibroblast differentiation and collagen synthesis mediated by TGF-β and fibroblast growth factor (FGF) suppression. In addition, has been shown modulate inflammatory signalling pathways with reduction in TNF-α, IL-1β, IL-6, IL-8 and IFNγ cytokine production, reduce immune cell infiltration and limit oxidative stress via several mechanisms.

The mechanism of Nintedanib is better understood, it is a tyrosine kinase inhibitor that targets signalling downstream of platelet-derived growth factor receptor (PDGF), fibroblast growth factor receptor (FGF) and vascular endothelial growth factor receptor (VEGFR) receptors. It has been shown to modulate fibrotic processes in IPF specifically reduce fibroblast proliferation and migration, myofibroblast activation, collagen synthesis and extra cellular matrix (ECM)[40]. Nintedanib as a broad tyrosine kinase inhibitor is also recognised to supress colony stimulating factor 1 receptor (CSF1R) signalling[41] involved in macrophage proliferation, migration and survival, and has been shown to restrict CCR2 mediated macrophage infiltration in murine models[41, 42] and restrict expansion of subsets that emerge during fibrosis[43].

1.2 Pathogenesis of IPF

The precise pathophysiological mechanisms that result in the development and progression of IPF are not fully understood. Although historically IPF was considered an inflammatory disease process, the current paradigm is centred on genetic and environmental factors that confer increased susceptibility to chronic epithelial injury and alveolar epithelial cell dysfunction. Chronic injury initiates abnormal wound-healing responses, characterised by impaired epithelial regeneration and persistent fibroblast activation, with subsequent collagen and ECM synthesis and deposition.

1.2.1 Susceptibility: Genetic, environmental and age-related factors

The aetiology of IPF is not fully defined; however, susceptibility involves interactions between genetic predisposition, environmental exposures, and ageing, which together contribute to the development of a vulnerable and dysfunctional alveolar epithelium.

A number of genetic mutations have been identified in both familial pulmonary fibrosis and sporadic IPF. Genome-wide association studies (GWAS) have identified mutations in the promoter region of *MUC5B* in 38% of patients with sporadic IPF and 34% of those with familial fibrosis[44]. Increased expression of mucin 5B in the distal airways results in excess mucus production and impaired mucociliary clearance of inhaled particulates, including pathogens, which may increase alveolar epithelial stress and chronic injury[45].

Mutations affecting telomerase activity, including *TERC, TERT, RTEL1*, and *PARN*, have been identified in approximately 8% of patients with familial pulmonary fibrosis. These mutations result in telomere shortening, impaired alveolar epithelial cell replicative capacity, and premature senescence[46]. Although these mutations are less common in sporadic IPF (approximately 3%), telomere shortening is widely observed in alveolar epithelial cells and is associated with increased apoptosis, impaired regeneration, and heightened sensitivity to environmental insults[47].

Type II alveolar epithelial cells (AT2 cells) produce pulmonary surfactant, which is essential for maintaining alveolar surface tension and preventing alveolar collapse during expiration. Mutations in surfactant genes (*SFTPC, SFTPA2*) have been reported in familial pulmonary fibrosis and result in misfolding and aggregation of surfactant proteins within these cells[48, 49]. These mutations induce endoplasmic reticulum (ER) stress and persistent activation of the unfolded protein response (UPR), leading to epithelial inflammation and apoptosis[50]. Although these mutations are rare in sporadic IPF (approximately 1%)[51], evidence of ER stress and UPR activation is commonly observed in alveolar epithelial cells[52].

In addition to genetic predisposition, environmental factors have been implicated in disease development. Epidemiological studies have identified associations with gastroesophageal reflux disease[53], cigarette smoke exposure[54], air pollution, and occupational exposures to wood, metal, and organic dusts[55], as well as viral infections[8, 56]. These exposures may induce cumulative oxidative stress, DNA damage, and epigenetic alterations in alveolar epithelial cells, contributing to disease development in susceptible individuals[57].

The marked increase in IPF prevalence with advancing age[58] highlights ageing as a critical risk factor. Studies of familial pulmonary fibrosis have provided insight into mechanisms linking ageing to disease susceptibility, including telomere shortening and ER stress[46, 52]. In addition, multiple hallmarks of ageing—including telomere attrition, DNA damage, mitochondrial dysfunction, impaired proteostasis, dysregulated autophagy, and cellular

senescence—are evident in IPF, particularly within alveolar epithelial cells, supporting a central role for ageing in disease initiation[59].

1.2.2 Alveolar epithelial cell injury and dysfunction

In the healthy lung, the alveolar epithelium is comprised of two alveolar epithelial cell (AEC) populations. Type 1 alveolar epithelial (AT1) cells facilitate gas exchange, forming a thin barrier for the diffusion of oxygen and carbon dioxide, while AT2 cells, in addition to surfactant production, act as progenitor cells capable of self-renewal and differentiation into AT1 cells during homeostasis and following injury. It is widely proposed that in IPF, a combination of genetic and environmental susceptibility factors, together with intrinsic age-related changes, results in AT2 dysfunction, which impairs the ability to effectively regenerate and repair the epithelium in response to repetitive environmental insults[57, 60].

Cellular senescence, linked with ageing and age-related disorders, is characterised by cell cycle arrest, limiting proliferation and differentiation in response to injury[59]. AT2 cell populations have been shown to express markers of senescence in IPF compared to controls in several studies[61, 62, 63, 64]. Yao et al demonstrated that induction of AT2 senescence using a Sin3a loss-of-function model resulted in spontaneous fibrosis in mice, whereas whilst the use of senolytics directed at senescent AT2 cells protected against fibrosis development[64]. Senescent cells also adopt a senescence-associated secretory phenotype (SASP), resulting in the release of both pro-inflammatory and profibrotic mediators, including TGF-β and matrix metalloproteinases (MMPs), the latter of which have been proposed as a mechanism through which AT2 cells may initiate fibrogenesis[64].

Several causes of AT2 senescence have been proposed. Telomere shortening has been observed in AECs in both familial and sporadic IPF[47] and is recognised to promote a senescent phenotype through persistent activation of a DNA damage response (DDR)[65]. Induction of telomere dysfunction in mice resulted in telomere shortening, the emergence of senescent AECs, and subsequent lung remodelling and fibrosis[66]. Separately, smoking is associated with both telomere shortening and increased AT2 oxidative stress and mitochondrial dysfunction, which can directly cause DNA damage and senescence[67, 68].

In addition, impaired mitochondrial homeostasis, a hallmark of both cellular senescence and ageing, is a prominent feature of IPF[69, 70]. AT2 cells from patients with IPF demonstrate dysmorphic mitochondria with swollen cristae, impaired oxidative

phosphorylation, and defective mitophagy, leading to accumulation of dysfunctional organelles[70, 71]. These alterations result in increased production of mitochondrial reactive oxygen species, which can induce DNA damage and further promote cellular senescence[59].

ER stress represents another mechanism linking epithelial dysfunction to fibrosis and has been identified in AT2 cells in sporadic IPF, in addition to familial cases associated with surfactant gene mutations[52, 72]. In sporadic IPF, increased AT2 ER stress has been attributed to mitochondrial dysfunction[70] and viral infections[52]. Persistent ER stress promotes epithelial apoptosis and senescence, both key pathological features of IPF. Importantly, induction of AT2-specific ER stress in murine models, for example through deletion of the ER chaperone GRP78, results in epithelial cell apoptosis, senescence, and progressive fibrosis, while pharmacological attenuation of ER stress ameliorates fibrotic responses[73].

In addition to intrinsic cellular dysfunction, disruption of epithelial barrier integrity may further perpetuate injury. Increased permeability of the alveolar barrier allows enhanced exposure to environmental and endogenous stimuli, amplifying epithelial stress and sustaining a cycle of damage and maladaptive repair. Collectively, these findings support the concept that AEC dysfunction is a central feature in the initiation of IPF pathogenesis, linking susceptibility factors such as ageing and genetic predisposition to downstream fibrotic remodelling[57, 60].

1.2.3 Epithelial – mesenchymal interactions

Progression from epithelial injury to fibrosis is mediated, in part, by dysregulated epithelial–mesenchymal crosstalk. Injured epithelial cells secrete a range of profibrotic mediators, including TGF-β, PDGF, FGF, and connective tissue growth factor (CTGF), which collectively promote fibroblast recruitment, proliferation, and activation[74, 75].

Among these, TGF-β is widely regarded as the central mediator of fibrosis. It drives fibroblast differentiation into myofibroblasts, enhances extracellular matrix (ECM) synthesis, and suppresses matrix degradation[76]. Although multiple cell types contribute to increased TGF-β production in IPF, specific overexpression of AT2-derived TGF-β is sufficient to induce pulmonary fibrosis in murine models[77]. In addition, AT2 dysfunction secondary to non-injurious senescence or ER stress also results in increased TGF-β expression and fibrotic remodelling[50, 64].

Activation of latent TGF-β within the extracellular matrix is mediated by integrins, notably αvβ6 expressed on epithelial cells, thereby directly linking epithelial injury to fibrotic signalling[78].

1.2.4 Fibroblast activation and extracellular matrix deposition

Fibroblast activation and myofibroblast differentiation represent the fibrogenic phase of IPF pathogenesis. Activated fibroblasts accumulate within fibroblastic foci, which are sites of active ECM deposition. Myofibroblasts within these foci are characterised by expression of alpha smooth muscle actin (αSMA) and produce large quantities of ECM components, including type I and III collagen, fibronectin, and proteoglycans[79].

A defining feature of IPF is the persistence of fibroblast activation, for which several mechanisms have been proposed. Studies have demonstrated that fibroblasts are resistant to apoptosis, mediated in part by downregulation of the death receptor Fas and upregulation of anti-apoptotic genes[80]. In addition, decreased prostaglandin E2 in IPF further protects against fibroblast apoptosis and limits myofibroblast dedifferentiation[81, 82].

Mechanical factors related to the ECM also contribute to sustained fibroblast activation. Increased ECM stiffness, driven in part by continual matrix remodelling, activates mechanosensing pathways in fibroblasts, resulting in persistent activation. Studies have shown that culture of normal fibroblasts on acellular IPF lung tissue induces TGF-β expression and myofibroblast differentiation mediated by Rho/ROCK signalling[83].

The transcriptional regulators yes-associated protein (*YAP*) and transcriptional coactivator with PDZ-binding motif (*TAZ*) have also been identified as key mediators of mechanosensing-driven fibroblast activation. *YAP/TAZ* expression is upregulated in IPF fibroblasts and in fibroblasts cultured on pathologically stiff ECM, but not on soft matrices. Knockdown of both factors attenuates fibroblast activation, ECM synthesis, and proliferation, whereas transfer of fibroblasts overexpressing YAP or TAZ into murine lungs promotes fibrosis[84].

In addition to promoting ECM synthesis and fibrogenesis, a recent study demonstrated that genetic ablation of *YAP/TAZ* induces a PDGF receptor-negative fibroblast phenotype. YAP/TAZ$^{-/-}$ fibroblasts cultured with AT2 cells promoted AT2 proliferation and differentiation compared to wild-type counterparts, indicating that fibroblast YAP/TAZ signalling may also impair normal AT2 regeneration[85]. Collectively, these studies demonstrate that fibroblasts within the ECM-dense IPF lung can establish a self-sustaining cycle in which tissue remodelling perpetuates fibrotic signalling.

Recent transcriptomic studies have further highlighted the heterogeneity of fibroblast populations in IPF, with distinct subsets performing specialised roles in matrix production, inflammation, and tissue remodelling[62, 86, 87]. These findings suggest that targeting specific fibroblast subpopulations may represent a future therapeutic strategy.

1.2.5 Contribution of immune cells

As outlined above, the current model emphasises the central role of repetitive alveolar epithelial injury, aberrant epithelial–mesenchymal crosstalk, and dysregulated wound repair as the key mechanisms, rather than chronic inflammation. This paradigm shift is, in part, a result of the failure of broad immunosuppression in clinical trials to improve patient outcomes, most notably in the PANTHER-IPF trial, where the use of prednisolone, azathioprine, and acetylcysteine resulted in increased rates of hospitalisation and death in the treatment arm[88]. However, significant infiltration of both innate and adaptive immune cell populations is evident in IPF histopathological sections. Moreover, although immune-mediated inflammation may not be central to disease initiation, accumulating evidence suggests that immune dysfunction contributes to epithelial injury, fibroblast activation, extracellular matrix remodelling, and disease progression.

Increasing evidence implicating monocytes and macrophages has begun to emerge and is outlined below. In addition, other innate and adaptive immune cells have also been associated with disease development.

Neutrophils are consistently associated with disease severity in IPF, although their precise pathogenic role remains incompletely defined. Bronchoalveolar lavage (BAL) neutrophilia is associated with poor prognosis and early mortality[89], while increased circulating neutrophil counts and higher neutrophil-to-lymphocyte ratios are consistently associated with greater lung function decline and mortality[90].

Mechanistically, neutrophils contribute to fibroblast activation through degradation of ECM components via the release of serine proteases, particularly neutrophil elastase[91, 92]. In experimental models, neutrophil elastase-deficient mice exhibit reduced fibrosis following bleomycin and asbestos-induced lung injury, associated with lower TGF-β expression, reduced fibroblast infiltration, and diminished myofibroblast activation. However, neutrophil depletion during the inflammatory phase following bleomycin injury does not prevent fibrosis development, although levels of matrix metalloproteinases are reduced at early time points[93].

In addition, neutrophils can release neutrophil extracellular traps (NETs), containing chromatin and granular proteins, which have been shown in vitro to promote fibroblast activation and differentiation into collagen-secreting myofibroblasts[94]. These findings suggest that neutrophils may contribute to IPF by promoting fibroblast activation and modulating ECM degradation, rather than directly inducing epithelial injury.

Innate lymphoid cells (ILCs), particularly type 2 ILCs (ILC2s), have also been implicated in IPF. These cells are located in close proximity to AECs and are activated by epithelial-derived alarmins, including IL-33 and thymic stromal lymphopoietin (TSLP), released by

AECs in response to injury. Upon activation, ILC2s secrete type 2 cytokines, including IL-13 and IL-25.

ILC2s are increased in IPF BAL samples, and depletion of ILC2s or IL-13-deficient ILC2s results in reduced fibrosis in *Schistosoma mansoni* egg–induced fibrosis models[95]. However, it is important to note that this model is characterised by granulomatous inflammation and fibrosis, which is not a typical feature of IPF, and this must be considered when interpreting these findings. Notably, the alarmin IL-33 is highly expressed in IPF[96]. In bleomycin-induced fibrosis, exogenous IL-33 exacerbates fibrosis and is accompanied by increased ILC2 expansion and IL-13 expression. Furthermore, adoptive transfer of ILC2s increases TGF-β expression and enhances fibrosis in these models, whereas IL-33 blockade reduces fibrosis severity[97].

Adaptive immune responses in IPF are complex and reflect lymphocyte heterogeneity and function. Although lymphocyte infiltration is well documented in IPF, with aggregates of $CD4^+$ T cells present within fibrotic lung tissue, their specific contribution to disease remains incompletely understood.

Among $CD4^+$ T cells, T helper 2 (Th2) and T helper 17 (Th17) subsets have been implicated in fibrotic processes. Th2 cytokines, particularly IL-4 and IL-13, promote fibroblast activation and ECM deposition[98]. IL-13 expression is increased in IPF BAL fluid and lung tissue[99]. Furthermore, blockade of this pathway limits fibroblast proliferation and restricts fibrosis development in humanised murine models[99]. However, an early-phase trial of IL-13 blockade with tralokinumab in IPF failed to demonstrate clinical benefit, as measured by lung function decline at 52 weeks[100].

Th17 cells have also been implicated in pulmonary fibrosis. Increased IL-17 has been observed in IPF BAL samples[101], and IPF fibroblasts express the IL-17 receptor and show enhanced activation following IL-17 exposure[102]. In murine models, IL-17 blockade protects against bleomycin- and radiation-induced fibrosis[103, 104]. In addition, Th17 cells highly express the checkpoint inhibitor programmed death-1 (PD-1) and represent a major TGF-β-expressing $CD4^+$ subset. Co-culture of $CD4^+PD1^+$ cells with fibroblasts promotes collagen production, whereas PD-1 blockade reduces $CD4^+$ IL-17 expression and fibroblast collagen synthesis[105].

Studies of regulatory T cells (Tregs) have yielded conflicting results, with both increased and decreased Treg abundance reported in IPF BAL fluid and blood samples[106, 107]. A recent transcriptomic study demonstrated that circulating Treg proportions are reduced in stable disease compared to controls but return to control levels in patients with progressive IPF[108]. Functional studies in murine fibrosis models show that both depletion and adoptive transfer of Tregs can influence the development and extent of fibrosis[109, 110]. A further study suggests that Tregs may have stage-dependent effects, promoting TGF-β

production and collagen synthesis during the inflammatory phase of fibrogenesis while inhibiting TGF-β production in established fibrosis[111].

B cells have also been implicated in IPF. Increased B cell numbers are observed in IPF tissue, where they localise with $CD4^+$ T cells in lymphoid aggregates within the interstitium and persist into advanced disease[112]. Circulating autoantibodies against antigens localised to the alveolar epithelium and vimentin, expressed on mesenchymal cells, are more frequently detected in patients with IPF than in those with sarcoidosis or controls[113, 114]. Expression of autoantibodies against vimentin also correlates with poorer outcomes in IPF patients. Functional studies demonstrate that $CD4^+$ T cells exhibit increased proliferation and effector function when stimulated with vimentin in an HLA-DR–dependent manner, indicating evidence of autoreactivity[115]. In addition, increased expression of B cell activating factor (BAFF), a key regulator of B cell maturation and survival, has been reported in IPF blood and BAL samples[116]. Despite these observations, the direct contribution of B cells and autoreactive antibodies to fibrosis has not been established.

In summary, IPF is a disease of aberrant wound healing driven by repetitive epithelial injury in a susceptible host, with epithelial dysfunction and fibroblast activation representing central pathological processes. Immune cells, including both innate and adaptive populations, likely play an important but incompletely defined role in modulating these pathways. Elucidating these contributions will aid in identifying therapeutic targets[117, 118, 119]. The contribution of monocytes and macrophages to IPF pathophysiology, which is the focus of this study, is explored in the next section.

1.3 Monocytes and Macrophages

1.3.1 Monocyte subsets and function

Monocytes are bone marrow derived members of the mononuclear phagocyte system and often considered the circulating counterparts to tissue macrophage populations.

Circulating monocytes can be divided into three broad populations based on expression of the lipopolysaccharide (LPS) coreceptor, CD14 and FCγIII receptor CD16[120, 121]. In humans $CD14^+$ $CD16^{-/lo}$ monocytes comprise ~ 80% of circulating monocytes and also referred to as ‘classical monocytes’. $CD14^{lo}CD16^+$ monocytes, account for 10-15% of peripheral monocytes, and often referred to as ‘non-classical’ or ‘patrolling’ monocytes. A population of $CD14^+$ $CD16^+$ comprise ~ 5% circulating monocytes and often referred to as Intermediate monocytes. In conventional flow cytometry all three populations of

monocytes are detectable in the PBMC fraction after excluding lymphocytes and NK cells followed by examining CD14/CD16 expression which allows identification of these monocytes subsets. In mice two monocyte subsets are described: Ly6C^{hi} CX3CR1^{lo} CCR2^{hi} are analogous to classical monocytes whilst Ly6C^{lo}, CX3CR1^{hi} CCR2^{lo} share transcriptional overlap with non-classical monocytes[122, 123].

Classical monocytes represent a transient cell population, with a lifespan in the circulation of approximately 1 day. In steady state conditions these cells then either migrate into tissue to replenish tissue macrophage populations[124], or remain in the circulation where they differentiate into non classical monocytes that remain in the blood for between 7-14 days[124]. During steady state tissue engraftment classical monocytes undergo significant transcriptional reprogramming, in response to local environmental cues and adopt a phenotype similar to tissue resident macrophage populations although transcriptional and functional differences do remain[125, 126, 127, 128].

In addition to steady state replenishment, classical monocytes are recruited to tissues following localised injury, infection and sterile inflammation[129]. This process is largely mediated by CC-chemokine receptor 2 (CCR2) which is highly is expressed on this monocyte subset although redundancy in CCR expression also exists. Upon recruitment, classical monocytes adopt a pro-inflammatory phenotype characterised by the production of cytokines including tumour necrosis factor a (TNF-α), expression of inducible nitric oxide synthase (iNOS), and secretion of chemokines, enabling antimicrobial activity and recruitment of additional immune cells. Infiltrating inflammatory monocytes also participate in antigen presentation[130, 131]. In the context of sterile inflammation, autoimmune disease, cancer and tissue fibrosis monocytes can differentiate into macrophages with a range of functional phenotypes including inflammatory, antigen presentation, regulatory and fibrotic states depending on the injury or disease context and are implicated in both progression and resolution of tissue pathology[121].

In contrast, non-classical monocytes do not contribute to tissue macrophage populations in homeostatic conditions, as demonstrated by preserved tissue macrophage populations when these cells are depleted[132]. Instead, non-classical monocytes are primarily located adherent to the luminal aspect of vascular endothelium and display a distinct crawling motility pattern[133]. At these sites, they survey the vasculature for pathogens and pathogen associated molecular products (PAMP)s including nucleic acids[134]. Non classical monocytes also perform homeostatic functions at the intimal aspect of the endothelium including scavenging microparticles and the detection and phagocytosis of apoptotic or injured endothelial cells[135].

Intermediate monocytes exhibit high expression of major histocompatibility complex (MHC)II molecules indicating a role in antigen presentation. In addition, these cells also demonstrate increased proinflammatory cytokine production in response to toll like receptor (TLR) stimulation[136]. Consistent with these observations this subset is enriched in systemic infection[137] and in inflammatory mediated diseases including atherosclerosis[138] and rheumatoid arthritis[139].

1.3.2 Lung macrophages in homeostasis

Macrophages are the most abundant immune cell population in the lung. Over the past decade the complexity and phenotypic heterogeneity of both tissue resident and infiltrating macrophage populations in the lung and other organs have become increasingly recognised[140, 141, 142].

Lung macrophages can be broadly categorised based on anatomical location and by ontogeny. Anatomically two fundamental populations are recognised; alveolar macrophages (AMs) which reside on the luminal aspect of the alveoli and conducting airways and interstitial macrophages (IMs), which are located within the lung interstitium and surrounding airways and pulmonary vessels[143].

The populations are morphologically and phenotypically distinct and perform a number of crucial homeostatic and effector functions. Differences in function are in part determined by local factors including nutrient availability, cellular metabolism and the cytokine and growth factor milieu secreted by neighbouring populations. AM exhibit a lipid metabolic profile with reduced glycolysis[144, 145] and rely on AT2 derived colony stimulating factor 2 (CSF2) for survival[146, 147, 148, 149]. In contrast IMs rely on CSF1 for survival at least in mice. The understanding of environmental factors influencing the phenotype of IMs is less well established compared to AMs[150]. The importance of the lung environment is further highlighted in a study demonstrating that murine AMs undergo substantial transcriptional and epigenetic changes *ex vivo*, which is reversed with adoptive transfer back into the lung environment[145].

AM and IM subsets and can be identified and distinguished by surface marker expression in both humans and mice [151, 152, 153]. Although marker expression differs between species single cell studies have confirmed transcriptomic overlap between analogous populations[154]. Single cell studies have also enabled different subsets of myeloid populations to be identified based on transcriptomic profile in both species including AM and IM subsets that can also be distinguished from lung monocytes and DCs[141, 155, 156].

The primary homeostatic function of AMs is the clearance of inhaled particles, pathogens, and apoptotic alveolar epithelial cells through efferocytosis and degradation in an immunologically 'silent' manner, thereby limiting excessive inflammation. Homeostatic AMs exhibit high efferocytosis capacity[157], facilitated by high expression of scavenger receptors including Marco, MerTK and Axl[158]. AMs highly express TGF-β, IL-1 receptor antagonist (IL-1ra) and prostaglandins to modulate localised inflammation[159]. In addition, AMs play a central role in pulmonary surfactant homeostasis and deficiency of AMs results in spontaneous pulmonary alveolar proteinosis in both humans and mice[160, 161].

The homeostatic function of IM's is less well defined although they also confer an immune regulatory role through the production of IL-10[162, 163]. IMs are also capable of efferocytosis[164] and support epithelial cell and fibroblast homeostasis via platelet derived growth factor production[165]. Single cell transcriptomic studies have revealed further heterogeneity exists particularly within the broader IM population with at least three subsets identified in both mice and humans occupying distinct anatomical locations. Transcriptomic analysis has begun to identify differences in these distinct populations[150, 166].

1.3.3 Lung macrophage ontogeny in ageing and following injury

In addition to anatomical location, lung macrophages can be classified based on ontogeny as tissue resident macrophages (TRM) and monocyte derived macrophages (MDM).

Yolk sac and fetal liver monocytes colonise the lung during embryonic development and prior to birth. These populations are capable of self-renewal and give rise to TRMs that maintain both AM and IM pools in steady state. This has been demonstrated in mice by parabiotic studies[148, 167, 168] and humans through analysis of sex mismatched lung transplant recipients[169, 170].

However, with increasing age, MDMs contribute to both AM and IM pools in health in both mice[164, 166] and humans[171]. Fate-mapping studies provide further insight into the temporal dynamics of this process. Chakarov et al. employed a model in which *S100a4*-expressing monocytes were labelled with EYFP[166]. In this model, at 8 weeks of age, EYFP expression was present in IM populations but not in AMs indicating that the monocyte contribution to the IM compartment occurs earlier in life, whereas replacement of AMs by MDMs occurs later[166].

In the context of infection or inflammatory insult, a reduction in TRM populations is often seen, accompanied by a significant influx of monocytes that differentiate into MDMs[172, 173]. Lineage tracing studies examining recruited MDMs following bleomycin have confirmed MDM populations are capable of long-term renewal, persist alongside TRM populations and have been observed up to 12 months after recruitment[172].

MDM often exhibit an initial inflammatory transcriptional phenotype, in addition, they can retain an altered transcriptional profile and functional properties for a period after injury[172, 173, 174, 175]. For example, one month after influenza infection, AMs display increased IL-6 expression and protection from subsequent *streptococcus pneumonia* infection compared to AMs from mice not exposed to influenza. Adoptive transfer experiments have demonstrated the protective AM population were monocyte derived and retained a transcriptomic profile resembling circulating monocytes[173]. Similarly, following intratracheal BCG vaccination, monocyte derived IMs, persist in the lung and confer protection against both *mycobacterium tuberculosis* and *streptococcus pneumonia* 8 weeks after vaccination[174].

Despite this, several studies indicate that over time, recruited MDMs progressively adopt phenotypic and transcriptional characteristics similar to TRMs as the lung environment returns to homeostasis[172, 173, 174] . Collectively, these studies highlight that recruited MDM populations contribute to lung macrophage heterogeneity. In the context of chronic injury or disease, where the lung environment is persistently altered, this heterogeneity may be further amplified.

1.3.4 Contribution of monocytes to IPF pathogenesis

There is increasing evidence supporting a role for monocytes in the pathogenesis of IPF. Several large clinical observational studies have identified an association between peripheral blood monocyte counts and disease prognosis in IPF[14, 176, 177].

Scott et al. demonstrated that the proportion of $CD14^+$ monocytes within peripheral blood mononuclear cells (PBMCs) were increased in patients with IPF compared to healthy controls. Furthermore, absolute $CD14^+$ monocyte counts were significantly higher in patients with progressive disease compared to those with non-progressive disease. Importantly, a total monocyte count >0.95 $\times 10^3$ cells/μL at the time of diagnosis was independently associated with an increased risk of all-cause mortality or lung transplantation, after adjustment for age, baseline lung function, and the GAP (Gender, Age, Physiology) index—established predictors of prognosis[16, 17]. Notably, this threshold conferred a greater hazard ratio than age, sex, baseline lung function, or GAP index[176].

These findings were subsequently replicated in a larger retrospective study of 2,067 patients with IPF. In this study patients with a monocyte count of >0.65 $\times 10^3$ cells/μL were associated with an increased risk of disease progression, hospitalisation, and all-cause mortality[177].

In addition, a study investigating patients with indeterminate usual interstitial pneumonia (iUIP)-a radiological entity considered a precursor to clinical IPF-demonstrated that higher monocyte counts, analysed both as a continuous variable and using a threshold (>0.9 $\times 10^3$ cells/μL), were significantly associated with an increased risk of progression to IPF. This association remained significant in both univariate and multivariate analyses adjusting for established predictors, including age, sex, smoking status, and FVC[14].

Murine studies in several lung injury models provide evidence supporting a causal role for monocytes in the development of pulmonary fibrosis. Depletion of circulating $Ly6C^+$ monocytes using intraperitoneal (i.p.) administration of liposomal clodronate resulted in a significant reduction in fibrosis following both bleomycin and TGF-β induced lung injury. This was demonstrated by reduced collagen deposition on Masson's trichrome staining and decreased whole-lung expression of Col1a1 and αSMA. Conversely, adoptive transfer of $Ly6C^+$ monocytes during the fibrogenic phase following bleomycin injury exacerbated fibrosis compared to bleomycin treatment alone[178].

In a separate study a specific AT2 injury model using transgenic mice expressing the human diphtheria toxin receptor under the control of the surfactant protein c (SFTPC) promotor was used to selectively deplete AT2 cells. Diphtheria toxin administration resulted in lung fibrosis accompanied by accumulation of $Ly6C^+CCR2^+$ monocytes and an exudative macrophage (ExM) population. Genetic deletion of CCR2 reduced the accumulation of both cell populations and was associated with attenuated fibrosis, as well as reduced weight loss and mortality[179].

A distinct lung monocyte population, termed segregated nucleus-containing atypical monocytes (SATMs), has been shown to directly contribute to the development of bleomycin-induced fibrosis. Morphologically, SATMs exhibit a bi-lobed, segregated nucleus and originate from granulocyte, rather than macrophage or dendritic cell, progenitors in the bone marrow. This population uniquely expresses *CCAAT/enhancer-binding protein β* (*C/EBPβ*) among lung myeloid populations. Depletion of SATMs in *C/ebpβ*$^{-/-}$ mice reduced fibrosis following bleomycin injury whereas adoptive transfer of SATMs into *C/ebpβ*$^{-/-}$ or wild-type mice restored and exacerbated fibrosis respectively[180]. How this SATM population relates to $CCR2^+$ dependent classical monocytes described in other studies remains unclear.

A separate study from my supervisor's group investigating circulating monocytes in patients with IPF identified several phenotypic and functional abnormalities. Both the proportion and absolute number of circulating monocytes were increased in IPF compared to age and sex matched controls, consistent with findings from larger observational studies. In addition, monocytes exhibited increased expression of CD64 which correlated with CT fibrosis scores and interferon-stimulated gene (ISG) expression. $CD14^+$ monocytes ex vivo demonstrated increased expression of type 1 interferon (type 1 IFN) related gene sets compared to controls and showed an exaggerated ISG response following IFN-β stimulation. Furthermore, patients with IPF exhibited elevated serum levels of IL-6, CCL2, and CSF-1, cytokines associated with monocyte activation, recruitment, and differentiation. Collectively, these findings suggest that $CD14^+$ monocytes in IPF display an activated phenotype, characterised by heightened basal type 1 IFN signalling and an increased responsiveness to further IFN stimulation[181].

Overall, current evidence suggests that monocytes contribute to IPF pathogenesis, with clinical associations and experimental models indicating roles in disease progression, although their precise contribution in human disease remains to be fully defined.

1.3.5 Contribution of lung macrophages to IPF pathogenesis

In addition to circulating monocytes there is growing evidence implicating lung macrophages in IPF pathogenesis and highlighting the relevance of macrophage heterogeneity in disease development.

Murine studies have demonstrated selective depletion of MDM, but not TRMs protects against the development of fibrosis in several murine models of pulmonary fibrosis. In a bleomycin injury model, Misharin et al demonstrated expansion of monocyte derived AMs and depletion of TR-AMs following injury. Using a strategy to induce necroptosis in differentiating monocytes, monocyte derived AMs were depleted whilst preserving monocyte and TR AM populations. Depletion of monocyte derived AMs resulted in a reduction in collagen staining and preservation of lung tissue architecture. In contrast, selective depletion of TR-AMs using intratracheal liposomal chlodronate did not confer protection against fibrosis[172].

These findings were supported in an asbestos induced model, where selective depletion of monocyte derived AMs either through necroptosis or blockade of CSF1 receptor signalling, also attenuated fibrosis[43]. Notably CSF1 receptor blockade also significantly reduced IM populations. Consistent with this, further studies have also demonstrated selective depletion of $CD11b^{hi}$ IM macrophages protects against bleomycin induced

fibrosis[182]. Although circulating monocyte numbers were not significantly reduced in these models, $CD11b^+$ IM populations are thought to be derived, at least in part, from monocytes.

Further supporting a role for monocyte-derived IMs, Brody employed a peptide-based radiotracer (^{64}Cu-DOTA-ECL1i) targeting $CCR2^+$ cells, including classical monocytes. Using mass cytometry, the authors demonstrated that $CCR2^+$ cells expanding following bleomycin injury comprised predominantly $Ly6C^+CCR2^+$ monocytes and monocyte-derived interstitial macrophages. In human lung tissue, $CCR2^+$ cells were primarily identified as $CD14^+CD16^-$ classical monocytes[183].

In murine models, positron emission tomography–computed tomography (PET-CT) imaging revealed increased uptake of the ^{64}Cu-DOTA-ECL1i tracer in the lungs of bleomycin-treated mice compared to both untreated controls and bleomycin treated $CCR2^{-/-}$ mice. Similarly, in patients with IPF, tracer uptake was significantly increased compared to healthy controls and co-localised with regions of reticulation and honeycombing on CT, corresponding to areas of active or established fibrosis. These findings support the expansion and recruitment of $CCR2^+$ monocytes and their progeny to sites of fibrotic injury in both experimental models and human disease[183].

In contrast, not all IM populations exert pro fibrotic effects. Chakarov et al identified two phenotypically distinct IM subsets: $Lyve1^{hi}$ $MHCII^{lo}$ and $Lyve1^{lo}$ $MHCII^{hi}$ IMs. The authors demonstrated depletion of $Lyve1^{hi}$ $MHCII^{lo}$ led to increased monocyte and neutrophil infiltration alongside increased collagen deposition following bleomycin injury[166].

Collectively, these findings demonstrate that distinct macrophage populations exert both pathogenic and protective roles in experimental fibrosis. Monocyte derived AM and IM appear to promote fibrotic responses, whereas other macrophage subsets may confer protection.

Further evidence highlighting a role of particularly macrophages in IPF have emerged from single cell transcriptomic profiling of lung digests from IPF patients undergoing transplantation. Amongst immune cell populations, several groups have identified a macrophage population in IPF expressing osteopontin (SPP1)[62, 86, 184, 185]. This population has been shown to be expanded in IPF patients[86, 185] and in close proximity to αSMA expressing fibroblasts[86].

1.4 Type 1 Interferon Signalling

1.4.1 Overview of the type 1 IFN signalling pathway

Findings from the study described above[181] (Section 1.3.4) identified increased type 1 interferon (IFN) signalling in circulating monocytes in IPF. To provide context to this finding, the following section outlines the type 1 IFN signalling pathway, biological consequences of IFN signalling on cellular function and diseases associated with dysregulated type 1 IFN responses.

There are three groups of interferons, type 1 (IFN-α/β), induced downstream of PRR signalling; type 2 (IFN-γ), produced mainly by activated immune cells and Th1 responses; and type 3 (IFN-λ), with similar function as type 1 IFN but restricted to mucosal epithelial cells.

The type 1 IFN signalling pathway comprises two key stages: activation of innate immune sensing pathways leading to transcription and secretion of type 1 IFNs. These cytokines then bind to the interferon α/β receptor (IFNAR), initiating downstream signal transduction and resulting in the expression of hundreds of interferon-stimulated genes (ISGs) within both the producing cell and neighbouring cells. This pathway is evolutionarily conserved, and most cell types are capable of both producing and responding to 1IFNs

Type 1 IFN production is initiated following recognition of pathogen-associated molecular patterns (PAMPs) and damage-associated molecular patterns (DAMPs) by pattern recognition receptors (PRRs). These include endosomal Toll-like receptors (TLR3, TLR7/8 and TLR9), cytosolic RNA sensors such as RIG-I and MDA5, and DNA-sensing pathways including cyclic GMP–AMP synthase (cGAS)–stimulator of interferon genes (STING)[186, 187, 188, 189]. TLR4, localised at the cell surface, can also initiate can initiate type 1 IFN responses following stimulation by ligands such as LPS and RSV fusion protein[190]. Activation of these pathways initiates downstream signalling cascades converging on phosphorylation of interferon regulatory factors 3 and 7 (IRF3/7) resulting in transcription of type 1 IFNs. Many PRRs involved in type 1 IFN transcription, including TLR 3/4, RIG I like receptors and cGAS-STING signalling also activate NF-κB signalling promoting transcription of additional inflammatory cytokines and chemokines.

These PRR pathways are typically associated with antimicrobial immunity responding to viral and bacterial nucleic acids, including endosomal viral ssRNA (TLR7/8) and dsRNA (TLR3), unmethylated CpG DNA (TLR9), as well as cytoplasmic dsRNA (RIG-I, MDA5) and cytoplasmic dsDNA (cGAS-STING)[186, 187]. In addition, increasing evidence demonstrates that endogenous DAMPs released during tissue injury or intrinsic cellular stress can

activate the same pathways. These include mitochondrial DNA (TLR9, cGAS-STING)[191, 192] and self-ds DNA/RNA (RIG-I, cGAS-STING)[188, 193] that can activate the same PRR pathways inducing sterile inflammation.

The transmembrane IFNAR consists of two subunits, IFNAR1 and IFNAR2, associated with TYK2 and JAK1 respectively. Binding of type 1 IFNs induces receptor dimerization, leading to autophosphorylation of TYK2 and JAK1 and subsequent phosphorylation and activation of STAT proteins. In canonical type 1 IFN signalling, STAT1–STAT2 heterodimers associate with IRF9 to form the interferon-stimulated gene factor 3 (ISGF3) complex, which translocate to the nucleus and promotes transcription of genes containing interferon-stimulated response elements (ISREs), including classical antiviral ISGs[194, 195, 196]. Additional STAT complexes can form following IFNAR dimerization including STAT1 homodimers that bind to genes expressing gamma-activated sequence (GAS) elements driving transcription of pro-inflammatory genes. In addition, STAT3 homodimers that competitively bind to GAS elements preventing gene transcription and promote transcription of IL-10 to supress the IFN response[197]. Beyond JAK–STAT signalling, type 1 IFN signalling can also activate a range of non-canonical pathways (Figure 1.4.1). These include MAPK, PI3K–AKT, and mTOR signalling cascades, that further modulate cellular activity and alter the response to IFN signalling (Figure 1.4.1).

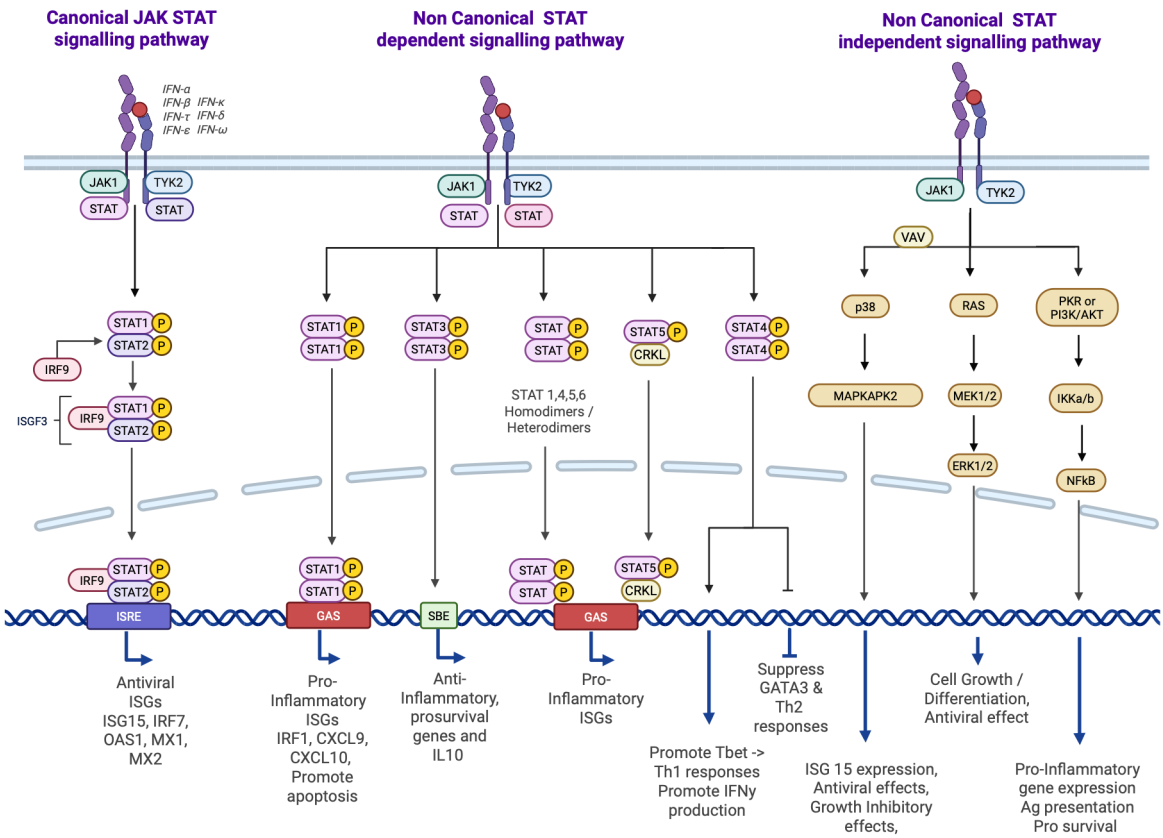


***Figure 3.3.5. Overview of downstream responses following type 1 IFN signalling**. Binding of type I IFNs to the IFNAR1/2 receptor complex activates JAK1 and TYK2, leading to phosphorylation of STAT1 and STAT2, formation of the ISGF3 complex (STAT1–STAT2–IRF9), and transcription of ISGs via ISREs. In addition, STAT1 homodimers, induced by both type 1 and type 2 IFNs, bind to GAS elements to promote transcription of pro-inflammatory and pro-apoptotic genes. STAT3 homodimers can also be activated, promoting anti-inflammatory responses, including induction of IL-10. Type 1 IFNs also initiate STAT-dependent and STAT-independent non canonical signalling pathways, depending on cell type and context, including STAT4,5,6, PI3K–AKT signalling, which, contributes to IL-10 production, and activation of p38 MAPK and mTOR pathways resulting in diverse cellular outcomes, including antiviral defence, inflammatory signalling, cell survival, and differentiation. Abbreviations; IFNAR, interferon-α/β receptor; JAK, Janus kinase; TYK2, tyrosine kinase 2; STAT, signal transducer and activator of transcription; IRF9, interferon regulatory factor 9; ISGF3, interferon-stimulated gene factor 3; ISG, interferon-stimulated gene; ISRE, interferon-stimulated response element; GAS, gamma-activated sequence; PI3K, phosphoinositide 3-kinase; MAPK, mitogen-activated protein kinase; mTOR, mechanistic target of rapamycin. Figure adopted from Gonzalez Navajas Nature Review Imm 2012[198].*

In addition to the diversity in downstream signalling, multiple additional layers of regulatory control exist that alter the type 1 IFN response including IFNAR expression, availability of cytoplasmic STAT proteins and post translational modification of STAT proteins. In addition, activation of other innate pathways and cytokines can cross regulate the type 1 IFN response by priming or altering the STAT response or promoting expression of negative regulators such as SOCS proteins or USP18 that supress IFN signalling. Together, these mechanisms alter the magnitude, duration, and ISG profile of IFN responses and influence downstream cellular behaviour[196, 199].

1.4.2 Type 1 IFN signalling in myeloid cell function

As outlined above, the effects of type-I IFN signalling on cellular function are highly dependent on both cell type and biological context. The complexity and heterogeneity of IFN responses across different cell populations, in both health and disease, remain incompletely understood. This section summarises current understanding of type 1 IFN-mediated effects on myeloid cell function in the context of infection.

In acute viral infection cells respond to autocrine type 1 IFN signalling, produce hundreds of ISGs that induce an anti viral state. Infected cells also secrete inflammatory cytokines and chemokines that recruit immune cell and module the innate and adaptive response. In this context type 1 IFNs enhance antigen presenting cell function by upregulation of MHCII molecules and co-stimulatory molecules CD80/CD86, thereby enabling T cell activation[200, 201]. Concurrently, Concurrently, type 1 IFNs stimulate monocyte and macrophage production of iNOS[202]and proinflammatory cytokines including IL-6, IL-1β and TNF-α amplifying inflammatory and phagocytic responses[201].

However, the innate antiviral response can also contribute to immune mediated pathology. This was first described in influenza infection, where type 1 IFNs activation resulted in epithelial cell injury mediated by expression of TRAIL in inflammatory

monocytes and lung macrophages, leading to apoptosis of DR5 expressing epithelial cells[203, 204, 205]. Similarly, sustained type 1 IFN responses have been implicated in lung injury and epithelial dysfunction following SARS-CoV infection[206, 207].

In models of chronic viral infection, such as lymphocytic choriomeningitis virus (LCMV), prolonged type 1 IFN signalling exerts predominantly immunosuppressive effects on immune cell populations, including monocytes and macrophages. Sustained IFN signalling promotes increased expression of IL-10 and PD-L1 in antigen-presenting cells, including dendritic cells and macrophages. In these models, elevated type 1 IFN signalling is associated with impaired viral control and reduced survival, whereas blockade of IFNAR signalling reduces IL-10 and PD-L1 expression, restores lymphocyte numbers, and improves control of persistent infection[208, 209, 210].

1.4.3 Insights from type 1 IFN mediated diseases

Increased type 1 IFN signalling has been implicated in a number of inflammatory and autoimmune conditions including systemic lupus erythematosus (SLE), systemic sclerosis (SSc), Sjogrens syndrome and dermatomyositis (DM). A common feature of these diseases is the presence of a 'type 1 interferon signature' characterised by increased expression of ISGs in either circulating or tissue cell populations, which correlate with disease severity[211].

Several insights can be drawn from SLE, a disease where dysregulated type 1 IFN signalling has been extensively studied. In SLE, increased circulating type 1 IFN and ISG expression are associated with increased disease activity. Furthermore, type 1 IFN and ISGs, including MX1 have been detected in affected tissues in both skin and renal biopsies[212].

In SLE immune complexes containing nucleic acids are internalised by mononuclear phagocytes and activate endosomal TLRs 7/9 driving type 1 IFN production. Plasmacytoid DCs (pDCs), the principal producer of type 1 IFN have been implicated in disease progression found in regions of disease and sites of epithelial injury[212, 213]. Consistent with this depletion of pDCs improves disease outcomes in lupus animal models[214].

In addition to pDCs, monocytes have also been shown to produce type 1 IFNs in SLE[215] and also exibit increased ISG expression[216]. These cells also show enhanced inflammatory activity with increased expression of inflammasome associated genes and IL-1β production following prolonged exposure to IFN-α. Increased inflammasome expression was shown to be mediated by IFN signalling as IRF1 silencing reversed this[216].

A recent study has also demonstrated monocyte IL-1b expression was mediated by the ISG MxA but not associated with monocyte pyroptosis an inflammatory cell death often associated with inflammasome activation[215]. Collectively, these findings indicate that monocytes in SLE adopt a pro-inflammatory phenotype in response to sustained type 1 IFN exposure.

Systemic sclerosis (SSc) is an inflammatory disease characterised by progressive fibrosis affecting multiple organs, including the lung, where it manifests as an inflammatory ILD that is often complicated by pulmonary fibrosis. Notably, recent clinical trials have demonstrated that antifibrotic therapies used in IPF also reduce the rate of lung function decline in SSc-associated interstitial lung disease[217].

Increased type 1 IFN activity has also been implicated in SSc[218]. Elevated ISG expression has been identified in PBMCs[219] and IFN-α producing pDCs have been detected in areas of skin fibrosis[220]. In addition, increased ISG transcript levels and protein expression of OAS1 and IFI44 have been identified in lung tissue of patients with SSc associated fibrosis[221]. Consistent with this depletion of pDCs protects against disease in experimental models indicating an important role for these cells in disease pathology[220].

Importantly, an increased type 1 IFN signature has been observed in monocytes at the earliest stage of diseases, suggesting abnormal monocyte responses to type 1 IFN are also present and may contribute to disease initiation[222]. In addition, monoclonal antibody blockade of IFNAR in animal models reduced both dermal inflammation and skin fibrosis implicating abnormal IFN signalling in both inflammatory and fibrotic processs[223].

Collectively, studies in SLE and SSc demonstrate that dysregulated type 1 IFN signalling is associated with immune activation, altered myeloid cell function, and disease progression, with evidence that both pDCs and monocytes contribute to these responses. Notably, sustained type 1 IFN signalling promotes a pro-inflammatory and functionally altered monocyte phenotype, characterised by enhanced cytokine production and altered differentiation. Experimental studies in animal models with blockade of type 1 IFN signalling reduces fibrosis provides preliminary evidence this may contribute to tissue injury and fibrosis. These findings provide important insight into the potential relevance of increased type 1 IFN activity observed in IPF.

1.5 Study Aims

Despite evidence linking epithelial injury, aberrant repair, and fibroblast activation in IPF, the role of immune pathways in integrating these processes remains incompletely understood. In particular, while monocytes and macrophages are increasingly implicated in disease progression, their functional heterogeneity and the signals that govern their activation and function within the fibrotic lung are not fully defined. It is likely that these cells comprise distinct subsets with context-dependent roles that promote, sustain, or potentially restrain fibrotic remodelling.

Type 1 interferon signalling is a plausible candidate pathway linking epithelial dysfunction to myeloid activation. The pathway is activated downstream of both pathogen-associated and damage-associated molecular signals and is capable of exerting broad effects on monocyte and macrophage function, including modulation of inflammatory responses, antigen presentation, and cellular differentiation. Sustained or dysregulated interferon signalling can drive altered myeloid phenotypes that contribute to tissue injury and remodelling. In IPF, preliminary observations indicate increased interferon-stimulated gene expression and responses in circulating monocytes. However, it remains unclear whether this finding represents a systemic predisposition, a local tissue response, or a coordinated process linking circulation and lung. Furthermore, the spatial context in which interferon-associated myeloid states arise within the lung is unknown.

Given the central role of epithelial injury in IPF, it is plausible that dysfunctional epithelial cells provide a local source of signals that initiate or amplify interferon responses in neighbouring immune cells. Mechanistically, epithelial stress pathways associated with mitochondrial dysfunction, DNA damage, and senescence are capable of activating innate immune sensing pathways, including cGAS–STING and Toll-like receptor signalling, leading to production of type 1 IFNs. Whether such epithelial-derived signals contribute to the emergence of interferon-activated monocyte and macrophage populations in IPF, and how these interactions shape downstream fibrotic processes, remains to be determined.

Addressing these gaps requires an integrated, multi-scale approach that spans systemic immune profiling, tissue-level characterisation, spatial mapping, and experimental modelling. In this thesis, I examine type 1 IFN signalling across three interconnected contexts: circulating immune cells, the alveolar macrophage compartment, and the spatial microenvironment of the fibrotic lung. By combining high-dimensional single-cell technologies with spatial analysis and in vitro modelling, this work seeks to define how type 1 IFN signalling is distributed across monocyte and macrophage cell subsets, how

it relates to epithelial pathology, and whether epithelial injury can act as an initiator of disease in IPF.

I hypothesise that type 1 interferon signalling represents a unifying axis linking epithelial injury and myeloid cell activation in IPF.

The work in this thesis is structured around these aims -

1. To define type 1 interferon signalling in circulating immune cells in IPF, with a focus on monocyte subsets and their responsiveness to interferon stimulation.
2. To characterise monocyte and macrophage heterogeneity at the alveolar barrier, and to determine the association between interferon signalling and distinct transcriptional states.
3. To determine the spatial distribution and microenvironmental context of interferon-activated myeloid cells in IPF lung tissue, particularly in relation to epithelial injury and fibrotic niches.
4. To investigate epithelial–myeloid interactions using an in vitro alveolar organoid model, in order to assess whether epithelial dysfunction can induce interferon signalling and modulate myeloid cell responses.

Chapter 2 Materials and methods

2.1 Experiential Methods

Details of all reagents and antibodies used in this study, including vendor and product information, are provided in Table 2.1. Antibody panels for mass cytometry experiments are described in the relevant chapters

2.1.1 Peripheral blood mononuclear cell (PBMC) isolation and cryopreservation

Peripheral blood samples were collected in 9 ml EDTA-containing tubes and processed within 2 hours of collection. Peripheral blood mononuclear cells (PBMCs) were isolated by Ficoll density gradient centrifugation. Whole blood volume was recorded prior to dilution in an equal volume of R10 medium (RPMI-1640 (Sigma-Aldrich) supplemented with 10% fetal calf serum (FCS), 1% L-glutamine, and 1% penicillin–streptomycin).

A total of 25 ml of diluted blood was layered onto 15 ml of Lymphoprep™ (StemCell Technologies) and centrifuged at 2200 rpm for 20 minutes at room temperature with the brake disabled. The PBMC layer was collected, washed twice, and cell viability was assessed using trypan blue exclusion with an automated Countess haemocytometer.

Cells were centrifuged at 1500 rpm to obtain a pellet and resuspended in Gibco Recovery™ cell freezing medium (Thermo Fisher Scientific Scientific) at a concentration of 1 x 10^7 cells/ml. PBMCs were aliquoted into 1 ml cryovials and transferred to an insulated freezing container before storage at −80 °C overnight. Samples were subsequently transferred to liquid nitrogen for long-term storage.

2.1.2 Antibody conjugation to metal isotypes for mass cytometry

Antibody panel details (Antibody clone, catalogue number, metal isotope, dilution) outlined in Chapter 3.2 (suspension mass cytometry [CyTOF]), and Chapter 5.2 (imaging mass cytometry [IMC]).

Primary antibodies were conjugated to lanthanide metal isotopes using the Maxpar® X8 Antibody Labelling Kit (Standard Biotools) or to cadmium isotopes using the Maxpar® MCP9 Antibody Labelling Kit (Standard Biotools), according to the manufacturer's instructions. In brief, metal salts were combined with polymer chelators and incubated at 37 °C for 40 minutes. Antibodies (IgG subclass, albumin- and glycerol-free) were partially reduced by incubation with tris(2-carboxyethyl)phosphine (TCEP) for 30 minutes at 37 °C to generate free thiol groups. Reduced antibodies were then incubated with metal-loaded polymers for 90 minutes at 37 °C to allow conjugation. CD8 (CyTOF panel)

and HLA-E (IMC panel) were conjugated with 198Pt directly without initial polymer loading by conjugating partially reduced antibody with 198-Cisplatin (250μM) for 90 mins at 37°C.
Following conjugation, antibody concentration was determined by spectrophotometry at 280 nm. Conjugated antibodies were resuspended in antibody stabilisation buffer containing sodium azide at a final concentration of 0.5 mg/ml and stored at 4 °C.

Successful conjugation was confirmed by incubating 1 υL of conjugated antibody with UltraComp™ eBeads prior to acquisition on a third-generation mass cytometer (Standard Biotools) using CyTOF software (version 7.0).

2.1.3 PBMC IFN-β stimulation, antibody staining and CyTOF acquisition

Patient and donor selection criteria, demographic and clinical characteristics, ethical approval and antibody panel details (including dilutions) are described in Chapter 3.2.2

PBMC processing, IFN-β stimulation, antibody dilutions and staining performed as previously described by Rigby et al[224] Briefly, cryopreserved PBMCs were thawed at 37 °C, transferred into R10 medium containing benzonase (200 U/ml), and rested for 2 hours at 37 °C prior to automated cell counting. Cells were then incubated with the live/dead viability dye Cell-ID Cisplatin™ (Standard Biotools) for 5 minutes at 37 °C, followed by staining with fixation-sensitive lineage antibodies for 30 minutes at 37 °C. Cells from each sample were divided into two equal fractions and treated with either IFN-β (250 U/ml) or R10 medium alone for 15 minutes at 37 °C. Following stimulation, cells were washed in Maxpar PBS (Standard Biotools) and immediately fixed using Maxpar Fix I buffer for 10 minutes at 37 °C.

Each sample was subsequently barcoded using the Cell-ID 20-plex barcoding kit (Standard Biotools) according to the manufacturer's instructions. Barcoded samples were pooled, and Fc receptors were blocked for 10 minutes at room temperature prior to staining with cell surface antibodies for 30 minutes at room temperature. Cells were then permeabilised in ice-cold methanol and stored at -80 °C overnight.

The following day, samples were washed and stained with intracellular antibodies for 30 minutes at room temperature, followed by fixation in formaldehyde for 10 minutes. Cells were then incubated with Cell-ID Intercalator-Ir (125 mM; Standard Biotools), diluted in Maxpar Perm buffer, and stored at 4 °C overnight prior to acquisition.

Before acquisition, samples were washed, filtered through a cell strainer, and resuspended in Maxpar water containing EQ calibration beads (1:10 dilution). Data were

acquired on a Helios mass cytometer (Standard Biotools) at a rate of <300 events per second. Downstream data processing and analysis are described in Section 3.2.4.

2.1.4 Sample processing for droplet-based single-cell RNA sequencing

Patient and donor selection criteria, demographic and clinical characteristics, and ethical approvals are described in Sections 3.2.2 and 4.2.2.

Fresh peripheral blood and bronchoalveolar lavage (BAL) samples were collected from patients undergoing bronchoscopy at the John Radcliffe Hospital (Oxford University Hospitals NHS Foundation Trust) and processed within 30 minutes of collection. Samples were prepared for sequencing fresh and without cryopreservation. PBMCs were isolated as described in Section 2.1.1. Bronchoscopy was performed by a senior respiratory physician using an Olympus bronchoscope (Olympus KeyMed, Essex, UK). The bronchoscope was advanced into the right middle lobe, wedged, and 30 ml of sterile 0.9% saline was instilled and subsequently aspirated. BAL fluid was collected and transported on ice. Samples were passed through a 100 μm filter, centrifuged at 400G for 10 minutes at 4 °C, and resuspended in RBC lysis buffer (QIAGEN) for 10 minutes, followed by centrifugation. PBMC and BAL samples were stained with trypan blue and cell viability was assessed using both manual and automated live counting. Cells were then passed through a 70 μm filter and washed with sterile PBS to maximise cell recovery.

For sample multiplexing, cells were labelled with hashtag oligonucleotide-conjugated antibodies according to the manufacturer's instructions. Briefly, cells were resuspended in cell staining buffer (Biolegend) and incubated with TruStain Fc receptor blocking reagent (Biolegend) for 10 minutes at 4 °C, followed by incubation with TotalSeq™-A anti-human hashtag antibodies (Biolegend) for 30 minutes at 4 °C. Samples were washed three times and pooled prior to library preparation.

Droplet based single cell RNA sequencing was then performed using the 10x Chromium single cell platform (10x Genomics, 3' v3 chemistry) in accordance with the manufacturer's instructions. Downstream processing was performed by the Wellcome Trust Genomics institute in Oxford. In summary, approximately 30,000–40,000 pooled cells were loaded per lane for single cell encapsulation in gel beads in emulsions (GEM), enabling cell barcoding and reverse transcription of complementary DNA (cDNA). Subsequent cDNA amplification and library preparation were performed following standard protocols.

Library quality and integrity were assessed using Agilent Bioanalyzer TapeStation and final libraries were pooled and sequenced on an Illumina NextSeq 500/550 (High Output

v2.5, 150 cycles) using 150 base-pair paired-end reads. Processing of raw sequence data and downstream analysis described in Section 3.2.5.

2.1.5 Immunofluorescence staining of formalin fixed paraffin embedded tissue sections

Formalin-fixed, paraffin-embedded (FFPE) tissue blocks of healthy human tonsil, lung, and colon, as well as disease tissue from lung adenocarcinoma, COVID-19 infection, and idiopathic pulmonary fibrosis (IPF), were obtained from the Oxford Centre of Histopathology Research (OCHRe) under project ID 21/A019.

FFPE tissue blocks were sectioned at 5 μm thickness, mounted onto positively charged slides, and stored at room temperature. Prior to antibody staining, slides were incubated on a heat block at 65 °C for 10 minutes, followed by deparaffinisation in Histoclear II (National Diagnostics) for two 5-minute washes at room temperature. Sections were then rehydrated through three washes in 100% ethanol (10 minutes each) and rinsed in tap water. Permeabilisation was performed using 0.1% Triton X-100 for 15 minutes at room temperature. Heat-mediated antigen retrieval was carried out at 96 °C for 30 minutes in Tris–EDTA buffer (pH 9).

Following washing, sections were blocked with 2% bovine serum albumin (BSA) in Tris-buffered saline containing 0.1% Tween-20 (TBST) for 30 minutes at room temperature. Primary antibodies, diluted in TBST were added overnight at 4 °C. The following day, sections were washed prior to incubation with fluorophore-conjugated secondary antibodies, matched to the appropriate species and clone, diluted in TBST with 2% BSA for 30 minutes at room temperature. After three washes in TBST, sections were counterstained and mounted using DAPI-containing NucBlue mounting medium (Invitrogen). Slides were stored at 4 °C protected from light. Paired ‘no primary’ and isotype control slides were processed in parallel.

Stained sections were imaged using a Zeiss Axioscan Z1 fluorescence microscope configured for AF405, AF488, AF568, AF647, and AF750 channels at 20x magnification. Images were processed using QuPath (version 0.5.1). Signals arising from background or non-specific staining were identified and excluded using corresponding ‘no primary’ and isotype control slides.

2.1.6 Haematoxylin and eosin staining of formalin fixed paraffin embedded tissue sections

Adjacent tissue sections corresponding to immunofluorescence (IF) and imaging mass cytometry (IMC) slides were sectioned at 5 μm and stained with haematoxylin and eosin

(H&E) for signal localisation and histopathological assessment. H&E staining was also performed on formalin-fixed paraffin-embedded alveolar spheroids to assess spheroid size, morphology, and cellular architecture.

Tissue sections were deparaffinised, rehydrated, and washed as described in Section 2.1.5. Sections were then rinsed in tap water prior to staining with Mayer's haematoxylin (Lillie's modification; Abcam) for 4 minutes. Excess stain was removed by washing in distilled water, followed by incubation with bluing reagent (Abcam) for 15 seconds and two additional washes in distilled water. Sections were then dehydrated in 100% ethanol and stained with eosin Y solution (Abcam) for 2 minutes. Slides were subsequently cleared in 100% ethanol followed by Histoclear for 2 minutes each at room temperature and mounted using a synthetic resin mounting medium. Slides were stored at room temperature prior to imaging using a Zeiss Axioscan Z1 microscope configured for brightfield H&E acquisition at 20x magnification. Images were processed using QuPath software (version 0.5.1).

2.1.7 IMC antibody selection, specificity testing and titration

Prior to inclusion in the final IMC panel, antibodies were systematically evaluated to confirm epitope specificity and optimise staining conditions, with the aim of maximising signal-to-noise ratio and minimising background staining.

Antibody clones were initially selected from the Standard Biotools catalogue where validation in formalin-fixed paraffin-embedded (FFPE) tissue was available. Where IMC-validated clones were not available, antibodies previously validated in published IMC studies, immunohistochemistry, or immunofluorescence (IF) were selected for in-house testing. In these cases, specificity was first assessed by IF using both healthy and diseased lung tissue, with additional tonsil and colon samples included as positive and negative controls. IF staining was performed both before and after in-house lanthanide conjugation, as the conjugation process may alter antibody binding through disruption of disulfide bonds.

Antibody specificity was evaluated at several stages, including initial testing before conjugation, post-conjugation validation, and with pilot IMC staining, using criteria previously described[225, 226]. The following criteria were applied: i) mutually exclusive expression of key immune and structural lineage markers (e.g. CD68, EPCAM, CD3, CD20). ii) Marker expression that was consistent with expected subcellular localisation for example nuclear or cytoplasmic expression of markers such as ki67, p53, p16, phospho-proteins, IFITM3, ISG15, and membrane localisation of markers including CD68, EPCAM, CD206, KRT5, and KRT8. iii) Concordance between lineage marker expression and cellular morphology and anatomical location, assessed in conjunction

with adjacent H&E-stained sections (e.g. aSMA expression surrounding vessels and bronchi, and EPCAM expression localised to bronchial and alveolar epithelial cells. iv) Expected expression patterns, including assessing for non-physiological co-expression (e.g. CD68 and CD8) and presence of expected co-expression profiles (e.g. $EpCAM^+$ pro SPC^+ staining on type II alveolar epithelial cells).

Functional markers associated with epithelial dysfunction, cytokine signalling, and interferon-stimulated gene (ISG) expression were further validated by assessing expression patterns in disease lung tissue sections, including IPF and COVID-19, in comparison with healthy control samples. Markers associated with type 1 IFN signalling, including pSTAT1, pSTAT2, and ISGs, were also validated *in vitro*. THP-1 cells were stimulated with IFN-β, and marker expression was compared between unstimulated and stimulated conditions. Specificity was also confirmed using stimulated $IFNAR2^{-/-}$ THP-1 cells to confirm for reduced expression of type 1 IFN signalling proteins.

Antibody conjugation also considered isotope spill over were impurities or oxidation in certain affect mass and cause spill over. Lower performing antibodies were conjugated to metals with minimal spillover and higher detection. Staining conditions were also optimised directly in IMC using IPF tissue sections by performing antibody titrations and comparing incubation conditions of 5 hours at room temperature versus overnight incubation at 4 °C[227].

2.1.8 Antibody staining of formalin fixed paraffin embedded tissue sections for imaging mass cytometry

IPF tissue sample selection criteria, demographic and clinical characteristics, and ethical approvals are described in Section 5.2.2. Antibody panel composition and validation outcomes are detailed in Sections 5.2.3 and 5.3.2, and region of interest (ROI) selection criteria are outlined in Section 5.3.1. FFPE lung tissue blocks were obtained from the Oxford Centre of Histopathology Research (OCHRe) under project ID 21/A019.

Selected FFPE tissue blocks were sectioned at 5 μm mounted onto positively charged Superfrorst Plus™ slides and stored in dust free conditions at room temperature. Adjacent sections were prepared and stained with haematoxylin and eosin (H&E), as described in Section 2.1.6, to assess tissue integrity, confirm histopathological features, and guide final ROI selection.

Prior to staining, slides were incubated at 65 °C for 90 minutes on a prewarmed heat block followed by deparaffinisation in Histoclear II (National Diagnostics) for two 10-minute washes at room temperature. Sections were rehydrated with serial ethanol concentrations (100%, 100%, 95%, and 70%; 5 minutes each) and washed twice in

Maxpar water (Standard Biotools) for 5 minutes at room temperature. Heat-mediated antigen retrieval was performed by immersing slides in preheated Agilent antigen retrieval buffer (pH 9) at 96 °C for 30 minutes. Slides were then allowed to cool to approximately 70 °C before washing in Maxpar water and Maxpar PBS (Standard Biotools) for 5 minutes each. Sections were subsequently incubated with SuperBlock blocking solution for 45 minutes at room temperature in a humidified chamber.

Tissue sections were stained with an initial antibody cocktail containing 16 metal-conjugated antibodies optimised for room temperature incubation. Antibodies were diluted in SuperBlock solution and incubated for 5 hours at room temperature. Slides were washed three times in Maxpar PBS prior to incubation with a second antibody cocktail containing the remaining 24 metal-conjugated antibodies, diluted in SuperBlock solution, and incubated overnight at 4 °C in a humidified chamber.

The following day slides were washed in Maxpar PBS containing 0.2% Triton X-100, followed by two additional washes in Maxpar PBS. Sections were then stained with Cell-ID Intercalator-Ir (Standard Biotools), diluted in Maxpar PBS 250 μM, for 30 minutes at room temperature. Slides were washed in Maxpar water and air dried prior to acquisition.

Ablation of predetermined regions of interest (ROIs) was performed using the Hyperion Imaging System with CyTOF7 Software v7.0 (Standard Biotools). Processed mass cytometry data and visualized using MCD Viewer (Standard Biotools).

2.1.9 Human lung tissue collection and processing

For the establishment of primary cell type 2 alveolar epithelial cell spheroids, lung tissue was obtained from patients undergoing thoracic surgery for localised malignant or non-malignant disease. Patients aged 18–80 years provided written informed consent for donation of excess tissue through the Oxford Centre of Histopathology Research (OCHRe). Current smokers, those with active or chronic lung infection, a history of diffuse lung disease or evidence of interstitial lung disease or significant emphysema on CT were excluded.

Following surgery, lung tissue was macroscopically assessed by a consultant histopathologist, and 1–2 g of non-diseased distal parenchymal tissue, remote from the primary pathology, was excised. Tissue was stored in R10 medium at 4 °C and processed as soon as possible to preserve viability. Where immediate processing was not feasible, intact tissue was stored at 4 °C and processed the following day. Samples were transported on ice in sterile containers.

Following collection, tissue was inspected and pleura and large airways were removed. Samples were sectioned into 1–2 cm fragments, weighed, and washed in ice-cold phosphate-buffered saline (PBS) containing antibiotics (100 U/ml penicillin, 100 μg/ml streptomycin) and amphotericin B (25 μg/ml) for 10 minutes on ice. Tissue was then finely minced (~1 mm fragments) and incubated in 20 ml digestion buffer containing PBS supplemented with 1 mg/ml collagenase/dispase, 2 U/ml dispase II, and 10 U/ml DNase I for 1 hour at 37 °C with gentle agitation

Following enzymatic digestion, cell suspensions were filtered sequentially through 100 μm and 70 μm strainers to remove debris. Residual tissue was gently dissociated and rinsed with RPMI-1640 medium containing antibiotics and amphotericin B (R0) to maximise cell recovery. Cells were centrifuged at 1500 rpm for 10 minutes at 4 °C, and the pellet was resuspended in 5 ml red blood cell (RBC) lysis buffer for 5 minutes at room temperature followed by dilution in with R0 medium and further filtered through a 70 μm strainer prior to centrifugation. The cell pellet was resuspended in R10 medium plus amphotericin, for paired automated (Countess haemocytometer) and manual cell counting after adding trypan blue.

2.1.10 Magnetic bead activated cell sorting (MACS)

Following cell counting, samples were centrifuged at 4 °C and cell pellet were resuspended in MACS buffer (PBS supplemented with 0.5% bovine serum albumin (BSA) and 1 mM EDTA). During optimisation, higher concentrations of BSA (up to 2%) and EDTA (up to 2 mM) were tested to minimise cell clumping and non-specific binding.

Fc receptor blocking was performed with TruStain FcX (Biolegend) at a ratio of 5 μL per 1 x 10^7 cells for 10 minutes at 4 °C. Cells were then incubated with mouse HTII-280 IgM antibody at 1 μL per 1 x 10^6 cells (final dilution 1:50) for 60 minutes at 4 °C, followed by two washes in MACS buffer. Cells were then incubated with anti-mouse IgM-conjugated beads (20 μL per 1 x 10^7 cells) for 15 minutes at 4 °C. After washing, cells were resuspended in MACS buffer and applied to LS columns mounted on a magnetic separator. A maximum of 2 x 10^6 cells was loaded per column to minimise clogging. Columns were washed 3 times, and the negative population, collected by gravity. Columns were removed from the magnet, placed on a fresh collection tube and the HTII-280^+ cell fraction collected by flushing with 5 ml MACS buffer using a plunger.

Following separation, cell number and viability were assessed using trypan blue exclusion with both manual and automated (Countess haemocytometer) counting methods. The purity of the HTII-280^+ population was evaluated by flow cytometry using the antibody panel described below.

2.1.11 Fluorescent activated cell sorting (FACS) of AT2 cells

Following tissue digestion and cell counting, cells were incubated with TruStain FcX (Biolegend) and primary HTII-280 IgM antibody as described above. After two washes in FACS buffer (PBS supplemented with 2% bovine serum albumin (BSA) and 1 mM EDTA), cells were incubated with fluorophore-conjugated primary cell surface antibodies, dilution 1:50 and a secondary anti-mouse IgM conjugated antibody final dilution 1:50 for 30 minutes at 4 °C in the dark.

Cells were subsequently washed, filtered through a cell strainer, and resuspended in 1 ml FACS buffer prior to sorting. Fluorescence-activated cell sorting was performed independently using a Sony MA900 cell sorter and 100 μm sorting chip. Compensation was performed using single-stained beads for surface markers and unstained cells for viability dyes (7-AAD or DAPI). Gating strategies were defined using fluorescence minus one (FMO) controls. For live/dead discrimination, 7-AAD or DAPI (1 μL per 1 x 10^7 cells) was added 5 minutes prior to acquisition.

Cells were gated to isolate live, single $CD45^-$ $CD31^-$ $EpCAM^+$ $HTII\text{-}280^+$ AT2 cells, Sorting was performed using a 'normal' purity setting, maintaining a sort efficiency of approximately 90%.

Post-sort purity was assessed by re-analysis, and cell number and viability were determined using trypan blue exclusion with both manual and automated (Countess haemocytometer) counting methods. The final $HTII\text{-}280^+$ AT2 cell population was used for downstream culture.

2.1.12 AT2 alveolar spheroid culture media

Following enrichment by MACS or FACS, primary human AT2 cells were cultured using two previously published serum and feeder-free alveolar culture media formulations designed to support long-term expansion of adult AT2 cells[228, 229](Table 2.2).

Compound (Base Media)	**Youk et al.**	**Katsura et al.**	**Treatment Period**
Advanced DMEM / F12	500 ml	500ml	Throughout
HEPES	10mM	15 mM	Throughout
Pen/Strep	10 ml/ml	10 ml/ml	Throughout
NAC	1mM	1.25mM	Throughout
Nicotinamide	10mM		Throughout
Compound (Advanced Media)			
B27 supplement	1x	1x	Throughout
R Spondin	500ng/ml		Throughout
Human EGF	50ng/ml	50ng/ml	Throughout
FGF7 / KGF	100ng/ml		Throughout
FGF 10	100ng/ml	10ng/ml	Throughout
NOGGIN	100ng/ml		Throughout
SB431542	10 mM	10mM	Throughout
CHIR99021	3mM	3mM	Throughout
BIRB796		1mM	Throughout
Heparin		5mg/ml	Throughout
Y-27632	10 mM	10 mM	First 72 hours
Amphotericin	250 ng /ml	250 ng/ml	First 72 hours

Table 2.2. Composition of alveolar organoid culture media as described by Youk et al. and Katsura et al. *Abbreviations: NAC, N-acetylcysteine; EGF, epidermal growth factor; FGF, fibroblast growth factor. Proposed functions of key components in culture include: Noggin (BMP antagonist; restricts AT2 differentiation), R-spondin and CHIR99021 (activators of Wnt/β-catenin signalling; promote AT2 proliferation), SB431542 (TGF-β receptor inhibitor; restricts differentiation), BIRB796 (p38 MAPK inhibitor; promotes proliferation and limits differentiation), heparin (enhances FGF signalling), and Y-27632 (ROCK inhibitor; prevents dissociation-induced apoptosis*

AT2 growth and spheroid formation were assessed in both conditions by brightfield microscopy and live-cell imaging using the Incucyte™ organoid imaging module (Sartorius). Comparative analysis of culture performance is described in Section 6.3.2.

Based on these assessments, the culture formulation described by Katsura et al. was selected for subsequent experiments. Culture medium was initially prepared in-house

according to the published formulation. Following commercial availability of this formulation as alveolar organoid expansion medium (AVOE Stemcell Technologies), all subsequent AT2 cultures including downstream assays were performed using AVOE to minimise variability between batches.

2.1.13 AT2 cell plating and long-term culture

Following MACS or FACS enrichment, HTII-280^{+} AT2 cells were counted and resuspended in chilled alveolar base medium (Table 2.2) at a concentration of 5 x 10^{3} cells per 15 μL and maintained on ice. Growth factor-reduced Matrigel™ (Corning), thawed at 4 °C and kept on ice, was mixed with the cell suspension at an approximate ratio of 2:1 with 25 μL Matrigel and 15 μL cell suspension. A total of 40 μL of the Matrigel–cell mixture was carefully dispensed into wells of flat bottom, tissue culture-treated plates to form domes. Domes were allowed to polymerise for 10 minutes at room temperature, and a further 35 minutes at 37 °C with 5% CO_2. Alveolar culture medium with supplements produced in house, or alveolar organoid expansion medium (AVOE) supplemented with 1% penicillin–streptomycin was then gently added to each well. During the first 48 hours of culture, media was supplemented with ROCK inhibitor and amphotericin B.

Culture medium was replaced every 72 hours by carefully aspirating from the edge of the well and replenishing medium along the well wall to avoid disruption of the Matrigel dome. Spheroid growth was monitored by brightfield microscopy during routine media changes and by live-cell imaging using the Incucyte™ organoid imaging module (Sartorius).

2.1.14 Passaging of AT2 spheroids

Spheroids were passaged after 14 days of culture. Culture medium was aspirated and replaced with Dispase II (2 mg/ml) diluted in AVOE, followed by incubation at 37 °C for 45 minutes to degrade the Matrigel domes and release spheroids. During incubation, domes were mechanically disrupted by gentle pipetting every 15 minutes to facilitate Matrigel digestion. Released spheroids were collected using a cut P200 pipette tip, centrifuged at 400G for 5 minutes, and resuspended in 1x TrypLE Select®. Samples were incubated at 37 °C for 3 minutes, followed by gentle pipetting and assessment by brightfield microscopy. Where required, incubation was extended in 1-minute intervals (up to a maximum of 6 minutes) to achieve complete dissociation. Following dissociation, TrYPLE® was diluted and cells were centrifuged for automatic and manual cell counting with trypan blue exclusion.

Cells were subsequently used for downstream assays, further culture, or cryopreservation. For cryopreservation, cells were centrifuged and the pellet

resuspended in CS10™ cryopreservation medium (STEMCELL Technologies) at a concentration of 1 x 10^6 cells/ml.

2.1.15 Cell isolation, fixation, and staining for immunocytochemistry (ICC)

Following FACS sorting or enzymatic dissociation of spheroids, 5,000–10,000 cells in suspension were collected and loaded into cytospin chamber holders. Cells were centrifuged at 400 rpm for 5 minutes onto positively charged slides. Slides were air-dried and fixed by immersion in a 1:1 methanol–acetone solution for 30 minutes at room temperature. Following fixation, slides were washed and stored at 4 °C for short-term use or at −20 °C for longer-term storage.

Prior to staining, cells were permeabilised with 0.1% Triton X-100 for 10 minutes and then incubated in blocking buffer (1% bovine serum albumin (BSA) in Tris-buffered saline with 0.05% Tween-20 (TBS-T)) for 30 minutes at room temperature.

Primary antibodies diluted in TBS-T were applied to the slides and incubated overnight at 4 °C. The following day, slides were washed and incubated with appropriate fluorophore-conjugated secondary antibodies for 30 minutes at room temperature.

Slides were subsequently counterstained and mounted using DAPI-containing mounting medium (NucBlue, Invitrogen) and stored at 4 °C away from light prior to imaging.

Immunofluorescence images were acquired using a Zeiss Axioscan microscope and processed using QuPath (version 0.4.1) and ImageJ software, as described for FFPE tissue section analysis.

2.1.16 Paraffin embedding of intact AT2 spheroids

For immunofluorescence imaging of intact spheroids, Matrigel domes were digested after 14 days of culture using Dispase II (2 mg/ml), as described above. Released spheroids were collected using a cut P200 pipette tip, centrifuged at 300G for 5 minutes at 4 °C, and fixed in 10% neutral buffered formalin for 60 minutes at room temperature.

Following fixation, spheroids were centrifuged at 350G for 5 minutes and resuspended in 20 μL Histogel™ (pre-warmed to 70 °C). Samples were allowed to solidify at room temperature for 60 minutes before being transferred into histology cassettes and fixed in 10% neutral buffered formalin for 48 hours, followed by incubation in 70% ethanol for 24 hours.

Samples were dehydrated with a graded ethanol series (75% for 30 minutes, 90% for 30 minutes, and 100% for 1 hour), followed by clearing in Citrosolv for 60 minutes. Samples were then infiltrated with paraffin at 60 °C for 2 hours.

Processed samples were removed from cassettes and embedded in paraffin blocks for downstream sectioning and staining.

2.1.17 Bleomycin-induced injury of AT2 spheroids

Bleomycin (BLM) was used to establish an in vitro alveolar spheroid injury model. Bleomycin sulphate (Apollo Scientific) was reconstituted in AVOE to a stock concentration of 400 μg/ml. AT2 cells at passage 3 were plated and cultured under standard conditions as described above. At day 7, established alveolar spheroids embedded in Matrigel domes were treated with AVOE containing BLM at concentrations of 0, 2, 10, and 20 μg/ml for 72 hours. At defined time points following BLM exposure (days 3, 5, 7, and 10), spheroids were harvested by digestion of Matrigel domes using Dispase II, as described above.

Released spheroids were centrifuged at 400G for 5 minutes at 4 °C and resuspended in RLT buffer (QIAGEN) supplemented with b-mercaptoethanol (1:100 dilution). Samples were directly transferred to −80 °C for downstream RNA extraction.

2.1.18 RNA extraction and quantitative PCR

Total RNA was extracted using the RNeasy Mini Kit (QIAGEN) according to the manufacturer's instructions. Briefly, AT2 cell lysates were thawed and mixed with an equal volume of 70% ethanol, then transferred to a RNeasy spin column and centrifuged at 10,000 rpm for 15 seconds before discarding the flow through. Columns were washed sequentially with 700 μL RW1 buffer followed by two washes with 500 μL RPE buffer. Each wash was followed by centrifugation at 10,000 rpm for 60 seconds and the flow through discarded.

RNA was eluted by transferring the spin column to a fresh collection tube and adding 30 μL RNase-free water directly to the membrane, followed by centrifugation at 10,000 rpm for 1 minute. RNA concentration was determined by spectrophotometric measurement at 260 nm.

Complementary DNA (cDNA) was synthesised from RNA using the High-Capacity cDNA Reverse Transcription Kit (Applied Biosystems). 10 μl RNA combined with RT master mix (10x RT Buffer [2μl], 25x dNTP mix (100nM) [0.8μl], 10x RT Random primers [2μl], Multiscribe RT [1μl], RNAse free water [4.2μl]) to a final reaction volume of 20 μL. Reactions were repeated in triplicate for each sample. Reverse transcription was

performed in 96 well plates in a T100 thermal cycler under the following conditions; 25 °C for 10 minutes, 37 °C for 120 minutes, and 85 °C for 5 minutes.

Quantitative PCR (qPCR) was performed using TaqMan Fast Advanced Master Mix (Applied Biosystems). cDNA samples diluted in nuclease-free water to final volume of 4.5 µl per reaction and added to a 384-well plate. All reaction were performed in duplicate in a total reaction volume of 10 µl with 5 µL Taqman™ Master Fast Advanced Master Mix, 0.5 µL Taqman™ Gene Expression Assay (20x) and 4.5 µl diluted cDNA. Plates were sealed and stored at 4 °C and amplification carried out on a Quantstudio7 (Thermo Fisher Scientific) using the manufacturers recommended cycling conditions.

Relative gene expression was calculated using the log 2 ddCt ($2^{-\Delta\Delta Ct}$) method, normalised to GAPDH or TSP followed by control condition.

2.1.19 THP-1 cell culture and stimulation

THP-1 cells were cultured in R10 medium supplemented with 1% L-glutamine in tissue culture-treated flasks under standard conditions (37 °C, 5% CO_2) at a density of 2×10^5 cells/ml. Cells were monitored daily and passaged every 48–72 hours. During passage, cells were collected and centrifuged at 1500 rpm for 5 minutes. The cell pellet was resuspended in fresh R10 medium, and cell number and viability were determined using an automated cell counter. Cells were subsequently re-cultured, cryopreserved (as described in Section 2.1.1), or used for downstream assays.

For THP-1 stimulation experiments, 0.5×10^6 cells were seeded per well in 6-well plates and cultured under standard conditions for 24 hours prior to stimulation.

For lipopolysaccharide (LPS) stimulation, cells were treated with LPS at concentrations of 0, 10, 100, 1000, and 2000 ng/ml. Brefeldin A was added at the time of stimulation at a final concentration of 5 µg/ml. Following 6 hours of stimulation, cells were collected, washed, and resuspended in sterile phosphate-buffered saline (PBS) prior to analysis by flow cytometry.

For interferon-b (IFN- β) stimulation, cells were treated with IFN-β (250 U/ml) for 15 minutes to assess phosphorylated protein responses or for 6 hours to assess ISG) expression. Following stimulation, cells were cytocentrifuged onto positively charged slides and fixed by immersion in a methanol–acetone solution for ICC assessment, as described in Section 2.1.15.

2.1.20 Flow Cytometry

Cell surface and intracellular flow cytometry were performed using established protocols. Briefly, cells were first incubated with a fixable viability dye (Zombie Aqua, Biolegend) for 15 minutes in phosphate-buffered saline (PBS).

Cells were then incubated with TruStain Fc receptor block and TruStain monocyte block (Biolegend) diluted in 50 µL FACS buffer (PBS supplemented with 2% fetal bovine serum) for 5 minutes at room temperature. Fluorophore-conjugated primary antibodies were subsequently added directly to the cell suspension to a final staining volume of 100 µL and incubated for 20 minutes at 4 °C.

For intracellular staining, cells were permeabilised using 1× permeabilisation buffer (Invitrogen) prior to incubation with intracellular antibodies diluted in permeabilisation buffer for 25 minutes at 4 °C. Cells were then fixed using IC fixation buffer (Invitrogen) prior to acquisition.

All staining steps were performed in the dark. Fluorescence minus one (FMO) controls were included in all experiments to define gating boundaries and account for non-specific staining and autofluorescence.

Samples were acquired using a 4-laser, 18-detector flow cytometer (BD LSRFortessa™ X-20). Data were analysed using FlowJo software (version 10, Tree Star Inc.).

2.1.21 AT2–THP-1 co-culture experiments

A series of co-culture experiments were performed using AT2 spheroids and THP-1 cells, as outlined in Sections 6.3.5–6.3.7.

For all experiments, AT2 cells were cultured under standard conditions for 7–10 days to allow spheroid formation when Matrigel domes were digested using Dispase II to release spheroids. THP-1 cells were passaged 24 hours prior to co-culture to ensure consistent cell state. For live-cell imaging experiments, AT2 cells were labelled with LysoTracker (100 nM, 30 minutes) prior to digestion, and THP-1 cells were labelled with CFSE (Invitrogen, 30 minutes) to enable identification of each population.

Initial optimisation experiments were performed to assess the effects of AVOE medium and / or culture with AT2 spheroids on THP-1 phenotype and response to LPS (Section 6.3.5). Additionally, co-culture conditions were evaluated to determine appropriate cell ratios and a ratio of 1:2 AT2 cells to THP-1 cells was selected to maintain physiological relevance while ensuring sufficient cell numbers for downstream analyses.

Preliminary live vell imaging experiments demonstrated that co-culture within Matrigel domes limited cell movement and prevented direct cell–cell interaction. Therefore, subsequent co-culture experiments were performed in ultra-low attachment plates.

For final experiments, AT2 cells (passage 3) were cultured to form spheroids and, after 7 days, were treated with bleomycin (20 µg/ml) for 72 hours to induce injury. Spheroids were then released by Dispase II digestion. A subset of cells was dissociated to enable accurate cell counting, and AT2 and THP-1 cells were co-cultured at a ratio of 1:2 in ultra-low attachment plates for 48 hours. THP-1 cells with and without IFNAR2, derived from the same clone, were used at passage 2 to minimise phenotypic drift and variability between conditions.

Following co-culture, cells were collected and processed for downstream analyses. A proportion of cells was dissociated and subjected to fluorescence-activated cell sorting (FACS) to separate AT2 and THP-1 populations prior to storage in RLT buffer for RNA extraction and qPCR analysis. Remaining cells were fixed in formaldehyde and embedded in Histogel™ and paraffin for immunofluorescence analysis. Culture supernatants were collected for assessment of secreted cytokines and other soluble factors.

Cell culture reagents	**Supplier**	**Cat No.**
Lymphoprep™	Stemcell Technologies	18061
RPMI-1640 Medium	Sigma Aldrich	R8758
Gibco Recovery Cell Freezing Media	Thermo Fischer	12648010
Mass cytometry reagents	**Supplier**	**Cat No.**
Cell-ID 20-Plex Pd Barcoding Kit	Standard Biotools	201060
Cell-ID Cisplatin	Standard Biotools	201064
Cell-ID Intercalator-Ir	Standard Biotools	201192B
EQ Four Element Calibration Beads	Standard Biotools	201078
Maxpar Water	Standard Biotools	201069
16% Paraformaldehyde solution	Thermo Fisher Scientific	28906
Maxpar X8 Antibody Labeling Kit	Standard Biotools	201300
Maxpar X9 Antibody Labeling Kit	Standard Biotools	201114A
Bond-Breaker® TCEP Solution	Thermo Fisher Scientific Scientific	PI77720
Antibody Stabilisation Buffer	Candor	131050
Human True Stain FcX	Biolegend	422301
True Stain Monocyte Block	Biolegend	426102
Maxpar Cell Staining Buffer	Standard Biotools	201068
Maxpar Fix and Perm Buffer	Standard Biotools	201067
Maxpar PBS	Standard Biotools	201058
Maxpar Fix I Buffer (5X)	Standard Biotools	201065
Maxpar Perm Buffer (10X)	Standard Biotools	201057
Ultracomp eBeads	Invitrgen	01-2222-42
Single Cell RNA seq Hastag antibdies	**Supplier**	**Cat No.**

TotalSeq™-A0251 anti-human Hashtag 1	Biolegend	394601
TotalSeq™-A0252 anti-human Hashtag 2	Biolegend	394603
TotalSeq™-A0253 anti-human Hashtag 3	Biolegend	394606
TotalSeq™-A0254 anti-human Hashtag 4	Biolegend	394607
TotalSeq™-A0255 anti-human Hashtag 5	Biolegend	394609
TotalSeq™-A0256 anti-human Hashtag 6	Biolegend	394611
TotalSeq™- A0257 anti-human Hashtag 7	Biolegend	394613
TotalSeq™- A0258 anti-human Hashtag 8	Biolegend	394615
Immunofluorescence & imaging reagents	**Supplier**	**Cat No.**
Histo Clear II	National Diagnostics SLS	NAT 1330
Triton X %	Sigma Aldrich	9036-19-5
Antigen Retrieval Buffer Tris EDTA (pH9)	Abcam	ab93684
Tween 20	Sigma Aldrich	9005-65-6
Nuc Blue Moutnign Media	Invitrogen	R37606
Antigen Retrieval Buffer Citrate (pH6)	Abcam	ab93678
H&E Staining Kit	Abcam	ab245880
Imaging Mass Cytometry reagents	**Supplier**	**Cat No.**
Agilent Antigen Retrieval solution (pH 9)	Agilent technologies	S2367
Maxpar Water	Standard Biotools	201069
Maxpar PBS	Standard Biotools	201058
Alveolar spheroid		
Tissue processing and media reagents	**Supplier**	**Cat No.**
Dispase II powder	Sigma Aldrich	49420780001
DNASE	Sigma Aldrich	10104159001
Collagenase Dispse	Sigma Aldrich	1026963801
Corning Matrigel Growth Factor Reduced (GFR) Basement Membrane	Corning	356231
Y-27632 (ROCK inhibitor)	Sigma Aldrich	Y0503
B27 supplement	Thermo Fisher Scientific	17504044
FGF 7	Pepro Tech	100-19
FGF 10	Pepro Tech	100-26
Noggin	Pepro Tech	120-10C
EGF	Pepro Tech	100-15
N-Acetylcysteine	Sigma Aldrich	A9165
Nicotinamide	Sigma Aldrich	N0636
SB431542	Sigma Aldrich	616461
CHIR99021	Tocris	4423
BIRB796	Tocris	5989
HEPES	Sigma Aldrich	15630-080
Amphotericin B	Sigma Aldrich	A2942
TrypLE Select	Thermo Fisher Scientific	12563-029
MACS LS Columns	Miltenyl Biotec	130-042-401
Pneumacult	Stem Cell Technologies	100-0847
CS10	Stem Cell Technologies	7959
Heparin 0.2% Solution	Stem Cell Technologies	7980

Flow Cytometry and FACS antibodies	Supplier	Cat No.	Clone
Anti mouse IgM Microbeads	Miltenyl Biotec	130-047-302	RMM-1
Anti-human CD31 AF 700	Biolegend	303134	WM59
Anti-human CD45 Pe-Cy7	Biolegend	304016	H130
Anti-human EpCAM per CP-Cy5	Biolegend	324214	9C4
Anti-mouse IgM APC	Bioegend	406509	RMM-1
Anti-human PDPN APC-Cy7	Biolegend	337029	NC-08
Anti-human CD45 - PE	Bioegend	324245	HI30
Anti-human EpCAM APC-Cy7	Biolegend	304007	9C4
Anti-human HTII-280	Terrace Biotech	TB-27AHT2-280	n/a
Flow Cytometry reagents	**Supplier**	**Cat No.**	
Human True Stain FcX	Biolegend	422301	
True Stain Monocyte Block	Biolegend	426102	
IC 10x Permeabilsation Buffer	Invitrogen	00-8333-56	
IC Fixation Buffer	Invitrogen	00-8222-49	
Immunofluorescence antibodies	**Supplier**	**Cat No.**	**Clone**
Rabbit anti-pro-SFTPC	Sigma Aldrich	Ab3786	EPR19839-8
Rabbit anti-CRB3 Antibody	Novus	NBP1-81185	Polyclonal
Rabbit anti-SCRIB	Thermo Fisher Scientific	PA554821	Polyclonal
Goat anti-RAGE/AGER	R&D	AF1145	Polyclonal
Recombinant Anti-Aquaporin 5	Abcam	ab92320	[EPR3747]
Rabbit anti-HOPX	Santa Cruz	sc 398703	E-1
Rat anti-SCGB1A1	R&D	MAB4218	394324
Rabbit anti-KRT5	Biolegend	905501	Polyclonal
Mouse anti-tp63	Abcam	ab735	aA4
Rabbit anti-SCEL	Thermo Fisher Scientific	PA5 59082	Polyclonal
Mouse anti-HLADR	Thermo Fisher Scientific	14-9956-82	LN3
Lysotracker Red	Thermo Fisher Scientific	L7528	n/a
CFSE	Invitrogen	C34554	n/a
RNA extraction and qPCR	**Supplier**	**Cat No.**	
cDNA RT Kits	Thermo Fisher Scientific	4368814	
RNesy Mini Kit	QIAGEN	74104	
TaqMan Fast Advanced Master Mix	Thermo Fisher Scientific	4444556	
Genes	**Supplier**	**TaqMan unique ID**	
STFPC	Thermo Fisher Scientific	Hs00951326_g1	
ETV5	Thermo Fisher Scientific	Hs00927557_m1	
LCN2	Thermo Fisher Scientific	Hs01008571_m1	
LRG1	Thermo Fisher Scientific	Hs00364835_m1	
KRT8	Thermo Fisher Scientific	Hs01595539_g1	
CDKN1A	Thermo Fisher Scientific	Hs00355782_m1	
CCND1	Thermo Fisher Scientific	Hs00765553_m1	
CAV1	Thermo Fisher Scientific	Hs00971716_m1	
SCEL	Thermo Fisher Scientific	Hs01557103_m1	
SCGB1A1	Thermo Fisher Scientific	Hs00171092_m1	
CDKN2A	Thermo Fisher Scientific	Hs00923894_m1	
TMEM173	Thermo Fisher Scientific	Hs00736955_g1	

SFTPC	Thermo Fisher Scientific	Hs00161628_m1
IL1B	Thermo Fisher Scientific	Hs01555410_m1
TNFA	Thermo Fisher Scientific	Hs00174128_m1
IFNB1	Thermo Fisher Scientific	Hs01077958_s1
STAT1	Thermo Fisher Scientific	Hs01013996_m1
CD36	Thermo Fisher Scientific	Hs00354519_m1
ISG15	Thermo Fisher Scientific	Hs00192713_m1
MX1	Thermo Fisher Scientific	Hs00895608_m1

***Table 2.1. Details of reagents used in the Methods**, including supplier, catalogue number, and monoclonal antibody clone information*

Chapter 3 Type 1 IFN signalling in circulating immune cells in IPF

3.1 Introduction

The aim of this chapter is to examine type 1 interferon (type 1 IFN) signalling in IPF compared to control PBMC populations using high resolution, single cell suspension mass cytometry (CyTOF). This is complemented by examination of the single cell transcriptome of PBMCs in a small subset of patients and controls, with an emphasis on type 1 IFN signalling.

Several studies have shown that higher circulating monocyte counts are associated with worse outcomes in IPF. Elevated $CD14^+$ monocyte proportions and an absolute monocyte cell count of >0.95 $x10^3$ / ul correlated with increased risk of mortality and shorter time to transplant[176]. Monocyte count was a more sensitive prognostic marker than age, lung function, or GAP index. A lower monocyte count of >0.65 $x10^3$ cells / µl also predicted IPF progression at 12 months, hospitalisation and mortality[177]. Furthermore, higher monocyte counts also identified patients with indeterminate usual interstitial pneumonia (iUIP) – a radiological feature of that often precedes IPF, are at increased risk of developing IPF[14].

In murine studies, depletion of circulating $Ly6C^+$ monocytes with liposomal clodronate markedly reduced fibrosis while adoptive transfer of $Ly6C^+$ monocytes enhanced fibrotic severity[178]. Furthermore, in two depletion studies, loss of CCR2 prevented recruitment of $Ly6C^+$ monocytes to the lung and emergence of exudative and interstitial lung macrophage populations resulting in reduced lung fibrosis and improved survival[179, 230].

Collectively these studies suggest a role for monocytes in fibrogenesis. However, the mechanisms by which circulating monocytes contribute to IPF are not fully understood.

A previous study from our group provided early evidence that monocytes are altered in patients with IPF[181]. Circulating monocyte proportions and counts were higher in IPF compared to controls with increased monocyte CD64 expression. Increased monocyte CD64 expression also correlated with expression of interferon stimulated gene (ISG)s and extent of fibrosis on CT lung imaging. Preliminary data also suggested increased type 1 IFN signalling in magnetic activated cell sorting (MACS) bead isolated $CD14^+$ monocytes with higher type 1 IFN gene set expression in IPF ex vivo and increased ISG expression measured by qPCR following IFN-β stimulation. In addition, raised levels of IL-6, CCL-2 and CSF-1 were observed in the serum of IPF patients. These elevated cytokine levels could be secondary to monocyte activation and could impact their trafficking and differentiation.

These observations highlight abnormalities in monocyte-associated immune pathways in IPF. However, several questions remain unresolved. The initial analysis was restricted to $CD14^+$ monocytes, therefore, it is unclear whether alterations in type 1 IFN signalling and responsiveness are observed for all monocyte populations and if other PBMCs exhibit increased response to type 1 IFN. Furthermore, engagement of IFNAR by type 1 IFNs can activate multiple downstream signalling pathways, which may differentially shape cellular responses[199, 201]. Downstream signalling pathways after type 1 IFN stimulation and whether these are altered in IPF compared to controls are questions that have also not been characterised. Finally, the elevated levels of circulating cytokines and chemokines and increased monocyte CD64 expression, raises the question around additional functional or phenotypic abnormalities in circulating monocytes in IPF.

In this chapter, I address the following questions

i) Which signalling pathways are activated downstream of type 1 IFN - IFNAR binding and are there differences in the downstream response to IFN-β in IPF compared to controls?
ii) Is the increased response to type 1 IFN in IPF restricted to a specific monocyte subset or found in all monocyte subsets or other PBMC populations?
iii) Apart from increased type 1 IFN signalling, are there additional aberrant signalling pathways or transcriptomic differences in PBMCs, specifically monocytes in IPF?

3.2 Study Design and Methods

3.2.1 Overall Study Design

Two complementary studies were performed. In the first study, PBMCs were isolated from IPF patients and healthy controls (Cohort A) and analysed using single-cell mass cytometry. For this analysis a 38 plex, metal conjugated antibody panel that was designed and optimised by collaborators at the MRC WIMM (Rachel Rigby and Jan Rehwinkel) was used to measure type 1 IFN pathway activity downstream of the interferon alpha receptor (IFNAR) in both the basal state *ex vivo* and following stimulation with IFN-β[224]. In the second study, PBMCs from IPF patients and controls (Cohort B) were profiled using single-cell RNA sequencing to examine transcriptional differences in circulating immune cell populations *ex vivo*.

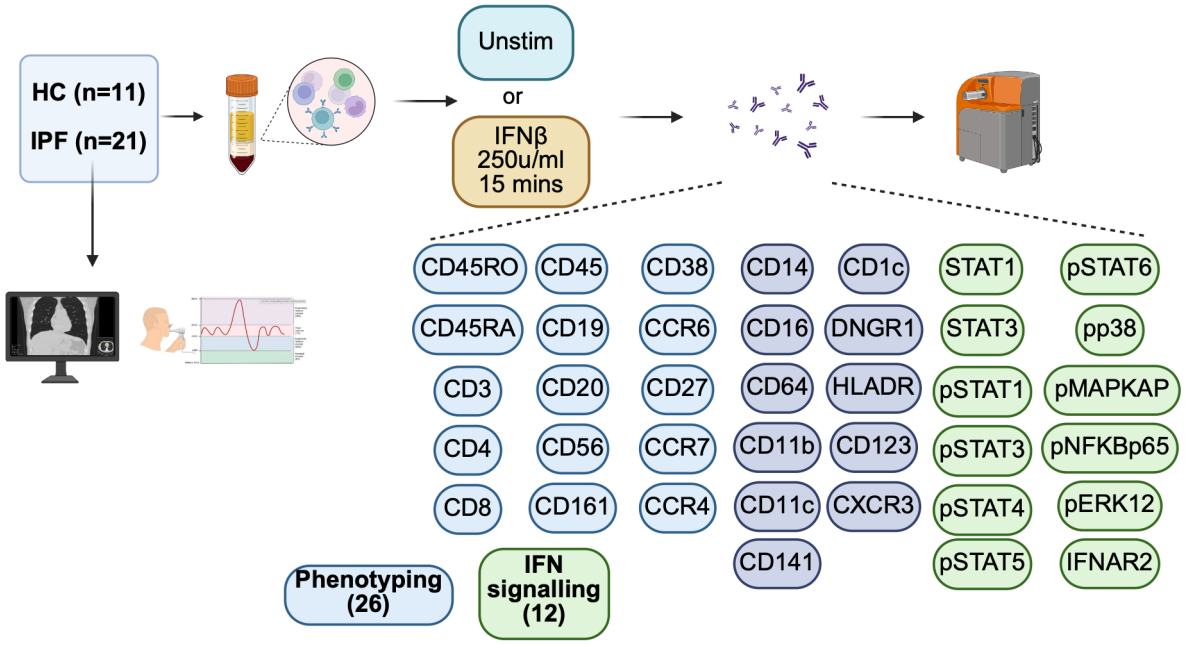


Figure 3.2.1. Experimental overview. *IFN-β stimulation of PBMCs followed by metal conjugated antibody staining using 26 phenotyping markers and 12 functional markers related to the type 1 IFN signalling pathway. Abbreviations; HC – healthy controls, Unstim – unstimulated.*

3.2.2 Patient selection

IPF patients in Cohort A and B were recruited from the regional Interstitial lung disease clinical service at Oxford University Hospitals. All patients had been diagnosed with IPF following review of patient clinical, radiological and serological features at a multi-disciplinary meeting using the criteria defined in the 2011 joint ATS / ERS / JRS / ALAT statement[20]. IPF Patients with coexisting additional pulmonary disease, immune

mediated disease, cancer and significant / chronic infection at the time of recruitment or at the time of blood sampling were excluded. Demographic and clinical details outlined for Cohort A (Table 3.2.1) and Cohort B (Table 3.2.2).

Healthy controls in Cohort A were recruited from patients attending routine peri-operative eye clinic prior to cataract surgery. Healthy controls in Cohort B were recruited from patients undergoing a clinical indicated bronchoscopy for discrete episodes of unexplained and resolved haemoptysis or persistent cough.

All Cohort B controls had no evidence of diffuse parenchymal disease on initial thoracic CT scan or diagnosis of respiratory disease prior to bronchoscopy and in the following one-year follow-up. Blood sampling in Cohort B patients was performed prior to bronchoscopy. All controls with coexistent lung disease, immune mediated disease, malignancy and infection were excluded.

Participants were recruited under regional ethics committee approved studies; REC 18/SC/0227, 21/WM/0244 for Cohort A and 14/SC/1060 for Cohort B.

	Patient ID	Gender	Age	Smoking status	Ethnicity	Radiological classification	Predicted FVC %	Predicted TLCO %	Medication	Active Co-morbidities
IPF	XIPS001-001	Male	78	Never	British Caucasian	UIP	78	34	Nintedanib	Nil
	XIPS001-003	Male	79	Ex	British Caucasian	UIP	80	66	Perindopril, Felodipine, Tamsulosin, Gaviscon	HTN, BPH, GORD
	XIPS001-005	Male	84	Never	British Caucasian	UIP	86	50	Lamotrigine, Co-careldopa, Metformin, Allopurinol, Atorvastatin	Parkinsons Disease, T2DM, Gout
	XIPS001-006	Male	77	Never	British Caucasian	UIP	56	46	Nil	Nil
	XIPS001-007	Male	65	Ex	British Caucasian	UIP	45	25	Pirfenidone, Simvastatin, Aspirin, Lansoprazole	Glaucoma
	XIPS001-008	Male	61	Ex	British Caucasian	UIP	72	42	Lansoprazole	GORD
	XIPS001-009	Female	77	Never	British Caucasian	UIP	89	46	Pirfendione, Levothyroxine, Mebeverine, Alendronic acid, Lansoprazole, Sumatriptan	Hypothyroidism, GORD
	XIPS001-010	Male	74	Never	British Caucasian	Probable UIP	81	59	Emagliflozin, Finasteride, Metformin, Aspirin, Atorvastatin, Pioglitazone, Ramipril, Tamsulosin	T2DM, HTN, BPH, IHD
	XIPS001-012	Male	63	Current	British Caucasian	UIP	84	54	Nintedanib, Apixaban, Digoxin, Metformin	T2DM, AF
	XIPS001-016	Male	76	Ex	British Caucasian	Probable UIP	91	44	Nintedanib	Nil

	XIPS001-019	Male	86	Ex	British Caucasian	UIP	79	49	Ramipril, Bisoprolol, Clopidogrel	IHD, HTN
	XIPS001-020	Female	76	Never	British Caucasian	Probable UIP	72	74	Omeprazole, Rosuvastatin, Amlodipine, Calcium-vit D	IHD, HTN
	XIPS001-021	Male	76	Ex	British Caucasian	Probable UIP	85	60	Clopidogrel, Lisinopril, Simvastatin, Carbocisteine	HTN
	XIPS001-022	Male	68	Ex	British Caucasian	Probable UIP	59	40	Allopurinol	GORD
	XIPS001-025	Male	86	Ex	British Caucasian	Probable UIP	86	39	Amlodipine, Omeprazole, Aspirin, Spironolactone	HTN, IHD, GORD
	XIPS001-027	Male	80	Ex	British Caucasian	Probable UIP	62	46	Omeprazole, Co-trimoxazole, Lorazepam, Tiotropium	GORD, COPD
	AEIPF 96	Male	74	Ex	British Caucasian	UIP	57	39	Furosemide, Omeprazole, Cardivelol, Atorvastatin, GTN	IHD
	AEIPF 70	Male	82	Ex	British Caucasian	UIP	82	91	Nintedanib, Bendroflumathiazide, Omeprazole, Simvastatin	BPH, HTN
	AEIPF 67	Male	73	Never	British Caucasian	UIP	69	39	Nintedanib, Bisoprolol, Apixaban, Carbocysteine, Fluticasone	AF, HTN
	AEIPF 64	Female	83	Never	British Caucasian	UIP	106	85	Nil	Nil
	AEIPF 58	Female	87	Ex	British Caucasian	UIP	61	60	Nintedanib, Esomeprazole, Losartan, Lantoprost	GORD

Control	HC 072	Male	80	Ex	British Caucasian	n/a	n/a	n/a	Pravastatin	Nil
	HC 071	Male	79	Never	British Caucasian	n/a	n/a	n/a	Amlodipine, Allopurinol, Colchicine, Ramipril, Bisoprolol, Rivaroxiban	AF, HTN, Gout, Hereditary haematochromatosis
	HC 070	Female	75	Never	British Caucasian	n/a	n/a	n/a	Losartan, Apixaban, Amlodipine	Chronic pulmonary thromboembolic disease, HTN
	HC 069	Female	72	Current	British Caucasian	n/a	n/a	n/a	Atorvastatin, Losartan, Bendroflumathiazide	HTN
	HC 068	Male	81	Ex	British Caucasian	n/a	n/a	n/a	Atorvastatin	Nil
	HC 044	Female	76	Never	British Caucasian	n/a	n/a	n/a	Nil	Nil
	HC 038	Female	73	Never	British Caucasian	n/a	n/a	n/a	Zopiclone	Nil
	HC 037	Male	72	Ex	British Caucasian	n/a	n/a	n/a	Latanoprost	Glaucoma
	HC 031	Female	73	Never	British Caucasian	n/a	n/a	n/a	Amlodipine, Denosumab	HTN
	HC 030	Male	72	Never	British Caucasian	n/a	n/a	n/a	Aspirin, Ranitidine, Bisoprolol	HTN, IHD
	HC 000	Female	56	Never	Asian	n/a	n/a	n/a	Nil	Nil

Table 3.2.1 - Demographic details of patients and controls for Cohort A used in CyTOF study. *Abbreviations - CKD - chronic kidney disease, T2DM - type 2 diabetes mellitus, BPH - benign prostate hypertrophy, GORD - gastro-oesophageal reflux disease, HTN - hypertension, IHD - ischaemic heart disease, AF - atrial fibrillation, AvR - aortic valve replacement, UIP – usual interstitial pneumonia. FVC – forced vital capacity, TLCO – total lung diffusion carbon monoxide. For smoking status – Ex smoker defined as abstinent for >12 months. Radiological Classification as per 2018 joint ATS/ERS classification[20].*

Condition	Sample ID	Gender	Age	Smoking status	Ethnicity	Radiological Classification	Predicted FVC %	Predicted TLCO %	Medication	Active Comorbidities
IPF	**HT1**	Male	85	Ex	British Caucasian	UIP	78	44	Pirfenidone, Omeprazole, Amlodipine, Pravastatin, Telmisartan, Febuxostat	Pulmonary hypertension, Peripheral vascular disease, hypertension, CKD
	HT3	Male	85	Never	British Caucasian	UIP	73	37	Nintedanib, Amlodipine, Atorvastatin, Clopidogrel	Hypertension
	HT1b	Female	74	Never	British Caucasian	UIP	72	52	Pirfenidone, Seretide, Metformin, Gliclazide, Lansoprazole, Levo-thyroxine, Simvastatin	Hypothryoidism, T2DM
Control	**HT2b**	Male	70	Ex	British Caucasian	Normal	n/a	n/a	Omeprazole	Nil
	HT3b	Female	47	Never	British Caucasian	Normal	n/a	n/a	Omeprazole	Nil
	HT4b	Female	67	Never	British Caucasian	Normal*	n/a	n/a	Fluoxetine, Amitriptylline, Zopiclone, Levo-thyroxine	Hypothyroidism

Table 3.2.2 - Demographic details of patients and controls for Cohort B single cell RNA sequencing of PBMC. **Increased infiltrates on CT on contralateral lung lobe to bronchoalveolar lavage sampling. Abbreviations; CKD - chronic kidney disease, T2DM - type 2 diabetes mellitus, UIP – usual interstitial pneumonia. FVC – forced vital capacity, TLCO – total lung diffusion carbon monoxide. For smoking status – Ex smoker defined as abstinent for >12 months. Radiological Classification as per 2018 joint ATS/ERS classification[20].*

3.2.3 Suspension mass cytometry - IFN-β stimulation and antibody staining

Full experimental details for sample preparation, IFN-β stimulation and metal conjugated antibody staining are detailed in Section 2.1.2 and 2.1.3. The details of antibody clones, lanthide metal conjugates, marker type and staining step are summarised in Table 3.2.3.

In brief, cryopreserved PBMCs from IPF patients and age matched controls were stained with fix sensitive antibodies before being equally divided for baseline (unstimulated) analysis or stimulated with 250U/ml recombinant IFN-β for 15 mins before fixation. Individual samples were barcoded and pooled into batches equally comprised of IPF and controls. Batches were stained with cell surface and intracellular metal conjugated antibodies as detailed in Section 2.1.3. Following staining batched samples were incubated overnight with Iridium DNA intercalator before being mixed with equalisation beds (EQ) then acquired on a Helios suspension mass cytometer at a rate of <300 events/second.

Marker	Clone	Metal	Cat no	Vendor	Conjugated In house?	Staining step	Dilution	Marker Class 'type' or 'state'	Myeloid cell re-cluster?
CD45	HI30	89Y	3089003B	Standard Biotools	No	Surface Stain	1:100	type	No
CD14	M5E2	114Cd	301843	BioLegend	Yes	Fix sensitive stain	1:100	type	Yes
CD11c	6.9	141Pr	301602	BioLegend	Yes	Surface Stain	1:100	type	Yes
CD11b	ICRF44	142Nd	301337	BioLegend	Yes	Surface Stain	1:200	type	Yes
CD45RA	HI100	143Nd	304102	BioLegend	Yes	Surface Stain	1:50	type	No
HLA-DR	L243	144Nd	307602	BioLegend	Yes	Surface Stain	1:400	type	Yes
CD4	RPA-T4	145Nd	300570	BioLegend	Yes	Surface Stain	1:800	type	No
CD19	HIB19	146Nd	302247	BioLegend	Yes	Surface Stain	1:100	type	No
CD20	2H7	147Sm	302343	Biolegend	Yes	Surface Stain	1:200	type	No
CCR6	G034E3	148Nd	353401	BioLegend	Yes	Fix sensitive stain	1:100	type	No
CD56	QA18A21	149Sm	398802	BioLegend	Yes	Fix sensitive stain	1:50	type	No
pSTAT5	Y694	150Nd	3150005A	Standard Biotools	No	Intracellular stain	1:50	state	No
CD45RO	UCHL1	151Eu	304239	BioLegend	Yes	Fix sensitive stain	1:100	type	No
CD27	O323	152Sm	302839	BioLegend	Yes	Fix sensitive stain	1:100	type	No
pSTAT1	Y701	153Eu	3153003A	Standard Biotools	No	Intracellular stain	1:50	state	No
CD1c	L161	154Sm	331502	BioLegend	Yes	Surface Stain	1:100	type	Yes
CD123	6H6	155Gd	306027	BioLegend	Yes	Surface Stain	1:200	type	Yes
pp38	T180/Y182	156Gd	3156002A	Standard Biotools	No	Intracellular stain	1:50	state	No
pSTAT3	Y705	158Gd	3158005A	Standard Biotools	No	Intracellular stain	1:50	state	No
pMAPKAPK2	T334	159Tb	3159010A	Standard Biotools	No	Intracellular stain	1:50	state	No
CD3	UCHT1	160Gd	300438	BioLegend	Yes	Surface Stain	1:100	type	No
DNGR1	8F9	161Dy	353802	BioLegend	Yes	Surface Stain	1:50	type	Yes
IFNAR2	MMHAR-2	162Dy	NBP2-89447	Novus Bio	Yes	Surface Stain	1:50	state	No
STAT1	246523	163Dy	MAB1490	R&D Systems	Yes	Intracellular stain	1:50	state	No

CD161	HP-3G10	165Ho	339919	BioLegend	Yes	Surface Stain	1:400	type	No
pNFkBp65	S529	166Er	3166006A	Standard Biotools	No	Intracellular stain	1:50	state	No
CCr7	150503	167Er	MAB197	R&D Systems	Yes	Fix sensitive stain	1:100	type	No
pSTAT6	Y641	168Er	3149004A	Standard Biotools	No	Intracellular stain	1:50	state	No
CD64	10.1	169Tm	305029	BioLegend	Yes	Surface Stain	1:100	type	Yes
CD141	M80	170Er	344102	BioLegend	Yes	Surface Stain	1:100	type	Yes
pERK12	D13.14.4E	171Yb	3171010A	Standard Biotools	No	Intracellular stain	1:50	state	No
CD38	HIT2	172Yb	303502	BioLegend	Yes	Surface Stain	1:100	type	No
STAT3	15H2B45	173Yb	371802	BioLegend	Yes	Intracellular stain	1:50	state	No
pSTAT4	Y693	174Yb	3148006A	Standard Biotools	No	Intracellular stain	1:50	state	No
CCR4	205410	175Lu	MAB1567-100	R&D Systems	Yes	Fix sensitive stain	1:50	type	No
CXCR3	G025H7	176Yb	353702	BioLegend	Yes	Fix sensitive stain	1:100	type	No
CD8	RPA-T8	198Pt	301074	BioLegend	Yes	Surface Stain	1:200	type	No
CD16	3G8	209Bi	3209002B	Standard Biotools	No	Surface Stain	1:100	type	Yes

Table 3.2.3. Antibody panel used for CyTOF experiments*, including antibody clones, metal conjugates, staining step, and marker classification. 'type' markers refer to phenotyping antibodies used to define cell populations and included in clustering analyses, whereas 'state' markers refer to functional antibodies associated with Type 1 interferon signalling.*

3.2.4 Suspension mass cytometry - data processing and analysis

Following acquisition, EQ bead normalisation within batches of cytometry data was performed using the 'FCS Processing' function (Standard Biotools 'CyTOF' package v7.0) followed by concatenation. Concatenated files were de-barcoded using CyTOF 'Debarcoder' function with standard parameters from the Plex 20-ID debarcoder key to generate individual .fcs files. Manual gating of gaussian parameters – residual, width, centre and offset, followed by EQ bead, doublet and dead cell exclusion was performed in Flow Jo (Version 10.8.1) following the gating strategy outlined in Figure 3.2.2.

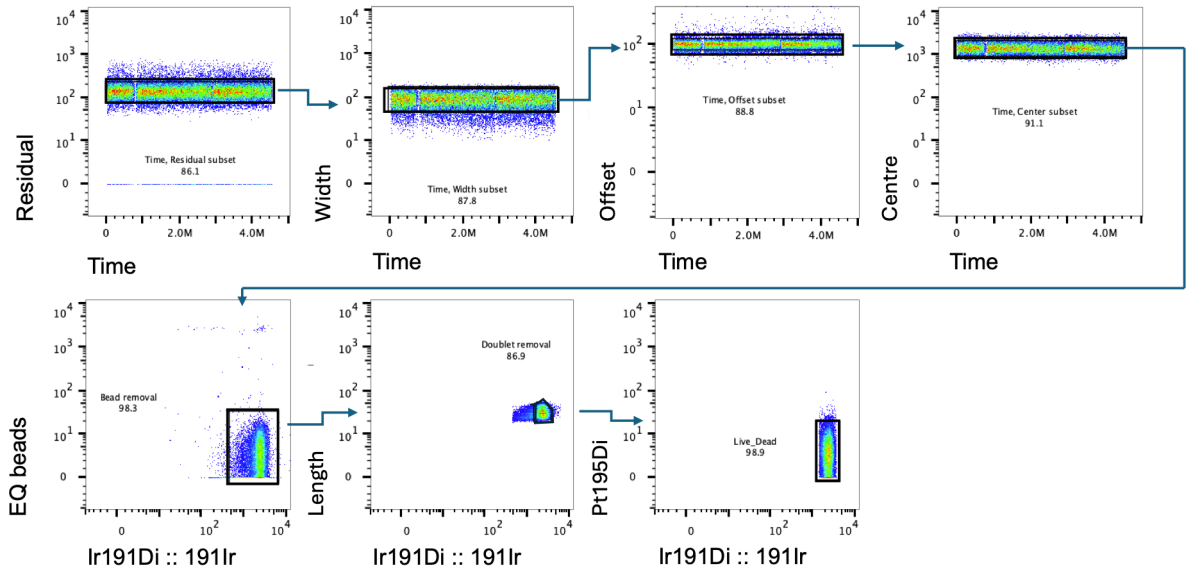


Figure 3.2.2. CyTOF gating strategy. *Initial quality control performed gating on gaussian signal parameters (residual, width, offset, and centre) against acquisition time plots, characterising the shape and signal intensity of each event ion cloud. Events outside the expected gaussian profile were excluded to remove periods of instrument instability and non-specific or poorly acquired signals. Following EQ calibration bead removal, doublets (increased Ir191/93 or event length) and debris (low Ir191/93) were then excluded. Cell viability was assessed using cisplatin (Pt195) and Ir191/93 plots, with Pt195-high events excluded to remove dead cells. Live, nucleated single cells (Ir191/193-positive, Pt195-low) were carried forward for downstream analysis. Abbreviations; EQ -Equilibration beads.*

Individual .fcs files were then imported into R studio to generate a data frame comprised of cells in rows and median metal marker expression in columns. Batch correction was performed on arcsinh transformed (co-factor=5) protein expression using the cyCombine[231] package where cells with shared marker expression are grouped using unsupervised clustering. The distribution of marker expression between batches of comparable populations was measured and aligned. Downstream analysis including cell clustering was performed using the Catalyst package[232].

Raw event count data were used to explore differences in proportions of populations between IPF and control samples. To examine differences in response to IFN-β, arcsinh transformed median metal intensity (MMI) values of IFN signalling markers were extracted for each cell population. Fold changes in phosphoprotein MMI expression between paired stimulated and unstimulated samples for each cell type were calculated for each cell population. Statistical differences in the mean fold change between IPF and control cell subsets was assessed using an unpaired student t-test after confirming normal data distribution.

This analysis was designed as a targeted, hypothesis-driven investigation to address biological questions regarding differential responses to IFN-β across PBMC populations in IPF and healthy controls. A phosphoprotein panel developed to interrogate signalling pathways downstream of IFNAR activation was used to investigate these questions. Consequently, formal multiple-testing correction was not applied, as the analysis was restricted to addressing predefined biological comparisons within the IFNAR signalling pathway rather than an exploratory discovery analysis.

3.2.5 PBMC processing and droplet based single cell RNA sequencing

PBMC sample processing and single cell sequencing methods are described in Methods, section 2.1.4.

3.2.6 Processing, quality control and analysis of single cell RNA sequencing data

Processing of raw sequencing data was performed in conjunction with Jeongmin Woo, a senior bioinformatician in the Ho group. Initial downstream analysis of the single-cell datasets was conducted by Dr Woo; following training, I performed additional analyses independently in RStudio with her guidance. Interpretation of the data and its alignment to biological and disease contexts was undertaken by myself in conjunction with members of the Ho group.

Raw base call files generated following Illumina sequencing from two independent sequencing runs were converted into FASTQ files using the Cell Ranger pipeline (version 3.1.0). These FASTQ files contain sequencing reads of gene expression with corresponding cell barcodes and unique molecular identifiers (UMIs), to enable assignment of reads to individual cells and molecular transcripts. The Cell Ranger pipeline was then used to process the FASTQ files by first, extracting cell barcodes and UMIs from each read, aligning reads to the hg38 (version 3.0.0) human reference genome, and then, quantifying gene expression by counting UMIs per gene per cell. This resulted

in the generation of a gene–cell expression matrix with gene expression counts (columns) for each cell (rows).

In parallel, hashtag oligonucleotide (HTO) libraries were processed separately using CITE-seq-Count (version 1.4.3). This tool identifies HTO sequences and corresponding UMIs associated with each cell barcode. These HTO counts were used to demultiplex pooled samples, allowing assignment of each cell to its sample of origin. Finally, gene expression data with HTO-derived sample assignments were integrated to generate a combined dataset containing both gene expression profiles and corresponding sample identities (HTO and cell barcodes) for each individual cell.

Additional cell quality filtering was performed using the 'emptyDrops' function from the *DropletUtils* package to examine the distribution of mRNA and mitochondrial RNA count distributions and exclude barcodes with low mRNA (containing ambient RNA) or high mitochondrial RNA to exclude low quality or dying cells. Hashtag oligonucleotide (HTO) demultiplexing was performed with the *Seurat* (version 3.3.0) 'HTODemux' function where cell barcodes that were unassigned or associated with multiple hashtags, representing doublets were excluded. Finally, additional filtering was performed to retain high-quality cells, excluding cell barcodes with fewer than 500 detected genes, greater than 10% mitochondrial gene expression, or greater than 5% ribosomal gene expression relative to total expression.

Further downstream analysis was performed using *Seurat* (version 3.3.0) for data processing for each batch. The UMI count matrix was log-normalised using the 'NormalizeData' function, and expression values scaled using the and 'ScaleData' functions to standardise gene expression across cells. Highly variable genes were identified by modelling the mean-variance relationship of genes, to identify and select those genes exhibiting greater variability than expected based on average expression. Dimensionality reduction was performed using principal component analysis (PCA) on highly variable genes and scree plots were used to determine the optimum number of PCAs. Batch correct and integration of the two sequencing runs was performed using Harmony (version 0.1.1) of the principal components that were adjusted for batch and sample variation. A k-nearest neighbour (kNN) graph was constructed using the harmonised principal components where each cell was connected to its nearest neighbours based on similar gene expression profiles before clustering was performed using the Louvain algorithm to identify groups of transcriptionally similar cells.

Cluster-defining genes (CDGs) were visualised using bubble plots. For each cluster, differentially expressed genes meeting the predefined thresholds (adjusted $P < 0.05$ and average log2 FC> 0.25 or < –0.25) were ranked according to average log2 FC, and the top 10 genes were displayed. Circle size represents the percentage of cells within the cluster expressing each gene, while colour intensity represents the average normalised gene

expression. Cluster annotation was performed by examining the top CDGs for each cell type in conjunction with manual comparison using published reports and reference datasets.

Differential gene expression (DEG) analysis was performed using the DESeq2 package with a psuedobulk approach whereby gene expression counts were aggregated across all cells belonging to the same sample within each cell population. Comparative gene expression was then performed between disease groups, with a false discovery rate (FDR) p-value threshold of 0.1 used to define significance. For visualisation, heatmaps were generated using the transformed pseudobulk expression values for significantly differentially expressed genes following hierarchical clustering of genes and donor samples.

To facilitate biological interpretation of CDGs or DEGs, either pathway enrichment analysis (PEA) or gene set enrichment analysis (GSEA) was performed depending on the number of DEGs identified.

PEA was used when sufficient numbers of DEGs were available. Pathway enrichment analysis was performed using significantly upregulated genes (typically log2FC > 1.5 and FDR -adjusted P < 0.05 unless specified). Enriched pathways were identified using Fisher's exact test to determine whether DEGs were over-represented within predefined biological pathways. The gene ratio represents the proportion of DEGs assigned to each pathway relative to the total number of DEGs included in the enrichment analysis. PEA results were generally visualised as bubble plots, where the x-axis represents the gene ratio (the proportion of DEGs assigned to each pathway relative to the total number of DEGs included in the enrichment analysis), bubble size represents the number of DEGs contributing to each pathway (gene count), and colour indicates the FDR adjusted P value. Pathways were ordered according to gene ratio unless otherwise stated.

When relatively few DEGs were identified, GSEA was performed. Unlike PEA, GSEA does not require prior filtering of genes based on differential expression thresholds. Instead, all genes were ranked according to differential expression between the comparison groups, and enrichment scores were calculated to determine whether predefined gene sets were preferentially represented towards the top or bottom of the ranked gene list. This approach enables detection of coordinated changes across biologically related gene sets, even when individual genes do not meet conventional significance thresholds. GSEA results were visualised and ranked according to the normalised enrichment score (NES), which reflects the relative strength of enrichment of each gene set after accounting for differences in gene set size.

Comparative analysis of regulon activity at both the single cell level and between disease states was performed using the Single-Cell rEgulatory Network Inference and Clustering (SCENIC) workflow[233] and described in Section 3.3.9.

3.3 Results

3.3.1 High resolution single cell antibody-based (CyTOF) analysis of PBMCs reveals six monocyte subtypes

PBMCs from IPF patients (n=21) and age-matched controls (n=11) from Cohort A were used to investigate downstream responses to type 1 IFN stimulation (Figure 3.2.1).

Following data acquisition and raw data processing (Chapter 3.2.4) $9.56x10^6$ single cells (IPF = $7.04x10^6$, HC = $2.52x10^6$) were available for clustering and downstream analysis. Clustering was performed using the FlowSom algorithm implemented in the *Catalyst* package designed for the analysis of CyTOF data[232]. The CyTOF antibody panel comprised 26 'phenotyping' markers to identify the main PBMC cell populations and 12 'functional' markers to enable investigation of type 1 IFN signalling pathways downstream of the IFNAR (Figure 3.2.1). Clustering was performed using phenotyping markers and included unstimulated and stimulated samples.

Cell clusters were annotated based on expression of phenotyping markers. Initial clustering identified all major PBMC subsets including $CD4^+$, $CD8^+$ T cells, NK cells, B cells, plasmablasts, monocytes and DC populations. T cell populations were further classified according to CD45RA and CD45RO expression to label naïve and memory subsets. NK cells were resolved into 2 distinct clusters based on CD56 and CD16 expression and were labelled $CD5h^{hi}$ NK cells and $CD56^{mid}$ NK cells as previously described [234, 235] (Figure 3.3.1).

The proportions of each cell population, expressed as a percentage of total PBMCs (combined IPF and control samples) were as follows; $CD4^+$ T cells (30.8%), $CD8^+$ T Cells (20.2%), monocytes (19.3%), NK cells (18.4%), B cells (6.3)% and DCs (1.47%) (Figure 3.3.1). Two populations were classified as undefined (UD) (<1% total PBMCs). UD_1 included cells expressing proteins attributed to multiple immune cell types likely representing doublets not excluded during manual gating (Figure 3.2.2). UD_2 comprised of cells with poor staining.

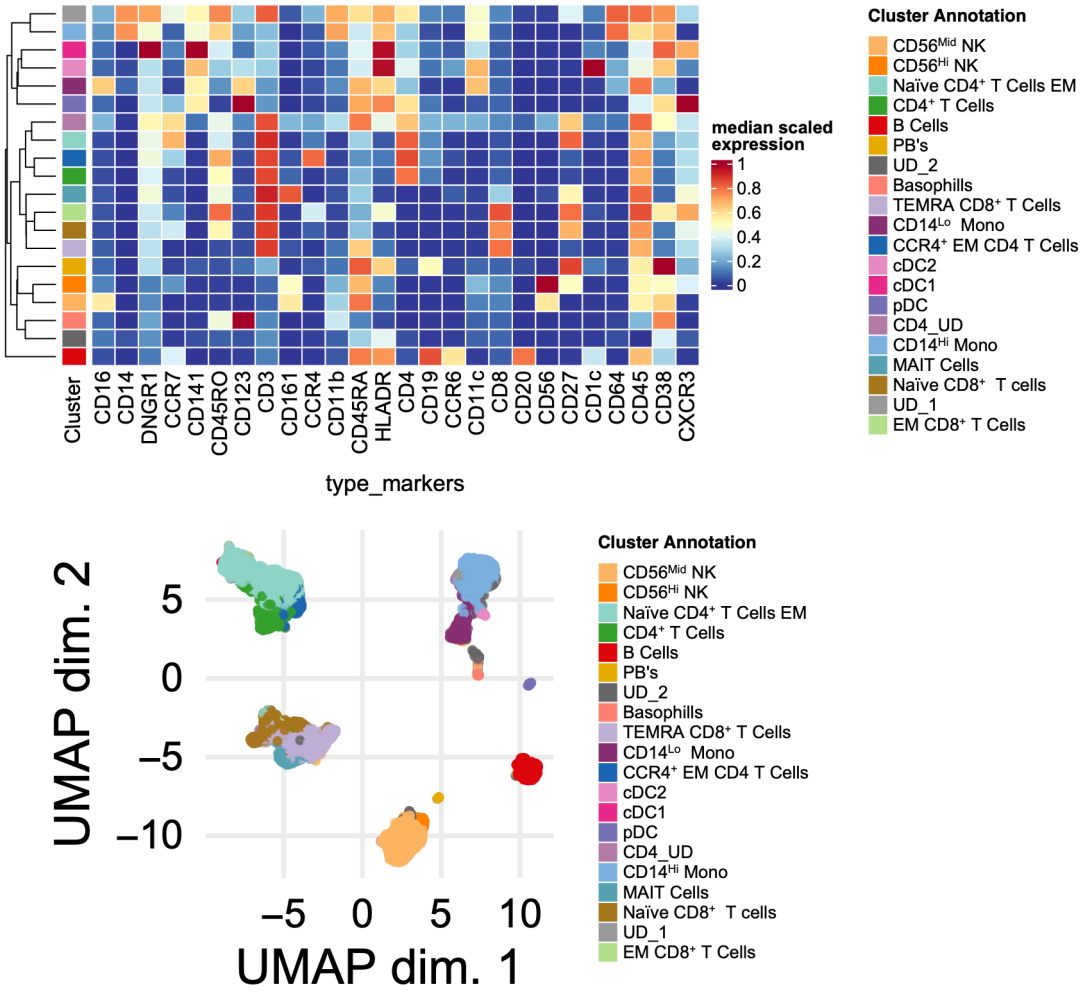


Figure 3.3.1. PBMC populations identified with CyTOF. *Top panel: Annotated expression heatmap and Uniform Manifold Approximation and Projection [UMAP] (middle panel) of PBMC populations following FloSOM clustering from IPF n = 21 and control samples n = 11. Bottom panel, composition of PBMC populations (% of all circulating PBMCs) in IPF and controls.*

Initial clustering revealed two monocytes subsets annotated as $CD14^{hi}$ and $CD14^{lo}$ monocytes. To characterise circulating monocytes at higher resolution, $CD14^{hi}$ monocytes, $CD14^{lo}$ monocytes and DC clusters were further re-clustered using myeloid-related phenotyping markers in line with a recent CyTOF study of PBMCs[236] (Figure 3.2.1 and Table 3.2.3).

Following reclustering, four DC populations were identified; plasmacytoid DCs (pDCs), 2 subsets of conventional DCs (cDC1 and cDC2) and monocyte derived DCs (monoDCs) annotated according to protein expression (Figure 3.2.2). Five monocyte subsets were identified; classical monocytes (cMono), non-classical monocytes (ncMono), a CD16 mid expressing ncMono population ($CD16^{Mid}$ Mono), a small $CD14^{+}CD16^{+}$ intermediate monocyte population (Intm Mono) and a separate classical monocyte population with increased CD64 and HLADR expression ($CD64^{hi}$ cMono) (Figure 3.3.2). This $CD64^{hi}$ population has been previously described in patients with severe COVID-19[236]. Notably, it exhibited the highest constitutive expression of phosphorylated proteins among myeloid subsets suggesting it may represent a monocyte subset in an enhanced inflammatory state. (Figure 3.3.2).

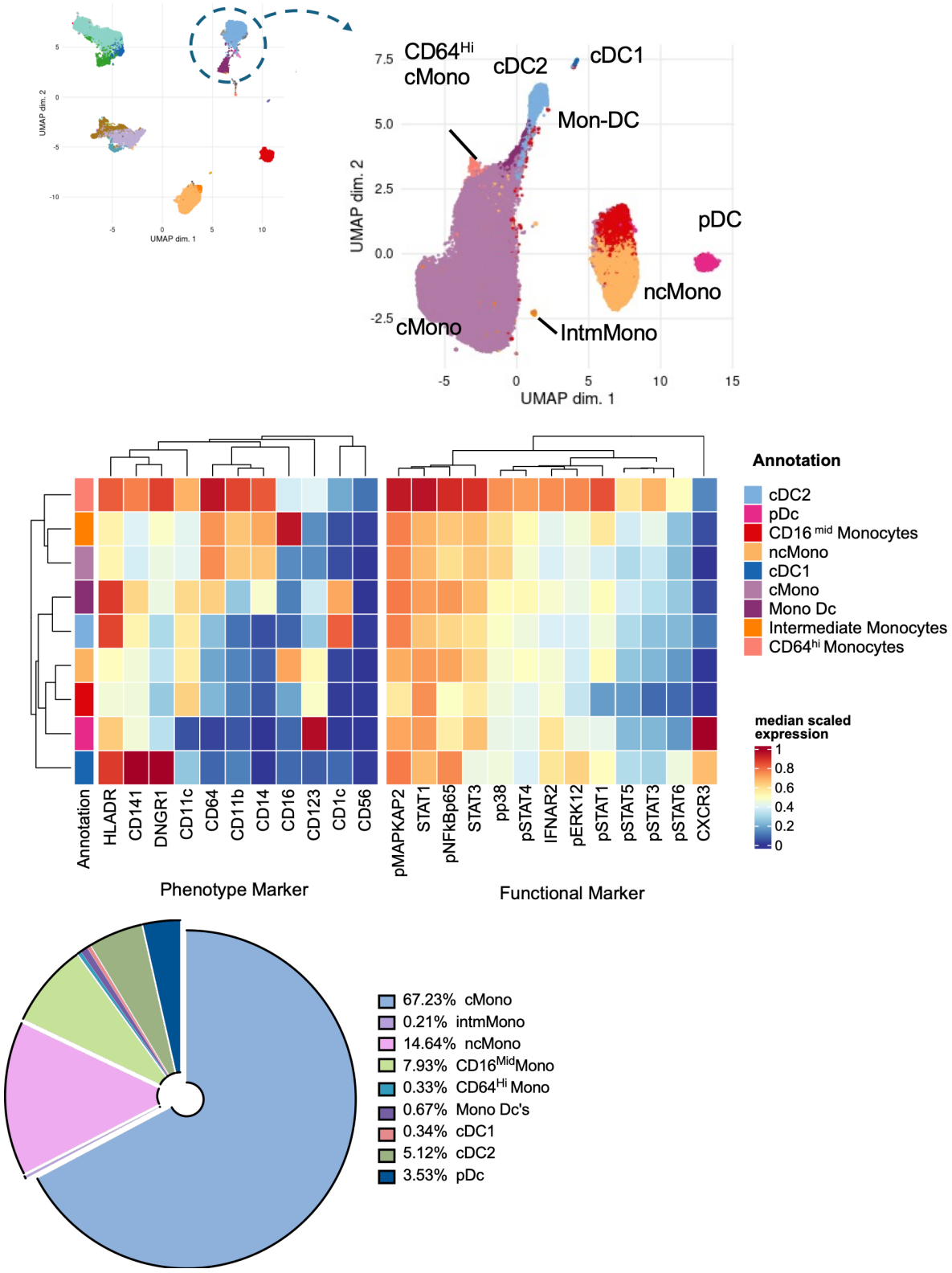


Figure 3.3.2. Monocyte and DC subsets identified with re-clustering. *Top Panel - UMAP of PBMCs clustered using Flowsom (monocytes and DCs are circled and further re-clustered). Middle panel - Heatmap of median marker scaled expression of phenotyping (type) marker expression and functional marker expression (state). Monocyte and DC subclusters annotated according to expression of proteins and analysed against labels generate by CyTOF analysis in COMBAT[236]. Bottom panel - composition of PBMC populations (% of all circulating monocytes and DCs.)*

3.3.2 Composition analysis show increased TEMRA CD8+ T Cells and reduced CD56hi NK cells in IPF patients

Comparison of cellular composition between IPF and controls, revealed the proportion of circulating $CD56^{hi}$ NK cells (as percentage of all PBMCs) were significantly reduced in IPF ($p<0.001$ student's t-test). In addition, circulating $CD8^{+}$ TEMRA (terminally differentiated effector memory re-expressing CD45RA) T cells were significantly increased in IPF compared to age matched controls ($p=0.046$ student's t-test) (Figure 3.3.3). A trend towards an increased proportion of all monocytes as a proportion of PBMCs was observed in IPF (0.2 vs 0.15 in controls) although this did not reach statistical significance ($p = 0.09$).

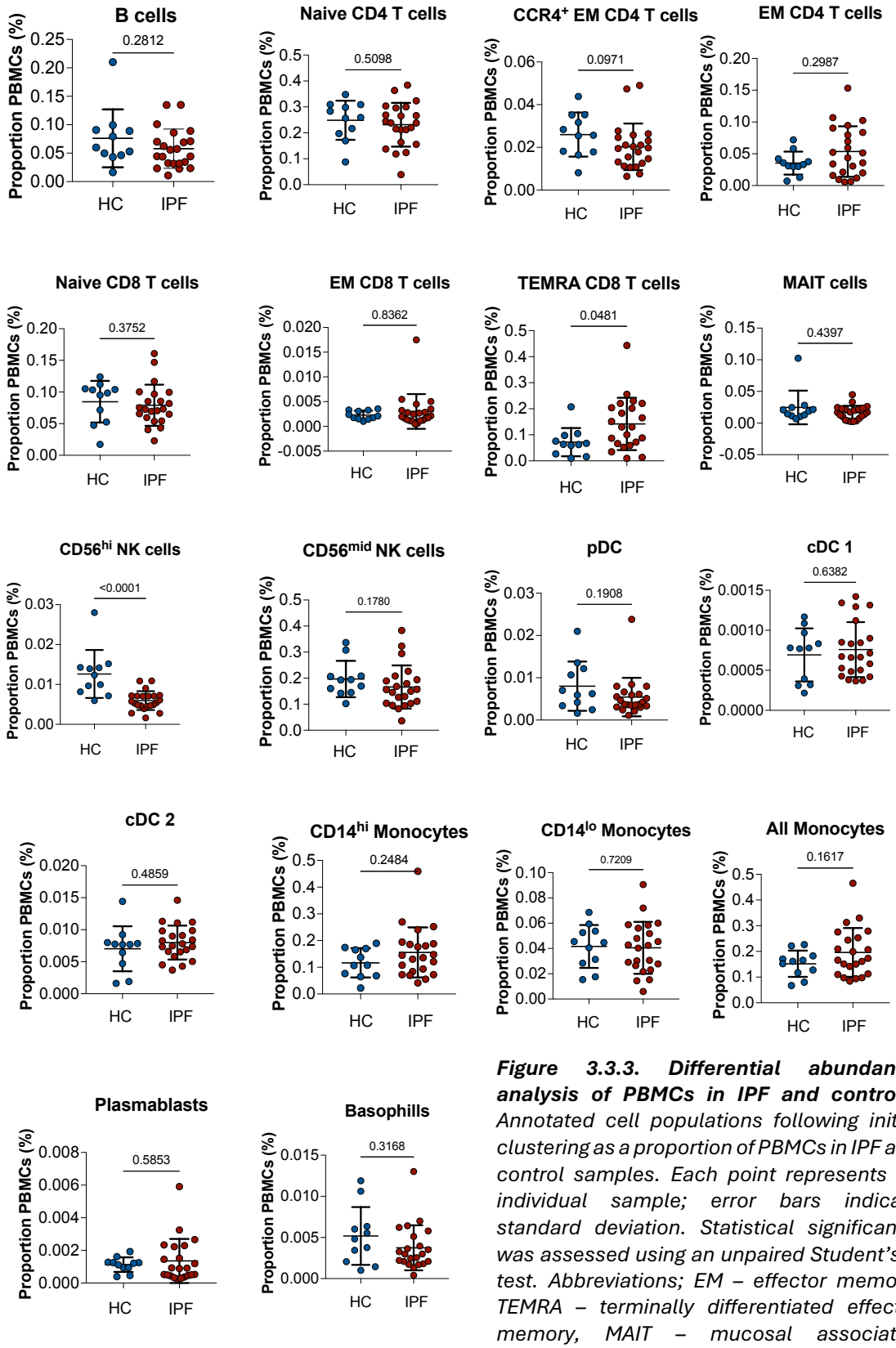


Figure 3.3.3. Differential abundance analysis of PBMCs in IPF and controls. *Annotated cell populations following initial clustering as a proportion of PBMCs in IPF and control samples. Each point represents an individual sample; error bars indicate standard deviation. Statistical significance was assessed using an unpaired Student's t-test. Abbreviations; EM – effector memory, TEMRA – terminally differentiated effector memory, MAIT – mucosal associated invariant T cells.*

There were no statistically significant differences in the proportion of re-clustered monocyte and DC populations in IPF compared to control (Figure 3.3.4).

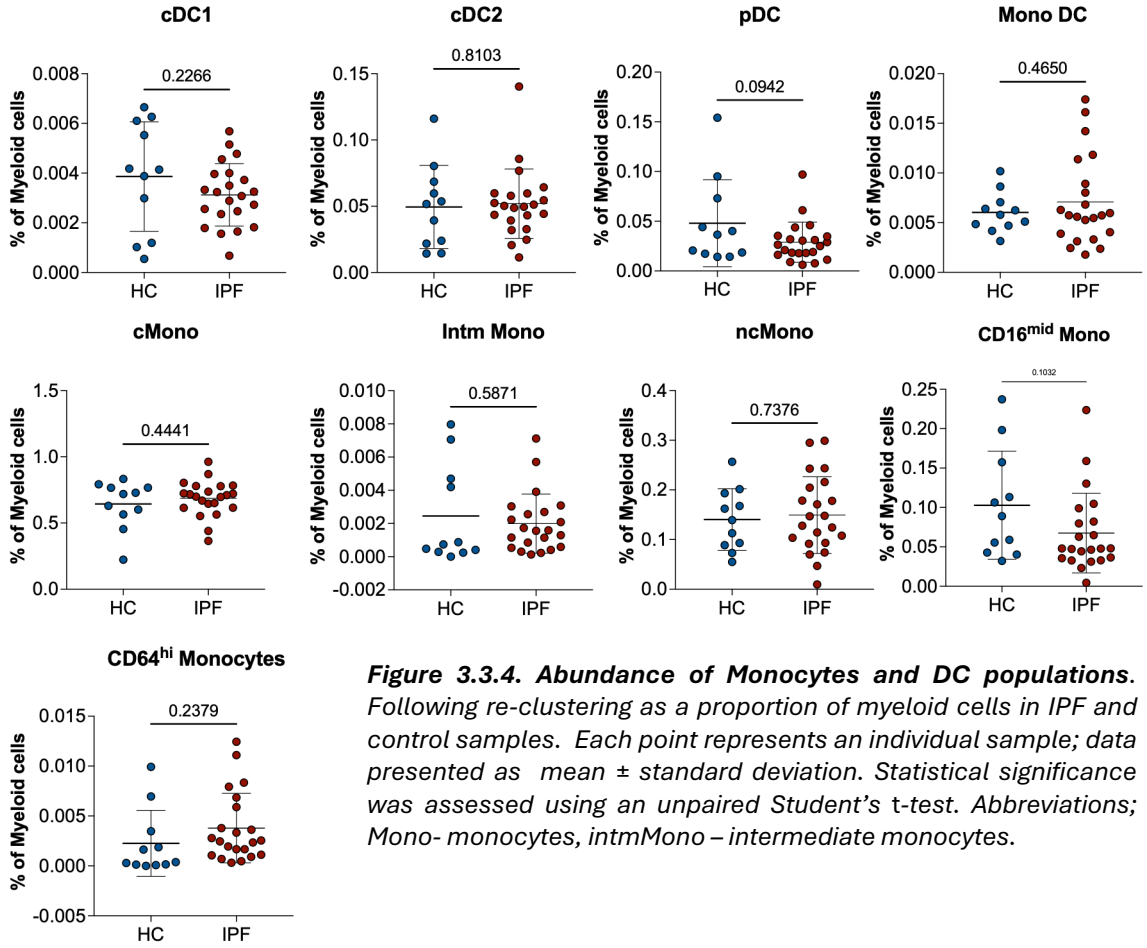


***Figure 3.3.4. Abundance of Monocytes and DC populations**. Following re-clustering as a proportion of myeloid cells in IPF and control samples. Each point represents an individual sample; data presented as mean ± standard deviation. Statistical significance was assessed using an unpaired Student's t-test. Abbreviations; Mono- monocytes, intmMono – intermediate monocytes.*

3.3.3 Classical monocytes in IPF show a heightened response to IFN-β stimulation with increased canonical pSTAT expression

Following the characterisation of circulating PBMC populations and myeloid subsets, downstream signalling pathway activation in response to IFN-β stimulation was investigated.

The CyTOF panel was designed to profile a key signalling pathways activated following IFN-β binding to IFNAR. These included pSTAT1 and pSTAT3 to outline 'canonical JAK-STAT signalling pathways'. In addition, pSTAT4, pSTAT5 and pSTAT6 were used to delineate non canonical, STAT-dependent signalling, while pNFκB, pMAPKAPK2, pERK1/2 and pp38 to outline non canonical STAT-independent signalling' pathways. (Table 3.2.1, Figure 3.3.5).

Following IFN-β stimulation, all PBMC populations demonstrated activation of canonical JAK-STAT signalling pathways with the largest increase in pSTAT1 and pSTAT3 expression (Figure 3.3.6).

Non-canonical, STAT-dependent signalling was also elevated with increased pSTAT4, pSTAT5 and pSTAT6 expression. Notably, increased pSTAT4 signalling was restricted to T lymphocyte and NK cell subsets with no change in expression in B cell, monocyte of DC populations consistent with previous reports[237]. Overall, non-canonical STAT signalling was lower than observed for canonical pSTAT1/3 signalling. In the IFN-β stimulation conditions used, (250U/ml for 15 mins) there was minimal activation of non-canonical, STAT-independent, signalling including pNFkB, pp38, pMAPKAP2 and pERK1/2 in line with previous observations[237] (Figure 3.3.5).

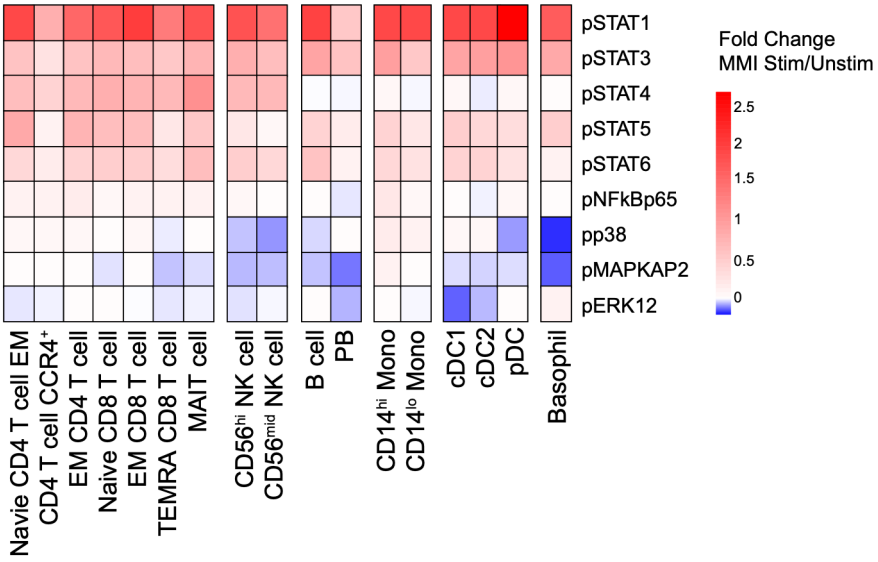


Figure 3.3.5. Cell type responses to type 1 IFN stimulation. *Heatmap of type1 interferon (type 1 IFN)-associated protein expression in PBMC populations following stimulation with IFN-β (250 U/mL) for 15 minutes. Cell populations from IPF and control samples were combined to assess cell type-specific responses. Protein expression is presented as fold change normalised median metal intensity (MMI) stimulated samples compared to unstimulated samples, averaged across all cells within each population. Red colour reflects higher fold change in stimulated samples. Abbreviations; EM – effector memory, TEMRA – terminally differentiated effector memory, MAIT – mucosal associated invariant T cells, Mono – monocytes, PB - plasmablasts.*

Next, differences in response to IFN-β stimulation between IPF and controls were assessed in circulating monocyte and DC populations (Figure 3.3.6). cMonos demonstrated a significantly increased response to IFN-β stimulation in IPF with an increase in pSTAT1 and pSTAT3 expression. MonoDCs also showed an increase in pSTAT3 expression in IPF compared to controls.

No other monocyte or DC subset showed a differential response to IFN-β stimulation in IPF. Notably these included pDCs the archetypal producers of type 1 IFNs and CD64^{hi}

cMonos, the latter which exhibited the highest phosphorylated STAT protein expression at baseline. (Figure 3.3.6).

While changes in pNFκB MMI between unstimulated and stimulated were small, IntMono showed a significant increase in pNFκB expression in IPF compared to controls.

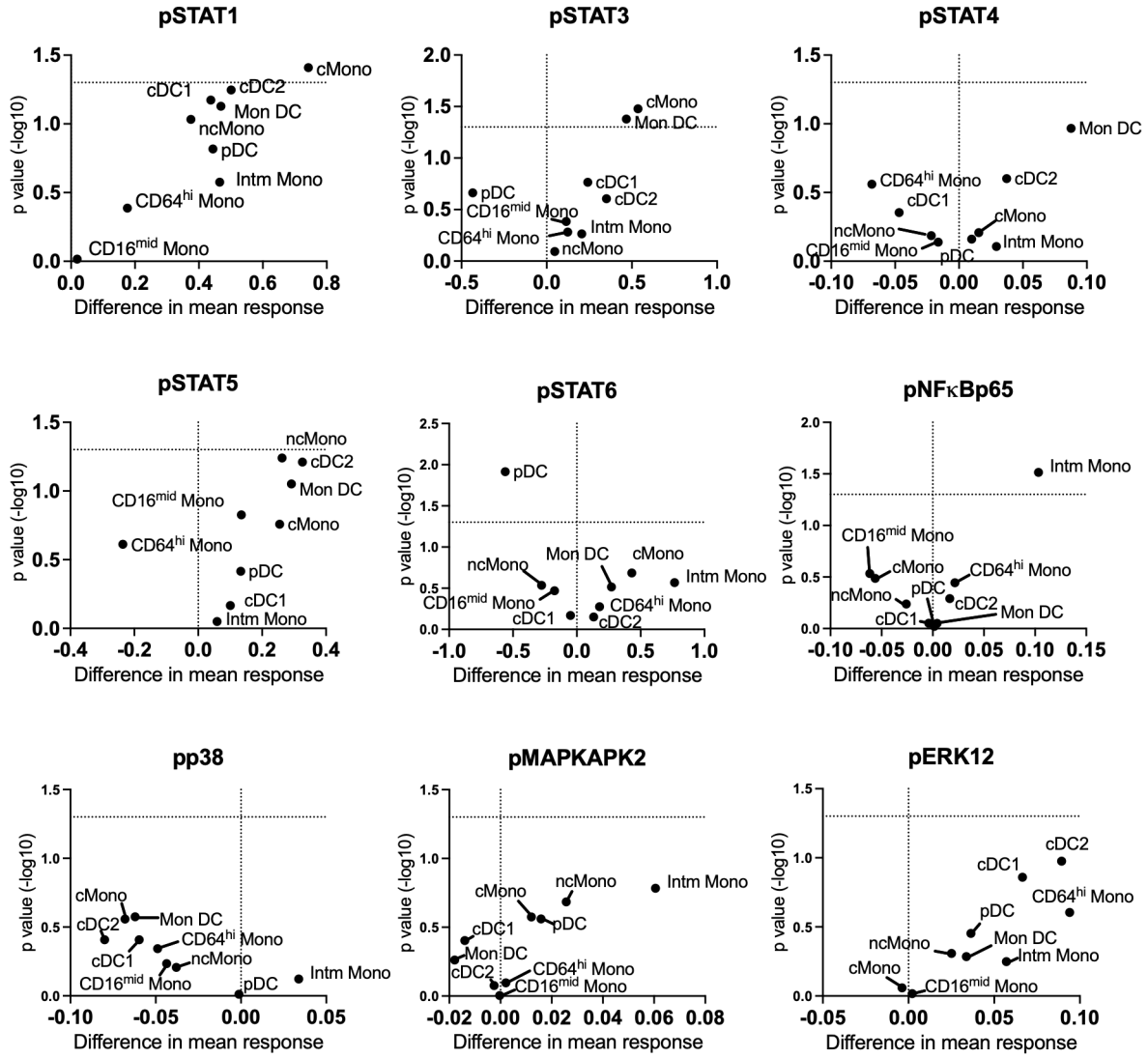


Figure 3.3.6. Statistical comparison of response to IFN-β stimulation in monocyte and dendritic cell populations between IPF and healthy controls (HC). *Data presented as volcano plots to enable simultaneous visualisation of all cell subtypes. The x-axis represents difference in response measured by calculating the fold change in MMI between stimulated and unstimulated cells in both conditions, then comparing the difference in fold change between IPF and controls. The y-axis represents statistical significance (−log_{10}* P*), determined using an unpaired Student's* t*-test. The vertical dashed line indicates no difference in response between groups, and the horizontal dashed line denotes the threshold for statistical significance (*P *< 0.05). Points above this threshold represent populations with significantly different responses between IPF and HC.*

These differences in IPF myeloid pathway activation were considered in the context of established transcriptional responses downstream of IFNAR. pSTAT1 homodimers

initiate transcription of ISGs harbouring the GAS motif in their promotor regions. Whereas, pSTAT1-pSTAT2 heterodimers induce transcription of classical antiviral ISGs[199]. pSTAT3 homodimers are linked to immunoregulatory responses following type 1 IFN stimulation via several mechanisms, including transcriptional repression of GAS binding sites that antagonise the pSTAT1 response and also via promoting IL-10 transcription.

3.3.4 NK cells, effector memory CD4$^+$ T cells and naïve CD8$^+$ T cells display increased responses to IFN-β stimulation

Examination of differential responses to IFN-β stimulation in other PBMC populations revealed several signalling pathways were differentially expressed in lymphocyte subsets. Effector memory CD4$^+$ T cells exhibited an increased response to type 1 IFN with increased pSTAT1 and pSTAT3 expression in IPF – similar to the finding seen in cMono. In addition, EM CD4$^+$ T cells also showed increased pSTAT5 expression in IPF (Figure 3.3.7). Increased, pSTAT3 and pSTAT5 expression was also observed in CD56^{mid} and CD56^{hi} NK cells in IPF. Furthermore, naive CD8$^+$ T cells also showed increased expression of pSTAT3 and pSTAT6 following stimulation in IPF compared to controls.

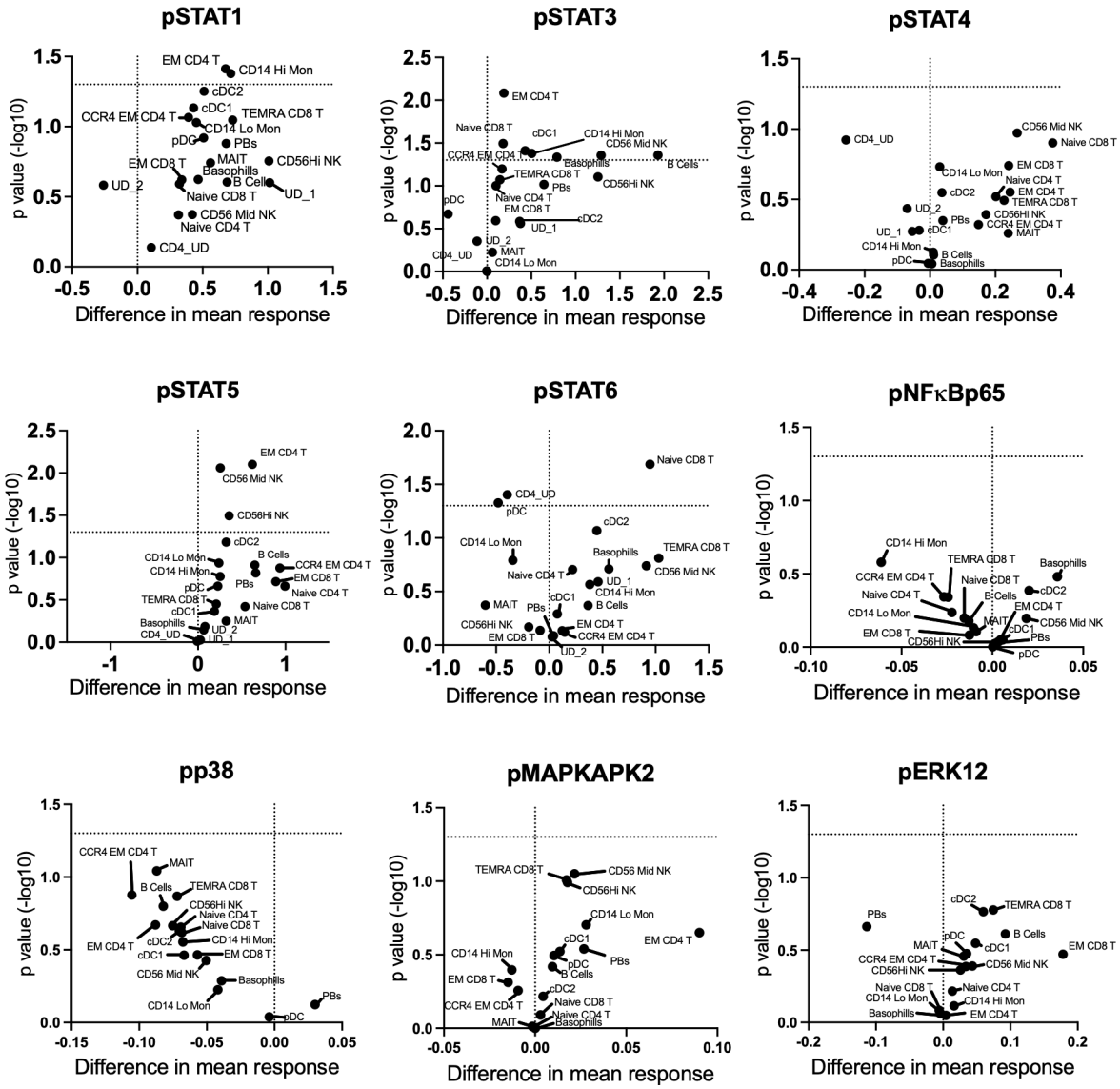


Figure 3.3.7. Statistical comparison of response to IFN-βstimulation in PBMC populations between IPF and healthy controls (HC). *Data presented as volcano plots to enable simultaneous visualisation of all cell subtypes. x-axis represents difference in response measured by calculating the fold change in MMI between stimulated and unstimulated cells in both conditions, then comparing the difference in fold change between IPF and controls. The y-axis represents statistical significance (−log$_{10}$* p*), determined using an unpaired Student's* t*-test. The vertical dashed line indicates no difference in response between groups, and the horizontal dashed line denotes the threshold for statistical significance (*p *< 0.05). Points above this threshold represent populations with significantly different responses between IPF and HC. Abbreviations; EM - effector memory, TERMA - terminally differentiated effector memory, Mon – monocytes, PB plasmablasts, UD – undefined*

These findings were considered in the context of existing literature on downstream responses to type 1 IFN signalling. In lymphocytes, pSTAT5 activation has been associated with the formation of pSTAT5–CRKL complexes, which initiate for transcription of pro-inflammatory GAS-driven ISGs in lymphocytes[194, 238].

STAT6 phosphorylation has also been described in lymphocytes following type 1 IFN stimulation[239], however its functional role in this context remains unclear. In hepatocytes and B cells, however type 1 IFN associated pSTAT6 signalling has been investigated where pSTAT6–pSTAT2 heterodimers form an ISGF3-like complex capable of inducing antiviral ISG expression[240].

3.3.5 pSTAT1:pSTAT3 expression is significantly higher in IPF cMonos following IFN-β stimulation

Results from Sections 3.3.3 and 3.3.4, together with existing literature, indicate that that differential responses across cell types (cMono, EM CD4 T cells, NK cells, and naïve CD8 T cells) in IPF are associated with increased phosphorylation of activating pSTATs (pSTAT1, pSTAT5, and pSTAT6), alongside elevated pSTAT3, which suppresses ISG expression.

Previous studies have also shown the net effect of type 1 IFN signalling is regulated, in part, by the balance of pSTAT1 and pSTAT3 where increased STAT3 is capable of restricting STAT1 mediated ISG transcription[199, 241].

Based on this, the relative expression of pSTAT1 and pSTAT3 was compared in cMono and EM $CD4^+$ T cells from IPF and HC samples as both populations showed increased activation of both these pathways in IPF.

In cMono, a statistically significant difference between pSTAT1 and pSTAT3 expression was observed in IPF but not in controls. In contrast, a difference between pSTAT1 and pSTAT3 fold change was evident in EM $CD4^+$ T cells in both IPF and control samples (Figure 3.3.8).

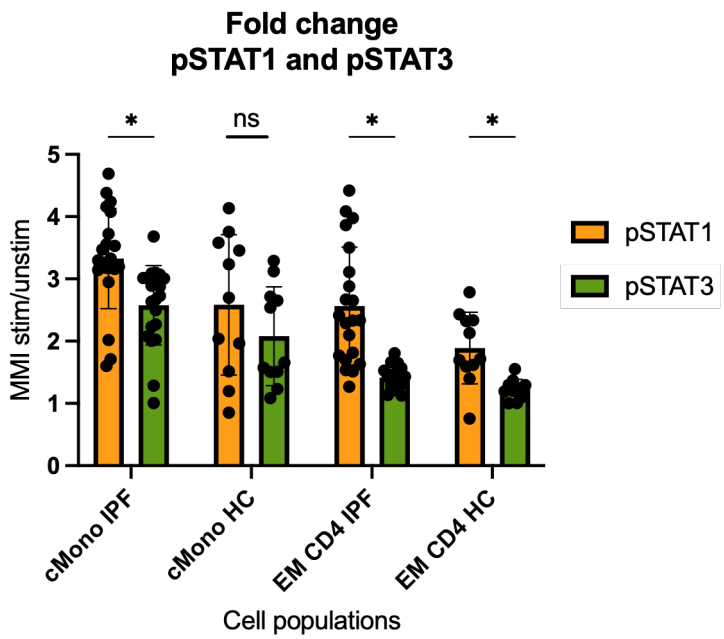


Figure 3.3.8. pSTAT1 and pSTAT3 fold change in IPF and controls. *Statistical comparison of fold change (stim/unstim) in median metal intensity (MMI) following IFN-β stimulation between pSTAT1 and pSTAT3 for cell populations that showed a differential response between IPF and controls. Each point represents one sample. Error bars show standard deviation. Statistical significance was assessed using an unpaired Student's t-test. Asterisks denote statistical significance as follows: *P< 0.05, **P < 0.01, ***P< 0.001, ns, not significant (P ≥ 0.05).*

3.3.6 Baseline unphosphorylated STAT1 and STAT3 or membrane expression of IFNAR2 do not account for increased response to IFN-β in IPF.

Previous studies have shown that low concentrations of type 1 or type 2 IFNs, as well as other cytokines such as TNF-α can increase intracellular STAT1 expression thereby priming cells for a heightened response to further type 1 IFN exposure[242, 243]. Given this, basal expression of unphosphorylated STAT1 and STAT3, as well as surface expression of IFNAR2, were assessed to determine whether they contribute to the heightened IFN-β response observed in IPF.

In the unstimulated state, no differences in basal levels of STAT1, STAT3, or IFNAR2 were observed in cell populations that exhibited an increased response to IFN-β stimulation in IPF (Figure 3.3.9).

Overall, no association between the enhanced IFN-β response in IPF cell types was related to increased basal expression of these signalling components when measured by protein expression.

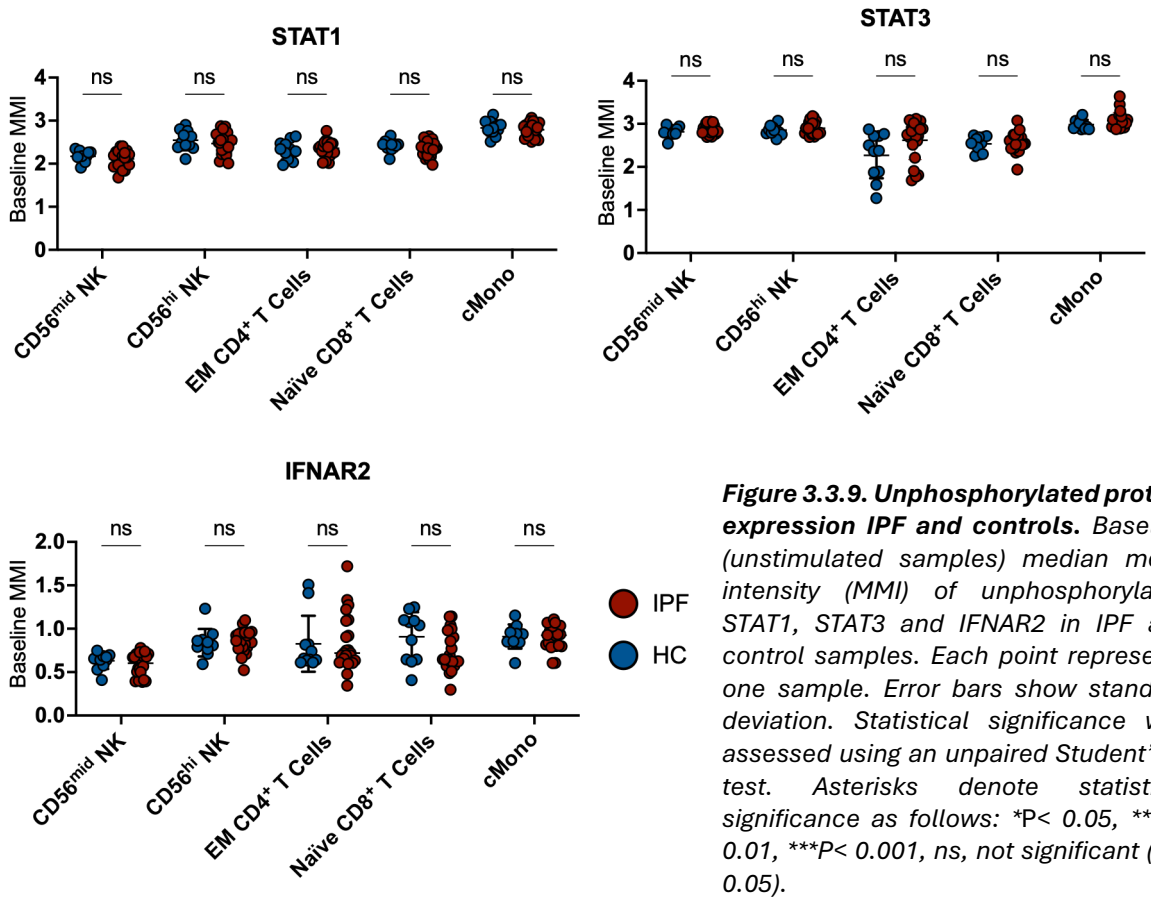


Figure 3.3.9. Unphosphorylated protein expression IPF and controls. *Baseline (unstimulated samples) median metal intensity (MMI) of unphosphorylated STAT1, STAT3 and IFNAR2 in IPF and control samples. Each point represents one sample. Error bars show standard deviation. Statistical significance was assessed using an unpaired Student's* t-*test. Asterisks denote statistical significance as follows:* *P< *0.05,* **P < *0.01,* ***P< *0.001, ns, not significant (P ≥ 0.05).*

3.3.7 Classical monocytes exhibit increased basal pNFkB in IPF

In addition to being activated in response to type 1 IFN stimulation, many of the proteins in the panel can be phosphorylated in response to a range of stimuli. To determine if any signalling pathways were activated at baseline, the expression of phosphorylated proteins was examined in unstimulated IPF and control PBMC populations.

In unstimulated monocyte and DC populations, cMono, IntMono, ncMono and CD16^{mid} Mono showed higher pERK1/2 expression in IPF (Figure 3.3.10). In contrast, the cDC1 subset, which demonstrated the highest constitutive pERK1/2 expression, demonstrated lower pERK1/2 expression in IPF.

In addition, pNFκBp65 expression was significantly increased in the unstimulated cMono subset in IPF. Although CD64^{hi} monocytes demonstrated the highest constitutive pNFκBp65 expression (Figure 3.3.2) there was no difference in basal pNFκBp65 expression in IPF. (Figure 3.3.10).

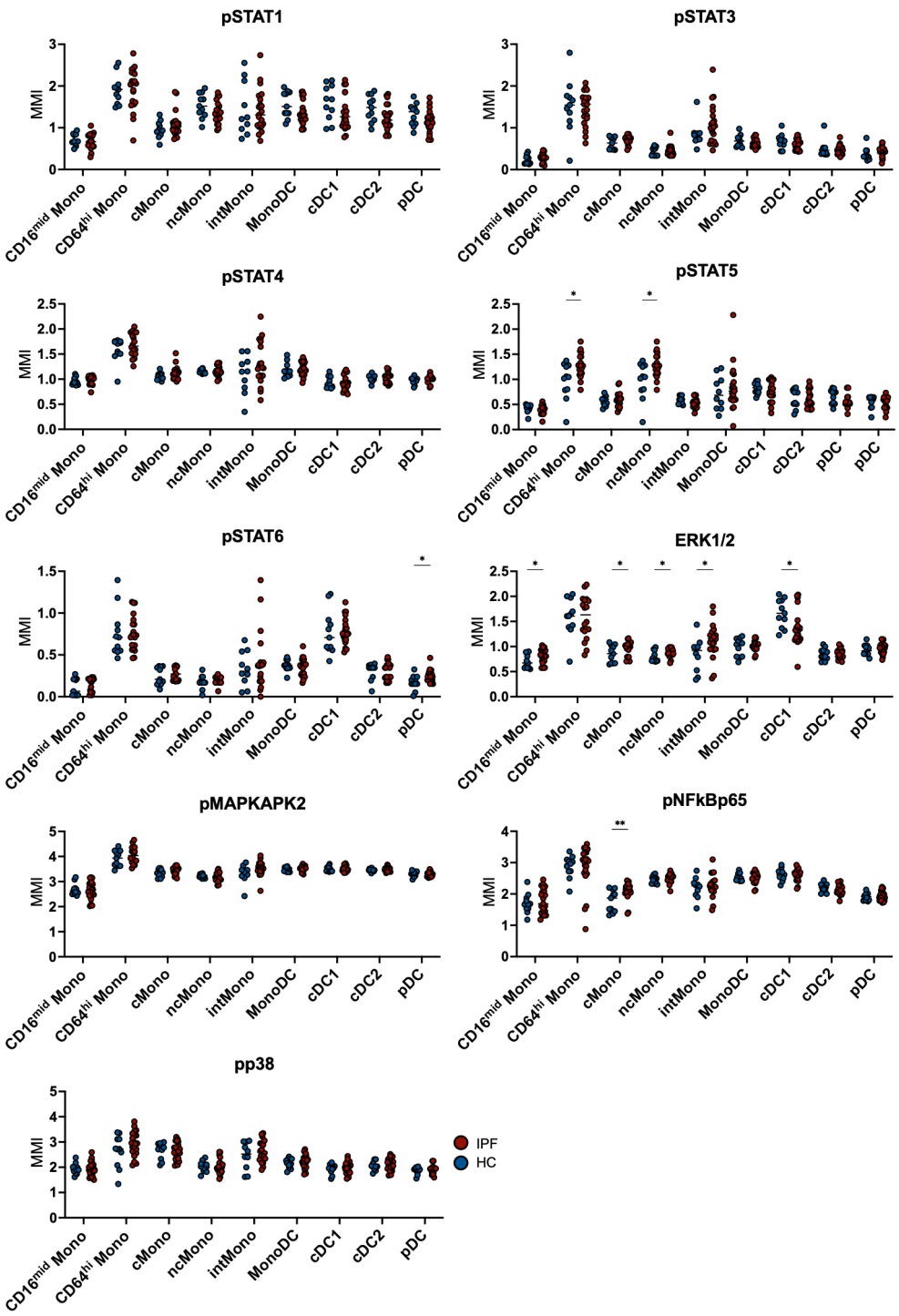


Figure 3.3.10. Baseline median metal intensity (MMI) of phosphorylated proteins in monocyte and dendritic cell subsets from IPF and control samples. *Each point represents an individual sample; data shows as mean ± standard deviation. Statistical significance was assessed using an unpaired Student's* t*-test. Asterisks denote statistical significance as follows:* *P< 0.05, **P < 0.01, ***P< 0.001.

In other PBMC cell types, naïve CD8⁺ T cells in IPF exhibited lower basal pSTAT6 and pSTAT3 expression compared to controls. CD4⁺ T Cells, MAIT cells, basophils and

plasmablasts also demonstrated increased baseline pERK1/2 expression in IPF (Figure 3.3.11).

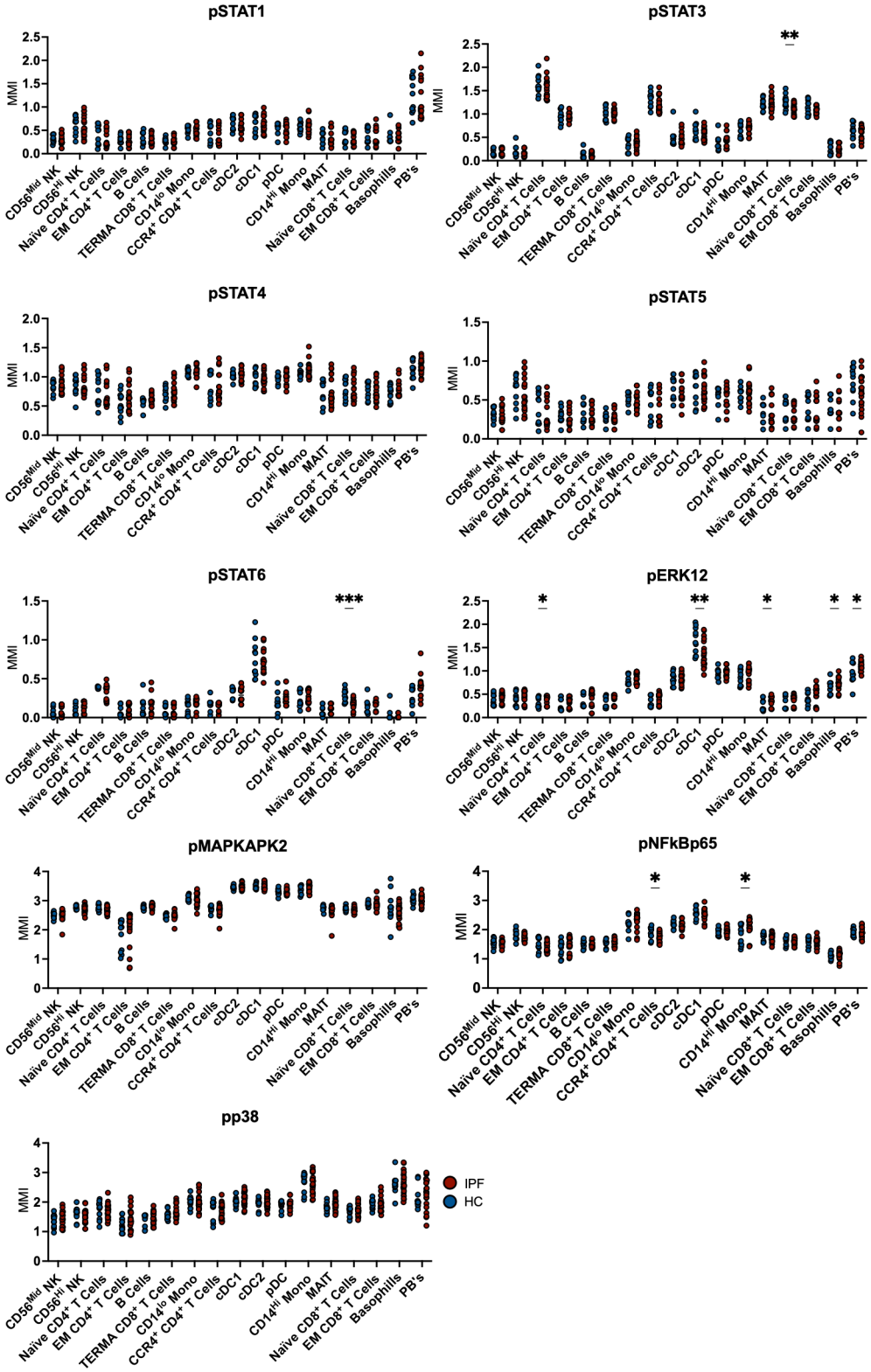


Figure 3.3.11. Baseline median metal intensity (MMI) of phosphorylated proteins in PBMC populations from IPF and control samples. *Each point represents an individual sample; error bars indicate mean ± standard deviation. Statistical significance was assessed using an unpaired Student's* t-*test. Asterisks denote statistical significance as follows:* *P< *0.05, **P < 0.01, ***P< 0.001*. ***Abbreviations****; EM – effector memory, TEMRA – terminally differentiated effector memory, MAIT – mucosal associated invariant T cells, PB – plasmablasts*

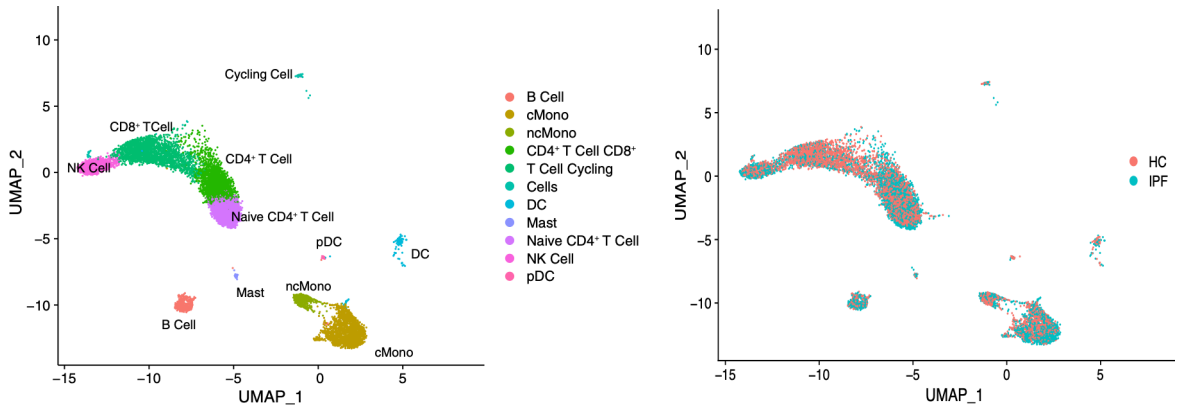
3.3.8 Single cell transcriptomic analysis of circulating PBMCs in IPF

In this section, the single-cell transcriptome of PBMCs from IPF and control samples were analysed (Cohort B.) The primary aim is to assess whether basal type 1 IFN signalling was increased in PBMC populations in IPF compared to controls. The secondary aim is to determine whether this occurred in isolation or alongside broader immune dysregulation in circulating PBMCs as suggested in the baseline phosphoprotein analysis in the mass cytometry study above (Chapter 3.3.7).

PBMCs were isolated from blood samples from IPF (n=3) and controls (n=3) and sent for single-cell sequencing using the Chromium 10x platform. Although every effort was made to minimise demographic differences between groups during recruitment, complete matching for age and sex was not possible due to the limited availability of eligible donors from whom fresh PBMC samples could be processed for single-cell RNA sequencing within the study timeframe. Demographic details in (Table 3.2.2).

Following raw data processing and QC (steps outlined in Section 3.2.7), clustering was performed and identified 11 cell populations, which were annotated based on their top clustering defining genes (CDGs) (Figure 3.3.12). Populations of cycling cells (n=42 cells) and mast cells (n= 28 cells) were excluded due to small cell numbers resulting in 10,076 cells for downstream analysis.

Due to small sample numbers, only qualitative (rather than quantitative with statistical analysis) compositional analysis was performed. This revealed an increase in the proportion of cMono in IPF (20.99%) compared to 16.60% in healthy controls consistent with the findings seen in the CyTOF analysis. In addition, the proportions of major PBMC cell populations were also comparable between the CyTOF and sc RNA seq datasets. (Figure 3.3.1 and Figure 3.3.12).



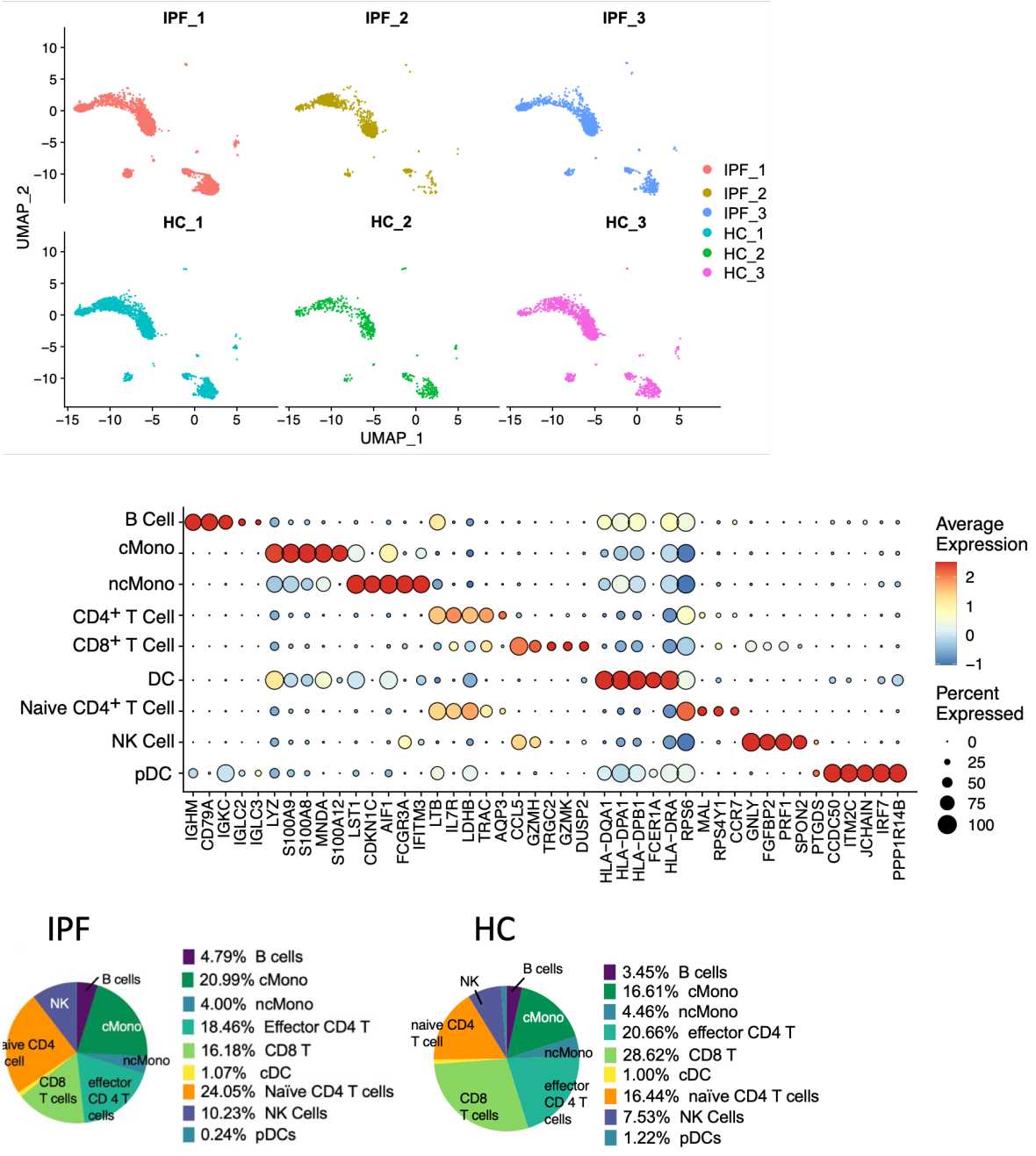


Figure 3.3.12. Single-cell RNA sequencing analysis of PBMC populations in IPF and healthy controls (HC). *Top panel: UMAP projections of PBMCs with IPF and control samples. Top left: IPF and HC combined donors and labelled according to cell cluster. Top right: split by disease. Lower left: split by donor. Middle panel: Dot plot showing the top five cluster-defining genes for each PBMC population; dot size represents the percentage of cells expressing each gene within the cluster, and colour indicates average gene expression. Bottom panel: Composition of PBMC populations (percentage of total cells) in IPF and HC samples. Mast cells were excluded due to low abundance (<0.05%) in both groups.*

Initial clustering identified two monocyte subsets, annotated as cMono and ncMono. To examine monocyte heterogeneity these populations were re-clustered which identified five monocyte subsets annotated based on gene expression; cMono.S100A8/9/12^{hi},

cMono.HLA-II^{hi}, ncMono, mono.type1 IFN and monoDC. Monocyte subsets were annotated based on their CDGs based on populations described in 2 reference dataset investigating monocyte heterogeneity in COVID 19 and systemic lupus erythematosus (SLE)[236, 244] (Figure 3.3.13).

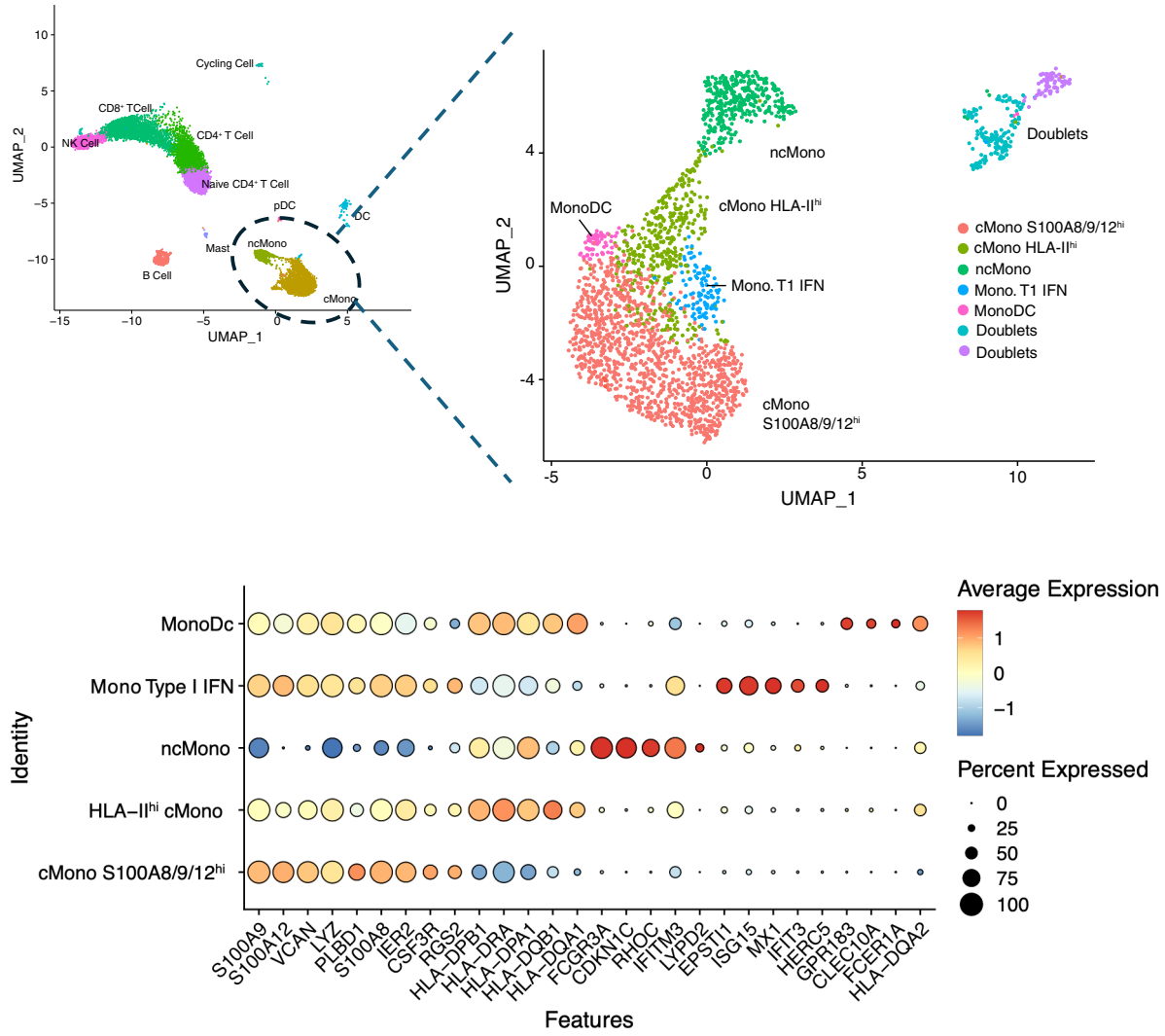
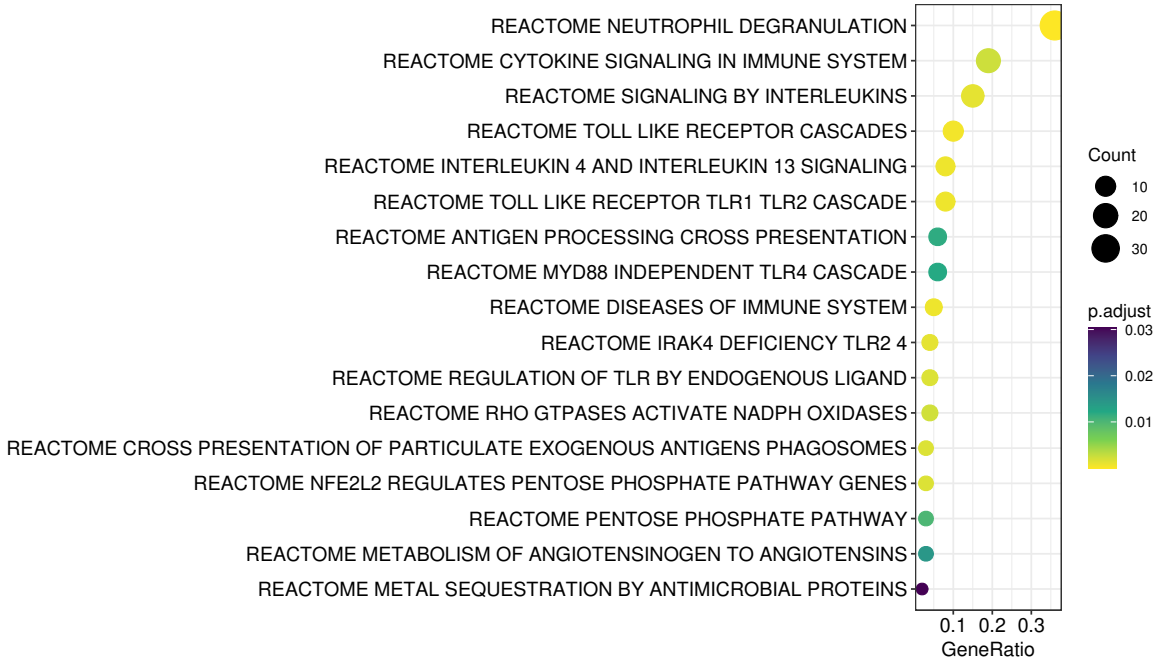


Figure 3.3.13. Re-clustering of monocyte populations identifies five distinct subsets. *Monocyte populations were isolated and re-clustered, with subsets annotated using a reference dataset (see main text). Top panel: Original UMAP highlighting monocyte populations and UMAP of re-clustered monocyte subsets. Bottom panel: Dot plot of the top five cluster-defining genes for each monocyte subset; dot size represents the percentage of cells expressing each gene within the cluster, and colour indicates average gene expression relative to other subsets.* ***Abbreviations****; MonoDc = monocytes derived DCs*

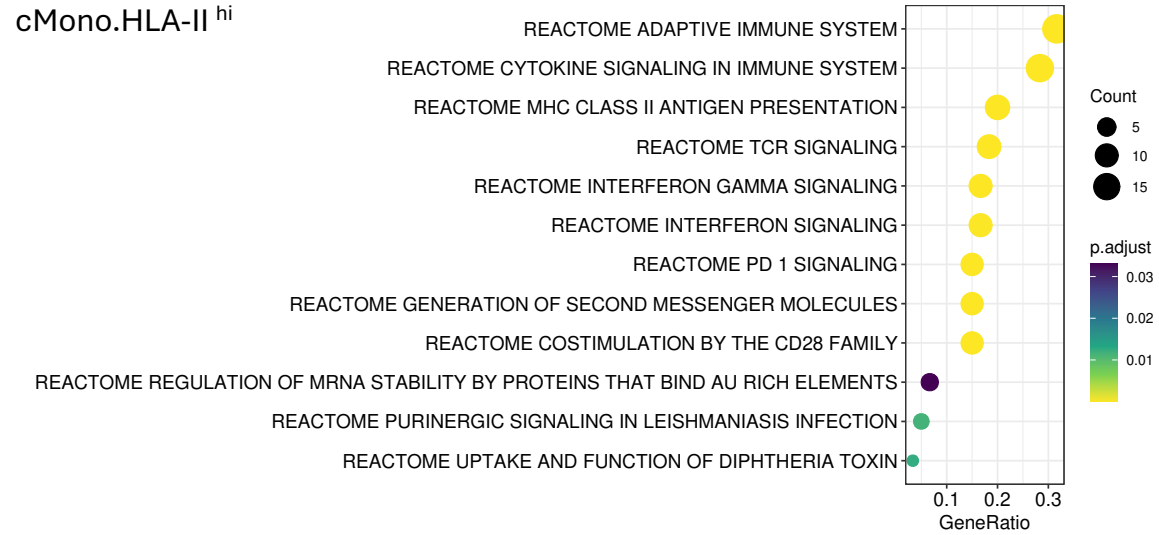
The functional characteristics of the monocyte subsets were inferred from CDG expression and pathway enrichment analysis. The cMono.S100A8/A9/12^{hi} subset showed the highest expression of canonical classical monocyte genes; *S100A8/A9, FCN1, VCAN* (Figure 3.3.13) and expressed inflammatory pathways related to neutrophil

degranulation, cytokine, interleukin signalling and innate toll like receptor signalling (Figure 3.3.14).

cMono. S100A8/9/12^{hi}



cMono.HLA-II ^{hi}



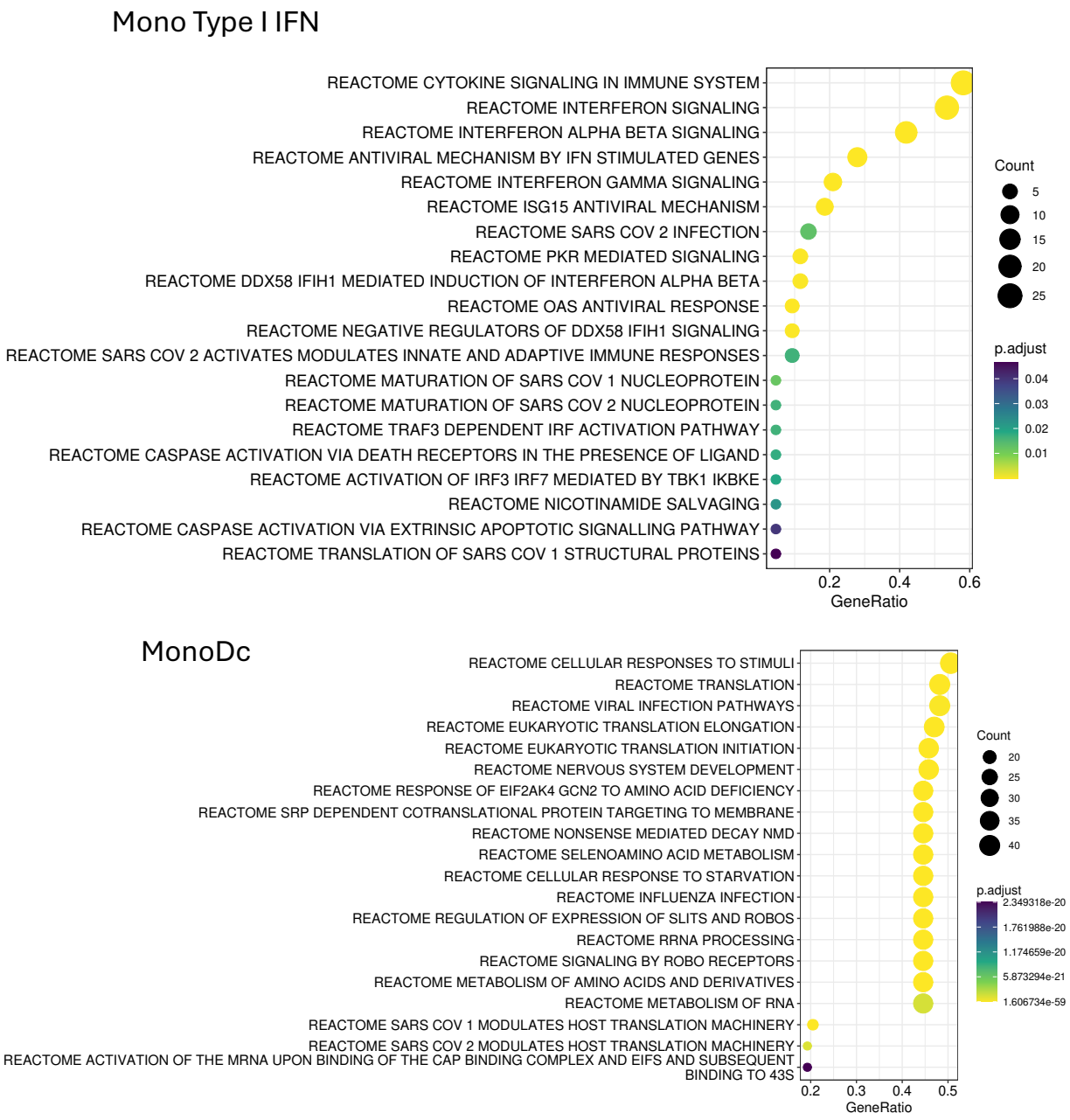


Figure 3.3.14. Functional characterisation of classical monocyte subsets in IPF and control samples combined. *Bubble plot of pathway enrichment analysis using the REACTOME database for four classical monocyte subsets. based on genes significantly upregulated (log2 fold change > 1.5 and false discovery rate (FDR)-adjusted* P < *0.05). Enriched pathways were identified using Fisher's exact test, to assess genes over-represented in each pathway*. The gene ratio (x-axis) represents the proportion of differentially expressed genes assigned to each pathway relative to the total number of differentially expressed genes. Bubble size reflects the number of differentially expressed genes within each pathway. Statistical significance was defined as FDR-adjusted $p < 0.05$. *Abbreviations: MonoDc - monocytes derived DCs.*

In contrast, the other largest cMono population cMono. HLA-II^{hi} upregulated pathways associated with antigen presentation and modulating the adaptive immune system (Figure 3.3.14).

Reclustering also revealed a monocyte population with increased DC associated transcripts (MonoDc) and a separate monocyte fraction with relative increased expression of type 1 IFN related transcripts and pathways (Mono Type 1 IFN).

Qualitative compositional analysis of monocyte subsets showed the following proportion of monocyte subsets - the (inflammatory) cMono.S100A8/A9/12^{hi} population in IPF (60.69%) compared to healthy controls (42.56%); cMono. HLAII^{hi} subset in IPF (15.27%) compared to healthy controls (27.01%) (Figure 3.3.15).

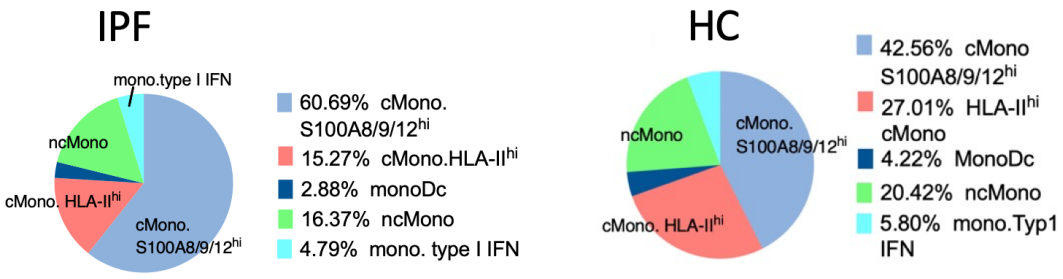


Figure 3.3.15. Composition of monocyte subclusters. *Proportion of monocyte subsets (as % of all circulating monocytes) in IPF and control samples. Abbreviations: MonoDc = monocytes derived DCs,*

3.3.9 Increased transcription factor activity related to type 1 IFN and inflammatory signalling in IPF circulating monocytes

Gene expression profiles between IPF and control PBMC and monocyte populations were compared using pseudobulk gene expression analysis. In this approach, gene expression counts are aggregated across all cells within an annotated cell population for each donor, enabling differential expression analysis of cell populations between donors rather than an individual cell level. This approach was selected because it accounts for biological variability between donors thereby providing a more robust assessment of disease-associated transcriptional differences. Sample expression profiles were also hierarchically clustered to assess sample similarity and identify potential disease-associated transcriptional patterns and outlier samples.

At the single-gene level, minimal transcriptional differences were observed in this dataset (Figure 3.3.16). In monocyte populations, only two genes were differentially expressed ($\log_2$ fold change > 1.0; FDR q < 0.1): *C1orf56* (function unknown) in cMono and ncMono and *SELL* (encoding L-selectin, involved in endothelial adhesion and tissue migration) in cMono.

Naïve CD4$^+$ T cells were the only other population exhibiting differential gene expression. Upregulated genes in IPF included those associated with T cell activation (*JUN*, *NEAT1*), as well as genes associated with inhibition and skewing naïve T cells toward regulatory or Th2 phenotype following T cell receptor engagement (*CAST*, *CCL18*).

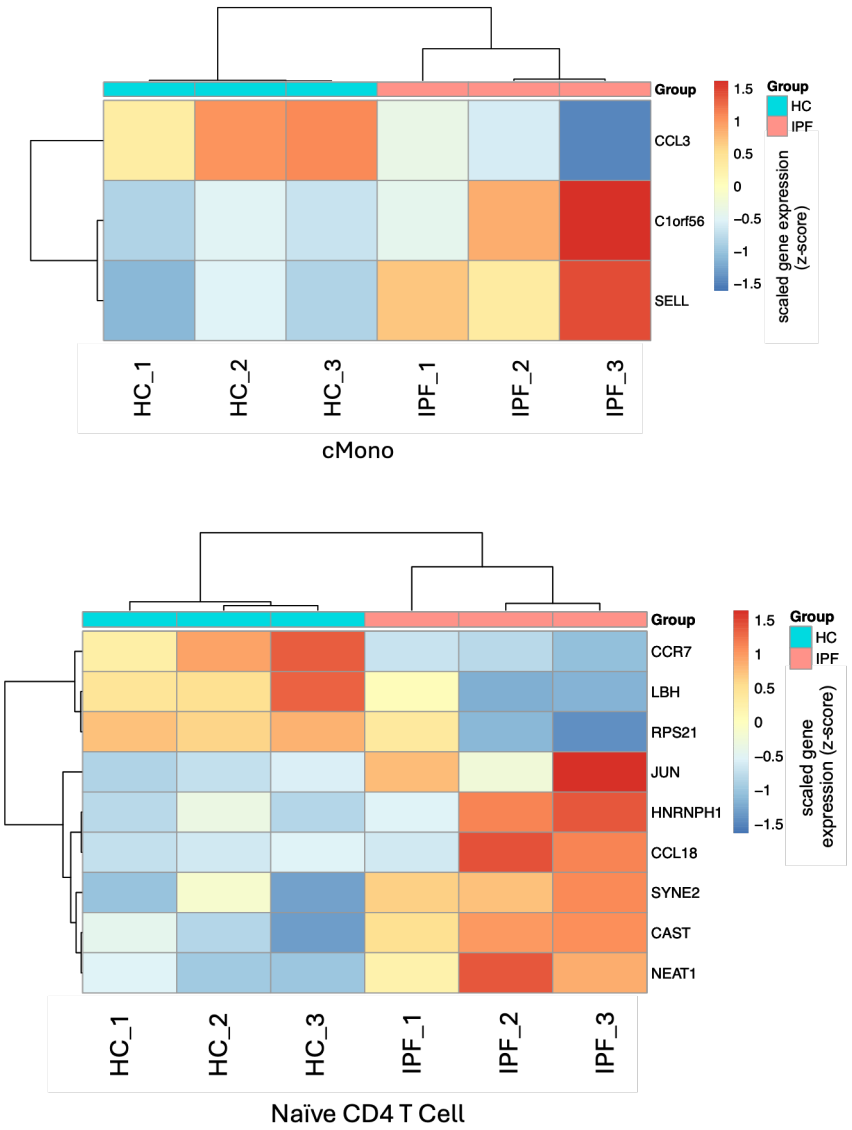


Figure 3.3.16. Differentially expressed genes in IPF PBMCs. *Heatmaps showing donor-level pseudobulk expression of genes identified as differentially expressed by DESeq2 between HC and IPF PBMC samples for classical monocyte (cMono) and naïve CD4$^+$T-cell populations. Columns represent individual donor samples labelled according to hashtag antibody assignment, with the upper annotation indicating donor group (HC or IPF). Rows represent DEGs between groups (FDR-adjusted P < 0.1 and log2FC >1 or <-1), grouped according to similarity in expression across donor samples. Heatmap colours represent scaled gene expression values, with red indicating relatively higher and blue relatively lower expression for each gene across samples.*

Differences in basal phosphoprotein expression in IPF monocytes (Section 3.3.7) indicated alterations in monocyte innate signalling. To further examine transcriptional

regulation of these pathways, SCENIC (Single-Cell rEgulatory Network Inference and Clustering)[233] was used to characterises differences in transcription factor activity and signalling gene sets rather than individual genes.

SCENIC constructs gene regulatory networks (GRNs) by identifying and grouping transcription factors (TFs) and downstream target genes or groups of genes that are co-expressed in each cell subset. Downstream genes can only be grouped with TFs if they express the TF DNA binding motif in their upstream promotor region - minimising the risk of false positives where TFs and unrelated genes are grouped together. Grouped TFs and downstream target genes that are referred to as 'regulons' in the original publication. The activity of each regulon in individual cells is quantified using *AUcell* which calculates the area under the curve (AUC) based on the ranked expression of genes belonging to the regulon to generate a regulon activity score, where higher regulon scores reflect enrichment of the gene set in that cell (or cell type). (See Figure 3.3.17 – adapted from Aibar et al 2017[233]).

Using this approach, the activity of TF-defined, biologically related groups of genes (regulons) was compared between disease and control samples to identify regulatory networks with differential activity in IPF. Analysis was performed on cMono and ncMono populations to retain sufficient cell numbers rather than re-clustered monocyte subsets.

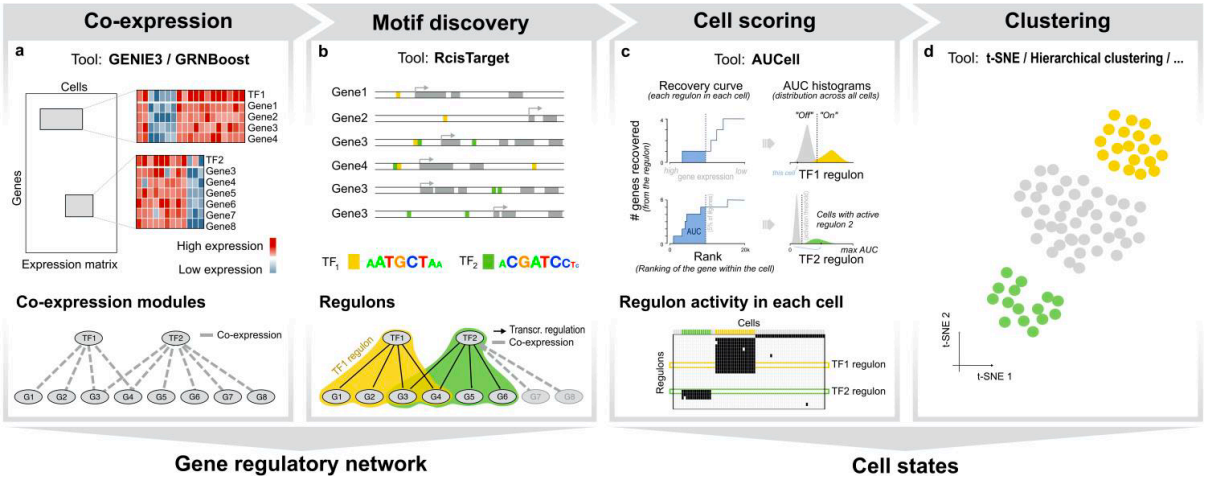


***Figure 3.3.17. Overview of Scenic Workflow (adapted from Aibar et al 2017**). Transcription factors and candidate target genes are first identified by constructing co-expression modules to infer potential transcription factor – target genes by expression patterns. In 'motif discovery' only co-expression modules, in which the TF motif is enriched in the corresponding target genes regulatory region are retained. Each TF, together with its predicted direct targets, defines a regulon. Regulon activity is then assessed at a single cell level using AUCell, which calculates the area under the recovery curve (AUC) score based on the fraction of TF target genes within the top ranking genes for each cell. These scores are used to generate a regulon activity matrix, which can be applied for clustering or comparative analysis of regulatory activity across cells or disease conditions.*

Among the top differentially expressed regulons, increased activity in IPF was observed for IRF5, STAT1 and STAT3 (Figure 3.3.18). These transcription factors are associated with type 1 IFN production and signal transduction but also regulate a range of additional immune and biological processes, including type 2 IFN signalling.

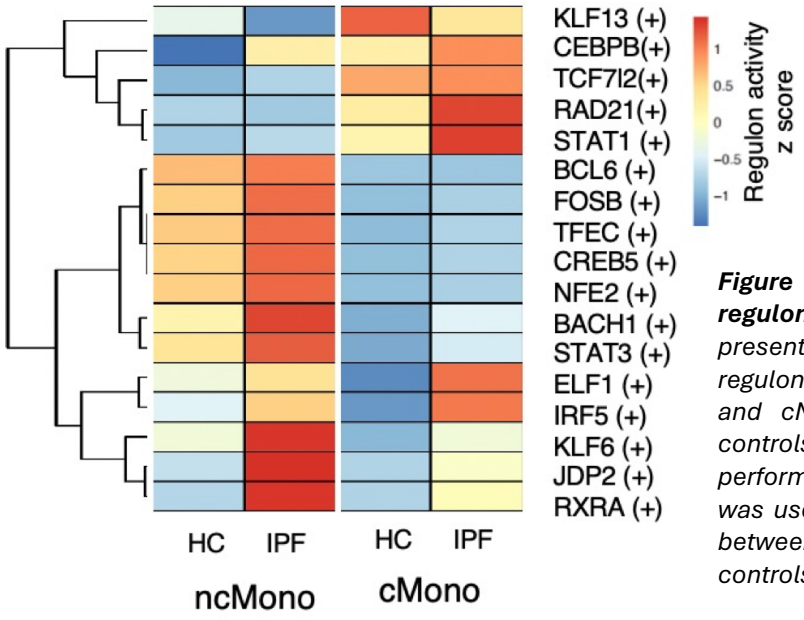


Figure 3.3.18. Differential expressed regulons in IPF monocytes. *Heatmap presenting regulons with differential regulon activity (FDR q <0.05) in ncMono and cMono populations in IPF and controls. Statistical testing was performed using Wilcoxon test which was used to compare TF activity score between IPF and HC. HC – healthy controls.*

In addition to regulons associated with type 1 IFN related activity, several additional regulons were also significantly increased in IPF monocytes. To understand the potential functional relevance of these TF-effector gene regulatory networks a comprehensive review of the literature was undertaken for each TF to profile its known biological function, mechanisms of action and potential effects.

Given TF function is often cell type and context specific, studies using conditional knockout models of the relevant transcription factor, restricted to monocytes, macrophages in adult mice were preferentially used. If these studies were not available, *in vivo* studies where the impact of a global knockout of the TF was specifically assessed in monocytes or macrophages was used or *in vitro studies* where the TF was investigated in monocyte or macrophage cell lines (Appendix Table 1 & Table 3.3.1). TFs were subsequently grouped according to effects on myeloid cellular activity (Table 3.3.1).

This comparative analysis identified increased activity of TFs associated with proinflammatory signalling pathways including NF-κB in IPF monocytes. Concurrently, increased activity of TFs associated with counter-inflammatory pathways were also observed, indicating partial restraint of inflammatory responses. In addition, increased

expression of TFs downstream of pattern recognition receptor pathways (PRRs) was also detected.

Pro inflammatory	Anti / Counter inflammatory	Promote NFkB signalling	Supress NFkB signalling	IFN signalling	Downstream PRR signalling
FOSB KLF6 IRF5	NFE2 CREB5 BCL6	KLF6	CREB5	ELF1 IRF 5 STAT1 STAT3	NFE2 FOSB BCL6 KLF6

Table 3.3.1. Classification of monocyte differentially expressed regulons. *Differentially expressed regulons, upregulated in IPF, grouped according to their reported functional effects on monocyte and macrophage activity, based on a structured review of published functional studies.*

3.4 Discussion

In this chapter, I show that classical monocytes from patients with IPF demonstrated a heightened response to type 1 IFN stimulation with increased expression of both pSTAT1 and pSTAT3 (Figure 3.3.10, Figure 3.3.11). This suggests that IPF classical monocytes are primed to respond to type 1 IFN. Upregulation of both pSTAT1 and pSTAT3 indicates parallel activation of pathways that promote and regulate ISG transcription. However, a significantly greater increase in pSTAT1 expression compared to pSTAT3 was observed following IFN-β stimulation in IPF cMono not seen in controls (Figure 3.3.12, Figure 3.3.13). Previous studies have demonstrated the relative balance of pSTAT1 and pSTAT3 can modulate the cellular response to type 1 IFNs with higher STAT1 promoting ISG transcription and higher STAT3 restricting this response[196, 241]. In keeping with this previous work from our group showed increased ISG expression in $CD14^+$ monocytes following IFN-β stimulation in IPF compared to controls[181]. Taken together, these findings suggest, despite concurrent increases in pSTAT3, the net effect in IPF classical monocytes is enhanced ISG expression at the time point assessed.

In addition to an increased response to type 1 IFN in the Cytof analysis, the monocyte regulon analysis also demonstrated increased basal activity of type 1 IFN-related transcriptional programmes in IPF monocytes with increased *STAT1* and *STAT3* regulons (Figure 3.2.21, Table 3.3.1). Pre-exposure to IFN-α, IFN-γ and TNF-α can 'prime' cells by increasing intracellular levels of STAT1, STAT2 and IRF9[245, 242] or by partial phosphorylation of STAT1 at different tyrosine or serine residues[246], while IL-6 exposure increases intracellular STAT3[114]. The regulon analysis findings may reflect prior exposure to a soluble factor in the IPF circulation *in vivo*, resulting in transcription of STAT1 and STAT3 as a mechanism of priming. However, the mass cytometry analysis did not reveal increased unphosphorylated or phosphorylated STAT1 or STAT3. This difference may reflect an increase in transcription but not translation of STAT1 and STAT3, alternatively, phosphorylation of STAT1 at serine residues that was not detected by the anti-pSTAT1 antibody used which only targets tyrosine phosphorylated residues.

The heightened response to IFN-β stimulation was not restricted to classical monocytes, but also observed in EM $CD4^+$ T cells, Naïve $CD8^+$ T cells, effector ($CD56^{mid}$) and regulatory ($CD56^{hi}$) NK cells suggesting broader evidence of type 1 IFN priming. As with classical monocytes, lymphocyte populations in IPF demonstrated a consistent increase in pSTAT3 expression. In EM $CD4^+$ T cells pSTAT1 expression was also elevated in IPF, otherwise the downstream response to IFN-β in lymphocyte populations was characterised by non-canonical STAT pathway activation. Specifically, increased pSTAT5 expression was observed in EM $CD4^+$ T Cells and both NK cell populations and pSTAT6 expression in naïve CD8 T cells in IPF.

The functional consequences of increased non-canonical STAT signalling are less well defined. pSTAT5 can homodimerize or form heterodimers with other STAT complexes including pSTAT1-pSTAT5 and pSTAT5-pSTAT6 or interact with CRKL complex to initiate transcription of GAS expressing ISGs[238]. In activated T cells the effects of pSTAT5 signalling are context-dependent; in the presence of pSTAT1, pSTAT5 has an apoptotic effect[247], while in the presence of pSTAT3 promotes cell proliferation and survival[196, 248]. Type 1 IFN-induced pSTAT5 can also modulate IL-2 signalling in a context-dependent manner, for example, IFN-α can also inhibit IL-2 induced STAT5 DNA binding in primary T cells thereby restricting proliferation[249]. Conversely, priming activated T cells with IFN-α results in upregulation of CD25, sensitising cells to IL-2 mediated proliferation[239].

The functional consequences of type 1 IFN–mediated pSTAT6 signalling in lymphocytes has not been specifically investigated. In other cell types including B cells, endothelial cells and hepatocytes pSTAT6 has been shown to form heterodimers with pSTAT2 to drive ISRE-dependent ISG transcription[240] and interact with other STAT complexes to promote GAS-dependent ISG expression[194].

While these findings do not allow definitive conclusions to be drawn on the cell-specific consequences of type 1 IFN signalling, they highlight downstream responses are complex, context dependent and highlight each cell specific effect warrant further investigation.

Aside from type 1 IFN signalling, this study showed evidence of additional inflammatory pathways activity in IPF classical monocytes. In the CyTOF analysis a notable finding was the specific increase in basal pNFκB expression restricted to classical monocytes. In addition, increased pERK1/2 expression in several IPF PBMC populations and monocyte subsets including classical monocytes (Figure 3.3.11). As both NFκB and ERK signalling can be activated downstream of multiple innate pathways, these findings suggest that signalling beyond type 1 IFN pathways is active in IPF monocytes.

Findings from the scRNA seq dataset also provide further evidence of increased inflammatory signalling in IPF monocytes. Reclustering identified two main classical monocyte subsets; S100A8/A9/A12^{hi} cMono and HLA-II^{hi} cMono. The S100A8/A9/A12^{hi} cMono subset exhibited increased inflammatory pathway signalling (Figure 3.3.17) and increased S100A8/A9 protein expression (Figure 3.3.16). *S100A8* and *A9* transcripts encode the S100 calcium family of proteins, which form the heterocomplex calprotectin. Monocyte expression of S100A8/A9 is increased in systemic infections including COVID 19 and in inflammatory conditions such as atherosclerosis, rheumatoid arthritis and IPF[250, 251, 252, 253]. Secretion of S100A8/9 following cellular and tissue damage promote inflammatory responses including neutrophil activation and phagocytosis, and monocyte proinflammatory mediator release and chemotaxis[254].

In this dataset the c.Mono.S100A8/9^{hi} population made up a larger proportion of the monocyte population in IPF compared to controls (Figure 3.3.18). In addition, a recent transcriptomic analysis of PBMCs from IPF patients (n=25) and healthy controls (n=13) reported elevated *S100A8* and *S100A12* expression and reduced *HLA-DR* expression in IPF classical monocytes[108].

While the differential abundance patterns observed in the reclustered c.Mono populations were not statistically tested, these findings, together with the recent study suggest the classical monocyte population in IPF is skewed to an inflammatory transcriptomic state.

The analysis of differentially expressed regulons (DERs) in monocytes (Figure 3.3.21, Table 3.3.1) provided further evidence of a broader activation of a range of innate and inflammatory signalling pathways in IPF. Furthermore, these findings provide a potential transcriptional explanation for the increased basal pNFκB and pERK1/2 observed in the CyTOF study.

Several regulons associated with pro-inflammatory signalling were increased in IPF monocytes, including KLF6, FOSB and IRF5[255], supporting activation of NFκB, AP-1 and PRR associated inflammatory pathways. Conversely, increased activity of regulatory transcription factors, including BCL6 and NRF2, suggests concurrent activation of counter-regulatory mechanisms that may partially restrain inflammatory responses.

Together, these findings suggest that increased type 1 IFN signalling in IPF monocytes is associated with broader activation of PRR and both pro- and anti-inflammatory regulatory pathways. Altered regulon activity was identified in both classical and non-classical monocytes, indicating immune dysregulation is not confined to a single circulating monocytes subset. However, the more pronounced inflammatory phenotype observed in classical monocytes including expansion of the S100A8/A9^{hi} subset, along with increased basal NFκB signalling at baseline in the cMono subsets in the CyTOF analysis suggests that classical monocytes may represent the primary circulating inflammatory monocyte population in IPF.

Overall, the CyTOF and scRNAseq analyses provided complementary information. CyTOF directly quantified signalling responses following IFNβ stimulation and basal signalling activity, revealing increased functional responsiveness of circulating immune cells in IPF. Supporting these functional findings, the scRNAseq analysis provided transcriptional insight into regulatory networks that may account for these functional differences. Together, these complementary findings support the presence of a primed IFN and inflammatory state in IPF monocytes.

In contrast to the regulon findings, the DEG analysis (Figure 3.3.19) revealed limited transcriptional differences compared to the analysis of DERs in monocytes (Figure 3.3.21). A recent, larger scRNAseq analysis examining PBMCs in IPF patients (n=25) and age- and gender- matched controls (n=13) also reported only 19 DEGs across all cell populations, with no upregulated gene sets or pathways in IPF[108]. This suggests the limited finding from DEG in the present analysis is not solely due to small samples size. By grouping individual genes into biologically related TF-regulated gene networks, regulon analysis may therefore provide greater sensitivity for detecting disease-associated regulatory changes. However, SCENIC infers transcription factor activity by examining the coordinated expression of transcription factors s and their predicted target genes rather than directly measuring activation and these findings should be considered as hypothesis generating. Additional validation, including assessment of transcription factor phosphorylation or nuclear localisation would be required to confirm increased activity in IPF. In addition, functional studies using transcription factor knockdown or pharmacological inhibition would allow further investigate the downstream functional consequences in IPF monocytes.

The relatively small number of donors for the PBMC scRNAseq study together with incomplete matching for age and sex represent important limitations of this analysis, as both factors may influence immune cell composition and transcriptional profiles. Furthermore, IPF is a heterogeneous disease, and therefore the small IPF cohort (n=3) is unlikely to capture the full spectrum of disease associated variation. To reduce the influence of donor specific variation, differential expression analysis was performed using a donor-level pseudobulk approach followed by donor-level clustering which demonstrated samples segregated predominantly according to disease status rather than individual donor effects. The relatively limited transcriptional differences together with differences in immune cell abundance, identified in this study are consistent with those reported in a larger published PBMC scRNAseq study comparing 25 IPF (13 stable and 12 progressive disease) and 13 age and sex matched control samples[108]. Furthermore, the concordance of these findings with the larger CyTOF dataset provides additional support that these immune alterations represent reproducible disease-associated features of IPF rather than cohort-specific observations.

3.5 Conclusion

This study demonstrates that circulating classical monocytes in IPF exhibit an increased response to type 1 IFN stimulation characterised by increased canonical STAT signalling. This heightened response is not restricted to monocytes, but is also observed in naïve CD8 T cells, EM $CD4^+$ T cells, and NK cells. This pattern indicates a more widespread priming of circulating immune cells to type 1 IFN in IPF and consistent with previous inflammatory conditions characterised by a 'type 1 IFN signature'. In addition, transcriptional analysis revealed increased type 1 IFN-related regulatory signalling in monocytes ex vivo, supporting the presence of a primed immune state. Finally, the concordance between the phosphoprotein and transcriptional analysis indicates that increased type 1 IFN signalling in IPF monocytes occurs within a wider context of innate and inflammatory pathway activation.

Chapter 4. Type 1 IFN signalling in lung monocytes and macrophages in IPF

4.1 Introduction

In the previous chapter I examined differences in circulating immune cell populations in IPF compared to healthy controls. In this chapter, I investigate monocytes and macrophages in the lung, the site of disease in IPF.

Lung macrophages are commonly classified according to both their anatomical location and ontogeny. Anatomically, they are broadly divided into alveolar macrophages (AMs), which reside within the alveolar lumen and are primarily responsible for surfactant homeostasis and pathogen clearance, and interstitial macrophages (IMs), which reside within the lung interstitium. Compared with AMs, IMs are less abundant, exhibit greater transcriptional heterogeneity, and are increasingly recognised as important regulators of immune homeostasis through antigen presentation, cytokine production and interactions with structural and immune cells. Ontogenetically, lung macrophages comprise both tissue resident macrophages (TRMs) and monocyte-derived macrophages (MDMs). With ageing[164, 166, 171] tissue injury, inflammatory insult[256] and disease circulating monocytes increasingly contribute to the lung macrophage population. MDMs have been implicated in lung fibrosis. Selective depletion of MDMs mitigates the development of fibrosis in several murine models of lung fibrosis including bleomycin, asbestos and TGF-β-induced fibrosis[43, 172, 182].

Whilst these studies implicate macrophages and MDMs in the development of fibrosis, how they contribute to IPF is not fully understood. Macrophages perform several ancillary functions in the lung, beyond immune surveillance including orchestrating tissue remodelling and repair, maintaining homeostasis and supporting and influencing the functional phenotype of structural cells[256].

Several groups have performed single cell transcriptomic profiling of lung digests from IPF patients undergoing transplantation. These studies have identified a macrophage population in IPF variously labelled as 'pro-fibrotic macrophages[86, 184]', 'SPP1^{hi} macrophages[185]', 'PLA2G7^{+} macrophages[257]' or unnamed[62] but characterised by expression of *SPP1, MMP7, MMP9, CHIT1, CHI3L1* and *RNASE 1*. This population is expanded in lung tissue[86, 184] and co-localises with αSMA^{+} fibroblasts within fibroblastic foci[185]. Cells in this population express transcripts and upregulate pathways associated with extra cellular matrix (ECM) remodelling, fibroblast activation and proliferation that have been proposed as the mechanisms by which they contribute to fibrosis. SPP1 is a secreted glycoprotein that binds to CD44 and integrin a3b1 and has been shown to

promote fibroblast to myofibroblast activation and SMAD phosphorylation resulting in TGF-β transcription[258, 259].

Much focus has been placed on this SPP1 expressing macrophage population however other aspects of lung macrophage biology have yet to be explored in IPF. With single cell transcriptomic studies, researchers have begun to identify additional discrete macrophage populations or cell states in the murine and human lung[150, 155, 156, 166]. Similar heterogeneity is observed in macrophages in other tissues[142, 260, 261] and in both health and in disease. These populations are present in the fibrotic lung though their behaviour has not yet been defined.

Current studies investigating macrophage activity in IPF have also not differentiated between monocytes and macrophages in the lung interstitium and those in the alveolar space, nor between different regions of the lung that may represent earlier and more advanced disease.

Overall, key questions remain regarding the presence of additional monocyte and macrophage subtypes or activation states in idiopathic pulmonary fibrosis (IPF) lungs beyond $SPP1^+$ and interstitial macrophages. It is also unclear how these populations differ at the transcriptomic level between IPF and control lungs, as well as across stages of disease progression. In light of evidence demonstrating activated type 1 IFN signalling in circulating monocytes, I hypothesised that this signalling pathway is similarly upregulated in monocytes and macrophages within the IPF lung microenvironment.

In this chapter, I address these questions through a comprehensive and unbiased analysis of lung monocyte and macrophage populations in IPF using single-cell transcriptomic datasets. This includes a detailed characterisation of alveolar macrophages derived from bronchoalveolar lavage samples. Comparative transcriptomic analyses were conducted between IPF and non-diseased control lungs tissue digests, as well as between early-stage and advanced IPF tissue, to delineate disease-associated and stage-specific cellular phenotypes.

4.2 Study Design and Methods.

4.2.1 Overall Study Design

Two single-cell transcriptomic datasets were used to address these questions (Figure 3.2.1). In the first, bronchoalveolar lavage (BAL) samples from patients with IPF and controls were processed for single-cell RNA sequencing using the 10x Chromium platform. BAL samples are enriched for alveolar macrophages, which comprise over 85% of recovered cells and are accessible throughout the disease course, enabling characterisation of macrophage transcriptomic profiles within the alveolar compartment.

To complement this, a publicly available single-cell RNA sequencing dataset of IPF and control lung tissue[185] was utilised to examine myeloid populations within the lung parenchyma. Although smaller than other publicly available IPF lung scRNA-seq datasets, including those generated by Adams et al.[86] and Habermann et al.[63], the Morse dataset was proactively selected because it enabled comparison across disease stage and included control lung tissue with histologically confirmed near-normal architecture. IPF is characterised by a basal and subpleural predominance, with disease typically initiating in the lower lobes before progressing to involve the upper lobes. In the Morse study[185], paired upper and lower lobe samples were obtained from IPF lung explants, with histological assessment confirming that lower lobe samples represented advanced fibrosis, while upper lobe samples reflected earlier-stage disease (Figure 3.2.1). This enabled comparison of transcriptomic profiles across disease stages, which was not possible with the larger datasets. Control samples were also obtained from declined donor lungs, as was the case in the other datasets, however Morse et al incorporated a H&E assessment of tissue adjacent to the sequenced biopsy confirming histologically near normal lung architecture prior to analysis. This provided confidence that the control samples represented histologically healthy lung tissue rather than simply non-fibrotic tissue. Collectively, these features made the Morse dataset particularly well suited to the objectives of the present study despite its smaller sample size.

To ensure consistency, a structured downstream analysis approach was applied to both datasets. This included in-depth characterisation of macrophage populations, incorporating assessment of regulatory activity to provide insight into the functional properties of discrete cell subsets. This was followed by comparative analysis of transcriptomic differences in myeloid populations between disease states and controls (Figure 3.2.1)

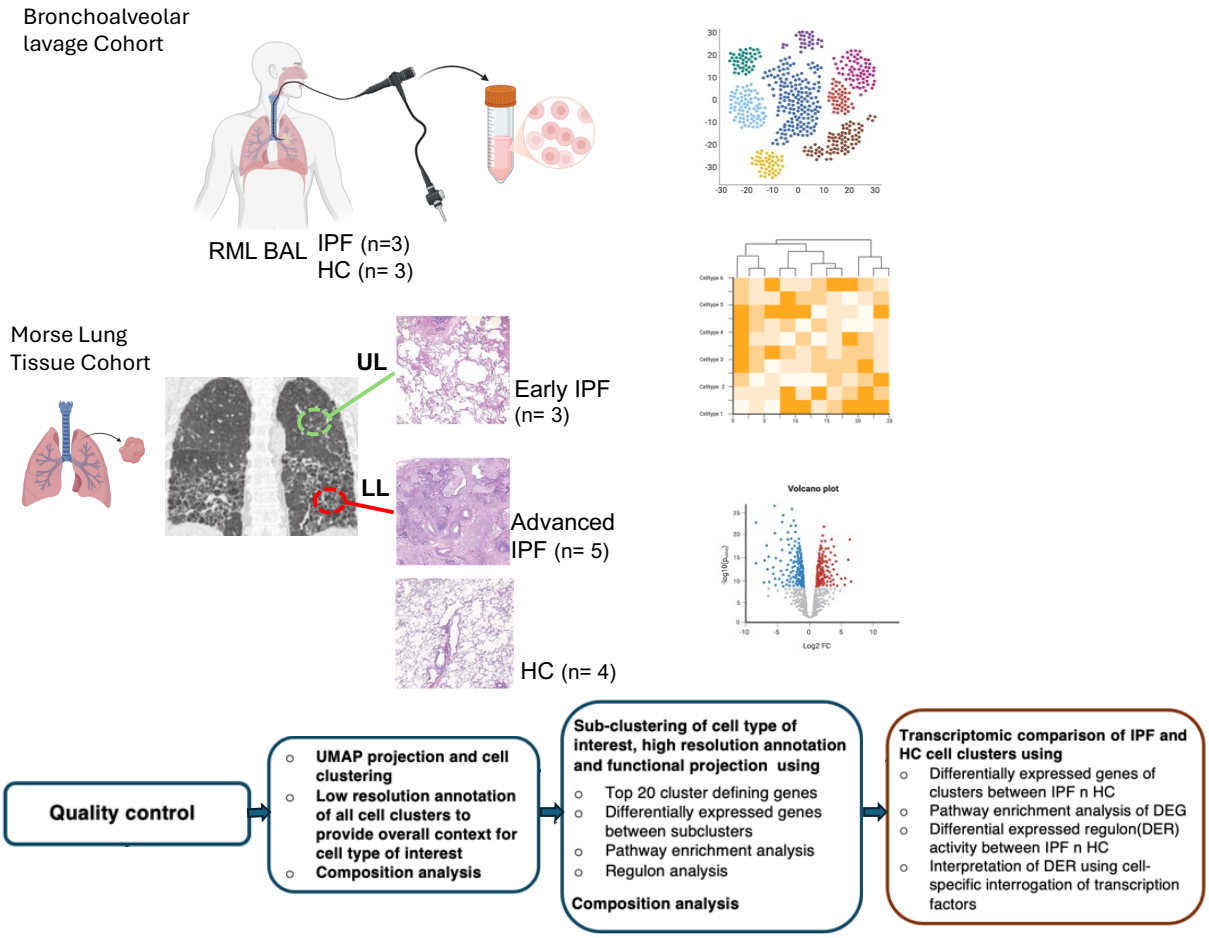


Figure 4.2.1. Experimental overview. *Bronchoalveolar lavage cohort - samples in the bronchoalveolar cohort were collected from the right middle lobe from IPF patients (n=3) and controls (n=3). Morse Cohort – Lung tissue biopsies from upper lobes (early [n=3]), lower lobes [advanced disease]) and controls n=4. Thoracic CT scan image depicting sites in the lungs where samples were obtained. Image shows typical honeycombing pattern for IPF fibrosis and peripheral or subpleural and basal distribution of disease. Red circle indicates advanced disease, green circle earlier disease. H&E stained lung sections show typical areas of dense fibrosis in lower lobe (LL) and presence of normal alveoli in early disease from the upper lobe (UL). An H&E section from one of Morse's healthy lungs (HC) is also shown for comparison.*

4.2.2 Patient Selection, patient and control demographic details

In the BAL dataset control donors were individuals undergoing a clinically indicated bronchoscopy for either haemoptysis of unclear aetiology or persistent cough with no clinical or radiological evidence of chronic lung disease. Patient demographic and clinical details outlined in Table 3.2.1. Participants were recruited under regional ethics service approved study; REC 14/SC/1060. In the Morse dataset demographic and histopathological information available in the original publication outlined in Table 4.2.2.

Condition	Sample ID (BAL)	Gender	Age	Smoking status	Ethnicity	Radiological Classification	Predicted FVC %	Predicted TLCO %	Medication	Active Comorbidities	BAL live cell count (x10^6)
IPF	HT2	Male	85	Ex	British Caucasian	UIP	78	44	Pirfenidone, Omeprazole, Amlodipine, Pravastatin, Telmisartan,	Pulmonary HTN, Peripheral vascular disease, HTN, CKD	13.2
	HT4	Male	85	Never	British Caucasian	UIP	73	37	Nintedanib, Amlodipine, Atorvastatin, Clopidogrel	Hypertension	11.5
	HT5	Female	74	Never	British Caucasian	UIP	72	52	Pirfenidone, Metformin, Gliclazide, Lansoprazole, Levothyroxine,	Hypothryoidism, T2DM	4.5
Control	HT6	Male	70	Ex	British Caucasian	Normal	n/a	n/a	Omeprazole	Nil	2.3
	HT7	Female	47	Never	British Caucasian	Normal	n/a	n/a	Omeprazole	Nil	4.8
	HT8	Female	67	Never	British Caucasian	Normal*	n/a	n/a	Fluoxetine, Amitriptylline, Zopiclone, Levothyroxine	Hypothyroidism	1.2

Table 4.2.1 - Demographic and experimental details of patients and controls for single cell RNA sequencing of bronchoalveolar lavage. *Sample ID refers to hashtag antibody label. BAL live cell count performed after sample processing prior to loadingsmoking status - Ex smoker defined as abstinent for >12 months. Radiological Classification as per 2018 joint ATS/ERS[20]. *Increased infiltrates on CT on contralateral lung lobe to bronchoalveolar lavage sampling, Abbreviations, CKD - chronic kidney disease, T2DM - type 2 diabetes mellitus, HTN - hypertension. UIP – usual interstitial pneumonia. FVC – forced vital capacity, TLCO – total lung diffusion carbon monoxide.*

Disease Group	Sample ID	Age	Gender	Ethnicity	Smoking status	Lung Function	Histopathology Report
Control Lung	SC 56	57	Female	not stated	not stated	not stated	Normal healthy lung
Control Lung	SC 59	18	Male	not stated	not stated	not stated	Healthy lung tissue; a bit of bronchitis probably due to ventilator. Some of the small airways are prominent and more muscular than expected, which may indicate that this patient had allergies or some asthma
Control Lung	SC 155	23	Female	not stated	not stated	not stated	Normal healthy lung
Control Lung	SC 156	23	Female	not stated	not stated	not stated	Normal healthy lung
IPF Lower Lobe	SC 87	70	Female	not stated	not stated	not stated	UIP: acute exacerbation of UIP, diffuse alveolar damage and inflammation
IPF Upper Lobe	SC 88	70	Female	not stated	not stated	not stated	Mostly UIP; more diffuse than lower lobe. Some mixed fibrotic and cellular NSIP (acute). Some honeycomb cysts
IPF Lower Lobe	SC 89	70	Female	not stated	not stated	not stated	UIP: acute exacerbation of UIP, diffuse alveolar damage and inflammation
IPF Lower Lobe	SC 93	69	Male	not stated	not stated	not stated	Classic end-stage lung: honeycomb cysts, bronchial metaplastic cells, some smooth muscle metaplasia
IPF Upper Lobe	SC 94	69	Male	not stated	not stated	not stated	Scarring around the airways, smoker, much better than the lower lobe. Some of the scarring may be from previous acute exacerbations. No UIP or fibrosis, maybe some COPD
IPF Lower Lobe	SC 95	69	Male	not stated	not stated	not stated	Classic end-stage lung: honeycomb cysts, bronchial metaplastic cells, some smooth muscle metaplasia
IPF Lower Lobe	SC153	69	Female	not stated	not stated	not stated	Complete replacement of the lung architecture by scar tissue with honeycomb change and end-stage lung disease
IPF Upper Lobe	SC 154	69	Female	not stated	not stated	not stated	Nearly complete replacement of the lung architecture by scar tissue with honeycomb change with end-stage lung disease

Table 4.2.2. Demographic and experimental characteristics of patients and controls from the publicly available dataset reported by Morse et al[185] . *Sample identifiers correspond to those used in the original study. Histopathological reports are included to highlight differences in the extent of fibrosis and associated pathological features between lower and upper lobe samples, alongside the corresponding disease group labels assigned in the original study. Abbreviations, UIP – usual interstitial pneumonia, NSIP – non-specific interstitial pneumonitis, COPD – chronic obstructive pulmonary disease.*

4.2.3 Analysis of single cell sequencing data

For the Morse dataset, raw data in the form of FASTQ files was accessed from the GEO repository GSE128033. Initial raw data processing, alignment and quality control steps in both datasets performed as described in Section 3.2.5 and performed in conjunction with Jeongmin Woo. Downstream analysis performed in Seurat as described in Section 3.2.5 with additional analysis steps outlined below.

Following analysis of differential regulon activity in AM populations, identified from BAL samples using SCENIC, additional filtering was applied to identify regulons that were both differentially expressed and exhibited significant changes in activity between IPF and control samples (Section 4.3.2 and Figure 4.3.8). The log2FC in regulon activity score was first calculated between conditions, and results were filtered to retain only those with false discovery rate (FDR) adjusted p-values < 0.05. The top 20 regulons within each AM population were then ranked by Log2FC. Regulons that were consistently differentially expressed in all AM subsets or specifically upregulated in individual AM populations were selected for downstream analysis. These were further evaluated through a structured review of the literature to identify regulatory pathways and cellular processes associated with IPF, and to define subset-specific functional characteristics.

In the Morse dataset, differential abundance analysis was performed to compare proportions of myeloid populations across IPF disease states (upper and lower lobes) and controls. This analysis was performed using SCCOMP which uses which a Bayesian framework for modelling compositional cell proportion data[262]. SCCOMP enables testing of differences in compositional data across multiple factors (in this case disease states). SCCOMP also models all cell populations together thereby accounting for the fact that in compositional data, cell proportions are interdependent and always sum to a total of one. The method also incorporates variability in population abundance across samples, improving robustness to outliers and reducing false positive findings. For statistical testing the model estimates a range of plausible differences in the abundance of a cell population between conditions summarised as 95% credible intervals supported by the data. Differences between conditions are estimated from posterior distributions, with credible intervals reflecting the uncertainty around these estimates and providing a measure of confidence in the observed effect.

In the Morse dataset differential gene expression analysis of monocyte and macrophage subsets across IPF disease states and control lung samples were performed using likelihood ratio testing (LRT) which enables testing across 3 conditions. LRT compares a full model, including disease state as a factor, to a reduced model excluding this variable. Genes fit better in the full model are those where expression varies significantly across

conditions. Genes were considered differentially expressed if they met the following criteria adjusted p-value < 0.05 and log2 fold change > 1.5.

4.3 Results

4.3.1 scRNAseq reveals a macrophage landscape characterised by distinct homeostatic and pro-inflammatory transcriptomic states at the alveolar barrier

To gain an overall understanding of monocyte and macrophage activity at the alveolar epithelial barrier single cell RNA sequencing was performed on cells from broncho-alveolar lavage (BAL) samples of IPF patients (n=3) and healthy controls (HC) (n=3). Patient demographics and clinical details are summarised in (Table [20] 4.2.1).

ScRNAseq was performed using the 10X chromium platform and analysed using the workflow outlined in Figure 4.2.1.

17 cell clusters from 16,524 BAL cells (IPF and HC combined) were identified following unsupervised Louvain clustering (Figure 4.3.1). First level annotation based on cluster defining genes (CDGs), identified 5 closely related subsets of alveolar macrophages (AM)s, two DC, two $CD4^+$ T cell, one $CD8^+$ T cell, one B cell cluster, two cycling macrophage subsets and one small cluster of epithelial cells. Only a small monocyte population was present in BAL samples (41 cells). Granulocyte populations, including neutrophils, were not identified in sufficient numbers for downstream analysis. This is consistent with other BAL[263] and lung tissue[63, 86] droplet-based scRNAseq datasets, including the Human Lung Cell Atlas[264], where granulocytes are similarly under represented because of their low RNA content, short ex vivo lifespan and increased susceptibility to cell loss during tissue dissociation and processing.

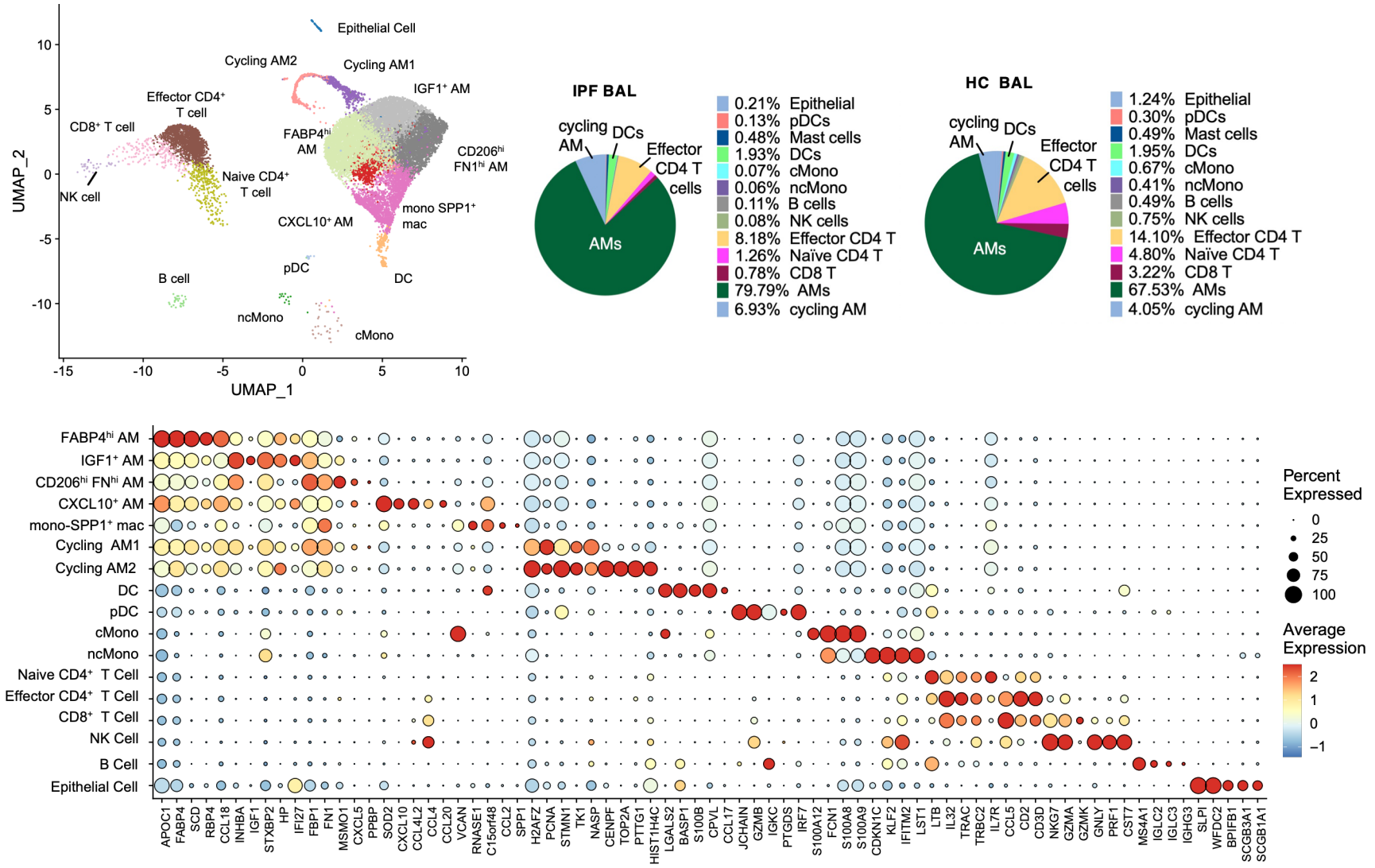


Figure 4.3.1. Single-cell RNA sequencing analysis of BAL populations in IPF and healthy controls (HC). *Top left panel: UMAP projection of BAL populations with IPF and control samples combined. Top right panel: Composition of BAL populations (percentage of total cells) in IPF and HC samples. Cycling AM 1 and 2 combined for composition analysis. Bottom panel: Dot plot showing the top ten cluster-defining genes for each BAL population (IPF and control combined); bubble size represents the percentage of cells expressing each gene within the cluster, and colour indicates average gene expression. Genes shown represent the top differentially expressed genes used to assist cluster annotation.*

In both IPF and HC samples, macrophages dominated the immune cell landscape in the alveolar space (79.8% of IPF cells and 67.5% of HC cells in BAL) followed by $CD4^+$ T cells, then cycling macrophages (Figure 4.3.1). There The proportions of immune cells in IPF and HC were comparable (Figure 4.3.1) but 5 times more immune cells (13,943 cells vs 2,667 cells) were recovered from IPF compared to HC BAL samples, using identical methods of harvesting (Table 4.2.1). The relative proportion of BAL T cells was lower in IPF compared to controls however the absolute number of BAL T cells was increased in the IPF group. This apparent discrepancy may be explained by the expansion of the AM compartment, resulting in a compositional change in other immune cell populations.

BAL sampling primarily recovers cells from the alveolar barrier - small airways and alveolar space, including AMs that reside on the luminal surface of the alveoli. In the present study, AMs were defined using established human transcriptomic markers of alveolar macrophages rather than immunophenotypic surface markers. AMs exhibit a distinct transcriptional profile shaped by the alveolar niche[140, 141] and are characterised by expression of a number of genes including *FABP4, CD52, C1Q* family genes, *APOC1, SERPINE1* and *PPARG*, the latter described as the master regulator of the AM phenotype[141, 142, 156]. Expression of these markers across all five AM populations, albeit to varying degrees, supports their annotation as AMs, consistent with the BAL sampling strategy. These five AM cell clusters were annotated using cluster defining genes (CDGs) (selection criteria described in Section 3.2.6 and visually displayed in Figure 4.3.2), in conjunction with six other key publications describing lung macrophage transcriptomic heterogeneity [141, 156, 263, 265, 266, 267] including the integrated lung health and disease dataset[264]. AM clusters are labelled 'subsets', however, for some of these clusters, the term 'transcriptomic states' representing a more transient, context-dependent phenotype may be more appropriate and is considered in the discussion.

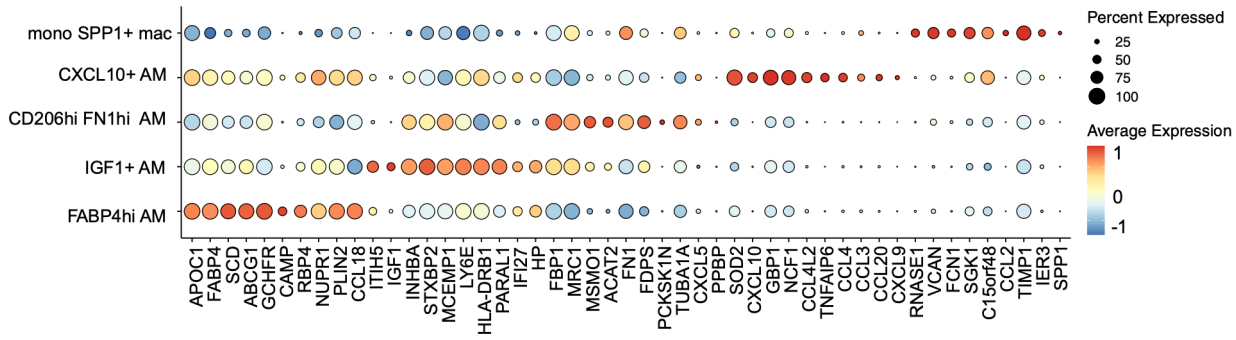
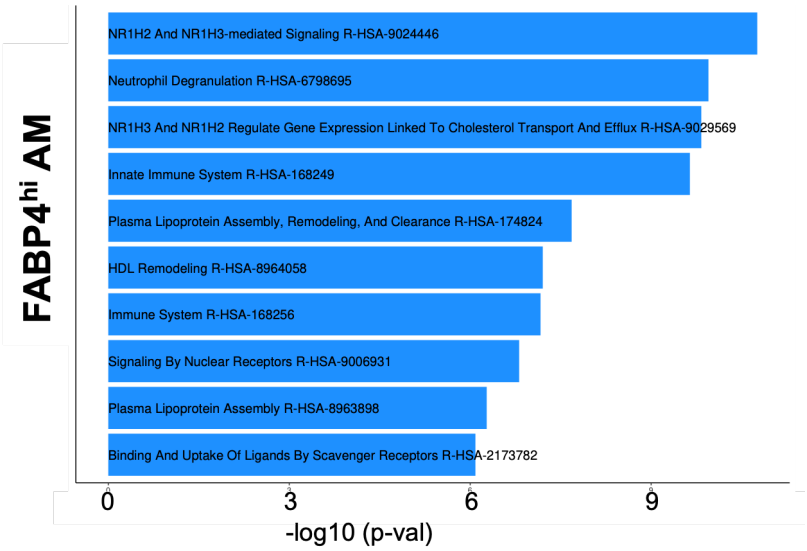


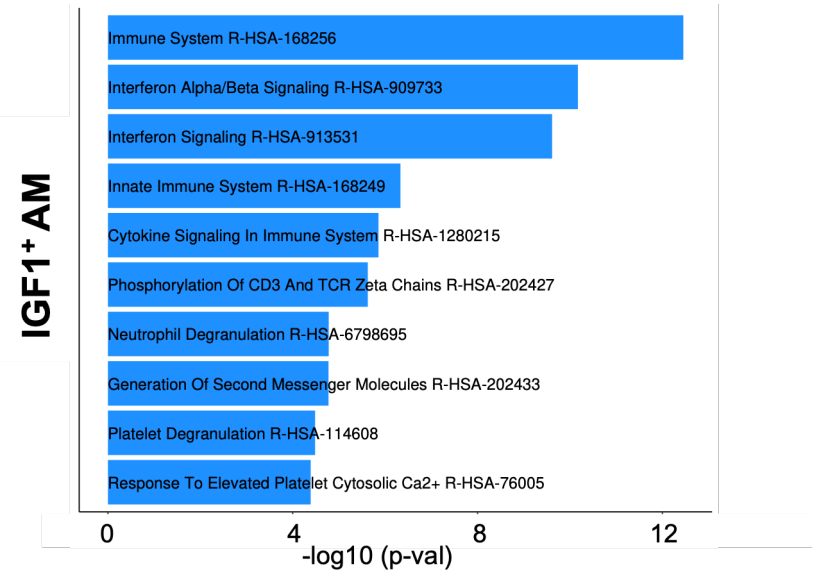
Figure 4.3.2. Alveolar macrophage subsets identified in bronchoalveolar lavage. *Bubble plot showing the top 10 cluster-defining genes for each AM subset, relative to other AM subsets; bubble size represents the percentage of cells expressing each gene within the cluster, and colour indicates normalised average gene expression. Cluster annotation was performed using these CDGs in conjunction with published lung macrophage reference datasets. Cycling cells are removed in this visualisation.*

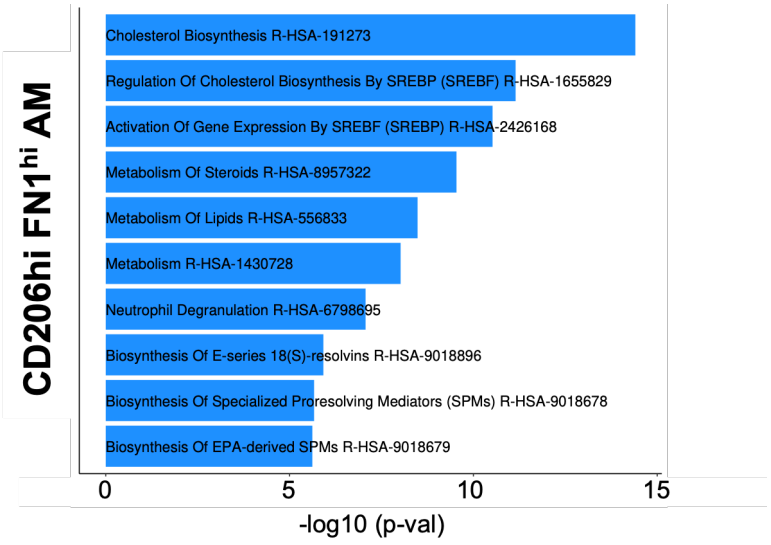
The two previously published lung macrophage subsets in IPF from lung digest samples[267] – FABP4^{hi} macrophage and SPP1^{+} macrophages were identifiable in BAL macrophage populations. FABP4^{hi} macrophages have also been described in other lung transcriptomic studies[141, 142, 155, 156, 263] as a subset expressing canonical mature alveolar cell markers including *FABP4, SERPING1, APOC1, CES1, MME* (Figure 4.3.2). The SPP1^{+} macrophage subset was also present however also contained cell types with markers for monocytes (*CD14, S100 A8/9*) and tissue macrophages[141, 142, 264] (Figure 4.3.2). Consequently, this cluster was annotated mono-SPP1^{+} Macs and interpreted as a mixed population comprised of monocytes at different stages of differentiation and interstitial SPP1 expressing macrophages. This population may represent macrophages that have recently migrated into the alveolar space or displaced from the interstitium during sample collection, consistent with their lower expression canonical AM markers[140, 141, 156]. Similar populations have been observed in other lung BAL datasets[155, 156, 263].

The three remaining AM subsets are previously undescribed in IPF lungs, and labelled CXCL10^{+} AM, IGF1^{+} AM and CD206^{hi} FN1^{hi} AM. CXCL10^{+} AMs, have been described in inflammatory lung conditions e.g. COVID-19[265], ARDS[263] and inflammatory diseases of other tissues including rheumatoid arthritis and inflammatory bowel disease[142]. They have also been observed in healthy BAL samples[156]. IGF1^{+} AMs uniquely expressed *IGF1* and mature AM transcripts displayed in the FABP4^{hi} AM subset. A population with a similar transcriptomic profile to IGF1^{+} AM has also been observed in healthy donor BAL samples[156]. CD206^{hi}FN1^{hi} AMs have not previously been described however noted to highly express fibronectin 1 (*FN1*) that facilitates assembly of extra cellular matrix (ECM) proteins, fibroblast chemotaxis and differentiation into myofibroblasts[268].

To characterise the functional profile of these five AM subsets pathway enrichment analysis (PEA) was performed using significantly upregulated genes (selection criteria described in Section 3.2.6), with enriched pathways identified using Fisher's exact test. (Figure 4.3.3).


FABP4hi AM
NR1H2 And NR1H3-mediated Signaling R-HSA-9024446
Neutrophil Degranulation R-HSA-6798695
NR1H3 And NR1H2 Regulate Gene Expression Linked To Cholesterol Transport And Efflux R-HSA-9029569
Innate Immune System R-HSA-168249
Plasma Lipoprotein Assembly, Remodeling, And Clearance R-HSA-174824
HDL Remodeling R-HSA-8964058
Immune System R-HSA-168256
Signaling By Nuclear Receptors R-HSA-9006931
Plasma Lipoprotein Assembly R-HSA-8963898
Binding And Uptake Of Ligands By Scavenger Receptors R-HSA-2173782
0
3
6
9
-log10 (p-val)


IGF1+ AM
Immune System R-HSA-168256
Interferon Alpha/Beta Signaling R-HSA-909733
Interferon Signaling R-HSA-913531
Innate Immune System R-HSA-168249
Cytokine Signaling In Immune System R-HSA-1280215
Phosphorylation Of CD3 And TCR Zeta Chains R-HSA-202427
Neutrophil Degranulation R-HSA-6798695
Generation Of Second Messenger Molecules R-HSA-202433
Platelet Degranulation R-HSA-114608
Response To Elevated Platelet Cytosolic Ca2+ R-HSA-76005
0
4
8
12
-log10 (p-val)


CD206hi FN1hi AM
Cholesterol Biosynthesis R-HSA-191273
Regulation Of Cholesterol Biosynthesis By SREBP (SREBF) R-HSA-1655829
Activation Of Gene Expression By SREBF (SREBP) R-HSA-2426168
Metabolism Of Steroids R-HSA-8957322
Metabolism Of Lipids R-HSA-556833
Metabolism R-HSA-1430728
Neutrophil Degranulation R-HSA-6798695
Biosynthesis Of E-series 18(S)-resolvins R-HSA-9018896
Biosynthesis Of Specialized Proresolving Mediators (SPMs) R-HSA-9018678
Biosynthesis Of EPA-derived SPMs R-HSA-9018679
0
5
10
15
-log10 (p-val)

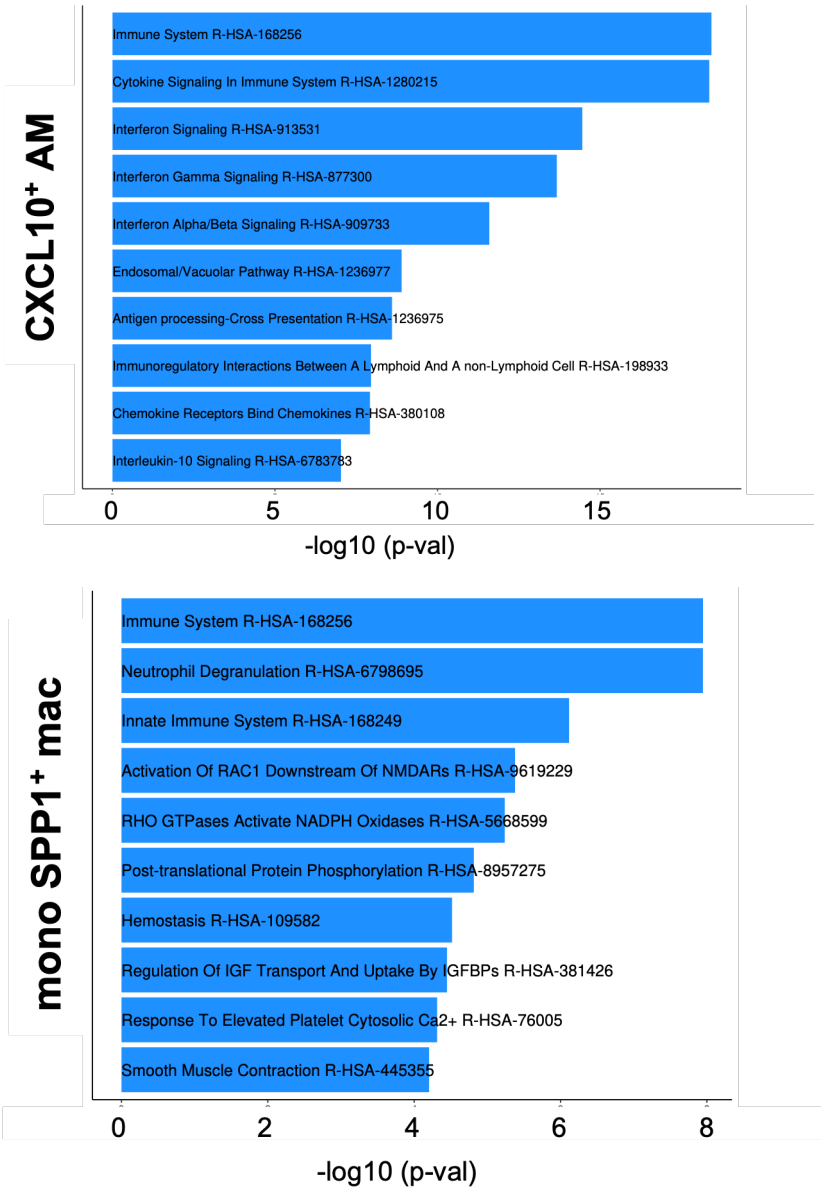


Figure 4.3.3. Pathway enrichment analysis of AM subsets *Pathway enrichment analysis was performed using EnrichR on gene ontology (GO) database of significantly upregulated genes Log2FC threshold >1.5 and adjusted P value <0.05). The x axis shows the -log10 (P value) with pathways displayed as bar plots, ranked by statistical significance.*

To complement the marker gene and pathway analyses, the regulatory transcriptomic profiles of each alveolar macrophage subset were examined using Single-Cell rEgulatory Network Inference and Clustering (*SCENIC*)[233] introduced in Section 3.3.8. Here, regulon analysis was used alongside conventional transcriptomic analyses to identify transcription factor-regulated gene networks enriched within individual AM subsets, providing additional functional insight into their biological phenotype. Unlike the disease focused analysis described in Chapter 3, for this analysis IPF and control cells were analysed together with regulon activity scores were compared across AM subsets to identify subset-specific regulon enrichment rather than disease associated differences.

To identify regulons characteristic of each AM subset, regulons were first ranked according to regulon activity score. Regulons within the top 10 for each subset were then ranked according to log2 fold change in regulon activity relative to all other AM subsets. Regulons present within the top 10 of both rankings were selected for functional interpretation and are highlighted by coloured boxes in Figure 4.3.4. Box colours correspond to the AM subset in which each regulon was selected and are carried through to Table 4.3.1 to facilitate comparison.

To interpret the functional relevance of these regulons, relevant published studies were reviewed, with an emphasis on functional studies where the corresponding TF was selectively depleted in macrophages. Regulons were subsequently grouped according to effects on cell function (Table 4.3.1). Findings from the SCENIC analysis and functional interpretation are summarised in Figure 4.3.4 and Table 4.3.1. Full analysis and reference studies outlined in Appendix.

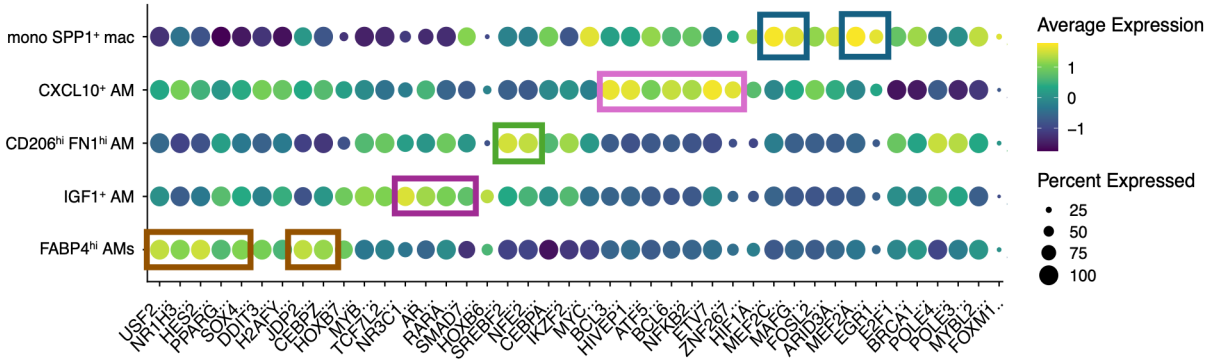


Figure 4.3.4. Regulon analysis of AM subsets. *Bubble plot showing the top 10 regulons for each AM subset ranked according to regulon activity score (AUCell). Bubble colour represents relative regulon activity across all AM subsets, while bubble size indicates the percentage of cells within each subset expressing the regulon. Coloured boxes highlight regulons selected for functional interpretation that were ranked within the top 10 by both regulon activity score and $\log_2$ fold change, indicating high regulon activity together with subset-specific enrichment (see main text). Box colours correspond to the AM subset in which the regulon was selected and are carried through to Table 4.3.1.*

Cluster	Regulation of Ox. stress	Phagocytosis / Efferocytosis	Surfactant / Lipid Metabolism	Stem Cell / Renewal	Immune Regulatory	Pro-Inflamm	Inteferon Signalling	Fibrogenic / ECM Orgnisation
FABP4^{hi} AM	CEPBZ	PPARG	NR1H3	SOX4	PPARG, JDP2			
IGF1^{+} AM		PPARG			PPARG, NR3C1, NFIL3, TCF4			
CD206^{hi} FN^{hi} AM	NRF2		SREBF2		NRF2			EGR2
CXCL10^{+} AM					BCL3*, HIVEP1*, BCL6	NFkB2, HIF1a HIVEP1*	IRF1, ETV7	
mono SPP1^{+} mac					MEF2A	NFkB2, HIF1a MEF2C,		MYC, EGR1

Table 4.3.1. Classification of subset-enriched regulons in alveolar macrophage (AM) subsets by proposed function. *Regulons selected for functional interpretation (highlighted in Figure 4.3.4) were grouped according to their reported effects on macrophage function based on a structured review of the published literature. Regulons marked with an asterisk (*) indicate those for which reported effects on macrophage activity are context-dependent.*

Findings from PEA and regulon activity analyses were broadly consistent (Figure 4.3.3 and Figure 4.3.4) with both approaches identifying similar biological processes within each AM subset. Specifically, pathways enriched by PEA were supported by enrichment of transcription factor-regulated gene networks associated with the same biological functions, providing complementary evidence for the proposed functional phenotype of each subset. These complementary analyses were subsequently used to characterise the likely functional characteristics of each AM subset.

FABP4^{hi} AMs highly expressed canonical alveolar macrophage associated TFs, including *PPARG*, a key regulator of homeostatic alveolar macrophage activity. In addition, transcriptional programmes associated with established AM roles were enriched in this subset[140, 141, 152] including pathways related to response to external stimuli, surfactant and lipid metabolism, phagocytosis, efferocytosis and physiological regulation of inflammation[269, 270]. IGF1^{+} AMs, also highly expressed *PPARG* indicating this population may perform a similar role in phagocytosis and efferocytosis. This population also expressed TFs associated with immune regulation including *NFIL3*, and *NR3C*[271, 272, 273]. IGF1^{+} AM pathway enrichment analysis also highlighted a specific role in antigen presentation and regulation of adaptive immune responses in this subset. Based on these features FABP4^{hi} AMs and IGF1^{+} AMs were therefore termed ‘homeostatic AMs’.

CD206^{hi}FN1^{hi} AMs expressed pathways related to lipid and cholesterol homeostasis, regulation of oxidative stress and inflammation indicating a partially homeostatic functional profile. This subset also exhibited high expression of *EGR2* which is associated with the resolution of injury but also implicated in initiating fibrotic responses[274]. CXCL10^{+} AMs demonstrated increased expression of TFs and pathways

associated with pro-inflammatory processes and interferon responses including *HIF1a, NFkB2, ETV7* and *IRF1*. This profile is consistent with a IFN-response transcriptional programme, induced by type 1 but also type 2 IFN signalling. In parallel, TFs associated with the negative regulation of inflammation notably *BCL3, BCL6* and *HIVEP1* were also enriched[275, 276]. mono-SPP1^{+} macs displayed a heterogenous pathway and regulon profile consistent with a mixed population comprising monocytes, and SPP1^{+} macrophages. This cluster exhibited concurrent upregulation of pro-fibrotic, pro-inflammatory and anti-inflammatory pathways and regulons. (Table 4.3.1).

All AM subsets or states were present in both healthy and IPF BAL but in markedly higher numbers in IPF (Table 4.2.1 and Figure 4.3.5). The homeostatic FABP4^{hi} AM and IGF1^{+} AM subsets comprised the largest AM populations in both conditions although their relative proportions were reduced in IPF (66.2% in HC vs 51.6% in IPF). In contrast, the proportions of mono-SPP1^{+} macs and CD206^{hi}FN1^{hi} AM were modestly increased in IPF (15.1% in IPF vs 10.0% HC), and (21.9% IPF vs 14.4% HC), respectively (Figure 4.3.5). Given the limited number of samples, these differences need to be interpreted cautiously, as may reflect both disease-associated changes and inter-individual variation.

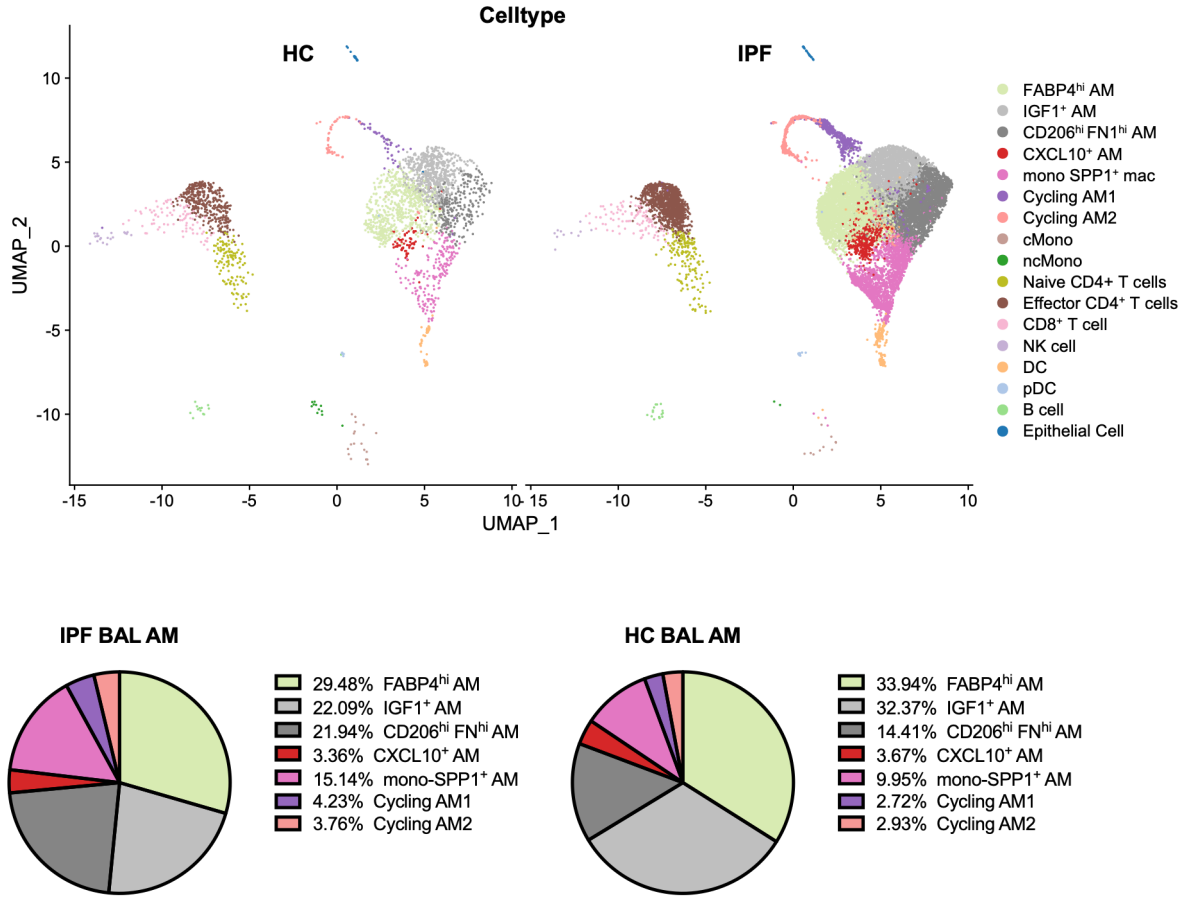


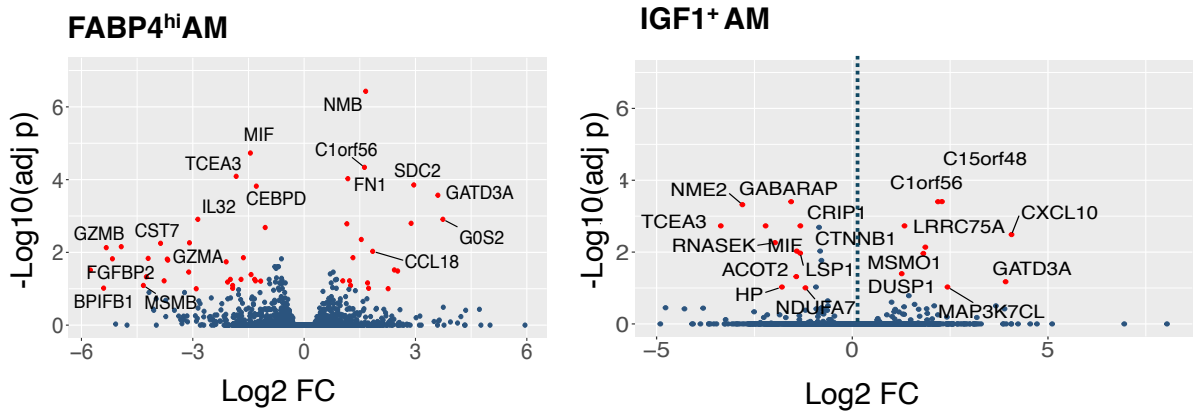
Figure 4.3.5. Composition of AM subsets in IPF and controls. *Top panel - UMAP from single cell analysis split by disease condition highlighting difference in cell number in IPF compared to control samples. Bottom panel - Composition of AM subsets (proportion of total AM population) in IPF and HC samples.*

In summary, macrophage subsets at the alveolar barrier could be categorised based on their inferred functional activity. FABP4^{hi} and IGF1^{+} AMs were associated with alveolar macrophage homeostatic functions, including phagocytosis and efferocytosis, while FABP4^{hi} and CD206^{hi}FN1^{hi} AMs exhibited lipid metabolic homeostatic activity. CXCL10^{+} AMs, IGF1^{+} AMs and mono-SPP1^{+} macs demonstrated both inflammatory and counter-inflammatory signalling profiles. In addition, mono-SPP1^{+} macs and CD206^{hi}FN1^{hi} AMs expressed pathways related to tissue repair and fibrosis.

4.3.2 Increased inflammatory and type 1 I IFN signalling activities in AMs at the IPF alveolar barrier

Having characterised macrophage subsets at the alveolar barrier, differences in the transcriptional phenotype of IPF and HC AM subsets were examined to identify disease specific transcripts and regulatory networks.

At the single-gene level, FN1 was consistently upregulated in CD206^{hi} FN1^{hi} AM, CXCL10^{+} AM and FABP4^{hi} AM in IPF (Figures 4.3.6). FN1 codes a glycoprotein involved in tissue repair, adhesion and migration to ECM, potentially reflecting the fibrotic environment in IPF. In addition, increased C*XCL10* expression was observed in the mono-SPP1^{+} AM and IGF1^{+} AM subsets in IPF compared with controls while *CCL-18* was upregulated in IPF FABP4^{hi} AMs (Figures 4.3.6). These chemokines are involved in immune cell trafficking and often upregulated in chronic inflammation. Both *CXCL10* and *CCL-18* have previously shown to be elevated in IPF BAL fluid compared to controls[277, 278].



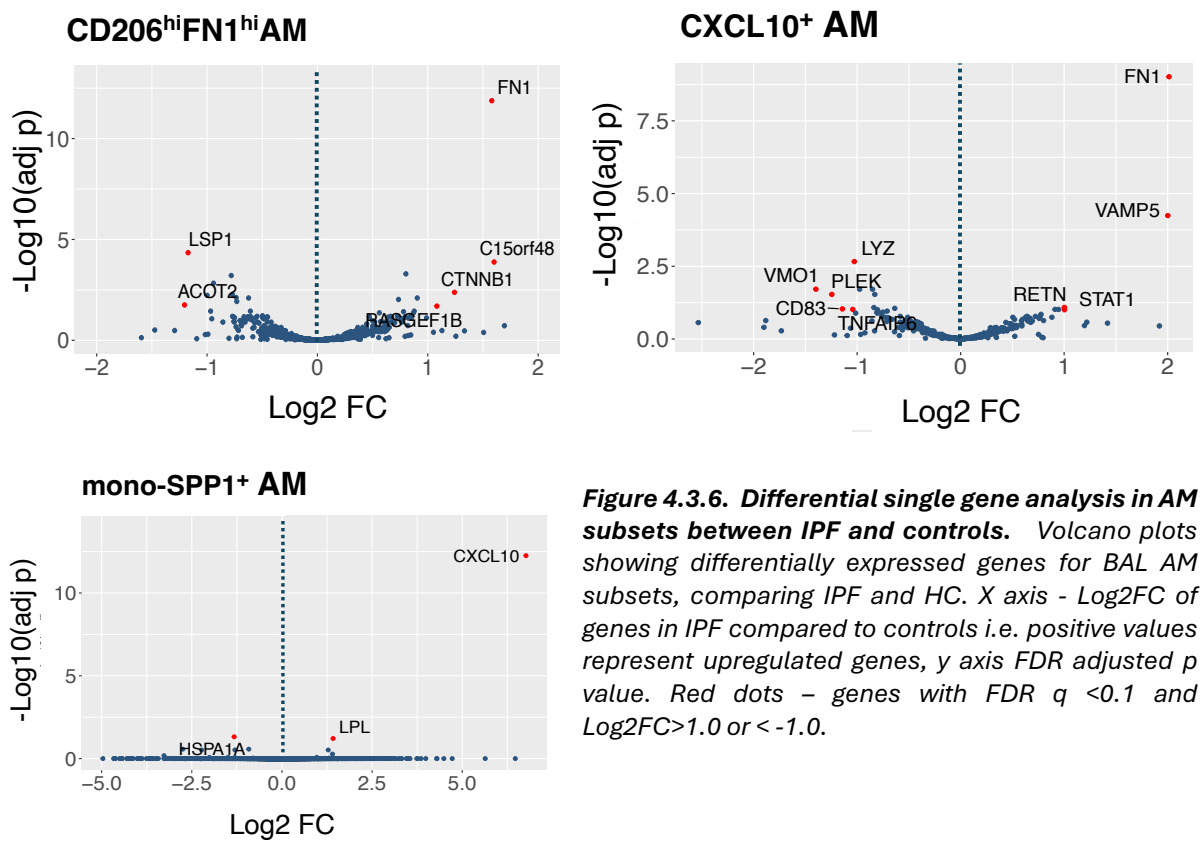


Figure 4.3.6. Differential single gene analysis in AM subsets between IPF and controls. *Volcano plots showing differentially expressed genes for BAL AM subsets, comparing IPF and HC. X axis - Log2FC of genes in IPF compared to controls i.e. positive values represent upregulated genes, y axis FDR adjusted p value. Red dots – genes with FDR q <0.1 and Log2FC>1.0 or < -1.0.*

As the number of DEGs between IPF and controls was limited, gene set enrichment analysis (GSEA) using the 'Molecular Signatures Database Hallmark collection[279] was performed.

Differentially expressed gene sets were identified in IGF1^{+} AM, CD206^{hi}FN1^{hi} AM and CXCL10^{+} AMs. In these subsets, enrichment of proinflammatory gene sets were observed notably - 'IL-6-JAK-STAT3' and 'TNFA via NFKB signalling' in IGF1^{+} AM, 'IFNG response' and 'IFNA response' in CXCL10^{+} AM, and 'TNFA via NFKB signalling' in CD206^{hi}FN1^{hi} AM (Figure 4.3.7).

In addition, gene sets associated with cholesterol homeostasis were also enriched in IPF compared to HC AMs, potentially reflecting increased uptake and processing of surfactant from degrading type II alveolar epithelial cells[60, 280, 281] . Gene sets associated with MTORC1 signalling, a regulator of cell metabolism and cell growth, were also increased in IPF CXCL10^{+} AM and CD206^{hi} FN1^{hi} AMs (Figure 4.3.7). Despite the larger number of DEGs observed in FABP4^{hi} AMs (Figure 4.3.6) no statistically significant gene sets were identified in this population.

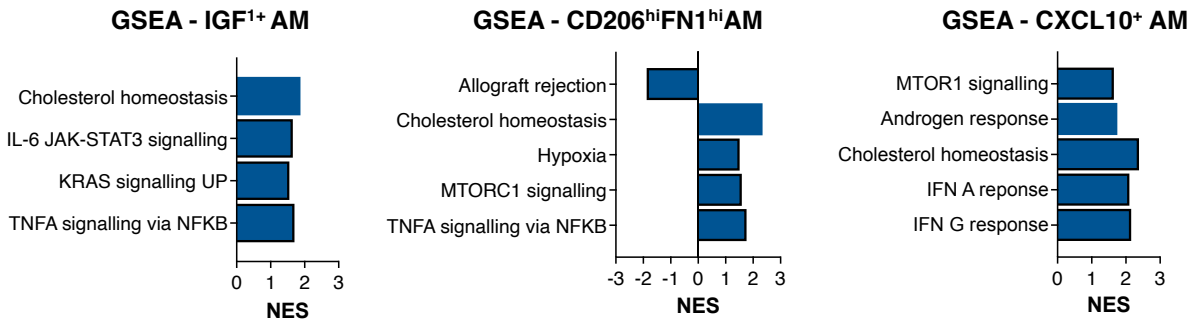


Figure 4.3.7. Differential gene set analysis in AM subsets between IPF and controls. *Bar charts depicting gene set enrichment analysis (GSEA) using the Molecular signatures database 'Hallmark' collection. The x axis represents normalised enrichment scores (NES) with positive score reflecting pathways enriched in IPF, bars detail enriched pathways in AM subsets ranked by false discovery rate (FDR) adjusted p-values. No significant enrichment was found in mono-SPP1^{+} AMs and FABP4^{hi} AMs comparing IPF to controls. Statistical significance of enrichment was assessed by permutation testing to generate a null distribution of enrichment scores, with correction for multiple comparisons.* ***Abbreviations****; GSEA – gene set enrichment score, NES – normalised enrichment score.*

I next identified transcription factor (TF)–driven gene programmes (regulons) in these AMs at the alveolar barrier using SCENIC. (Appendix Table 3).

Regulons were then grouped into two categories. First, those upregulated across all AM subsets, representing shared regulatory processes associated with IPF irrespective of functional state. Second, regulons exclusively upregulated within individual AM subsets, providing insight into subset-specific responses in IPF (Appendix Table 3).

Analysis of DERs revealed three key findings. First, there was an overall increase in regulon activity in IPF AMs compared with controls, indicating a global increase in regulatory and cellular transcriptional activity across all subsets. Second, several regulons, including *BHLHE40, CBFB, SMAD7, TCF7L2*, and *FOS*, were consistently enriched across all IPF AM subsets. These regulons are associated with inflammatory signalling (*BHLHE40, SMAD7, FOS*), TGF-β pathway activity and its regulation (*SMAD7*), cellular proliferation and self-renewal (*CBFB, TCF7L2*), and lipid metabolism (*BHLHE40*) (Table 4.3.2, Appendix Table 3).

Third, AM subset-specific DERs were investigated to understand subset specific responses in IPF (Figure 4.3.8 and Summary Table 4.3.2). As in Figure 4.3.4 and Table 4.3.1, disease-associated regulons were colour-coded according to the AM subset in which they were enriched. The same colour scheme was retained throughout to maintain consistency across figures and tables. This analysis revealed that FABP4^{hi} AM DERs were associated with counter-inflammatory pathways with upregulation of *ATF3* and *NR3C1* alongside increased cholesterol and lipid metabolism. In IPF, CD206^{hi}FN1^{hi} AMs upregulated regulatory networks related to a wound healing and potentially fibrotic

processes with increased *PRDM5* and *CEBPA* expression. In addition, *NFE2* a regulator that restrains IFN signalling in macrophages.

CXCL10^{+} AMs exhibited enrichment of regulons associated with activation of both type 1 and type 2 IFN-responsive transcriptional programmes including *IRF2, STAT1* and *IRF7*, the latter being a regulator of type 1 IFN induction, together with *ET7* and *STAT3*, that are implicated in the negative regulation of IFN responses. Mono-SPP1^{+} macrophages showed upregulation of regulons linked to both pro-inflammatory (*ATF2, STAT5A, STAT5A*) as well as pro-fibrotic and anti-inflammatory activities (*ELK4, MAF* and potentially *EP300* and *RREB1*), consistent with being a mixed population of monocytes and SPP1^{+} macs.

There were no macrophage-specific studies for the two regulons that were specifically increased in IGF1^{+} AM (*E2F4* and *LEF1*). Whilst not identified in the defined analysis approach described, visual inspection analysis of the top DERs also identified increased *STAT2* regulon activity in multiple AM subsets in IPF, including FABP4^{hi}, IGF1^{+}, and CXCL10^{+} AMs (Appendix Table 3).

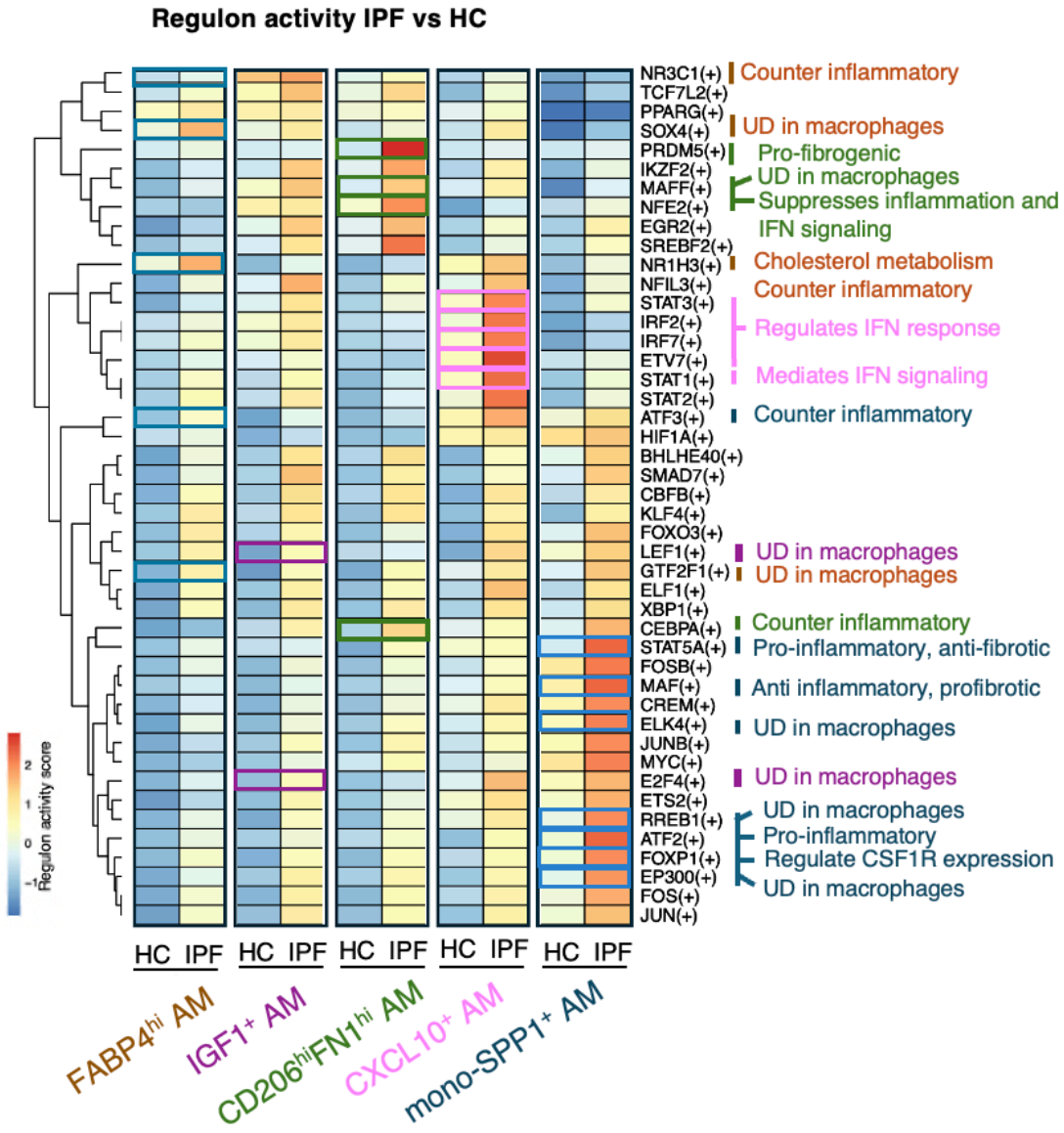


Figure 4.3.8. Differential Regulon activity in AM subsets in IPF controls gene set analysis AM subsets IPF and controls. *Heatmap depicting top differentially expressed regulons between IPF and control AM subsets based on AUC cell derived regulon activity score. Colour represents regulon activity score scaled across all AM subsets and both disease states, with positive values indicating enrichment of transcription factor (TF) gene expression.* Boxes and highlight differentially expressed regulons between IPF and HC with Log2FC >0.02 and adjusted p value <0.05 that were specific to individual AM subsets (see methods). Functional annotations and descriptions represent macrophage-specific effect derived from structured literature review. Note only subset specific differential expressed regulons annotated. *Abbreviations: UD – undefined function (no macrophage specific function identified in the literature).*

Cluster	Cholesterol / Lipid Metabolism	Proliferation/ self renewal	Pro Inflam.	Counter Inflam.	Pro IFN	Counter IFN	Pro-Fibrotic	Counter-Fibrotic	UD function
FABP4^{hi} AM	NR1H3			ATF3 NR3C1					GTF2F1
IGF1^{+} AM									E2F4 LEF1
CD206^{hi} FN^{hi} AM				CEBPA NFE2		NFE2	PRDM5. CEBPA		MAFF
CXCL10^{+} AM					STAT1 STAT2 IRF7	STAT3 IRF2 ETV7			
mono SPP1^{+} mac			ATF2 STAT5A	ELK4 FOXP1			MAF RREB1		EP300
Pan AM	BHLHE40	BHLHE40 CBFB TCF7L2	BHLHE40 SMAD7 FOS	TCF7L2				SMAD7	

Table 4.3.2. Classification of differentially expressed regulons IPF compared to controls by proposed function. *Regulons enriched in IPF AM subsets were grouped according to their reported functional effects on macrophage activity, based on a structured review of published studies. Colours depicting each AM subset correspond to heatmap in Figure 4.3.8 and represent AM subset specific effects. 'Pan AM' refer to regulons upregulated in all AM subsets and represent a disease specific effect. Abbreviations; UD – undefined function (no macrophage specific function identified in the literature).*

Taken together with the GSEA analysis, the regulon analyses indicate that alveolar barrier AMs in IPF exhibit increased inflammatory and wound repair activities; with evidence of increased type 1 IFN signalling activity in FABP4^{hi} AM and IGF1^{+} AM with increased STAT2 regulon activity, but most pronounced in CXCL10 AMs. Counter-inflammatory regulon activity was also observed in FABP4^{hi}, CD206^{hi}FN1^{hi} and CXCL10^{+} AMs, suggesting the presence of *regulatory* mechanisms that may act to restrain inflammatory signalling. Despite this, a net pro-inflammatory transcriptional profile was evident in IGF1^{+} AM, CD206^{hi}FN1^{hi} AM and CXCL10^{+} AMs in IPF, characterised by enrichment of TNF-α, IL-6, IFN-γ and IFN-α signalling pathways Figure 4.3.7. In addition, there was evidence of increased global transcriptional activity, together with enrichment of pathways associated with cellular proliferation (*CBFB, TCF7L2*), metabolism (mTOR signalling), and fibrotic signalling

4.3.3 Increased type 1 IFN regulatory network activity in alveolar barrier AMs from IPF lungs

Having first examined broader differences in macrophage transcriptional activity associated with IPF in Section 4.3.2, a targeted analysis was then performed to specifically investigate type 1 IFN related transcriptional activity in AM subsets at the epithelial barrier. This hypothesis-driven analysis was prompted by the enrichment of type 1 IFN associated gene sets and regulons identified in CXCL10^{+} AMs during the preceding unbiased analysis.

Mostafavi et al[282] curated a 'regulatory Interferon network' of transcription factors and their downstream target genes, derived from multiple mouse and human datasets by analysing transcriptomic expression at baseline and following type 1 IFN stimulation[282]. By measuring co-expression of known IFN regulators (including transcription factors, kinases and phosphatases) and downstream effector ISGs, regulator-downstream ISG target relationships were grouped into five regulatory modules.
These modules were functionally annotated based on the known effector functions of downstream ISGs; c1 and c2 (RNA processes), c3 (antiviral effectors), c4 (metabolic regulation, c5 (inflammatory effectors). Key regulators were also identified, notably that the Interferon Stimulated Gene Factor 3 (ISGF3) complex, comprising *STAT1, STAT2* and *IRF9* was identified as the principal regulator of gene modules c3 and c4. In contrast ISGs in modules c1 and c5 lacked the Interferon Simulated Response Element (ISRE) motif rather were associated with other regulators such as *KAT2B, TBK1, LYN* and *ETV6* [282].

Using SCENIC, regulon activity scores for type 1 IFN associated regulons defined by Mostafavi et al. were calculated, and Log2FC differences in regulon activity between IPF and HC AMs were compared (Figure 4.3.9).

Comparison of regulon activity scores between IPF and controls (Figure 4.3.9) revealed CXCL10^{+} AMs demonstrated the largest differences in type 1 IFN regulon activity in IPF consistent with the findings from the single gene and GSEA analysis, in addition, all other AM subsets also exhibited increased type 1 IFN associated regulon activity in IPF with the highest Log2FC values in FABP4^{hi} AM, IGF1^{+} AM.

Across AM subsets, upregulated regulons were predominantly associated with Mostafavi module c3 (antiviral processes) and module c5 (inflammatory effectors). A notable exception was ELF1 classified by Mostafavi in c2. However, *ELF1* has a broad ISG transcriptional profile and also known to specifically upregulate *OAS1*[283] a canonical c3 antiviral ISG.

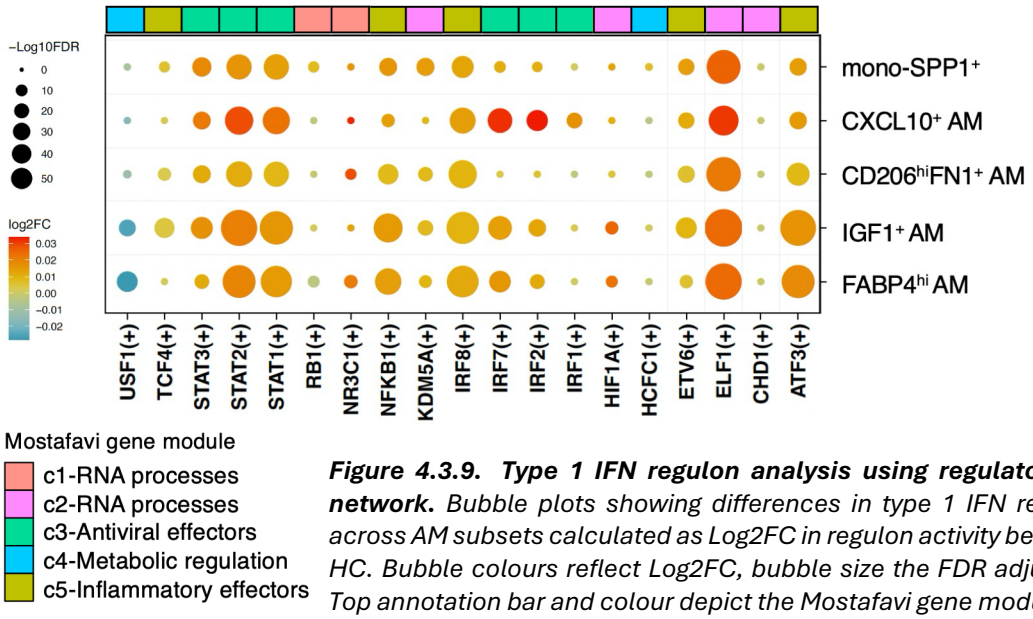


Figure 4.3.9. Type 1 IFN regulon analysis using regulatory Interferon network. *Bubble plots showing differences in type 1 IFN regulon activity across AM subsets calculated as Log2FC in regulon activity between IPF and HC. Bubble colours reflect Log2FC, bubble size the FDR adjusted p value. Top annotation bar and colour depict the Mostafavi gene module c1-c5.*

4.3.4. Single-cell RNA sequencing of lung digest identifies several monocyte and tissue macrophage subsets in IPF lung

Analysis of BAL macrophage subsets enabled in depth profiling of macrophage activity at the luminal side of the alveolar barrier in IPF but did not capture populations within the lung tissue. To address this, a publicly available scRNA seq dataset of lung tissue from patients with IPF undergoing transplantation and control donors was analysed[185]. The Morse dataset was selected for analysis because it enabled comparison of myeloid populations between early and advanced stage IPF and included histologically near normal control lung tissue.

Processed Morse scRNA seq data was obtained from the GEO repository GSE128033 and filtered using the same parameters applied to the BAL dataset to enable direct comparison. The dataset comprised 48,728 cells from 5 IPF LL samples, 3 UL samples and 4 healthy control samples. The Morse dataset included paired UL and LL samples from IPF patients to enable analysis of regional disease stage. Following initial clustering, 21,731 cells from myeloid populations (monocytes, macrophages, DCs and cycling macrophages) were identified based on marker expression and reclustered for downstream analysis (Figure 4.3.10).

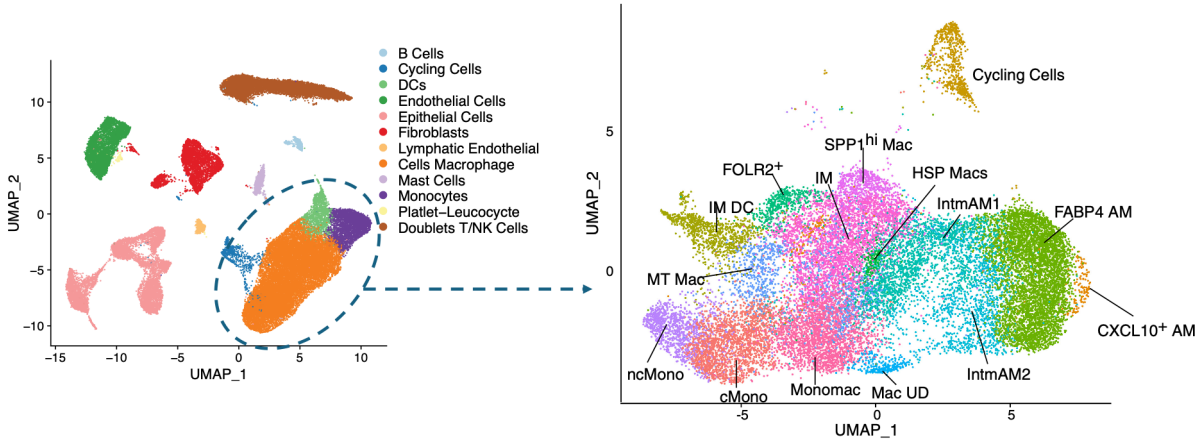


Figure 4.3.10. Single-cell RNA sequencing analysis of monocyte and macrophage populations in lung tissue. *Left panel – UMAP of all cell populations identified in lung tissue from publicly deposited lung tissue single cell dataset. Monocyte, macrophage DC and cycling cells identified and reclustered. Right panel – UMAP following re-clustering and annotation revealing 15 myeloid subsets. Abbreviations; IM – interstitial macrophages, MT metallothionine, US – undefined.*

Cluster annotation was informed using the same published lung macrophage reference datasets[141, 142, 156, 185, 263, 265] as those used for the BAL analysis, to provide a consistent annotation framework across analyses. Annotation was based on CDGs within the lung tissue dataset and was not constrained by the populations identified in the BAL study. Fifteen myeloid clusters were identified, comprising four AM subsets (FABP4 AM, Intm AM1, Intm AM2, CXCL10^{+} AM), seven tissue macrophage subsets (SPP1^{hi} mac, IM, FOLR2^{+} IM, HSP mac, MT mac, Mac_UD, Monomac), 2 monocyte subsets (cMono, ncMono), a DC subset and cycling cells (Figure 4.3.11). A full description of cluster annotation is detailed in (Appendix Table 4).

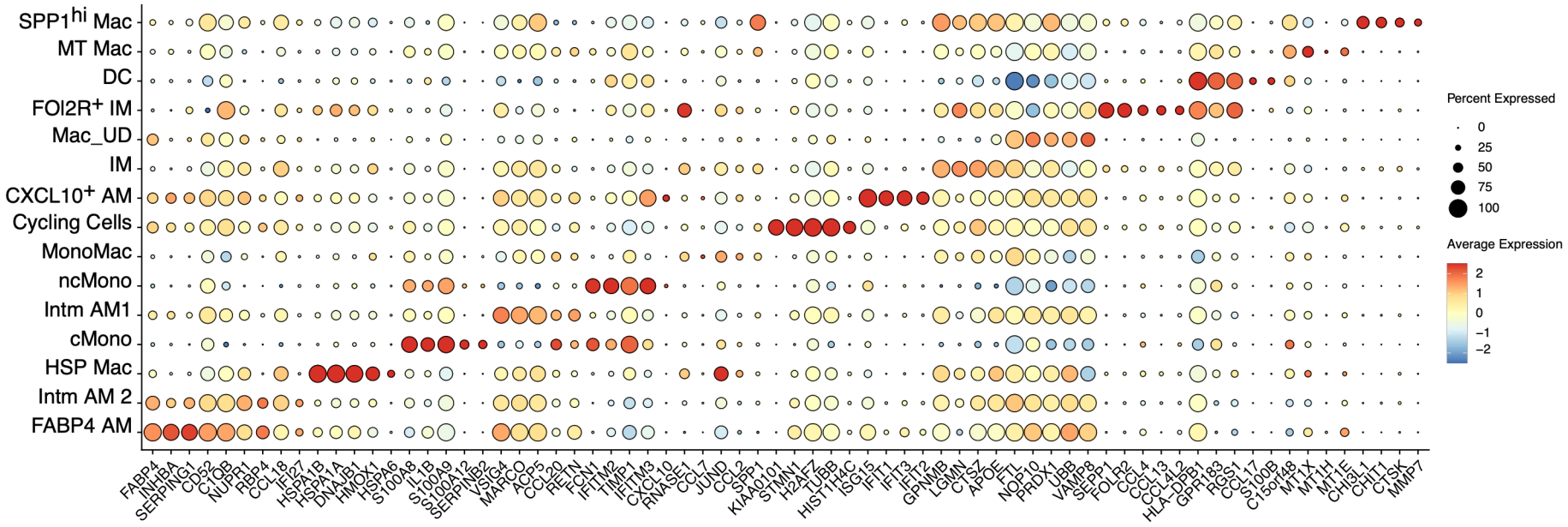


Figure 4.3.11. Fifteen distinct myeloid cell subsets identified. *Bubble plot showing the top 5 cluster-defining genes for each myeloid subset, relative to other subsets; bubble size represents the percentage of cells expressing each gene within the cluster, and colour indicates average gene expression. Abbreviations; MT metallothionine, US – undefined*

AM subsets were distinguished from macrophage tissue populations by expression of canonical AM marker genes - *FABP4*, *SERPING1*, *INHBA*, *CD52, RBP4* and *IFI27*.
Two clusters (IntmAM1, IntmAM2) exhibited low expression of these transcripts associated with the mature AM state and were felt to represent monocytes and macrophages progressively differentiating into AMs as the migrate into the alveolar space therefore labelled as 'Intermediate AM' subsets as described in a recent study[263].

Among tissue macrophage subsets, three clusters expressed markers associated with interstitial macrophages (IM)s including *LGMN, MARCKS, CPNMB, CTSB and C1Q* complement family transcripts[141].

One cluster showed high expression of *SPP1* alongside genes found in the SPP1+ macrophage subset previously described in IPF[62, 86, 184, 185] including *CHIT3L1, CHIT1, MMPs 7/9* and *PLA2G7*. This cluster was labelled SPP1^{hi} macrophages, reflecting higher SPP1 expression relative to other myeloid populations. One cluster expressed markers associated with IM 'subtype 1' including *FOLR2, F13A1, SLC40A1,* and was annotated FOL2R^{+} IMs[141]. Another cluster, labelled 'IM', expressed transcripts associated with interstitial macrophage 'subtype 2', including *SPP1* and *PLA2G7*, but at lower levels than SPP1^{hi} macrophages and without expression of additional fibrosis-associated genes such as *CHIT3L1, CHIT1, and MMP7/9*.

MT macs and HSP mac subsets expressed transcripts coding metallothionine metabolism and heat shock proteins respectively consistent with previously described populations[142, 156, 263, 264].

Two monocyte subsets were identified; classical monocytes (cMono) and non-classical monocytes (ncMono) that made up 10.1% of the entire lung digest myeloid population. In addition, a separate cluster expressed both monocyte and tissue macrophage-associated markers thus likely representing monocytes that were in the process of differentiating to tissue macrophages and were labelled 'Monomac'.

In the Morse dataset, the initial clustering resolved myeloid subsets observed in tissue, including monocytes, transitional differentiation states and IM subsets. However, the AM compartment was not resolved to the same level of transcriptional granularity observed in the BAL dataset. To further examine heterogeneity within the AM compartment, AM populations were subsequently reclustered to increase the resolution of transcriptionally distinct AM populations. Following reclustering, populations corresponding to the FABP4^{hi}, IGF1^{+} and CD206^{hi}FN1^{hi} AM subsets identified in the BAL dataset based on expression of characteristic marker genes and comparison with published reference datasets. (Figure 4.3.12).

Together, the BAL and lung tissue datasets provide complementary insights into lung macrophage biology in IPF. BAL sampling enabled high-resolution characterisation of discrete alveolar macrophage subsets, whereas lung tissue analysis incorporated a broader spectrum of myeloid populations, including interstitial and tissue-resident macrophages that are not accessible by BAL.

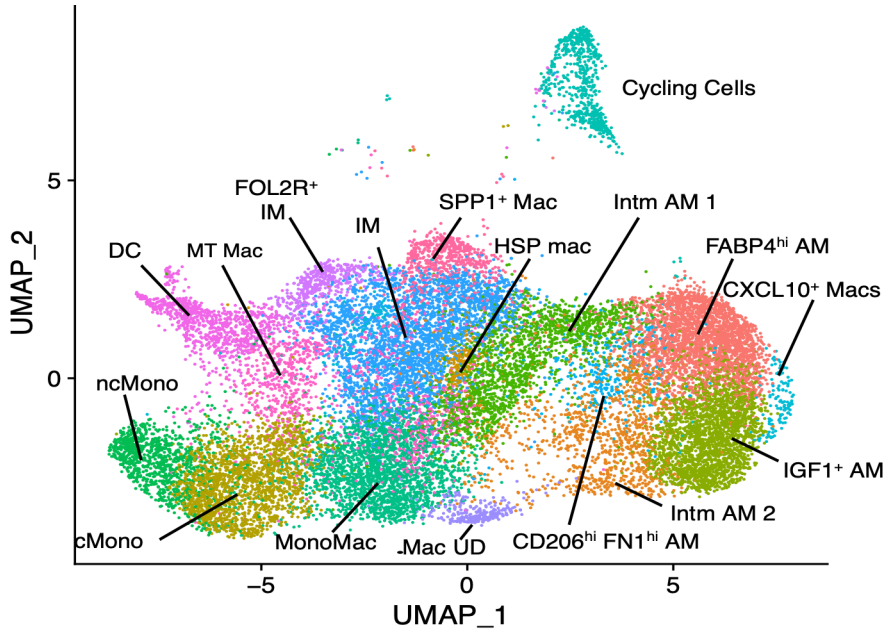


Figure 4.3.12. Further clustering of AM populations identified additional AM subsets seen in BAL. *UMAP of lung tissue myeloid populations after reclustering of AM subsets (FABP4 AM, Intm AM1, Intm AM2 enabled identification of IGF1+ and CD206hi FN1hi AM subsets. Abbreviations; MT metallothionine, UD – undefined.*

4.3.5 More advanced fibrotic states in IPF lung is associated with expansion of tissue macrophage subsets

In this section, differences in the composition and transcriptomic profile of myeloid cells were examined across early and late stages of IPF lung disease, represented using upper lobe (UL) and lower lobes (LL) biopsies of IPF lungs respectively, alongside healthy control samples. Digital H+E sections provided as part of the published Morse dataset were reviewed with a lung histopathologist experienced in interstitial lung disease. This confirmed UL sections were characterised by interstitial thickening with limited collagen deposition whilst LL tissue samples exhibited dense collagen deposition and lung tissue remodelling (Figure 4.2.1).

Comparative abundance testing was performed using SCCOMP which assess compositional differences in populations across multiple conditions[262] (Figure 4.3.13). This analysis identified significant differences in myeloid cell abundance in IPF LL

samples compared to controls. Specifically, there was an increase in tissue macrophage populations, including SPP1^{hi} macs, FOLR2^{+} IMs, and IMs. In contrast, the proportion of AM subsets was reduced, in particular the FABP4+ AM and Intm AM2 subsets.

Comparisons between IPF UL samples and controls showed less pronounced differences. A smaller number of tissue macrophage subsets were increased (SPP1^{hi} macs, IM and FOLR2^{+} IM) while no significant differences were observed in AM subsets.

Direct comparison between IPF LL and UL samples showed a pattern consistent with that observed between IPF LL samples and controls, with increased proportions of SPP1^{hi} macrophages and IMs and a decrease in AM subset in LL samples. These findings indicate that advanced fibrosis is associated with expansion of SPP1-expressing subsets alongside depletion of AM subsets (Figure 4.3.13).

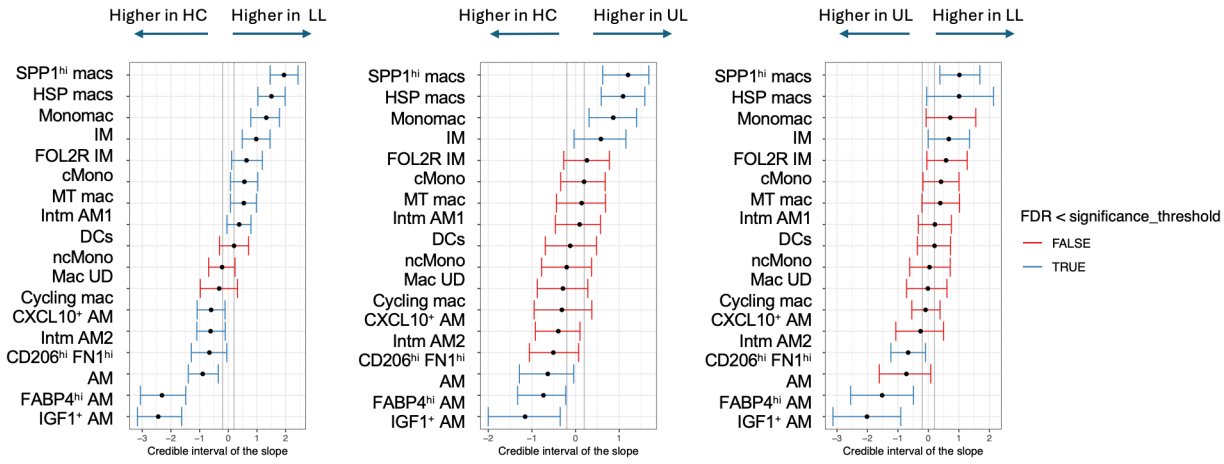


Figure 4.3.13. Differential abundance analysis of myeloid populations in IPF and control samples. *Bayesian differential abundance analysis was performed using SCCOMP to compare changes in abundance of each myeloid population (as a proportion of total myeloid cells). Left panel – comparison of abundance between IPF lower lobes and controls. Middle panel - IPF upper lobes and controls. Right Panel - IPF lower lobes compared to upper lobes. Statistical significance was assessed using posterior probabilities, and error bars represent 95% credible intervals. Significant differences are indicated in blue. Abbreviations; MT metallothionine, UD – undefined.*

4.3.6 - Advanced fibrosis is associated with activation of ECM remodelling and fibrotic pathways in macrophage subsets

In this section, differences in the transcriptome of monocyte and macrophage subsets in IPF disease states and control lung samples were compared using the Likelihood ratio testing (LRT).

LRT compares gene expression in two models, a full model that includes disease state as a factor and a reduced model where this factor is removed. Genes where the full model provides a significantly better fit—indicating that their expression varies across disease states—were identified as differentially expressed if they met the following criteria: likelihood ratio testing; adj p <0.05; fold change >1.5. Hierarchical clustering was the performed on the filtered gene list grouping DEGs into modules according to their expression patterns between controls and IPF disease states.

In seven macrophage populations (CXCL10^{+} AM, Intm AM2 FOLR2^{+} IM, FABP4 AM, HSP^{+} Mac, MT Mac and MonoMac) hierarchical clustering grouped DEGs into 2 gene modules, separating IPF samples (both UL and LL) from controls. (examples presented in Figure 4.3.14). In these modules, gene expression was consistently highest in IPF LL samples, followed by IPF UL samples and lowest in controls (Module 1 in Figure 4.3.14).

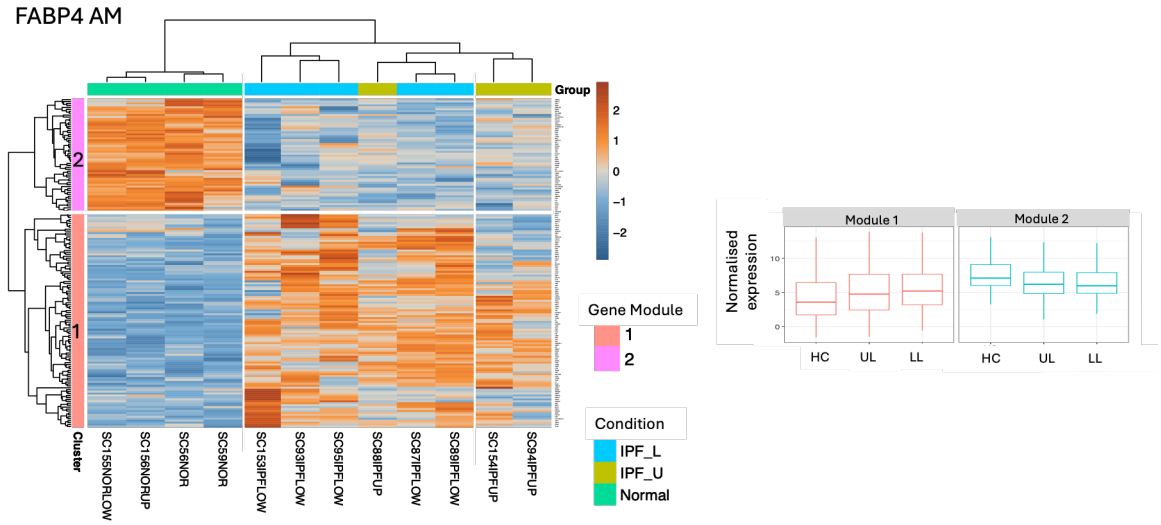


Figure 4.3.14. Likelihood ratio testing identifies two gene expression modules in seven myeloid populations (FABP4 AM shown as an example). *Heatmap showing differentially expressed genes (DEGs) identified using three-way LRT across IPF upper lobes, IPF lower lobes, and controls. Columns represent individual donor samples. For IPF donors, paired upper lobe (IPFUP refer to UL; early-stage disease) and lower lobe (LOW refers to LL; advanced-stage disease) tissue biopsies from the same donor are shown where available. In FABP4 AMs DEGs were grouped into two gene modules. Boxplots showing the aggregated median gene expression and 95% confidence intervals of genes within each module were used to assess differential of expression across conditions. In FABP4 $^{+}$AMs, gene module 1 comprises genes upregulated in both IPF disease states with higher expression in IPF LLs, while gene module 2 comprises genes downregulated in IPF, relative to controls. Column labels (e.g. "SC153IPFLOW") reflect original sample identifiers from Morse. Heatmap colour represents normalised gene expression (log2 fold change) across samples. On the heatmap the top annotation bar indicates experimental conditions, and the side annotation bar denotes gene module assignment. Abbreviations IPF_L – IPF lower lobe samples, IPF_U – IPF upper lobe samples, Normal – control samples.*

In contrast, five populations (cMono, ncMono, IM, SPP1^{hi} Mac and Intm AM1) exhibited greater transcriptional heterogeneity with DEGs grouped into 4 gene modules by hierarchical clustering. In these subsets gene expression patterns separated not only IPF from control samples but also between IPF UL and LL disease states indicating disease state specific transcriptional profiles (example presented in Figure 4.3.15 - cMono). Mac_UD, dendritic cell (DC) and cycling macrophage populations were excluded from downstream analyses because these clusters did not represent biologically discrete cell populations. The Mac_UD cluster lacked sufficient defining markers for confident annotation, the cycling macrophage cluster comprised proliferating macrophages originating from multiple macrophage subsets rather than a distinct biological population, and the DC cluster did not resolve into recognised dendritic cell subsets (cDC1, cDC2 or pDCs), instead representing a heterogeneous mixed population. Consequently, downstream analyses were restricted to well-defined macrophage subsets to ensure robust biological interpretation.

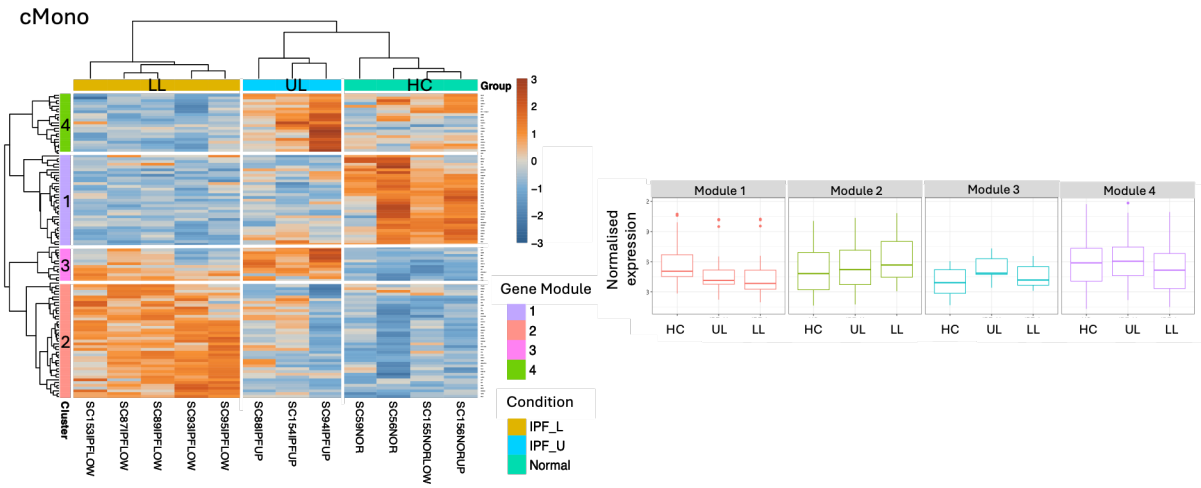


Figure 4.3.15. Likelihood ratio testing identifies four gene expression modules in five myeloid populations (cMono shown as an example). *Heatmaps showing differentially expressed genes (DEGs) identified using three-way LRT across IPF upper lobes, IPF lower lobes and healthy controls. Columns represent individual donor samples. For IPF donors, paired upper lobe (IPFUP refers to UL; early-stage disease) and lower lobe (IPFLOW LL; advanced-stage disease) tissue biopsies from the same donor are shown where available. In cMonos DEGs grouped into four gene modules. Boxplots showing the median expression and 95% confidence intervals of aggregated gene expression within each module and were used to assess differential expression across conditions. In cMono, gene module 1 comprises genes downregulated in both IPF disease states, while gene module 2 comprises genes upregulated in IPF with higher expression in LLs compared to lower lobes, Gene module 3 represents genes upregulated in IPF with higher expression in ULs. Abbreviations; IPF_L – IPF lower lobe samples, IPF_U – IPF upper lobe samples, Normal – control samples.*

To assess the biological relevance of DEGs within each gene module, PEA was performed using the REACTOME database[284]. Whilst regulon analysis was considered, biological interpretation of regulon activity requires detailed, context-specific evaluation of individual transcription factors. Given the large number of LRT derived gene modules identified across multiple myeloid populations, PEA was therefore considered the more

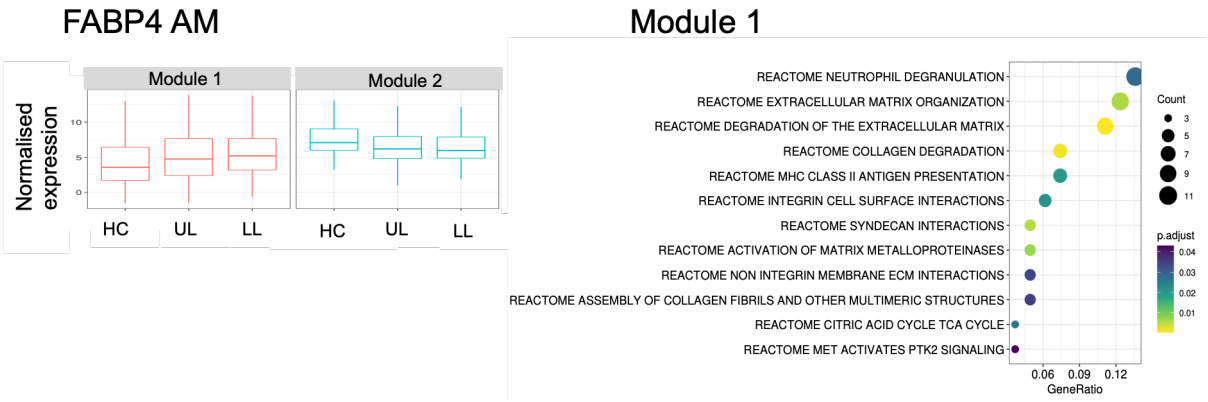
appropriate approach for summarising the biological processes associated with disease progression.

Gene modules showing highest expression in IPF LL samples (followed by IPF UL and controls) were investigated first to examine transcriptional programmes associated with advanced fibrosis. This included modules in all populations with two gene modules (Figure 4.3.16), and selected modules from populations with four modules; Intm AM2 - gene module 1, IM-gene module 2, SPP1^{+} Mac - gene module 1, cMono-gene module 2 and ncMono- gene module 1 (Figure 4.3.17).

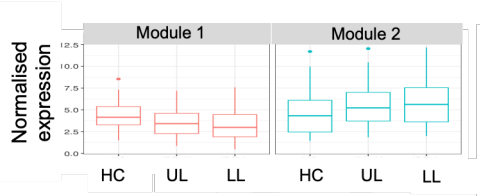
No pathways were identified by PEA in monocyte subsets (cMono, ncMono, MonoMac) for gene modules with highest expression in IPF LL samples.

All macrophage subsets, except CXCL10^{+} AMs and SPP1^{hi} macs, demonstrated upregulation of Reactome pathways terms - 'Extracellular matrix organisation', 'Cell extracellular matrix interactions', 'Assembly of collagen fibrils and other multimeric structures', 'Degradation of extracellular matrix', 'Collagen degradation', 'Activation of matrix metalloproteinases', indicating activation of cellular process involved in the formation, interaction with and degradation of ECM and collagen.

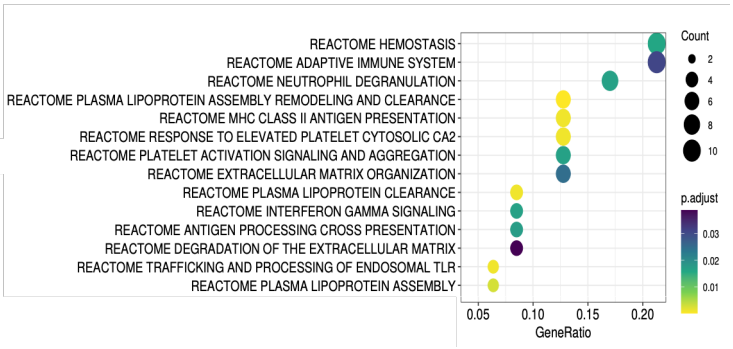
In addition, FABP4 AM, Intm AM1, Intm AM2, IM, HSP Mac and MT Mac subsets showed enrichment of 'Integrin cell surface interactions' and 'Syndecan interactions'. Integrin pathways regulate macrophage interactions with the ECM and fibrotic processes, including migration to sites of fibrosis, adhesion to the ECM, and promotion of TGF-β secretion and fibroblast activation[285, 286]. Syndecans cooperate with integrins to enable ECM-cell migration and adhesion and have been implicated in promoting[287] and restricting fibrosis[288].



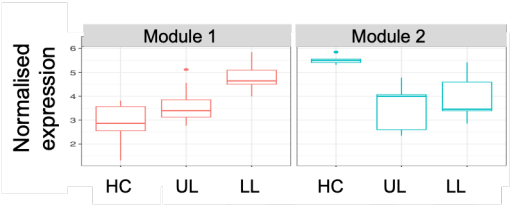
FOLR2⁺ IM



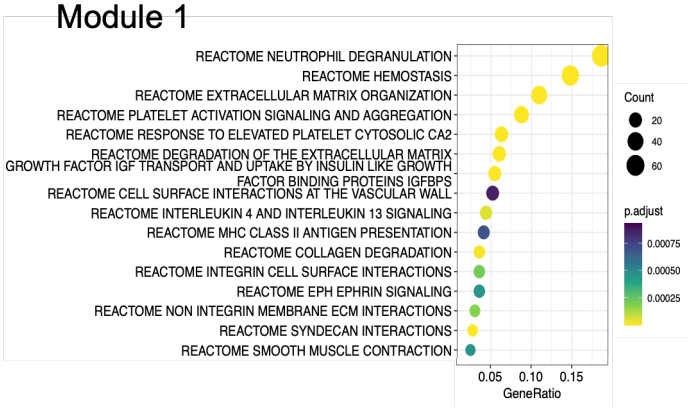
Module 2



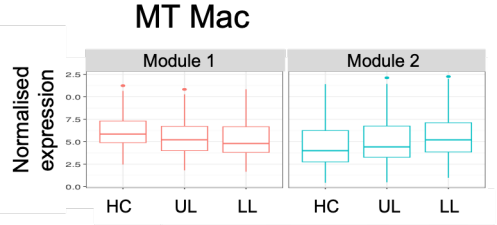
HSP⁺ Mac



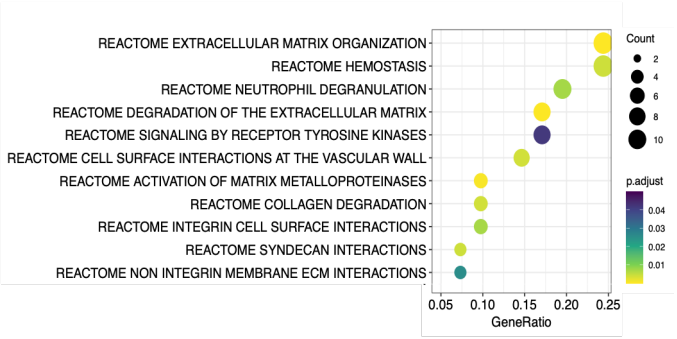
Module 1



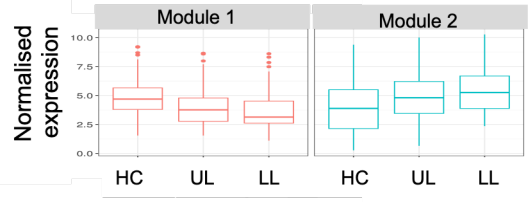
MT Mac



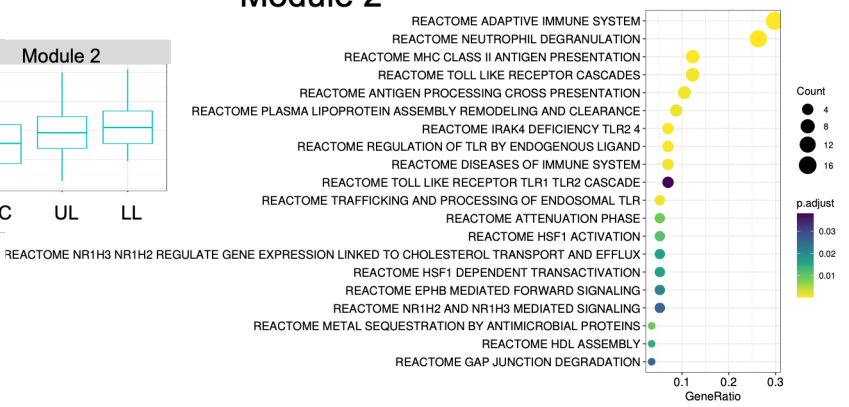
Module 2



CXCL10⁺ AM



Module 2



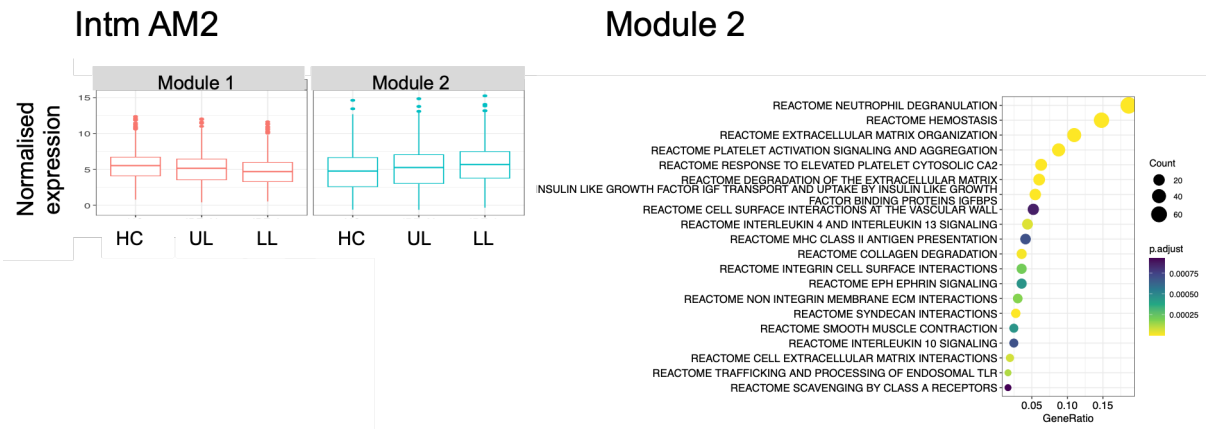


Figure 4.3.16. Pathway enrichment analysis of gene modules upregulated in IPF LL followed by IPF ULs. *Boxplots showing the median expression and 95% confidence intervals of aggregated gene expression within each module. Modules representing genes upregulated in IPF LL > IPF UL > HC highlighted with corresponding bubble plots pf pathway enrichment analysis. Enriched pathways were identified using Fisher's exact test, to assess genes over-represented in each pathway. The gene ratio (x-axis) represents the proportion of differentially expressed genes assigned to each pathway relative to the total number of differentially expressed genes. Bubble size reflects the number of differentially expressed genes within each pathway. Statistical significance was defined as FDR-adjusted p < 0.05.*

In contrast, CXCL10^{+} AMs and SPP1^{hi} macs did not show enrichment of ECM-related pathways. Instead, these subsets demonstrated upregulation of pathways associated with antigen processing and presentation, including 'Antigen processing and cross-presentation' and 'MHC class II antigen presentation', and TLR signalling

'MHC class II antigen presentation' was also enriched in additional subsets including FABP4 AM, Intm AM2 and FOL2R IM subsets. Additionally, pathways related to lipoprotein metabolism and cholesterol transport were also upregulated in CXCL10^{+} AM, Intm AM1, SPP1^{+} macs and FOL2R^{+} IM subsets as was observed in the BAL comparative analysis.

Finally, the pathway term 'Neutrophil degranulation' was enriched across all myeloid subsets. Although annotated as 'neutrophil degranulation', this pathway comprises genes involved in vesicle trafficking, lysosomal enzyme and protease secretion including matrix metalloproteases, which are release by neutrophils but also expressed by activated macrophages. This finding likely reflects increased secretory and tissue-remodelling activity in IPF myeloid populations.

Taken together, these findings demonstrate that in advanced IPF, macrophage subsets exhibit a shared transcriptional response characterised by increased ECM interaction, tissue remodelling and secretory activity, irrespective of their underlying transcriptional identity.

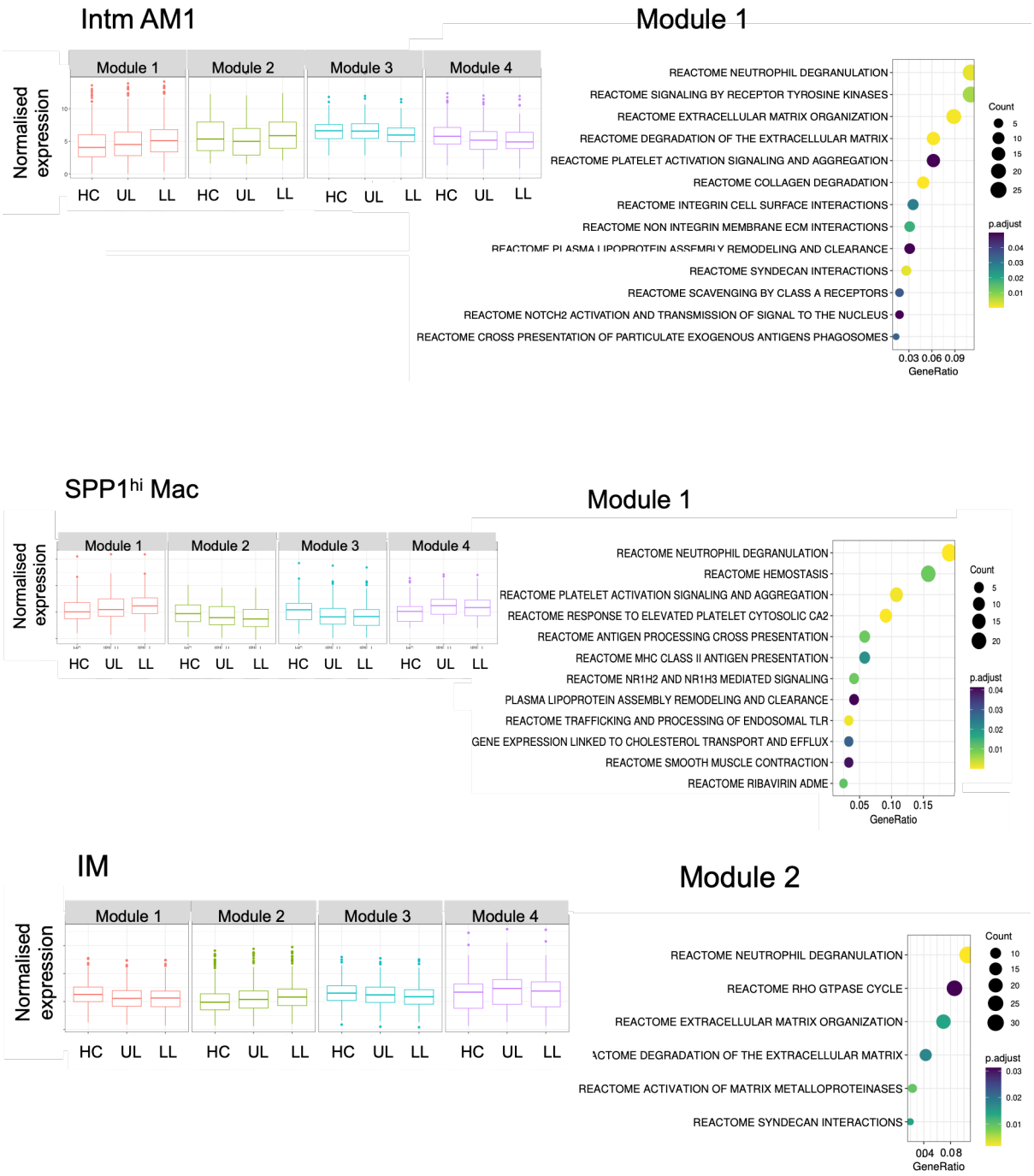


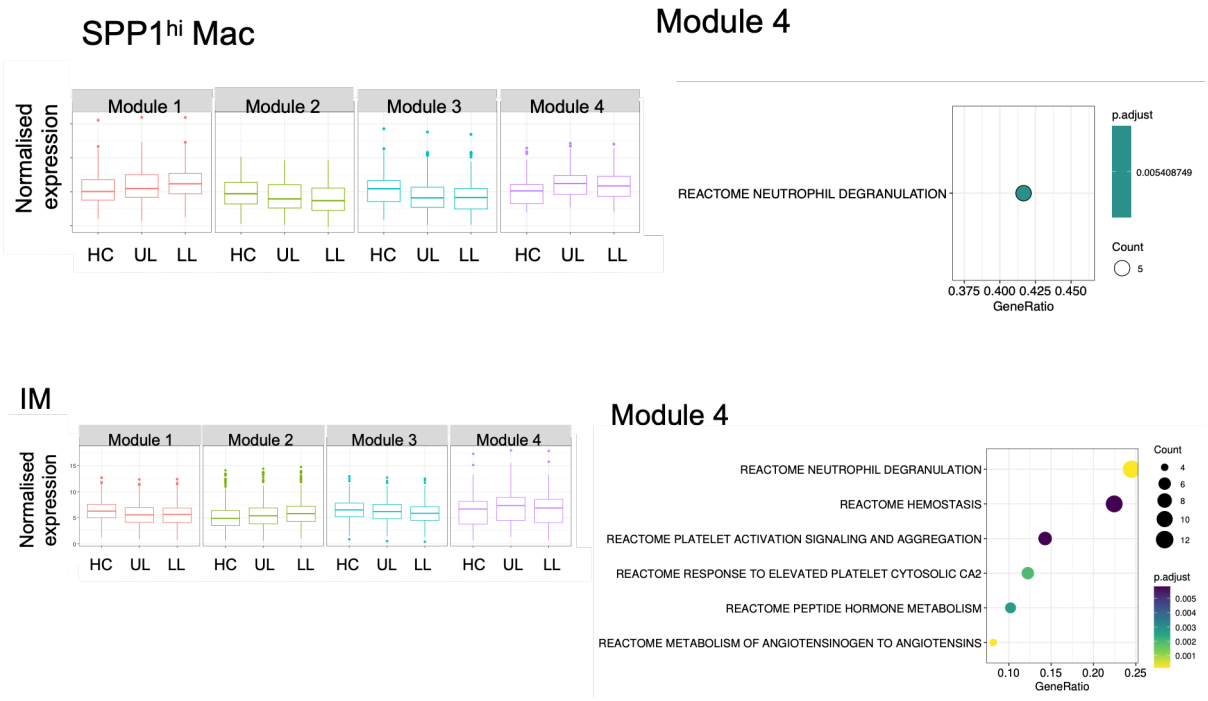
Figure 4.3.17. Pathway enrichment analysis of gene modules upregulated in IPF LL followed by IPF ULs in macrophage populations with 4 gene modules. *Boxplots showing the median expression and 95% confidence intervals of aggregated gene expression within each module. Modules representing genes upregulated in IPF LL > IPF UL > HC highlighted with corresponding bubble plots pf pathway enrichment analysis. Enriched pathways were identified using Fisher's exact test, to assess genes over-represented in each pathway. The gene ratio (x-axis) represents the proportion of differentially expressed genes assigned to each pathway relative to the total number of differentially expressed genes. Bubble size reflects the number of differentially expressed genes within each pathway. Statistical significance was defined as FDR-adjusted p < 0.05. Abbreviations; MT metallothionine, HC – healthy controls, LL – IPF lower lobe samples, UL – IPF upper lobe samples.*

4.3.7 Early disease is associated with increased interferon and cytokine signalling in lung monocytes and CXCL10^{+} AMs

Next, gene modules showing highest expression in IPF UL samples, followed by IPF LL and control samples, were examined to investigate myeloid transcriptional profiles associated with early disease. These gene modules included cMono- gene module 3, ncMono - gene module 3, IM - gene module 4 and SPP1^{hi} Mac - gene module 4.

PEA of these modules in SPP1^{hi} Macs and IM populations revealed pathways associated with neutrophil degranulation and platelet activation (Figure 4.3.18). In contrast, PEA of modules in cMono and ncMono subsets revealed enrichment of pathways associated with both type 1 and 2 IFN signalling as well as broader cytokine signalling including in IL-12 pathway activity (Figure 4.3.18).

In addition, gene module 4 in cMono demonstrated highest expression in IPF UL samples but reduced expression in IPF LL samples relative to controls, suggesting downregulation of these transcripts in advanced disease. PEA of this module identified pathways associated with PRR signalling and antigen signalling (Figure 4.3.18).



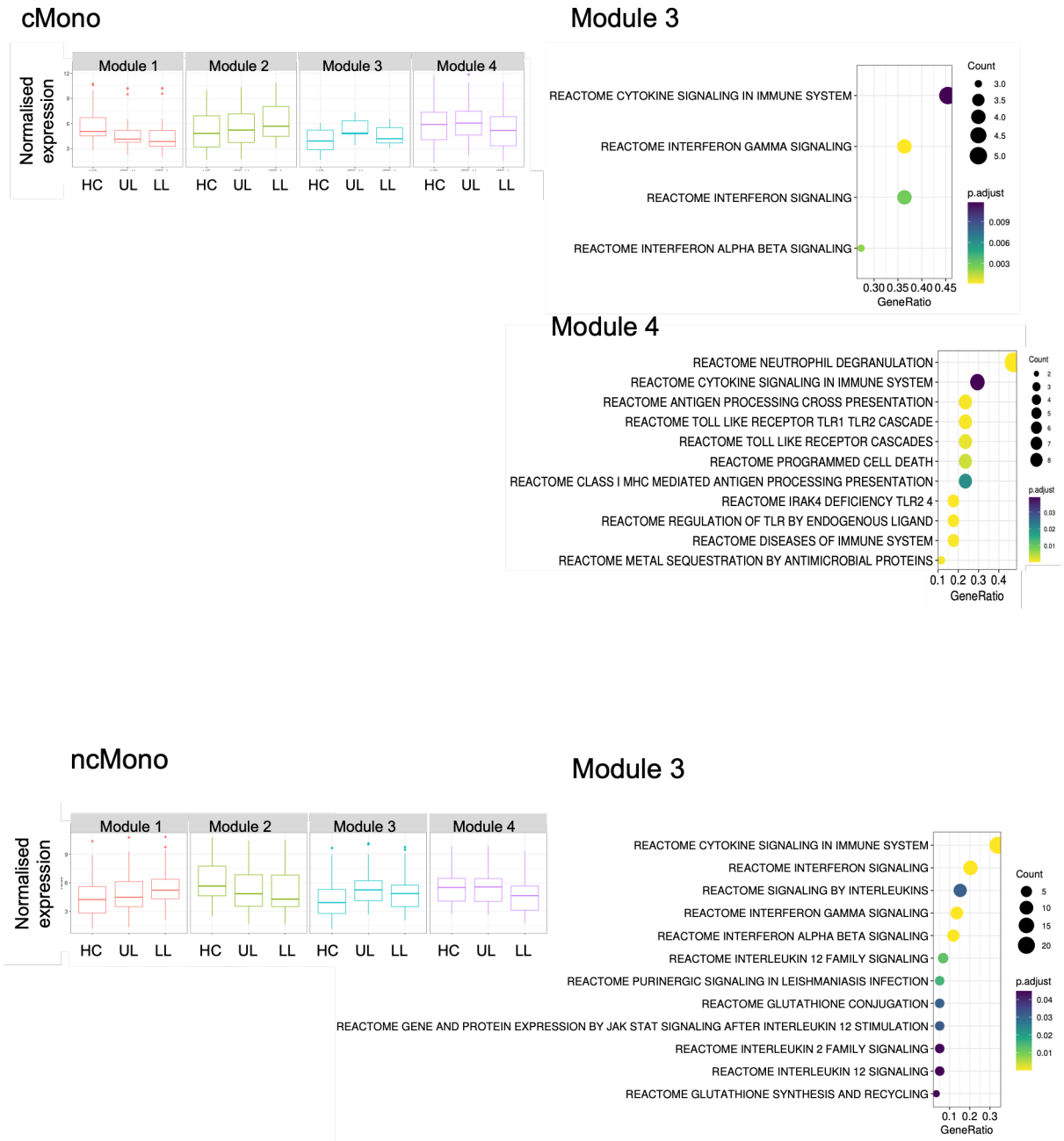


Figure 4.3.18. Pathway enrichment analysis of gene modules upregulated in IPF UL followed by IPF ULs. *Boxplots showing the median expression and 95% confidence intervals of aggregated gene expression within each module. Modules representing genes upregulated in IPF UL > IPF LL > HC highlighted with corresponding bubble plots pf pathway enrichment analysis. Enriched pathways were identified using Fisher's exact test, to assess genes over-represented in each pathway. The gene ratio (x-axis) represents the proportion of differentially expressed genes assigned to each pathway relative to the total number of differentially expressed genes. Bubble size reflects the number of differentially expressed genes within each pathway. Statistical significance was defined as FDR-adjusted p < 0.05.*

Given the increased IFN signalling observed in CXCL10^{+} AMs in the BAL transcriptomic analysis this population was further examined in the Morse tissue digest. In the LRT analysis DEGs in this subset were not separated for IPF UL and LL samples, instead hierarchical clustering grouped the IPF disease states together.

To directly or specifically examine if CXCL10+ AMs exhibit increased IFN signalling in early disease, pairwise DEG analyses were performed between IPF UL and control samples, and between IPF UL and LL samples (Figure 4.3.19 and 4.3.20). As the number of DEGs was small gene set enrichment analysis was performed using the hallmark database.

This analysis demonstrated enrichment of both type 1 and 2 IFN signalling in IPF UL samples compared with both control and IPF LL samples. In addition, CXCL10+ AMs in IPF ULs also showed upregulation of inflammatory pathways including IL-6 and TNF-α signalling compared to controls.

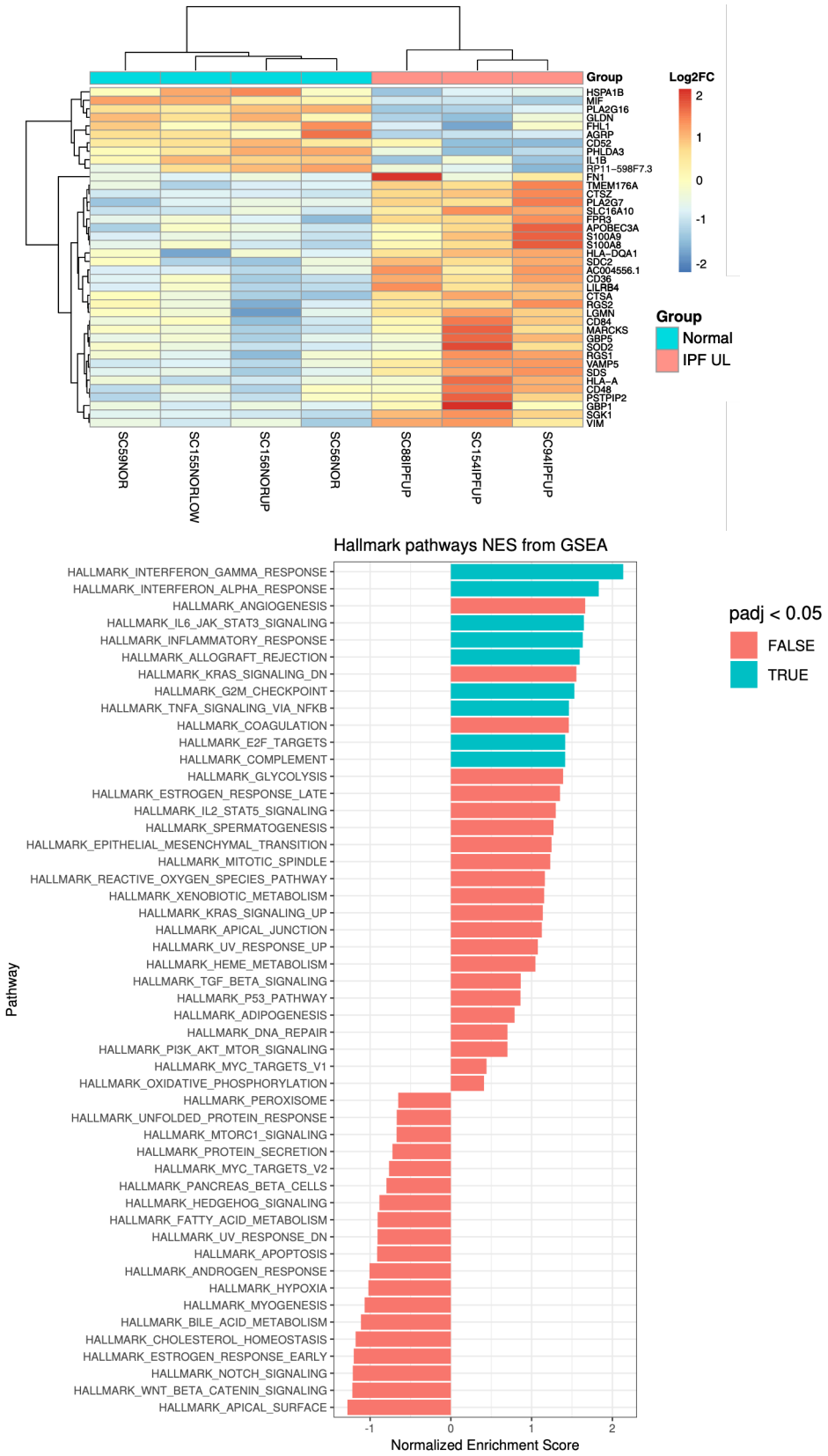


Figure 4.3.19. Differential gene and gene set analysis for CXCL10⁺ AMs upper lobes compared to healthy controls. *Heatmap showing differentially expressed genes for CXCL10⁺ AMs in lung tissue digest, comparing IPF UL samples to controls. Significant genes FDR q <0.1 and Log2FC>1.0 or < -1.0 Bar charts depicting gene set enrichment analysis (GSEA) using the Molecular signatures database 'Hallmark' collection. The x axis represents normalised enrichment scores (NES) positive score reflecting pathways enriched in IPF. Statistical significance of enrichment was assessed by permutation testing to generate a null distribution of enrichment scores, with correction for multiple comparisons. Abbreviations; GSEA – gene set enrichment score, NES – normalised enrichment score*

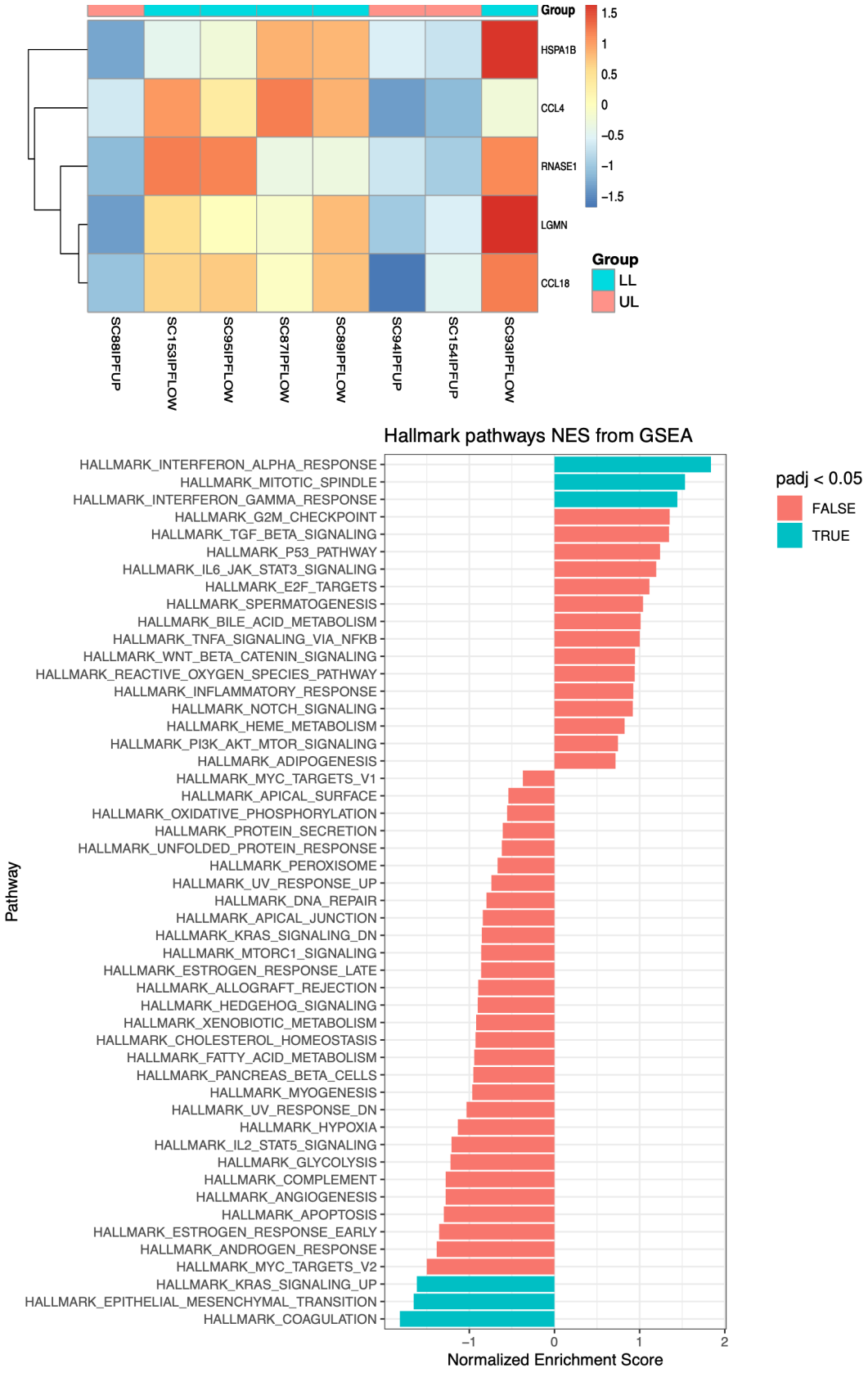


Figure 4.3.20. Differential gene and gene set analysis for CXCL10⁺ AMs upper lobes compared to IPF lower lobes. *Heatmap showing differentially expressed genes for CXCL10⁺ AMs in lung tissue digest, comparing IPF UL samples to controls. Significant genes FDR q <0.1 and Log2FC>1.0 or < -1.0 Bar charts depicting gene set enrichment analysis (GSEA) using the Molecular signatures database 'Hallmark' collection. The x axis represents normalised enrichment scores (NES) positive score reflecting pathways enriched in IPF. Statistical significance of enrichment was assessed by permutation testing to generate a null distribution of enrichment scores, with correction for multiple comparisons. Abbreviations; GSEA – gene set enrichment score, NES – normalised enrichment score.*

In conclusion, analysis of gene expression and pathway activity in IPF UL samples identified increased inflammatory and interferon signalling in early disease specifically within lung monocyte subsets and CXCL10^{+}AMs.

4.3.8 Circulating CD14^{+} monocytes exhibit increased ISG expression in early disease

The findings above indicate the lung environment in early IPF induces inflammatory and IFN signalling in infiltrating lung monocytes. I questioned if *circulating* monocytes may also exhibit increased IFN signalling or response to type 1 IFNs in early disease.

To investigate this, previously published basal ISG expression data from a previous study in the group by Fraser et al[181] was used. In the published study, basal ISG expression was measured by quantitative PCR in magnetic bead isolated CD14^{+} monocytes from PBMC samples. The present analysis extended the published dataset by retrospectively collecting clinical lung function measurements taken closest to the time of blood sampling and examined their relationship with the published basal ISG expression (Figure 4.3.21).

Expression of *STAT1*, *MX1* and *IRF7* in CD14^{+} monocytes showed a positive correlation with percentage predicted FVC, with similar trends observed across additional ISGs. These findings suggest that circulating monocytes exhibit higher basal ISG expression in early disease.

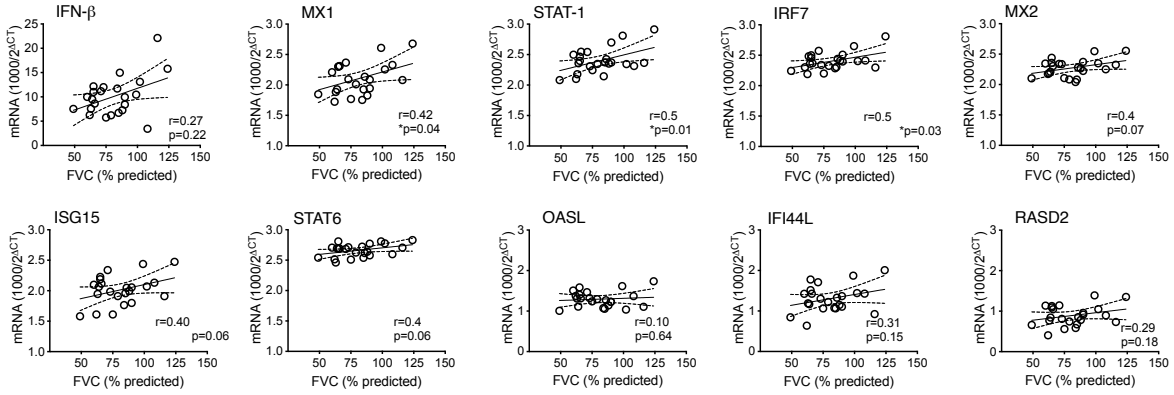


Figure 4.3.21. Correlation between type 1 IFN signalling genes expression in CD14^{hi} monocytes and lung function (FVC%) at point of blood sampling. *Correlation between patients forced vital capacity (percentage of predicted and CD14^{+} monocyte basal expression of interferon stimulated genes (ISGs) delta using qPCR. results were expressed as relative gene expression - delta log2 CT compared to GAPDH. Statistical significance was assessed using Pearson correlation analysis.*

4.4 Discussion

In this chapter, a comprehensive analysis of the lung macrophage compartment in IPF was performed using two single-cell transcriptomic datasets spanning the alveolar barrier and lung tissue. This approach enabled identification of distinct macrophage subsets and revealed compartment- and stage-specific transcriptional activity not previously described.

At the alveolar interface, discrete AM subsets (IGF1^{+}, CD206^{hi}, and CXCL10^{+}) exhibited increased inflammatory and type 1 IFN signalling in IPF compared to controls. In contrast, macrophages within lung tissue were characterised by enrichment of ECM organisation and fibrotic pathways[51, 57]. These findings align with current models of IPF in which epithelial injury drives aberrant repair and progressive fibrosis and support the concept that macrophage function is shaped by the local microenvironment.

Disease stage further influenced macrophage composition and activity. Advanced IPF was associated with expansion of interstitial and SPP1^{hi} macrophages and a convergence across macrophage subsets toward a shared fibrotic transcriptional programme, including pathways related to ECM remodelling and wound repair consistent with previous studies[86, 184, 185]. Notably, in this analysis, this transcriptional programme was observed in all macrophage subsets, indicating despite phenotypic heterogeneity, populations in advanced IPF converge on a shared fibrosis-associated programme driven by the local tissue environment.

A key finding was the identification of increased type 1 IFN signalling in IPF monocytes and macrophages. This was most prominent in CXCL10^{+} AMs at the alveolar barrier and enriched in early disease in lung monocytes and CXCL10^{+} AMs, with more limited expression in tissue macrophages. Regulon and pathway analyses indicated that AMs were primarily responding to, rather than producing, type 1 IFNs.

These findings, together with data from circulating monocytes (Chapter 3 and 4.3.8), suggest a continuum of type 1 IFN associated immune activation between the circulation and the lung. Although the alveolar macrophage phenotypes identified in this chapter cannot be directly confirmed by the PBMC CyTOF or scRNA seq analysis because these analyses examine distinct immune compartments, both datasets demonstrate enhanced type 1 IFN and inflammatory associated signalling. Therefore, it is plausible that circulating monocytes are 'primed' through transient exposure to type 1 IFNs within the pulmonary circulation, enhancing their responsiveness to subsequent stimulation. Within the IPF lung tissue environment continued exposure to IFN signals, appears to result in upregulation and activation of type 1 IFN responses. While IFN signalling persists across the disease course, the findings indicate type 1 interferon signalling is higher

during early stages of IPF, indicating IFN-mediated pathways may feature during disease initiation and progression

AM subsets in IPF also demonstrated increased inflammatory, metabolic, and proliferative activity, alongside upregulation of regulatory mechanisms, indicating a balance between activation and counter-regulation. Pathway analysis of transcripts upregulated in IPF, compared to controls revealed an increase in inflammatory signalling pathways in $IGF1^{+}$ AM, $CD206^{hi}FN1^{hi}$ AM and $CXCL10^{+}$ AM subsets indicating the net result of these opposing regulatory activities was inflammatory pathway activation. Notably, ECM-associated pathways were not enriched in BAL-derived AMs or lung monocytes, suggesting these populations adopt an inflammatory rather than directly profibrotic role.

In the lung tissue transcriptional analysis, unexpectedly, $SPP1^{hi}$ macs did not demonstrate enrichment of ECM related pathways despite their recognised association with fibrosis in IPF. One possible explanation is that $SPP1^{hi}$ macrophages represent a conserved transcriptional state that is present in both healthy and IPF lungs. IPF therefore appears to be characterised predominantly by expansion of this population, as observed in the abundance analysis, rather than an alteration of its core transcriptional programme. Consequently, LRT and pathway analysis within the $SPP1^{hi}$ population did not identify additional upregulation of ECM-related pathways, suggesting the transcriptional programme of this population is largely maintained in health. Despite the limited ECM-related transcriptional changes observed within the $SPP1^{hi}$ macrophage population in the present study, accumulating evidence supports a profibrotic role for these cells across multiple fibrotic diseases including cardiac, renal and liver fibrosis[289, 290], in addition to lung fibrosis[43, 290]. Experimental studies have demonstrated that SPP1-expressing macrophages promote fibroblast activation, extracellular matrix deposition and fibrosis through multiple mechanisms[257, 286], with depletion or inhibition of these populations reducing fibrosis in both pulmonary and extrapulmonary models[43, 289, 290]. These observations suggest that the pathological contribution of $SPP1^{hi}$ macrophages may relate more to expansion of this macrophage state and interactions with surrounding structural cells than to additional transcriptional activation of ECM pathways within the population itself.

The lung tissue analysis did also reveal widespread expression of ECM-remodelling programmes across the remaining macrophage populations. This finding raises questions about whether $SPP1^{hi}$ macrophages represent a distinct subset or a context-dependent activation state. This also highlights limitations of clustering-based approaches, which may overemphasise discrete populations rather than shared transcriptional programmes. Emerging gene programme–based methods may better capture these shared states and would complement clustering to identify transcriptional profiles shared across cell subsets[291, 292].

Whether macrophage IFN and inflammatory signalling actively contribute to fibrosis or reflect responses to tissue injury remains unresolved. While increasing evidence supports a profibrotic role for SPP1^{hi} macrophages, the role of IFN signalling in fibrogenesis is less clear and warrants further investigation.

This study has several limitations. Regional sampling was used to approximate disease stage despite knowing spatial heterogeneity in IPF. Future studies incorporating spatial transcriptomics and larger cohorts will be important to refine these findings. In addition, publicly available single-cell RNA sequencing datasets provide access to human tissue from diseases such as IPF that are otherwise difficult to study. However, secondary analyses can be limited by the demographic and clinical metadata reported by the original study. Consequently, potentially relevant variables, including smoking history, ethnicity, comorbidities, medication and respiratory infections, if unavailable or incompletely reported, limit the extent to which these factors can be considered during analysis and interpretation. Although participants in the BAL cohort were clinically screened for these clinical factors and symptomatic respiratory infection was excluded at the time of bronchoscopy, subclinical or early infection cannot be completely excluded. Equivalent clinical information was not available for the publicly available lung tissue datasets although histologically normal appearing lung tissue, confirmed by sequential H+E sections in the Morse dataset does provide some reassurance that overt inflammatory of infective pathology was absent.

A limitation of the transcriptomic analyses presented in this chapter is the relatively small number of donors included in both the BAL and lung tissue datasets. As IPF is a heterogeneous disease, inter-donor variability is likely to contribute to differences in both cell abundance and gene expression, and larger cohorts will be required to distinguish donor-specific from disease-associated effects with greater certainty. To help mitigate this limitation, complementary BAL and lung tissue transcriptomic datasets were analysed to determine whether key observations were reproducible across independent cohorts.

4.5 Conclusion

In this chapter, single-cell analysis of lung monocyte and macrophage populations across compartments and disease stages in IPF identified several previously undescribed features. Most notably, inflammatory cytokine and type 1 IFN signalling were increased in monocyte and macrophage subsets, localised to the alveolar epithelial barrier and most prominent in early disease.

These findings highlight substantial macrophage heterogeneity in IPF. However, despite this diversity, macrophage subsets in advanced disease converge on a shared transcriptional programme associated with extracellular matrix remodelling, reflecting the influence of the fibrotic microenvironment. In parallel, inflammatory and type 1 IFN signalling persists at the alveolar interface, suggesting spatially and temporally distinct roles for myeloid populations in IPF pathogenesis.

Integration with findings from the previous chapter suggests that circulating monocytes are primed for type 1 IFN responses prior to lung entry, with further activation occurring within the pulmonary environment.

The drivers and functional consequences of myeloid type 1 IFN signalling remain unclear. In particular, it is not yet established whether these inflammatory programmes contribute directly to fibrogenesis or represent responses to ongoing tissue injury. Addressing these questions will be important for defining the role of myeloid cells in IPF and is explored in subsequent chapters.

Chapter 5 Spatial context of type 1 IFN–activated monocytes and macrophages in IPF lungs

5.1 Introduction

In the previous chapter, increased type 1 IFN signalling was identified within discrete subsets of monocytes and macrophages in idiopathic pulmonary fibrosis (IPF). However, the local microenvironmental factors associated with the emergence of this phenotype remain unclear. In this chapter, monocytes and macrophages, together with their surrounding cellular neighbourhoods, are profiled within IPF lung tissue using imaging mass cytometry (IMC), with the aim of defining the spatial context that both drives and is influenced by type 1 IFN–activated myeloid states.

I hypothesise that dysfunctional epithelial states at the alveolar barrier act as a proximal driver of type 1 IFN activation in neighbouring monocyte and macrophage populations.

Current understanding of IPF pathogenesis (outlined in Section 1.2) centres on recurrent microinjury to vulnerable alveolar epithelial cells, leading to epithelial dysfunction, localised inflammation, and impaired regeneration in early disease. Sustained and dysregulated wound-healing responses subsequently promote persistent fibroblast activation, differentiation, and progressive extracellular matrix deposition, resulting in irreversible architectural lung distortion[51, 57].

These pathological processes are reflected histologically. Alveolar epithelial cell (AEC) injury and inflammation are observed as alveolitis on haematoxylin and eosin (H&E) staining, fibroblastic foci represent sites of active fibrogenesis, and dense collagen deposition together with smooth muscle hyperplasia define established fibrosis. Integration of histopathological classification with spatial profiling techniques such as IMC enables immune cell distributions to be examined across well-defined tissue niches and disease stages. This approach has recently been applied within our group to map cellular organisation across the spectrum of IPF pathology[225].

Findings from the previous chapter demonstrated increased type 1 IFN signalling within macrophage subsets localised to the alveolar barrier, particularly in early disease, suggesting a potential association between interferon activation and epithelial dysfunction. This raises the possibility that epithelial-derived signals contribute to the emergence of type 1 IFN-activated myeloid states.

Recent single-cell transcriptomic studies have provided further insight into epithelial heterogeneity in IPF. Under homeostatic conditions, type II alveolar epithelial (AT2) cells function as progenitors, differentiating into type I alveolar epithelial (AT1) cells to

maintain epithelial integrity and facilitate gas exchange. In murine models of lung injury and fibrosis, this differentiation process is accompanied by the emergence of transient intermediate epithelial populations expressing cytokeratins such as *KRT5, KRT7, KRT8,* and *KRT17*, typically associated with airway basal cells[293, 294, 295, 296]. Similar populations have been identified in human IPF tissue and described as $KRT5^{-}KRT17^{+}$ epithelial cells[63] (or aberrant basaloid intermediates (ABIs)[86] with transcriptional profiles closely resembling those observed in experimental injury models[293,297].

The expansion of these intermediate epithelial populations in IPF, together with the depletion of mature AT2 and AT1 cells and their localisation to regions of bronchiolisation, suggests a failure of normal AT2-to-AT1 differentiation. Consistent with this interpretation, persistent inflammatory signalling, sustained TGF-β activity, or repetitive injury promotes the accumulation of these transitional states and prevents terminal differentiation [294, 296, 297].

These intermediate and aberrant epithelial states share a common transcriptional phenotype characterised by cellular stress, mitochondrial dysfunction, DNA damage, and senescence[295]. Such stress responses can lead to the release of damage-associated molecular patterns (DAMPs), which activate pattern-recognition receptor (PRR) pathways[59]. Several PRRs—including the cGAS–STING pathway—are capable of inducing type 1 interferon and have been implicated in chronic inflammatory and age-related diseases[298, 299]. These observations provide a mechanistic basis by which epithelial dysfunction may initiate local interferon signalling within the lung microenvironment.

Previous IMC-based work from our group demonstrated that regions of alveolar epithelial metaplasia correspond to areas enriched for dysfunctional epithelial states, including ABIs[225]. In that study, spatial analytical approaches were developed to identify cell populations that co-localise within these abnormal regenerative niches, providing a framework to investigate cellular interactions in situ.

Building on these observations, this chapter aims to define the spatial relationship between type 1 IFN–activated myeloid cells and epithelial pathology in IPF. To achieve this, an IMC antibody panel was designed to identify major structural and immune cell populations, together with functional markers to capture dysfunctional AT2 states, intermediate epithelial populations, and type 1 IFN-activated myeloid subsets. Histologically defined regions of interest (ROIs) were selected to represent the full spectrum of IPF pathology, enabling analysis across disease stages. Spatial analysis methods were then applied to determine which cell populations co-localise with type 1 IFN–activated monocytes and macrophages, and to define the microenvironmental contexts in which these states arise.

5.2 Study Design and Methods

5.2.1 IPF lung biopsy donor selection, clinical and radiological characteristics

Patients who had undergone a surgical lung biopsy as part of their clinical diagnostic assessment for interstitial lung disease (ILD) that subsequently received a diagnosis of IPF after specialist ILD MDT review were identified. Diagnostic haematoxylin and eosin (H+E) stained tissue sections were reviewed by Prof Ho and a senior thoracic pathologist with experience in interstitial lung disease to confirm a usual interstitial pneumonia (UIP). Histological review was combined with radiological Lung tissue samples from 7 patients were included in this study. Participants were recruited under regional ethics service approved study; REC 14/SC/1060. Patient clinical, radiological and pathology details summarised in Table 3.2.1. The study was designed to investigate the spatial organisation and co-localisation of type 1 IFN-activated macrophages within IPF lung tissue, rather than to compare immune cell composition between healthy and diseased lungs. Consequently, the analysis focused on spatial relationships across regions representing different stages of IPF progression. Direct comparison with healthy lung tissue was also considered less informative because of the substantial architectural differences between normal and fibrotic lung, which complicate interpretation of spatial relationships. Although inclusion of healthy control tissue may have provided additional contextual information, access to appropriately matched healthy human lung tissue suitable for IMC is also limited.

5.2.2 Experimental workflow

The experimental workflow is outlined in Figure 5.2.1 with key methodological steps outlined below. Validation of antibody specificity is described in Sections 2.1.7 and 5.3.1. Region of interest (ROI) selection is described in section 5.3.2.

The final antibody panel selected for this study is detailed in Figure 5.2.2. The panel included ‘phenotyping’ markers used to identify cell populations together with ‘functional’ markers to characterise alveolar epithelial cell dysfunction seen in IPF including alveolar cell injury (ICAM1), senescence (p53, p16) and inflammatory phenotypes. In addition, markers relating to type 1 IFN production (pSTING and IFN-β) and downstream of interferon alpha receptor (IFNAR) signalling (pSTAT1, pSTAT2, ISG15, IFIT3 and CXCL10) to identify cell types that may act as potential producers or responders of type 1 IFNs.

Selection of the IMC antibody panel was guided by the primary aim of defining the spatial relationship between type 1 IFN activated myeloid cells and epithelial pathology in IPF within the technical constraints of a 40-antibody panel. Priority was therefore given to

markers required for identification of the major immune and structural cell populations together with functional markers of epithelial dysfunction and type 1 IFN signalling. Consequently, inclusion of additional lineage-defining markers required prioritisation according to the primary study objectives, limiting the extent to which more refined annotation of structural, lymphoid and myeloid cell populations, including IM subsets and adjunct markers for AMs, could be achieved.

Selection of epithelial markers was informed by both the original transcriptomic descriptions of aberrant basaloid cells[63, 86] and more recent studies describing transitional alveolar epithelial states during regeneration and fibrosis[293, 294, 295, 297, 300]. Although KRT17 is commonly included in transcriptomic definitions of aberrant basaloid cells, it was not incorporated into the IMC panel. Instead, KRT8 was selected in combination with KRT5, SFTPC, SCEL and markers of epithelial injury and senescence, as this marker combination was considered sufficient to identify ABI epithelial populations and more recent studies describing $KRT8^{+}$ transitional epithelial states. Annotation was subsequently supported through comparison with published transcriptomic reference datasets, including Habermann et al[63]., together with more recent protein-based characterisation of alveolar epithelial states including ABIs by Kathiriya et al[300]., which integrated both transcriptomic and protein expression data.

Although markers were categorised as phenotyping or functional markers according to their primary intended use, some markers, including CXCL10, contributed to both cell identification and functional characterisation. CXCL10 was included within the phenotyping panel during myeloid cell reclustering to facilitate identification of the $CXCL10^{+}$ macrophage population described in the single-cell RNA sequencing analysis in Chapter 4. As CXCL10 is also an ISG, its expression was additionally evaluated alongside other markers of type 1 IFN signalling as part of the functional assessment of type 1 IFN activation. The potential influence of CXCL10 on cluster assignment, was assessed by performing clustering of the myeloid population with or without CXCL10 (Section 5.3.6).

Following staining, tissue sections were ablated using the Hyperion Imaging System in balanced batches over 72 hours, with each batch including ROIs representing early, intermediate, and advanced disease to minimise batch effects. During data acquisition, 1 mm^2 regions are sequentially ablated, releasing ionised metal-tagged antibodies, which are then quantified by time-of-flight mass cytometry. Individual regions containing spatial coordinates and marker expression data are then reconstructed into high-dimensional images as mass cytometry data (MCD) files that can be visualised using MCD Viewer software.

Antibody performance and marker expression was then re-assessed by visual inspection of each marker using the same criteria applied to antibodies during selection (described in Section 2.1.7 and 5.3.2).

5.2.3 Analysis of imaging mass cytometry data

Downstream processing of expression data was performed using the Spatial Omics OXford (SpOOx) analysis pipeline[225,301], developed by Prof. Ho and members of the group, which integrates cell segmentation, dimensionality reduction, clustering, and spatial analysis. Cell segmentation was performed using the Mesmer framework in DeepCell[302] which uses nuclear markers to identify cells and cytoplasmic and cell membrane markers to define the shape of each cell and cell boundaries. Markers selected for input into DeepCell were chosen if they fulfilled the following criteria (i) specific localisation to nuclei or cytoplasm, (ii) high signal expression combined with iii) low non-specific or diffuse background staining of acellular regions of tissue. The following markers were used as input; for nuclear staining (DNA, ki67), and for cytoplasm/membrane staining (CD116, CD14, CD15, CD16, CD1c, CD20, CD206, CD3, CD31, CD4, CD8, CD45, CD68, EPCAM, HLADR, IFIT3, KRT8, ProSPC, SCEL, αSMA). Cell segmentation results in the generation cell masks, which were visually inspected against cell and nuclear boundaries in corresponding MCD images to assess the accuracy of segmentation. Particular attention to regions of tissue with high cell destiny i.e. lymphoid aggregates and areas of tissue containing cells were irregular morphology for example at the alveolar barrier and intimal aspects of blood vessels containing thin AT1 and endothelial cells respectively.

Following segmentation marker expression data was arcsinh-transformed (co-factor 5) and a single cell matrix was generated with cells in rows and corresponding spatial data (x,y coordinates) and marker expression in columns to enable downstream analyses analogous to single-cell datasets. Clustering was performed using the phenograph clustering algorithm and clustering strategy adopted to address the study objectives as detailed in Section 5.3.3. In brief initial cell clustering was performed to identify major cell populations followed by re-clustering of epithelial and myeloid compartments to resolve discrete cell subsets and states. Following re-clustering and annotation, updated cell-type labels were mapped back onto the full dataset derived from the initial clustering, enabling spatial analyses to be performed across all cell populations.

Spatial relationships between pairs of cell populations were analysed using select tools developed in SpOOx. The cross-pair correlation function (cross-PCF) was used to identify cells populations that are preferentially co-localised within a defined radius of

an anchor population. In addition, adjacency cell network (ACN) and contacting cell network (CCN) analyses were used to identify networks of cell populations in direct physical contact. These methods enable identification of cell population pairs that are preferentially co-localised and in direct physical contact within tissue than what would be observed above complete spatial randomness. Detailed descriptions of these spatial analyses are provided in Sections 5.3.8 (cross-PCF) and 5.3.9 (ACN/CCN).

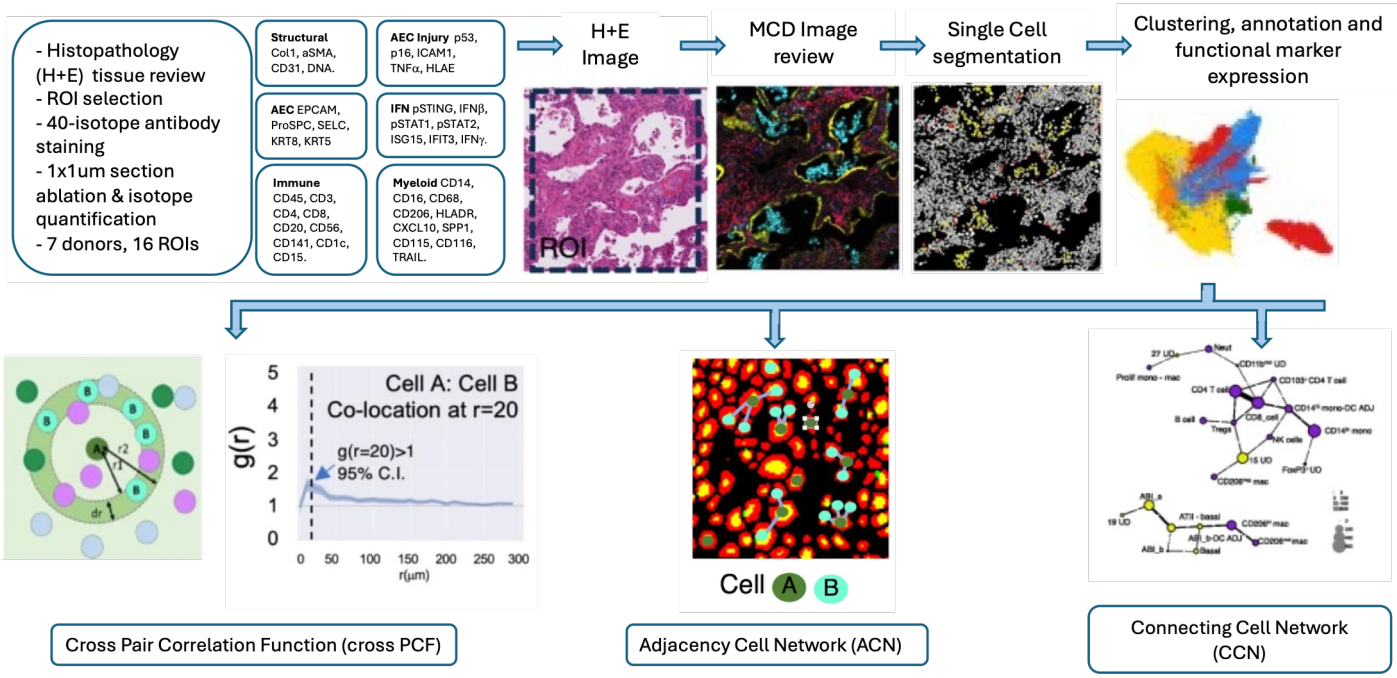


Figure 5.2.1. Experimental overview. *Schematic outlining the main steps from patient and region of interest (ROI) selection, antibody panel design, single cell segmentation, clustering and annotation through to spatial* ***Abbreviations:*** *MCD, mass cytometry data.*

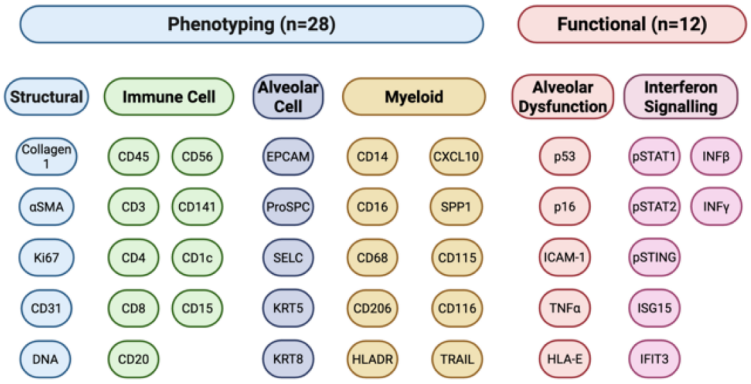


Figure 5.2.2. Antibody panel overview. *Schematic of the antibody panel used in this study. Phenotyping markers were included for initial cell clustering, while lineage-specific markers were used for targeted re-clustering of epithelial and myeloid populations.*

Hyperion Sample ID	Histopath ID	Block Chosen	Age	Sex	Race / Ethnicity	Comorbidities	Medication	Clinical Histopathology Conclusion	ILD MDT Diagnosis	ATS (Pathology)	ATS (Radiology)	ATS Summary
IPF_Sample_1	5514/14	2B	75	M	British / Caucasian	AvR, CVA	Bisoprolol, Ramipril	In keeping with usual intertsitial pnuemonia	IPF	Definite	Probable	IPF Definite
IPF_Sample_3	16506/16	2B	60	M	Other - Not stated	Ex Smoker, Mould exposure, Anxiety, Dysfunctional breathing, Prev Hep C infection	Nil	The features are entirely consistent with UIP pattern of fibrosis with focal honeycombing is seen.	IPF	Definite	Alternatnative	IPF likely
IPF_Sample_4	22926/17	2A	75	F	British / Caucasian	Glaucoma, Osteopenia, Hypothyroidism, OA, Cataracts, Diverticular disease, Raynauds	Levothyroxine, Calcium, Statin	The features are those of a usual interstitial pneumonia (UIP) pattern of fibrosing lung disease."	IPF with atypical Fx	Probable	Indeterminate	IPF Likely
IPF_Sample_5	6518/16	2A	71	M	Other - Not stated	Emphysema, Positive aspergillus precipitens	Lansoprazole	the features are in keeping with usual interstitial pneumonia.	Working diganosis IPF	Definite	Alternative	IPF Likely
IPF_Sample_7	18480/16	2C	82	M	British / Caucasian	AvR, CABG, Asbestos exposure, Ex smoker	Aspirin, Statin, Tamsulosin, Duloxetine	The features are those of a usual interstitial pneumonia (UIP) pattern of fibrosing lung disease.	IPF	Probable	Definitie	IPF Definite
IPF_Sample_8	38353/14	2C	74	M	Other - Not stated	HTN, Asthma, OA, Ex smoker	Lansoprazole, Losartan, Seretide, Salbutamol, Uniphyllin	Lower lobe and upper lobe biopsies, in keeping with usual intertsitial pnuemonia	IPF	Definite	Probabale	IPF Definite
IPF_Sample_9	52276/16	1Da	86	F	British / Caucasian	MI, PMR, cataracts, gastritis	Lansoprazole, Ramipril, Levothyroxine, Aspirin, Ranitidine, Fultium D3, Amitriptylline	Usual interstitial pneumonia	Mild IPF	Definite	Probable	IPF Definite

Table 3.2.1 - Demographic details of IPF patients used in imaging mass cytometry study. *Demographic and clinical details at time of biopsy (age, comorbidities, medication)**,** smoking status listed within comorbidities**,** American thoracic society classification applied to radiology and histopathological to give a final summary classification according to Raghu et al 2018. Abbreviations; OA - osteoarthritis, AVR - aortic valve replacement, CABG - coronary artery bypass graft, MI - myocardial infarction, PMR - polymyalgia rheumatica, HTN - hypertension, CVA - cerebrovascular accident, Hep - hepatitis, ATS - American thoracic society.*

5.3 Results

5.3.1 Histopathology analysis of IPF lung tissue and region of interest selection

In contrast to previous work from our group, which focused on the regenerating alveolar niche in IPF[225] regions of interest (ROIs; 1.5 × 1.5 mm) were selected to capture the full spectrum of histopathological change. ROIs were chosen based on characteristic features of IPF, including type II alveolar epithelial (AT2) metaplasia, fibroblastic foci, extracellular matrix deposition, interstitial expansion, and smooth muscle hyperplasia. Selection was performed in conjunction with a respiratory histopathologist to ensure accurate representation of disease pathology. Although less prominent in IPF compared to other interstitial lung diseases, lymphoid aggregates were also included to enable assessment of myeloid cell distribution across all histopathological contexts (Table 5.3.1).

Sample Name	Amount of airspace (% of ROI)	Inflam. Cells	Collagen presence*	Aggregates of 'grape like' alveolar macrophages	Fibroblasts*	Fibroblastic foci*	Smooth muscle hyperplasia*	Alveolitis	AT2 metaplasia	Interstitial expansion*	Lymphoid aggregate (n = number seen)	Bronchio-lisation and / or honeycombing	Large blood vessels	Disease Stage
IPF_Sample_1_ROI_2	60	+	-	-	-	-	-	++	-	-	0	-	-	Early
IPF_Sample_1_ROI_1	30	+	+	+	+	-	+	+	+	+	4	-	+	Intermediate
IPF_Sample_3_ROI_1	40	+	-	+	+/-	-	-	+	++	+/-	0	-	+	Early
IPF_Sample_4_ROI_1	5	+	++	+	++	-	++	-	++	++	0	-	-	Advanced
IPF_Sample_5_ROI_1	20	+	+	-	+	+	++	-	+	++	0	-	-	Advanced
IPF_Sample_5_ROI_2	20	+	++	+	+	-	++	-	++	++	0	-	-	Advanced
IPF_Sample_5_ROI_2	20	+	+	+	+++	+	+	-	+	+	0	-	+	Intermediate
IPF_Sample_7_ROI_1	5	+	++	-	++	+	++	-	-	++	0	+	-	Advanced
IPF_Sample_7_ROI_2	40	+	+	+	+	+	+	+	+	++	1	+	-	Advanced
IPF_Sample_8_ROI_1	50	+	-	-	-	-	-	++	-	-	0	-	+	Early
IPF_Sample_8_ROI_5	5	+	++	-	++	-	++	-	++	+	1	-	-	Advanced
IPF_Sample_8_ROI_2	20	+	+	-	+	+	+	+	+	+	1	-	+	Intermediate
IPF_Sample_8_ROI_3	40	+	+	+	+	+	+	+	+	+	0	-	+	Intermediate
IPF_Sample_8_ROI_4	30	+	+	+	+	-	-	+	++	+	3	-	+	Intermediate
IPF_Sample_9_ROI_2	50	+	-	-	-	-	-	++	-	+/-	0	-	+	Early
IPF_Sample_9_ROI_1	30	+	++	-	+	+	-	+	+	+	2	+	+	Intermediate
No of ROIs with Feature		16	12	8	13	7	10	11	12		6	3	9	

Table 5.3.1 – Histopathological features present in regions of interest. *Summary of histopathological features present on regions of interest (ROIs) selected for ablation and data acquisition, qualitatively by a senior histopathologist specialising in respiratory pathology. Histopathology review quantified presence of features and binary variables (Inflammatory cells, Fibroblast foci, lymphoid aggregates and Blood vessels as present (+) or absent (-). The number of lymphoid aggregates were quantified per ROI. The remaining pathological features classified according to extent as absent (-), possible (+/-), present (+) or extensive (++). Features demarcated with (*) used for classification of ROIs as Early, Intermediate or Advanced. Abbreviations; ROI – region on interest, Inflam. – inflammatory, AT2 – type 2 alveolar epithelial cells (cuboidal morphology).*

ROIs were subsequently classified into early, intermediate, and advanced stages of disease according to defined histopathological criteria (Table 5.3.2). Early-stage ROIs were characterised by mild interstitial expansion and the presence of alveolitis and AT2 cell metaplasia, in the absence of fibroblast infiltration, collagen deposition, or smooth muscle hyperplasia, reflecting epithelial injury and dysfunction prior to the development of fibrosis (Figure 5.3.1).

Disease Stage (n= ROI)	Expanded interstitium	Fibroblasts	Collagen	Smooth muscle hyperplasia
Early (4)	+/-	-	-	-
Intermediate (6)	+	+	+	+
Advanced (6)	++	+	++	++

Table 5.3.2 – Histopathological classification of regions of interest. *The presented features were used to classify ROIs of interest as Early, Intermediate of Late. Interstitial expansion refers to presence of interstitium in between alveolar septae the other histopathological features reflect development or presence of fibrosis. Outline of criteria used - Early; mild interstitial expansion, no fibroblast infiltration, collagen or smooth muscle hyperplasia. Intermediate; interstitial expansion with fibroblast infiltration, less collagen and smooth muscle hyperplasia. Advanced; interstitial expansion with fibroblast infiltration, more collagen and smooth muscle hyperplasia*

Intermediate-stage ROIs exhibited interstitial expansion with fibroblast infiltration, including loosely organised fibroblasts or fibroblastic foci, together with emerging collagen deposition and smooth muscle hyperplasia, consistent with developing fibrosis (Figure 5.3.2). Advanced-stage ROIs demonstrated extensive collagen deposition, prominent smooth muscle hyperplasia, and areas of bronchiolisation, indicative of established fibrosis with architectural distortion (Figure 5.3.1). Notably, occasional regions of alveolitis were observed within advanced ROIs, reflecting the spatial and temporal heterogeneity that is characteristic of usual interstitial pneumonia (UIP).

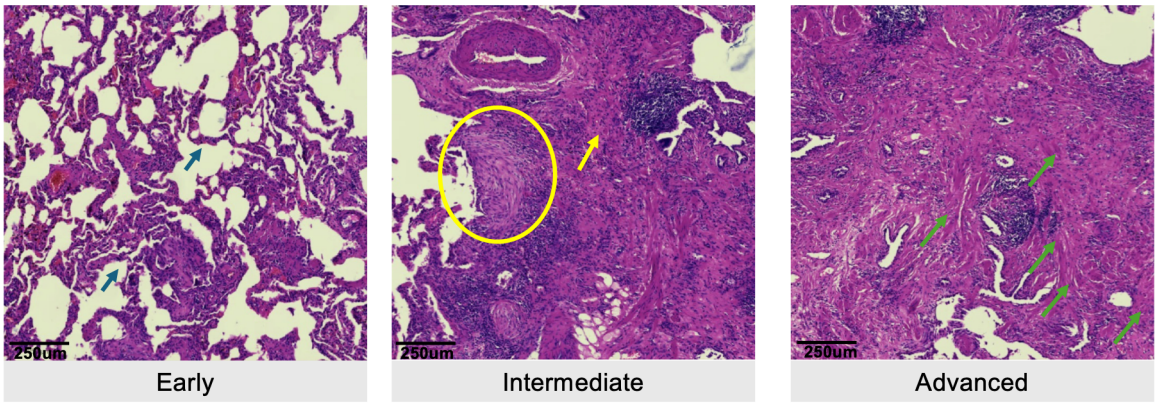


Figure 5.3.1 – Representative H&E-stained sections from IPF_ROI Sample 8. *Early disease; left panel, with thickened alveolar septae (blue arrows) with no collagen deposition or fibroblast infiltration. Intermediate disease; (middle panel) fibroblast infiltration and fibroblastic foci (yellow circle) in conjunction with collagen deposition (yellow arrow) but limited smooth muscle hyperplasia. Advanced disease; extensive smooth muscle hyperplasia (green arrows) and collagen deposition with architectural distortion.*

5.3.2 Antibody panel validation

Antibody specificity was assessed both prior to and following conjugation to lanthanide metals using a combination of complementary validation approaches tailored to individual markers.

For tissue-specific markers, appropriate staining patterns were confirmed using positive and negative control tissues. For example, expression of Pro-SPC, KRT8, and KRT5 was verified in expected epithelial compartments. For cell phenotyping markers, specificity was further supported by demonstrating mutually exclusive expression patterns between structural and immune markers; for instance, KRT8 expression was restricted to epithelial cells and absent from immune populations.

Markers were also evaluated for correct subcellular localisation, including expected membrane-associated (e.g. ICAM1, KRT5, KRT8, pro-SPC), cytoplasmic, or nuclear staining (e.g. p53, p16, Ki67). In addition, immunofluorescence (IF) and IMC staining patterns were compared with adjacent haematoxylin and eosin (H&E)-stained sections to confirm that labelled cell populations aligned with known anatomical distributions, such as collagen and αSMA expression surrounding airways and vascular structures.

Functional markers associated with epithelial dysfunction, cytokine signalling, and interferon-stimulated gene (ISG) expression were validated by comparing staining patterns across disease tissues, including IPF, lung cancer, and COVID-19 lung sections, alongside healthy control tissue (Figure 5.3.2).

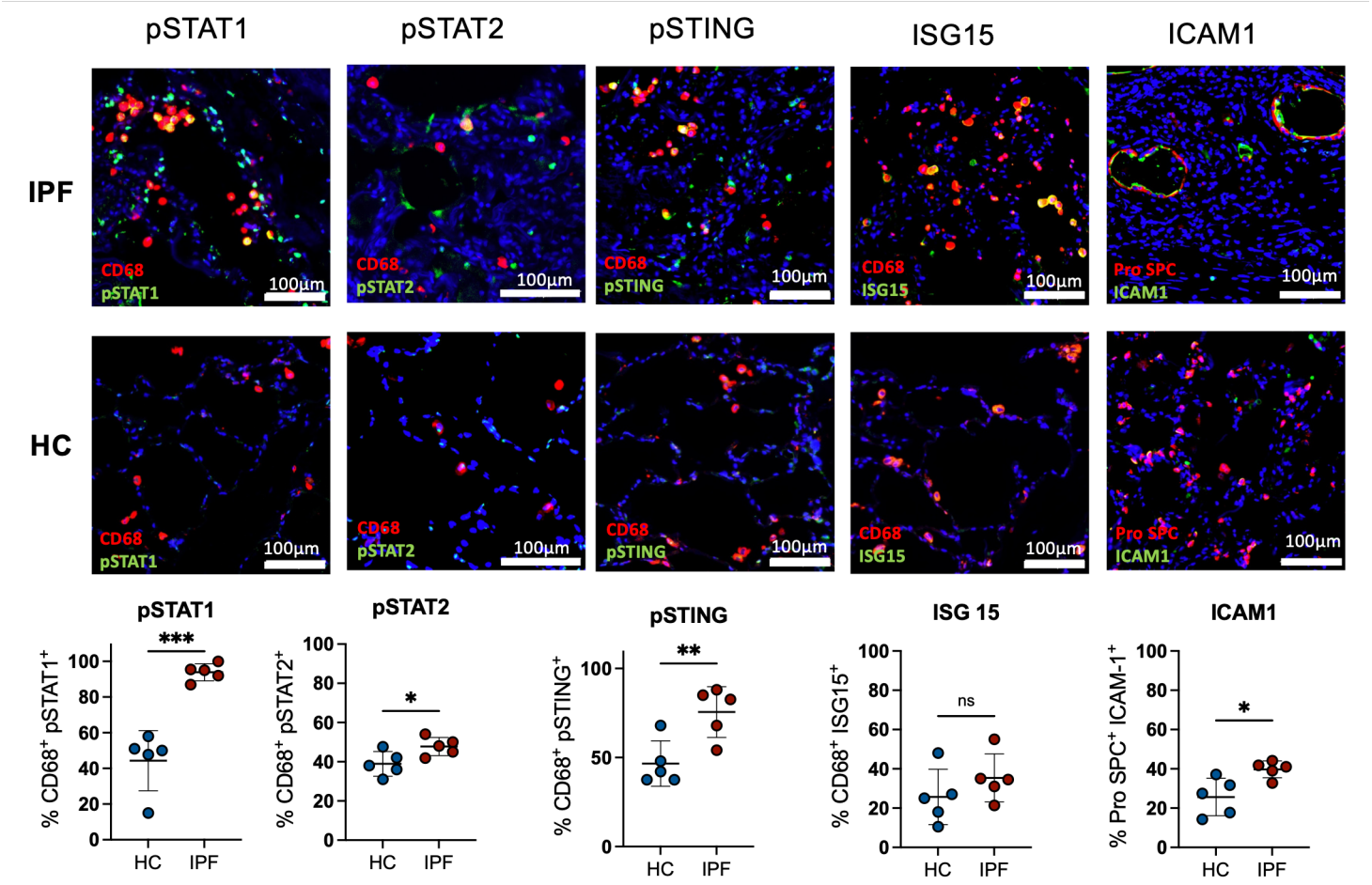


Figure 5.3.2. Comparison of markers associated with epithelial dysfunction and type 1 IFN signalling in disease and control tissues. *Expression of markers associated with epithelial dysfunction (ICAM1 shown as a representative example) and type 1 interferon signalling was assessed in IPF and control tissues alongside relevant cell-type markers. Increased co-expression of CD68⁺ cells with pSTAT1, pSTAT2, pSTING, and ISG15 was observed in IPF compared to control tissue. ICAM1 expression was detected in endothelial and selected cells in control tissue but showed increased co-expression with pro-SPC⁺ alveolar epithelial cells in IPF. Plots represent the proportion of CD68⁺ or pro-SPC⁺ cells expressing the indicated markers across five randomly selected regions of interest (ROIs), with each point representing a single ROI. Co-expressing cells were quantified using the cell quantifier tool in QuPath. Statistical significance was assessed using an unpaired Student's t-test (*p < 0.05, **p < 0.01, ***p < 0.001; ns, not significant [p ≥ 0.05]). Abbreviations: ICAM1, intercellular adhesion molecule 1, ROI – region of interest*

Markers related to type 1 interferon signalling, including phosphorylated STAT proteins (pSTAT1, pSTAT2) and ISGs, were further validated using THP-1 cells under controlled stimulation conditions. Increased marker expression following IFN-β stimulation, together with reduced expression in IFN-β-stimulated IFNAR2-deficient THP-1 cells, confirmed the specificity and pathway dependence of these markers (Figure 5.3.3).

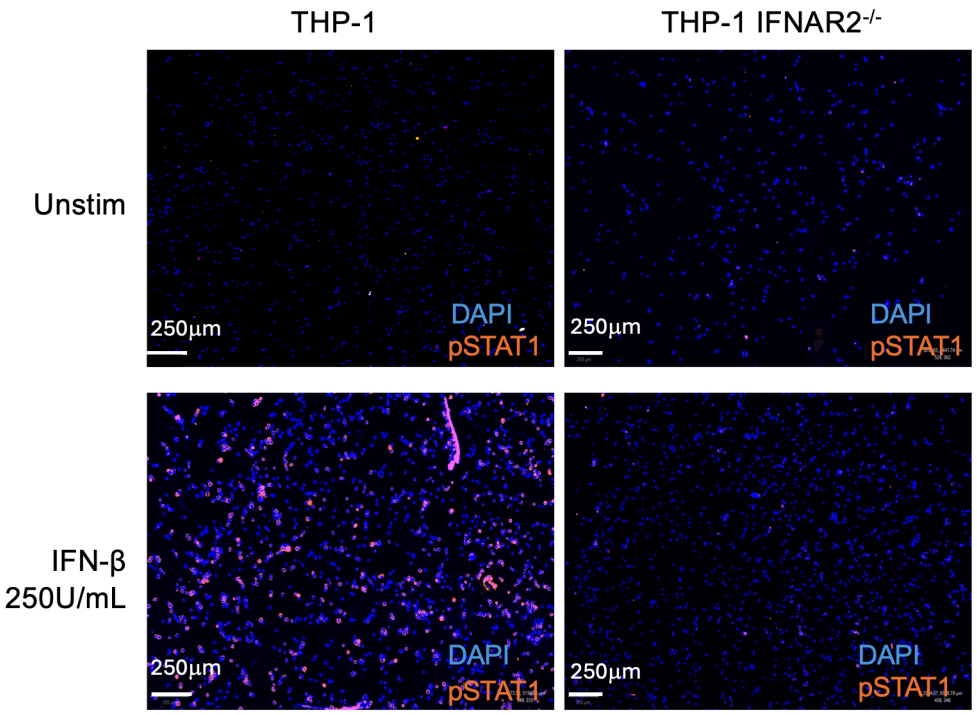


Figure 5.3.3. Increased pSTAT1 expression following IFN-β stimulation in THP-1 cells. *THP-1 cells expressing IFNAR2 and IFNAR2$^{-/-}$ cells were either left unstimulated or stimulated with IFN-β (250 U/mL) in alveolar medium. Cells were collected after 15 minutes for cytospin preparation and stained for IFN-responsive markers, with pSTAT1 shown as a representative example to assess specificity. Expression of interferon-stimulated genes (ISGs; IFIT3 and ISG15) was assessed following 6 hours of stimulation. Visual assessment of staining patterns was used to evaluate changes in marker expression. Increased pSTAT1 expression was observed in THP-1 cells following IFN-β stimulation, but not in unstimulated conditions. Abbreviations; IFNAR2 – interferon alpha receptor subunit 2, Unstim – unstimulated.*

5.3.3 Characterisation of the cellular landscape of IPF lung tissue

Following antibody staining and laser ablation, imaging mass cytometry (IMC) data were acquired and reconstructed into MCD files for downstream analysis, as outlined in Figure 5.2.1 and MCD images displaying expression of all 40 markers were reviewed alongside adjacent haematoxylin and eosin (H&E)-stained sections to confirm signal quality and marker specificity.

Cell segmentation was performed using the Mesmer model within DeepCell, and enabled the generation of a high-dimensional single-cell dataset incorporating spatial coordinates, cellular morphology, and protein expression for each cell (Figure 5.2.1). In total, 187,028 cells were identified across 16 regions of interest (ROIs), representing 31 mm^2 of tissue from seven IPF donors.

Dimensionality reduction and unsupervised clustering were performed using the PhenoGraph algorithm based on phenotyping marker expression (Figure 5.3.4). Functional markers were excluded from clustering to ensure that cells were grouped according to lineage and identity rather than shared activation states.

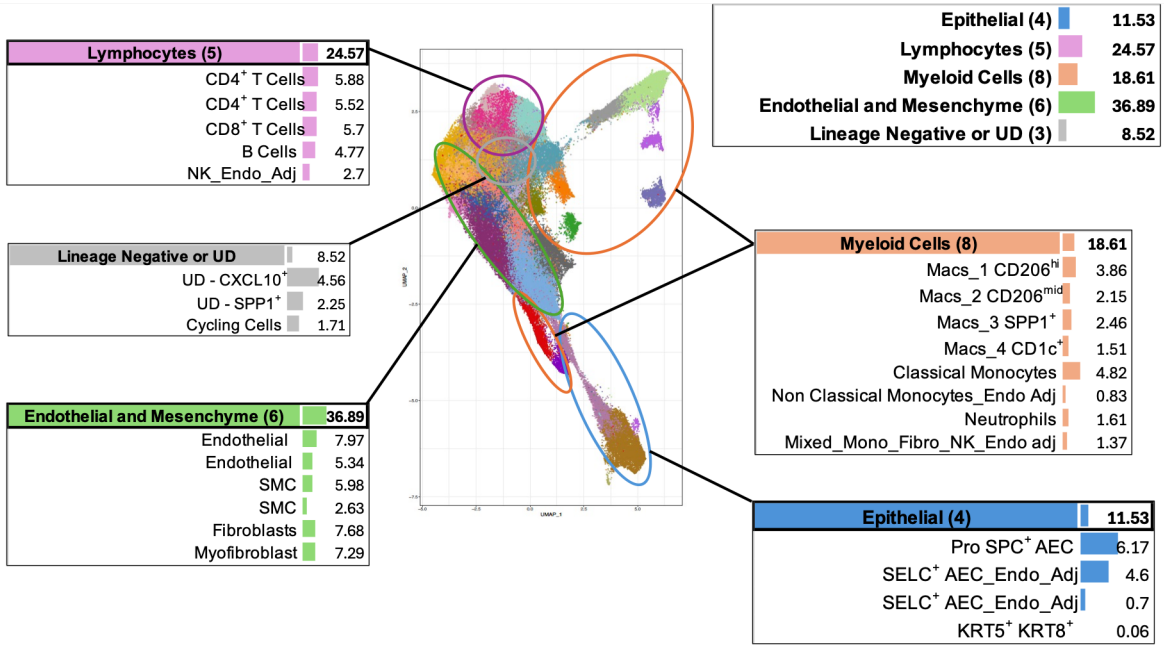


Figure 5.3.4. Overview of the cellular landscape in IPF identified by imaging mass cytometry. UMAP visualisation of major cell populations, grouped by lineage following initial clustering of 187,028 cells using the PhenoGraph algorithm. The top right panel shows the proportion of major cell lineages expressed as a percentage of all segmented single cells. Additional panels, stratified by cell lineage, display the proportions of individual cell populations as a percentage of total cells. Initial annotations represent broad classification of epithelial and myeloid cell populations prior to further re-clustering and detailed characterisation. Coloured circles indicate the location of corresponding major cell lineages on the UMAP. Abbreviations; Adj - adjacent; UD - undefined; SMC - smooth muscle cell; Endo- endothelial cells; Fibro, fibroblasts.

This analysis identified 26 distinct cellular populations (Figure 5.3.4). Epithelial and myeloid populations were initially annotated using broad labels to enable subsequent targeted re-clustering. Final cell annotation was performed by integrating marker expression profiles with spatial localisation using cell centroid maps generated in a

multidimensional viewer, together with adjacent H&E sections. This approach allowed annotation to be informed not only by marker expression but also by expected morphology and anatomical context. For example, thin, elongated SCEL-expressing AT1 cells lined alveolar structures; αSMA-expressing smooth muscle cells localised to the walls of larger vessels; $CD31^+$ endothelial cells were present at the intimal layer; and $CD3^+$ T cells and $CD20^+$ B cells were organised within lymphoid aggregates (Figure 5.3.5).

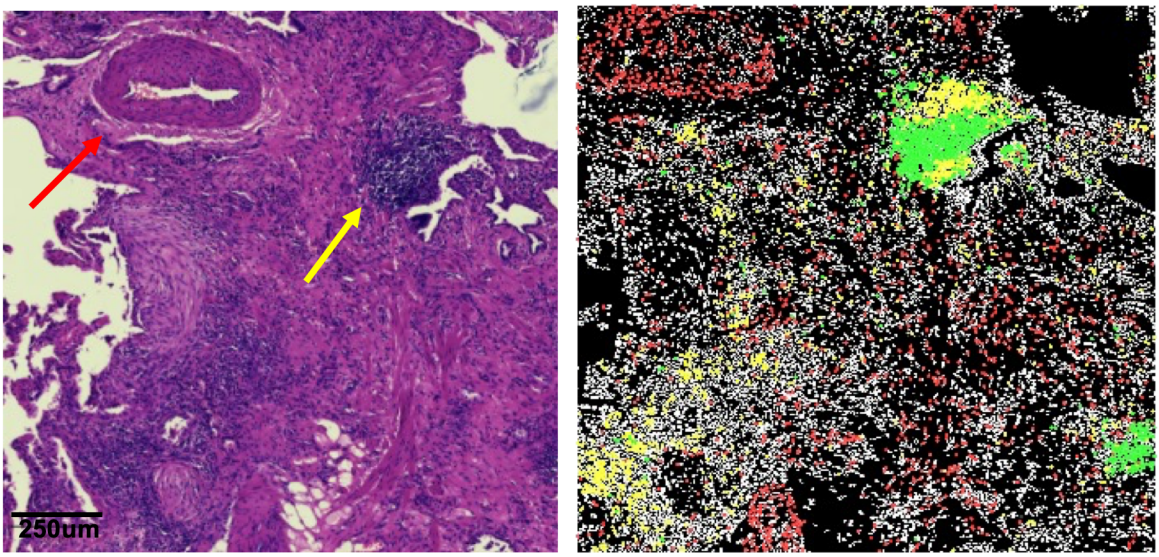


Figure 5.3.5. H&E in conjugation with cell centroid plots to enhance annotation. *Adjacent H&E with cell centroid plots generated from MDV file. Arterial blood vessel with smooth muscles surround present on H&E (red arrow) correspond to $aSMA^+$ smooth muscle cells on cell centroid (coloured red). H&E also shows a lymphoid aggregate (yellow arrow) with corresponding to $CD20^+$ B cells (coloured green) surrounded by CD4+ T cells (coloured yellow) on cell centroid plot. Sample ID - IPF_5_ROI2*

Annotated populations were subsequently grouped into major lineage categories, including lymphoid, myeloid, epithelial, endothelial, and mesenchymal compartments. Mesenchymal populations—including fibroblasts, myofibroblasts, and smooth muscle cells—comprised the largest proportion of cells (24.6%), followed by lymphocytes (24.6%), myeloid cells (18.6%), endothelial cells (13.3%), and epithelial cells (11.5%) (Figure 5.3.9). These proportions were comparable to those reported in whole-section spatial analyses of IPF lung tissue[303] (Table 5.3.3), supporting the ROI selection strategy, which was designed to capture the full spectrum of histopathological features. The relatively higher proportion of lymphocytes in this dataset likely reflects the deliberate inclusion of ROIs containing lymphoid aggregates.

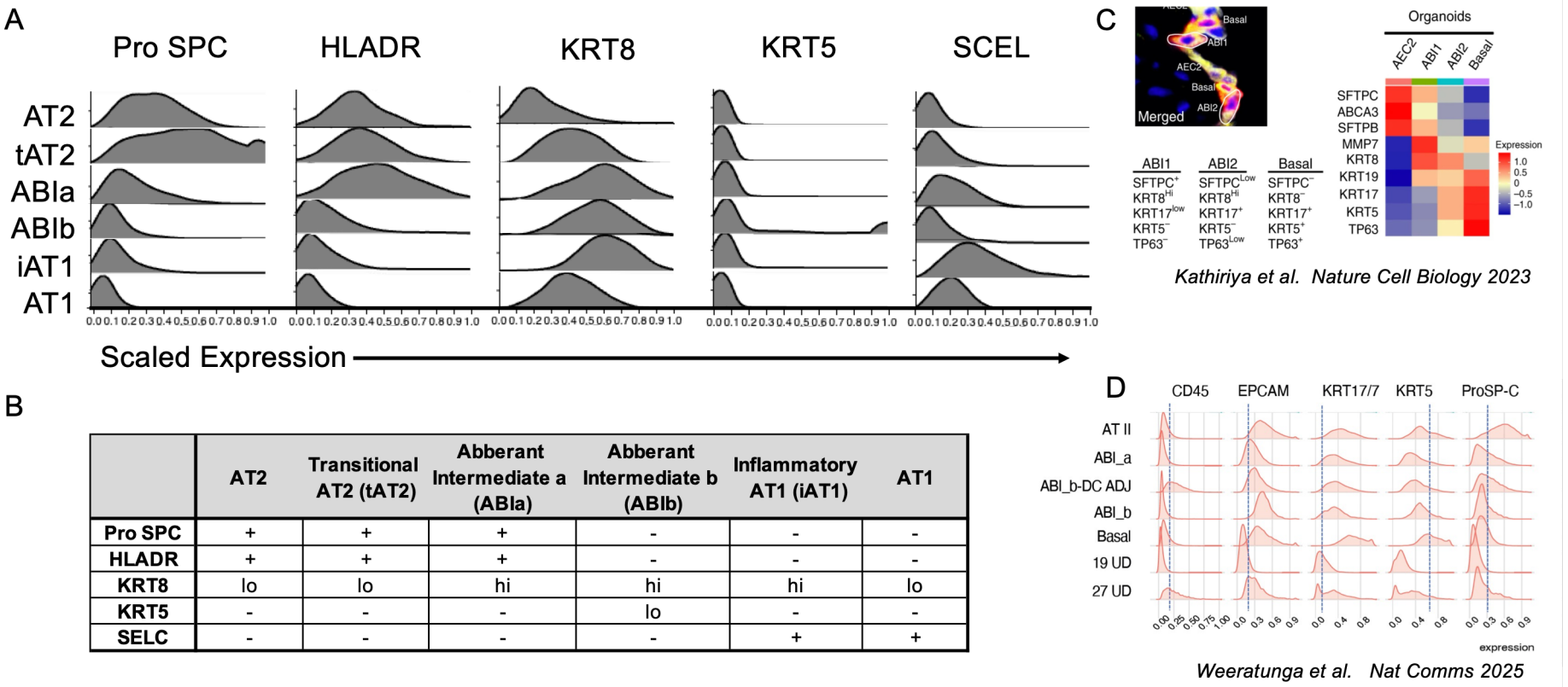
Cell Type	Percentage of all cells (IMC)	Percentage of all cells (Vannan[303])
Mesenchymal	25.6	27.5
Myeloid	18.6	17.3
Lymphocyte	24.6	13.4
Epithelial	11.5	14.4
Endothelial	13.3	15.6

Table 5.3.3. Comparison of major cell populations with published spatial transcriptomic dataset *Proportions of major cell populations identified in the study were compared to the corresponding populations identified by at study by Vannan et al where a spatial transcriptomic analysis of IPF lung tissue was performed using the xenium probe based platform[303]. Cell groups are detailed above with separation of mesenchymal and endothelial cell types. Mesenchymal refers to fibroblasts, activated fibroblasts, myofibroblasts and smooth muscle cells. Proportions presented as percentage of all cells (excluding undefined populations)*

A small number of clusters displayed co-expression of markers associated with multiple cell lineages, most commonly combinations of immune or epithelial markers with endothelial markers. Inspection of centroid maps indicated that these clusters represented closely apposed cells that could not be resolved during segmentation. These were therefore annotated as adjacent cell populations (_Adj). Two additional clusters expressing CXCL10 and/or SPP1 could not be definitively characterised using the available marker panel and were classified as undefined. A further cluster, defined by Ki67 expression and exhibiting mixed lineage marker expression, was annotated as cycling cells.

5.3.4 Alveolar epithelial cell populations in IPF include aberrant basaloid and transitional states

To characterise epithelial heterogeneity in IPF lung tissue, epithelial cells were re-clustered using epithelial-specific phenotyping markers, including EPCAM, Pro-SPC, HLA-DR, SCEL, KRT8, and KRT5 (Figure 5.3.6). This approach enabled the identification of intermediate and aberrant alveolar epithelial cell (AEC) states.



B

	AT2	Transitional AT2 (tAT2)	Abberant Intermediate a (ABIa)	Abberant Intermediate b (ABIb)	Inflammatory AT1 (iAT1)	AT1
Pro SPC	+	+	+	-	-	-
HLADR	+	+	+	-	-	-
KRT8	lo	lo	hi	hi	hi	lo
KRT5	-	-	-	lo	-	-
SELC	-	-	-	-	+	+

Figure 5.3.6. Identification of intermediate and aberrant alveolar epithelial cell populations. *Epithelial cells were re-clustered to resolve distinct subsets, which were initially annotated based on phenotypic marker expression.* ***(A)*** *Expression density histograms showing cell populations (y-axis) against scaled (arcsinh-transformed) marker expression (x-axis), allowing visual comparison of marker expression across subsets.* ***(B)*** *Summary of alveolar epithelial cell populations with qualitative assessment of marker expression profiles.* ***(C–D)*** *Figures adapted from Kathiriya et al. and Weeratunga et al. 2025. Marker expression used as reference frameworks to annotate type II alveolar epithelial cells (AT2) and aberrant basaloid intermediate cells (ABIs) based on overlapping marker expression. ABI annotation was performed in line with Weeratunga et al. 2025, with ABIa corresponding to ABI1 and ABIb corresponding to ABI2 as described by Kathiriya et al. Abbreviations; ABI - aberrant basaloid intermediates, AT2 - type II alveolar epithelial cells, AT1 - type I alveolar epithelial cells, tAT2 - transitional AT2, iAT1 - inflammatory AT1.*

Marker expression profiles of the re-clustered epithelial populations were compared with previously described transcriptomic and protein signatures derived from human alveolar organoid models[300], murine injury–fibrosis studies[293, 294], human single-cell RNA sequencing datasets[63, 86, 300], and prior IMC analyses of the regenerating alveolar niche performed within our group[225]. Although KRT17 was not included in the IMC antibody panel, annotation of intermediate AEC populations was based on the combined expression of KRT8, KRT5, Pro-SPC, SCEL and markers of epithelial dysfunction, together with comparison to these published reference datasets. In particular, comparison with integrated transcriptomic and protein-based characterisation of transitional alveolar epithelial states published by Kathiriya et al[300]. and Weeratunga et al[225]. (Figure 5.3.6C,D), together with published transcriptomic reference data from Habermann et al[63]. (Figure 5.3.7), enabled annotation using markers measurable in the by IMC while maintaining consistency with published epithelial cell-state definitions.

This comparative analysis enabled identification of canonical AT2 and AT1 populations, together with aberrant basaloid intermediate (ABI) states consistent with those reported in prior studies. AT2 cells were defined by expression of established markers including Pro-SPC and HLA-DR, while AT1 cells were identified by expression of SCEL, a marker associated with differentiated AT1 cells (Figure 5.3.6).

Two ABI populations were resolved based on differential expression of KRT8 together with AT2 and basal-associated markers. The ABIa population exhibited low pro-SPC expression together with high KRT8 expression, consistent with the ABI1 population described by Kathiriya et al.[300] In contrast, ABIb cells lacked pro-SPC expression and showed low KRT5 expression, resembling the ABI2 population. In time-course and trajectory inference analyses, ABI1 has been shown to represent an early intermediate population arising from AT2 cells, while ABI2 emerges later along the differentiation trajectory[300] (Figure 5.3.6).

In addition to these previously described populations, two further epithelial clusters were identified. One population expressed high levels of pro-SPC and HLA-DR, consistent with an AT2 phenotype, but also demonstrated elevated KRT8 expression. Similar populations have been reported by Haberman in a human scRNA-seq IPF dataset[63] (Figure 5.3.7) and murine injury models[293, 295], where they are interpreted as transitional AT2 states associated with epithelial injury and repair. Given these features, this population was annotated as transitional AT2 (tAT2) cells.

A second population expressed the AT1 marker SCEL together with high KRT8 expression. As this population also exhibited increased expression of inflammatory and senescence-associated markers (described in Section 5.3.5), it was annotated as inflammatory AT1 (iAT1) cells.

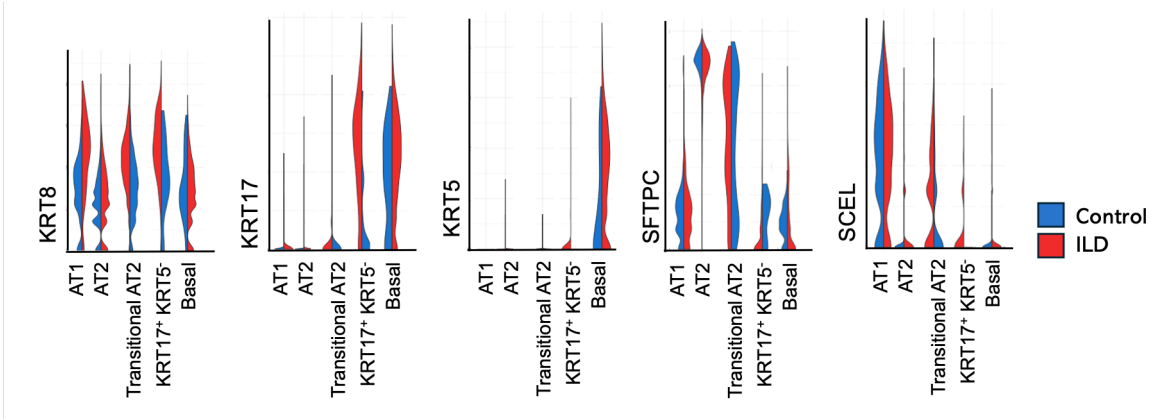


Figure 5.3.7. Overlap between tAT2 protein expression and transitional AT2 transcriptomic profiles. *Violin plots reproduced from publicly available single-cell transcriptomic data generated by Habermann et al.[63] and accessed through the IPF Cell Atlas[304]. The plots show normalised gene expression across annotated epithelial cell populations (x-axis), stratified by disease state. These published transcriptomic data were used to compare the protein expression profile of the tAT2 population identified in the present study with previously described transitional AT2 and intermediate epithelial populations. Transitional AT2 populations demonstrate high SFTPC (Pro-SPC) expression, comparable to AT2 cells, together with increased KRT8 expression, low SCEL expression, and minimal or absent KRT17 and KRT5 expression.*

To position these epithelial states within the AT2-to-AT1 differentiation continuum, marker expression patterns were compared with published time-course studies of epithelial differentiation in vitro and in murine injury models[293, 294, 295]. In these systems, intermediate epithelial states progressively downregulate AT2 markers while upregulating KRT8 and other cytokeratins. Based on these comparisons, the epithelial populations identified here align along a putative differentiation trajectory from AT2 cells through transitional AT2 states to ABI populations (Figure 5.3.8). The expression of SCEL in both tAT2 and ABIa populations suggests that the iAT1 population may arise from one or both of these intermediate states.

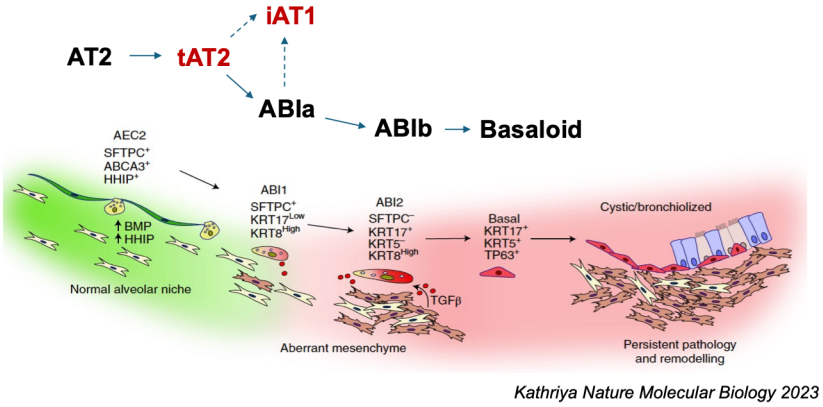


Figure 5.3.8. *AT2- differentiation trajectory incorporating tAT2 and iAT1 populations. Schematic illustration adopted from Kathiriya et al[300], with additional intermediate populations incorporated into the AT2 – ABI differentiation trajectory proposed by the study authors. Populations in red depict those described here, dashed lines potential precursor populations to iAT1 based on SCEL expression.*

5.3.5 Transitional and ABI cell states express markers associated with inflammation

Analysis of functional marker expression across re-clustered AEC populations demonstrated that aberrant basaloid intermediate (ABI) and inflammatory AT1 (iAT1) populations exhibited the highest levels of injury- and senescence-associated markers. These populations also showed increased expression of pSTING, cytoplasmic IFN-β, and TNF-α, consistent with activation of innate immune signalling pathways (Figure 5.3.9).

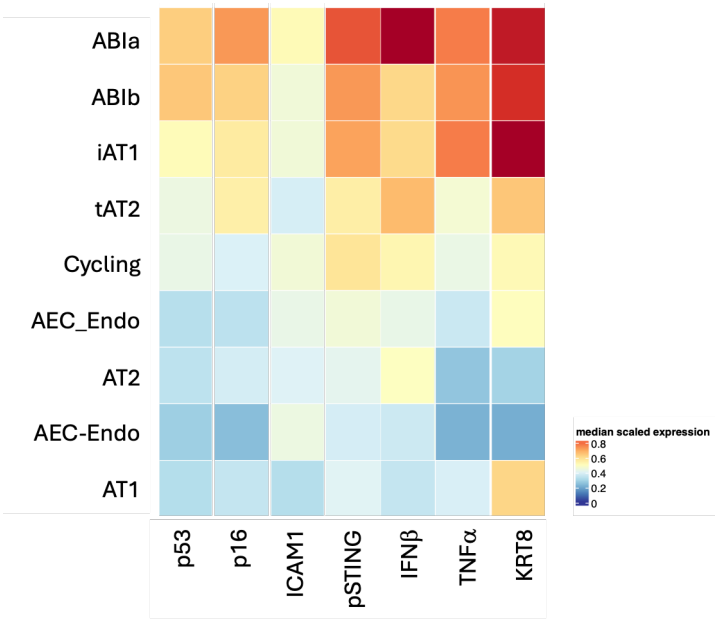


Figure 5.3.9. Alveolar epithelial cell functional marker expression. *Heatmap depicting expression on functional markers associated with epithelial cell injury, senescence, and cytokine production across epithelial cell subsets. Colour intensity reflects median marker expression Abbreviations; ABI – aberrant basaloid intermediates, iAT1 – inflammatory AT1, tAT2 – transitional AT2 cells*

Transitional AT2 (tAT2) cells displayed lower levels of senescence-associated markers compared to ABI populations but exhibited the second highest levels of IFN-β expression. This suggests that induction of type 1 interferon signalling may occur prior to the establishment of a fully senescent epithelial phenotype.

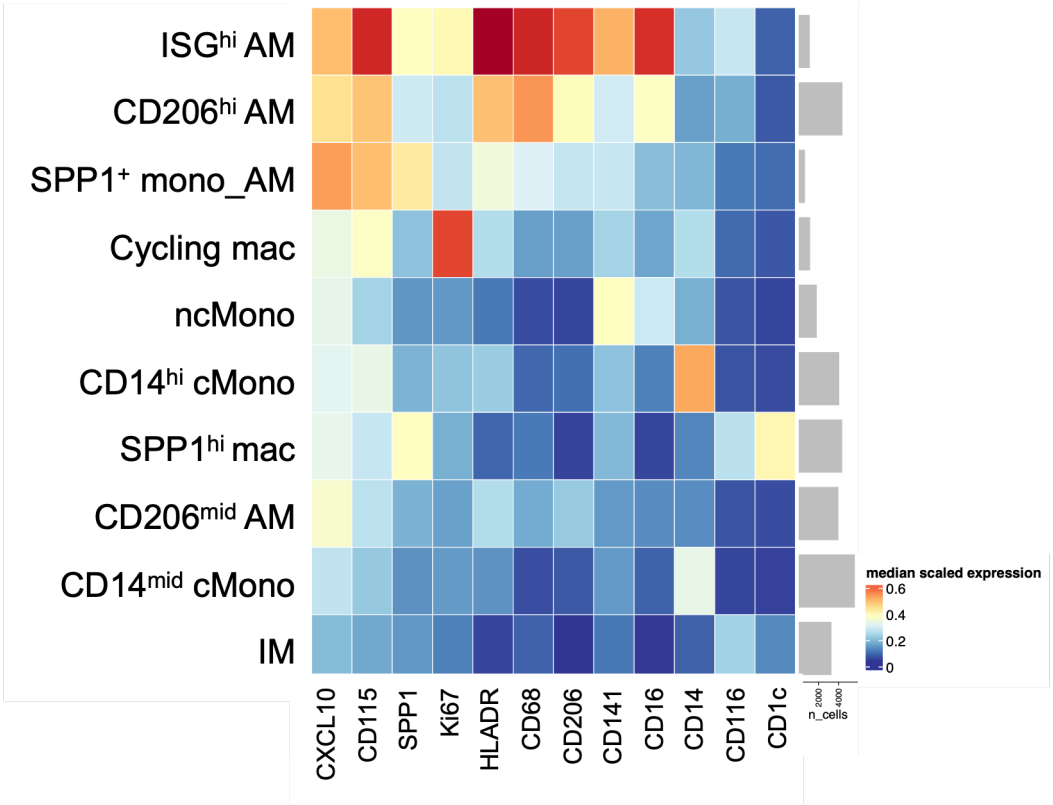
Collectively, these findings indicate that intermediate epithelial states—including tAT2, ABIa, ABIb, and iAT1 populations—are associated with epithelial injury and senescence and show evidence of inflammatory cytokine production together with activation of the cGAS–STING pathway. These observations support a model in which dysfunctional epithelial states represent a potential local source of interferon signalling within the IPF lung microenvironment.

5.3.6 Alveolar macrophage subtypes express highest levels of type 1 IFN activation markers

To further resolve myeloid heterogeneity, monocyte and macrophage populations identified during initial clustering were re-clustered using myeloid-specific phenotyping

markers, including CD68, CD206, CD14, CD16, CD141, CD1c, CXCL10, SPP1, CD115, CD116, and HLA-DR.

Final annotation of myeloid populations was performed by integrating marker expression profiles with spatial localisation using multidimensional viewer (MDV) centroid plots alongside adjacent H&E-stained sections. This enabled discrimination between macrophage populations residing within the alveolar space and those located in the lung interstitium (Figure 5.3.10).



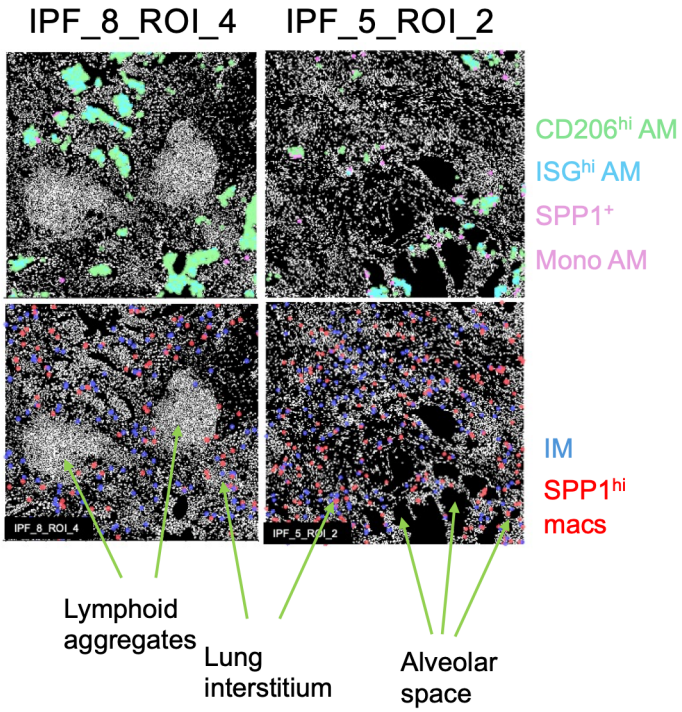


Figure 5.3.10. Profiling and spatial localisation of lung monocyte and macrophage populations. *Macrophage annotation was undertaken using a combination of marker expression using heatmaps (top panel) and expression density histograms (not shown) in conjunction with localisation in tissue using cell centroid plots generated in multidimension viewer (MDV). Top panel – heatmap of phenotyping markers used for re-clustering monocyte and macrophage subsets, with colour intensity reflecting median marker expression. Bottom panel - cell centroid plots with cells coloured by subset and localised to either the alveolar space (CD206^{hi} AM, ISG^{hi} AM, and SPP1^{+} mono_AM) or interstitial space (IM and SPP1^{hi} macrophages) to support refined annotation. Histological features are indicated by arrows and were identified using adjacent H&E-stained sections.*

Monocyte populations were defined by expression of CD14 and/or CD16 in the absence of macrophage-associated markers such as CD68 and CD206. CD68^{+} macrophage clusters were further classified as alveolar macrophages (AMs) or interstitial macrophages (IMs) based on anatomical localisation. This classification was supported by marker expression patterns: AM populations exhibited higher expression of HLA-DR and CD206, consistent with previous reports[152, 153, 154, 305], whereas tissue macrophage populations including IMs and SPP1^{hi} macs showed lower CD206 expression and increased expression of markers such as CD1c and SPP1[153, 154]. SPP1^{hi} macs shared a marker expression profile with IMs, consistent with both the transcriptomic analysis presented in Chapter 4 and previous studies describing SPP1 expression within interstitial macrophage populations[86, 184, 185]. However, several experimental murine studies[43, 172] and spatial analyses of human IPF lung tissue[303, 306] have also identified SPP1 expressing macrophages within alveolar airspaces, suggesting these cells are not

exclusively confined to the interstitium. Given this uncertainty regarding their anatomical localisation and ontogeny, a conservative annotation strategy was adopted.

Within the AM compartment, four clusters were identified and further stratified based on CD206 expression. Among the CD206^{mid} populations, one cluster also expressed both SPP1 and CD14, suggesting a monocyte-derived origin; this population was annotated as SPP1^{+} mono_AM and may correspond to the airspace associated SPP1 expressing populations described above[303, 306].

Three AM populations exhibited elevated expression of interferon-stimulated genes (ISG15, IFIT3) together with phosphorylated STAT1 and STAT2, indicating active signalling downstream of the interferon α/β receptor (IFNAR). Among these, a smaller CD206^{hi} AM population showed the highest levels of type 1 IFN-associated proteins. This population also expressed CD14, consistent with a potential monocyte-derived origin, and may correspond to the CXCL10^{+} alveolar macrophage population identified in the transcriptomic analysis (Chapter 4.3.1). Notably, these interferon-active AM populations also exhibited increased TNF-α expression (Figure 5.3.11).

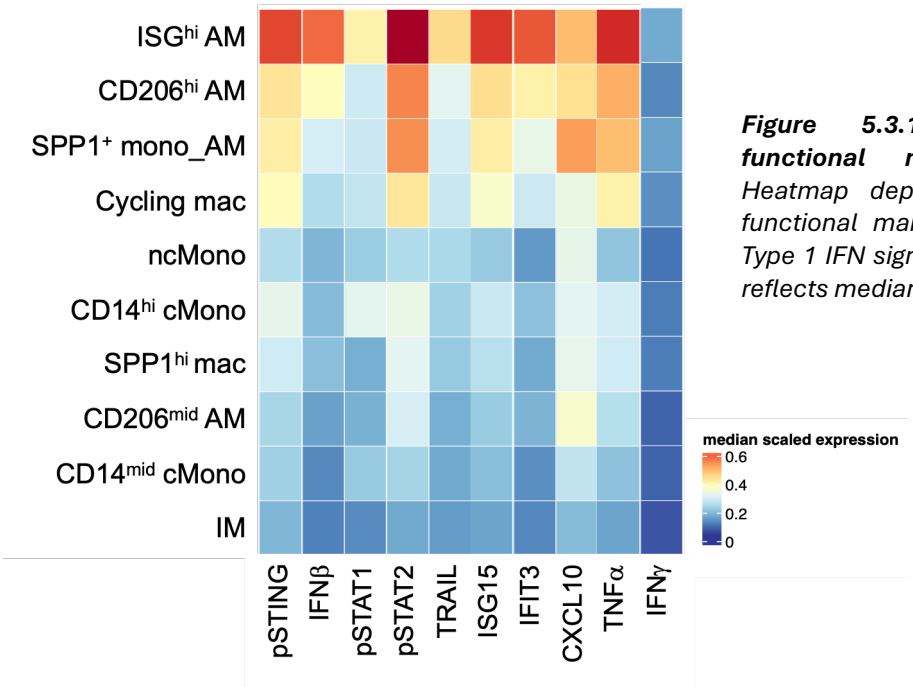


Figure 5.3.11. Myeloid cell functional marker expression. *Heatmap depicting expression on functional markers associated with Type 1 IFN signalling Colour intensity reflects median marker expression*

In contrast, interstitial macrophage and monocyte populations-predominantly located within the lung interstitium-displayed lower overall levels of type 1 IFN pathway activation. Among these, CD14^{hi} monocytes showed the highest expression of interferon-related proteins, particularly pSTAT1, although levels remained lower than those observed in alveolar macrophage populations.

Together, this integrated spatial and protein expression analysis identifies distinct macrophage subsets characterised by type 1 interferon activation. Notably, the highest levels of interferon signalling were observed in alveolar macrophage populations localised to the luminal surface of the alveolar barrier, suggesting that this microenvironment may represent a key niche for interferon-driven myeloid activation in IPF.

Recognising that CXCL10 is a well-established ISG, and that its inclusion as a phenotyping marker could potentially influence clustering, myeloid clustering was repeated with exclusion of CXCL10 from the phenotyping marker panel. Exclusion of CXCL10 did not alter the overall number of myeloid clusters, the overall organisation of clusters within the UMAP embedding, or the identification of the ISG^{hi} AM population. The principal difference observed was reduced separation of the two CD206^{mid} AM populations based on SPP1 expression (Figure 5.3.12)

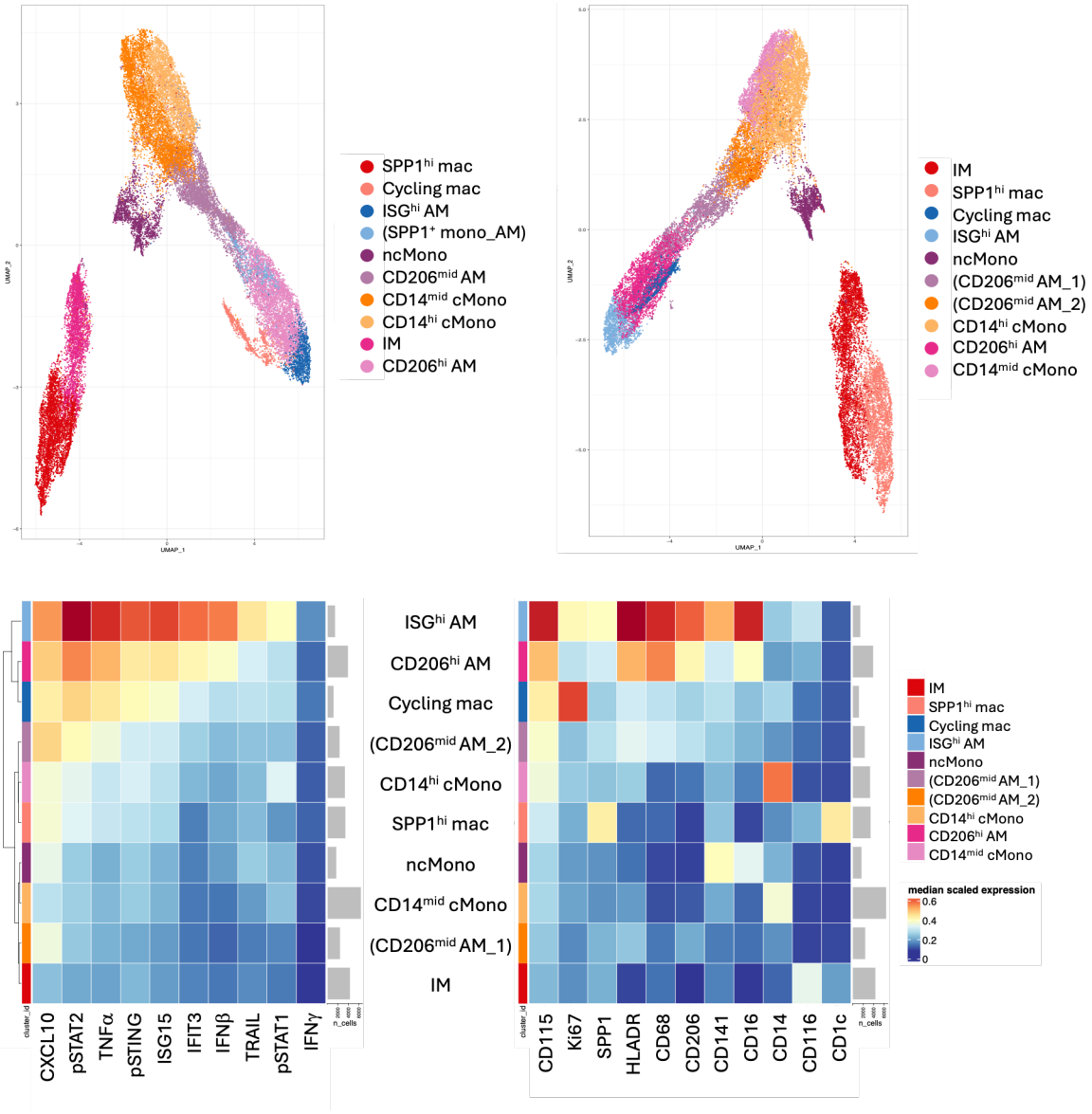


Figure 5.3.12. Comparative analysis of clustering following exclusion of CXCL10 from the phenotyping marker panel. Comparison of UMAPs generated using the selected clustering strategy including CXCL10 (top left) and following exclusion of CXCL10 from the phenotyping marker panel (top right). Heatmaps of phenotyping (bottom right) and functional (bottom left) marker expression for the revised clustering are shown for comparison with the selected clustering heatmaps in Figure 5.3.10 and 5.3.11. Cluster identities and proportions were largely preserved following exclusion of CXCL10 with the principal difference being altered separation of the CD206^{mid} AM populations (highlighted with brackets).

5.3.7 Type 1 IFN-activated myeloid populations and type 1 IFN signalling are increased in early and intermediate stages of IPF

Transcriptomic analysis of the Morse dataset[185] (Chapter 4) demonstrated increased type 1 IFN signalling in myeloid cells from the upper lobes of IPF lungs-regions corresponding to earlier-stage disease-compared to lower lobes with more advanced fibrosis.

To assess whether this pattern is recapitulated at the protein and tissue level, the composition of myeloid populations and expression of type 1 IFN–related markers were compared across ROIs histologically classified as early, intermediate, or advanced disease.

Myeloid subset abundance was quantified as the percentage of total myeloid cells within each ROI (Figure 5.3.13). Although differences between disease stages did not reach statistical significance for most populations, the distribution of myeloid subsets demonstrated trends that were broadly consistent with the regional transcriptomic abundance analysis of the Morse dataset in Chapter 4. All three IFN-activated alveolar macrophage populations (ISG^{hi} AM, CD206^{hi} AM, and SPP1^{+} mono_AM) were tended to be more abundant in early-stage ROIs. In contrast, CD206^{mid} AMs, which exhibited lower levels of type 1 IFN signalling, remained relatively stable across disease stages (Figure 5.3.13).

Macrophage populations localised to the interstitium were expanded in intermediate and advanced ROIs, consistent with their increased abundance in fibrotic lower lobe regions described in Chapter 4.3.5. Among circulating-derived populations, non-classical monocytes were most prominent in early-stage regions but were infrequently observed in intermediate and advanced disease.

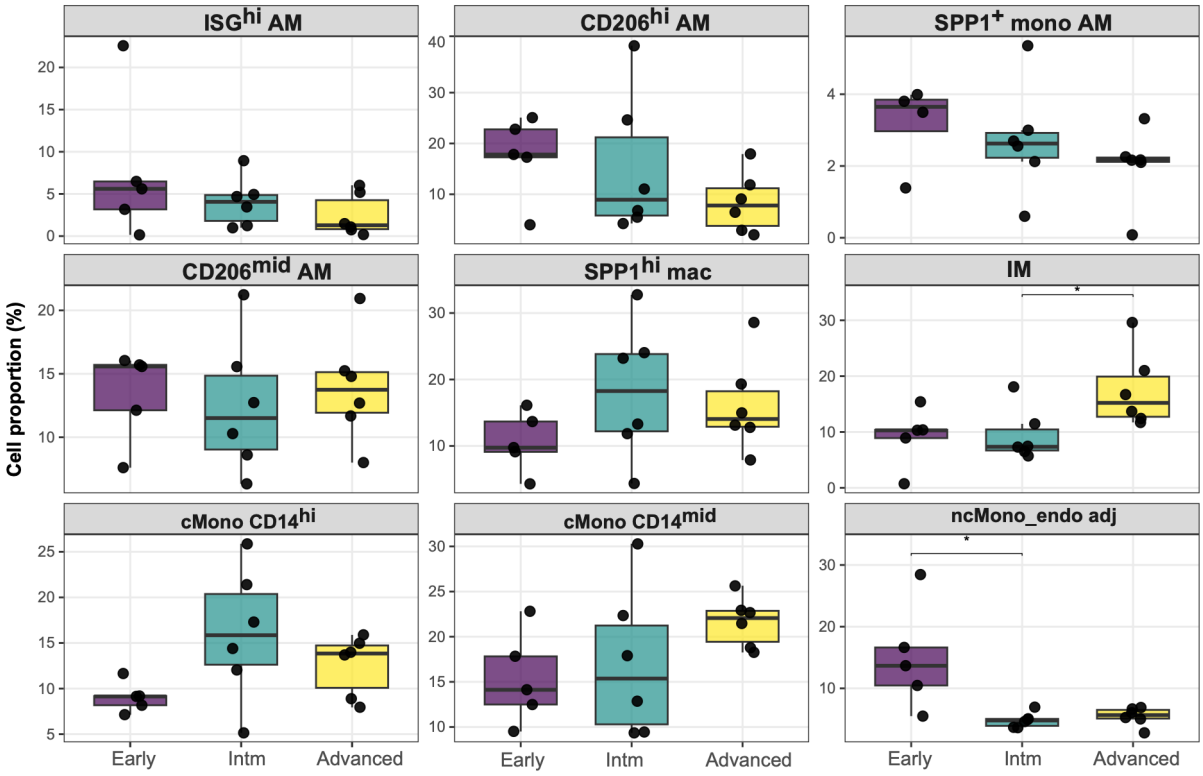


Figure 5.3.13. Differential abundance of myeloid populations across IPF disease stage. *Myeloid cell abundance was quantified as the proportion of cells per ROI belonging to each population. For each ROI, cell counts were normalised to the total number of myeloid cells and expressed as a percentage. Each point represents an individual ROI, grouped by disease stage (Early, Intermediate, Advanced), with boxplots indicating the median and interquartile range. Differences in cell-type abundance across disease stages were assessed using a Kruskal–Wallis test for each population, followed by Dunn's post hoc test for pairwise comparisons with false discovery rate correction. Adjusted p-values are indicated as * $p \leq 0.05$, ** $p \leq 0.01$ and *** $p \leq 0.001$. Abbreviations; ROI – region of interest, Intm – intermediate, AM – alveolar macrophage, IM – interstitial macrophage, mac – macrophages, cMono – classical monocytes, ncMono – non classical monocytes*

To determine whether type 1 IFN activity varied across disease stages, median expression of interferon-related proteins was compared across all myeloid subsets. Overall, type 1 IFN protein expression was highest in intermediate-stage ROIs, with several markers also elevated in early disease (Figure 5.3.14).

In contrast, multiple interferon-associated proteins were significantly reduced in advanced disease. In CD206^{hi} AMs, pSTAT2 and IFIT3 expression were decreased in advanced ROIs compared to earlier stages. Similarly, in CD206^{mid} AMs, expression of pSTAT2, IFIT3, ISG15, IFN-β, and TNF-α was significantly lower in advanced disease. A comparable pattern was observed in SPP1^{+} mono_AMs, where IFIT3 expression was reduced in advanced ROIs (Figure 5.3.14).

This stage-dependent reduction in interferon signalling extended to interstitial macrophage and monocyte populations, which overall exhibited lower type 1 IFN activity compared to alveolar macrophages. Within these populations, pSTAT1 and pSTAT2 expression in interstitial macrophages, and pSTAT2 expression in non-classical monocyte–endothelial adjacent cells, were significantly decreased in advanced disease relative to early and intermediate stages (Figure 5.3.14).

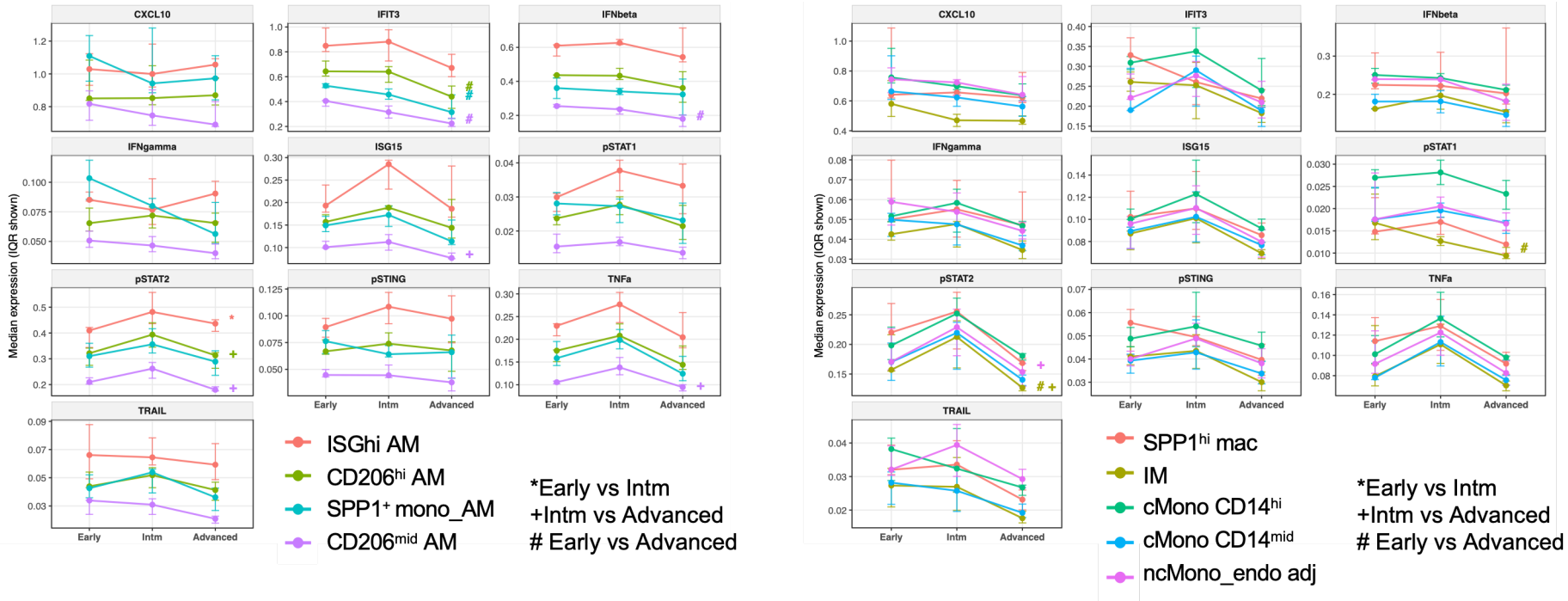


Figure 5.3.14. Protein expression in myeloid populations with disease stage. *Line plots of median expression of type 1 IFN related proteins in myeloid populations across disease stages. Points represent the median expression per disease stage for all ROIs with error bars indicate the interquartile range (IQR; 25th–75th percentile). Populations split into two groups between AM populations (left panel) and tissue macrophage populations and monocytes with lower type 1 IFN expression (right panel). Statistical significance between disease stages was assessed for each protein within each cell type using a Kruskal–Wallis test, followed by Dunn's post hoc analysis to perform pairwise comparisons FDR adjusted p values. Significant pairwise comparisons between disease stages coloured by cell type and labelled as follows; * Early vs Intm, + Intm vs Advanced, #Early vs Advanced. Abbreviations; ROI – region of interest, Intm – intermediate*

These findings demonstrate that type 1 interferon activation in myeloid cells is highest in early and intermediate stages of IPF and declines with progression to advanced fibrosis. This reduction was observed in multiple myeloid populations suggesting that increased type 1 IFN signalling is associated with earlier stages of disease.

5.3.8 Spatial analysis reveals co-location between type 1 IFN-activated myeloid cells and ABIs, iAT1 and tAT2 epithelial cell populations

To determine which cell populations are spatially associated with type 1 IFN - activated myeloid cells, spatial analysis methods previously developed within the group were applied[225]. These approaches, enable statistical identification of cell types that are preferentially co-located within tissue.

Spatial association between cell populations was first assessed using the cross-pair correlation function (cross-PCF) which quantifies whether two cell types are observed within a defined distance (r) more frequently than expected under complete spatial randomness (CSR). The cross-PCF is expressed as g(r), where $g(r = 20) > 1$ indicates that two cell types are found within a 20 μm radius more frequently than expected by chance, while $g(r = 20) < 1$ indicates reduced proximity. A value of $g(r = 20) = 1$ indicates no spatial association. In this study, r = 20 μm was selected to approximate the distance between cell centroids in direct physical contact. Cell pairs with $g(r = 20) > 1$ and a 95% confidence interval entirely above 1 were considered significantly co-localised.

For this analysis, each myeloid population was designated as the “anchor” cell type to identify neighbouring cell populations that preferentially co-localise with it (Figure 5.3.15).

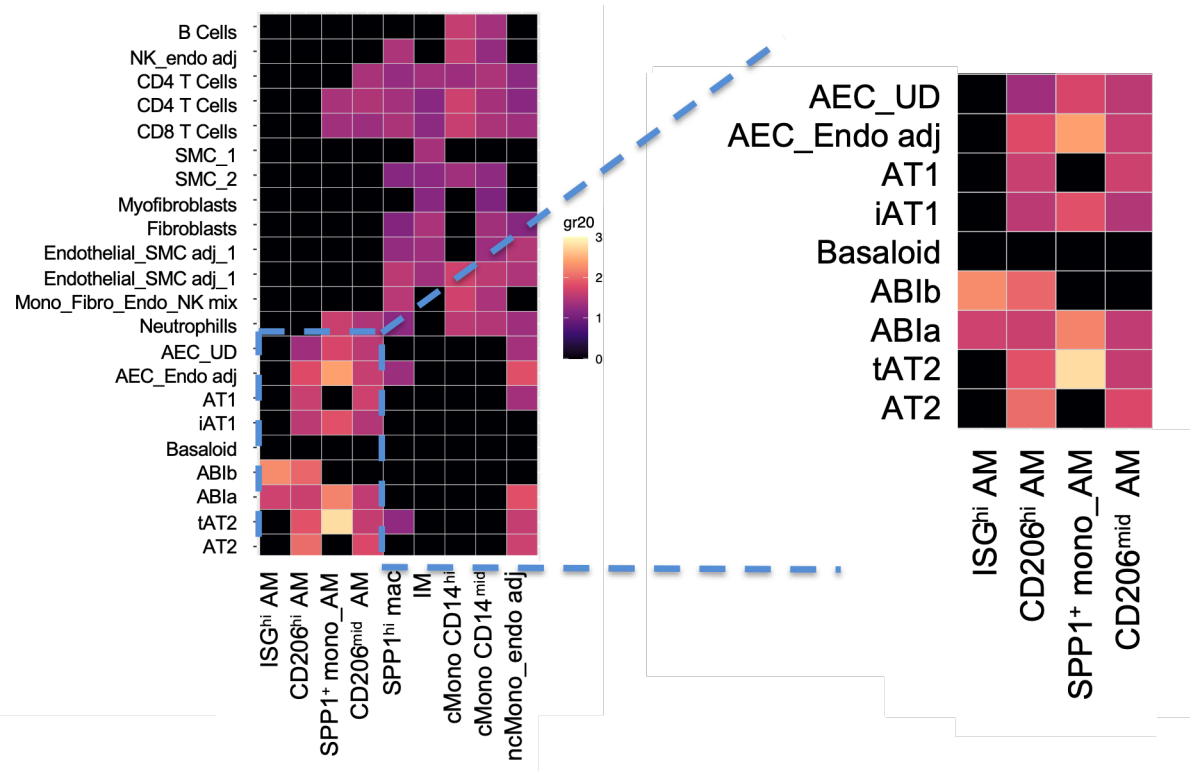


Figure 5.3.15. Cross PCF analysis examining cells cell pairs co-locating with macrophage and monocytes. *Heatmap showing spatial co-localisation between anchor cell populations - monocytes and macrophages, (x axis) and neighbouring cell populations (y axis). Only significant co-locating cell pairs coloured, significance defined by g(r = 20) > 1 and a 95% and lower bound of 95% CI > 1. Coloured intensity represents median g(r=20) value for each cell pair. Higher g(r=20) values represent how many times more frequently neighbouring cells (Cell type B), are found within a 20μm radius of the anchor cell above complete spatial randomness. Abbreviations: endo – endothelial cells, SMC – smooth muscle cells, adj – adjacent, AEC alveolar epithelial cell.*

The most abundant type 1 IFN-activated population, CD206^{hi} AMs, were co-located with all AEC populations. In contrast, the smaller ISG^{hi} AM subset-characterised by the highest levels of type 1 IFN signalling showed selective co-localisation with ABI populations. SPP1^{+} mono_AMs were preferentially co-located with transitional AT2 (tAT2), ABIa, and inflammatory AT1 (iAT1) epithelial populations, all of which represent intermediate epithelial states associated with injury and repair (Figure 5.3.15) with representative visualisations of the patterns of co-localisation (Figure 5.3.16).

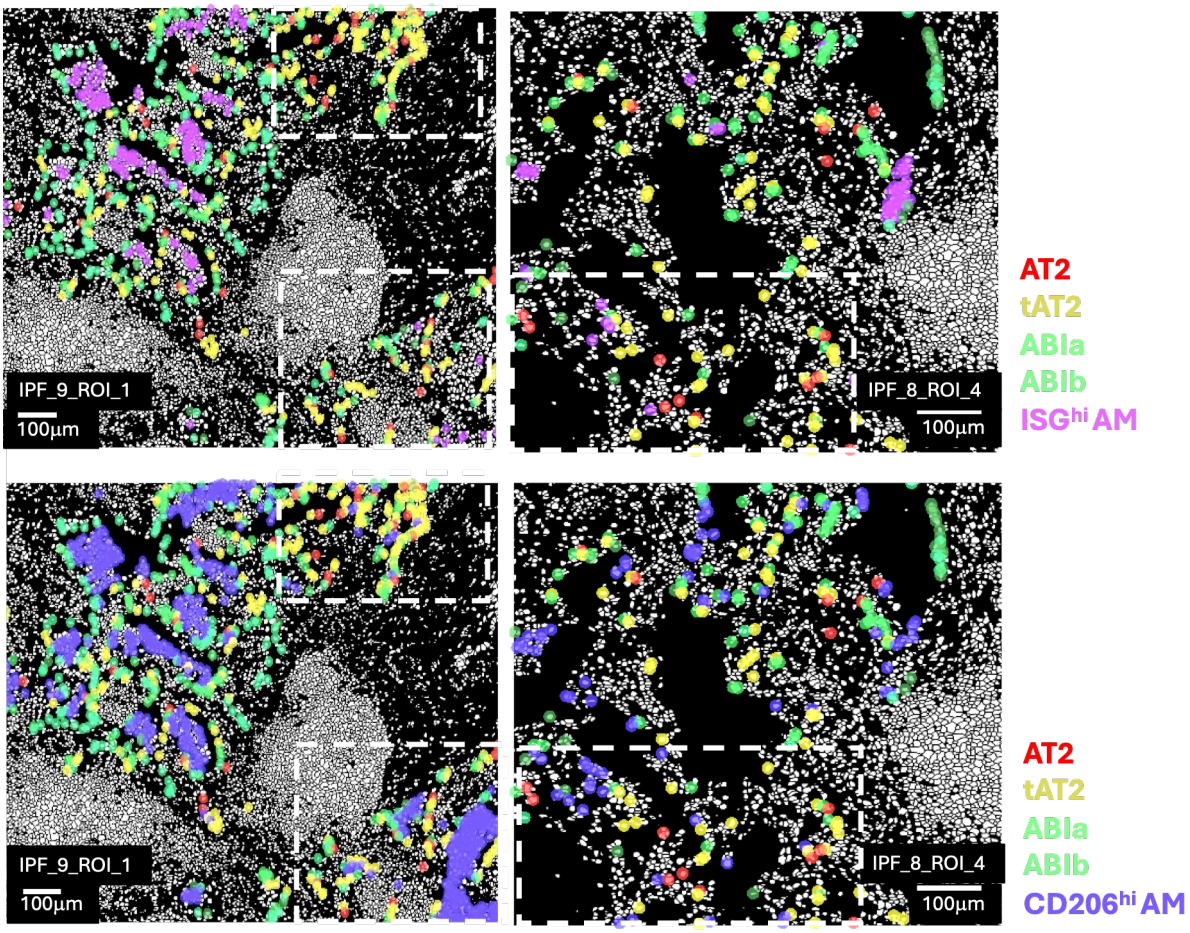


Figure 5.3.16. Spatial distribution of ISG^{hi} and CD206^{hi} AM subsets relative to AECs. *Representative cell centroid plots illustrating the spatial relationships identified by the quantitative co-localisation analysis (Figure 5.3.15) from two between ISG^{hi} AMs (magenta; top panels) and CD206^{hi} AMs (blue; bottom panels). ISG^{hi} AMs predominantly co-localise with aberrant basaloid intermediate (ABI; green) populations. In contrast, CD206^{hi} AMs co-localise with ABI populations but are also observed in proximity to AT2 (red) and transitional AT2 (tAT2; yellow) epithelial cells, most clearly demonstrated within the white dashed insets. Scale bars = 100 µm.*

In addition to epithelial associations, both SPP1^{+} mono_AM and CD206^{mid} AM populations were co-located with neutrophils and T lymphocytes (CD4^{+} and CD8^{+}). No further significant spatial associations were observed between AM populations and other immune, mesenchymal, or endothelial cell types.

In contrast, interstitial macrophage and monocyte populations exhibited broader spatial associations. SPP1^{hi} macrophages, interstitial macrophages, and lung monocytes were co-located with a wider range of lymphoid, mesenchymal, and endothelial cell populations. However, with the exception of SPP1^{hi} macrophages, which were co-located with tAT2 cells, interstitial myeloid populations did not show significant spatial association with AEC populations above the threshold for complete spatial randomness.

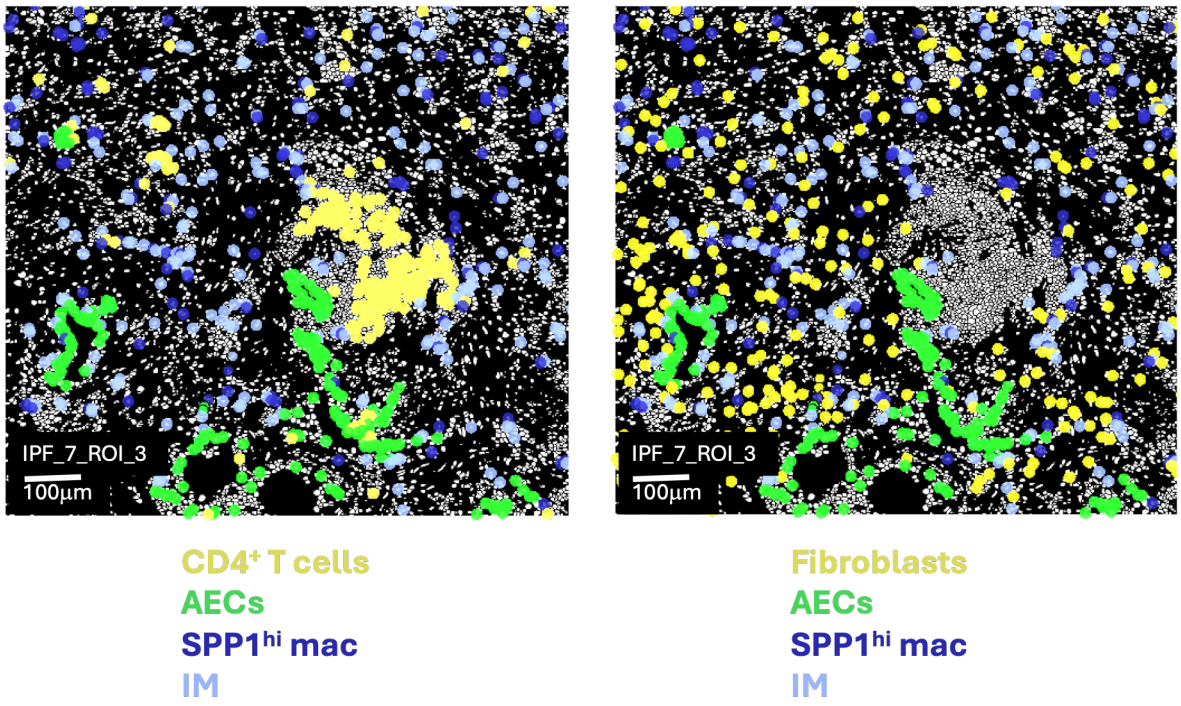


Figure 5.3.17. Spatial distribution and co-localisation of SPP1^{hi} macrophage and IM subsets with immune and structural cell populations. *Representative cell centroid plots illustrating the spatial relationships identified by the quantitative spatial analysis. SPP1^{hi} macs (dark blue) and IMs (light blue) are shown relative to selected immune and structural cell populations. CD4^{+} T cells are shown in yellow in the left panel and fibroblasts in yellow in the right panel. AEC populations (AT2, tAT2 and ABIa/b) are shown in green for spatial reference. Scale bars = 100 µm.*

5.3.9 Type 1 IFN-activated AM populations form a cell network with ABIs, tAT2 and iAT1

To determine whether the spatial co-location identified by cross-PCF analysis reflected direct cell–cell contact, adjacency cell network (ACN) and contacting cell network (CCN) analyses were performed. ACN analysis uses cell segmentation masks to identify cells that are both spatially co-located and in direct physical contact.

CCN analysis extends this approach by quantifying, for each cell-type pair (A–B), the proportion of cells of type A that are in direct contact with at least one cell of type B. Statistical significance is assessed by generating a null distribution under complete spatial randomness (CSR), achieved by permuting cell-type labels 1,000 times while preserving spatial coordinates. A contact z-score is calculated to quantify deviation from CSR, and significance is determined using associated p-values. Cell pairs were filtered to retain those that were significantly co-located in cross-PCF analysis ($g(r = 20\ \mu m) > 1$), with positive z-scores and false discovery rate (FDR)-adjusted p-values < 0.05. The resulting CCN therefore identifies cell pairs that are both spatially enriched and in direct physical contact at frequencies greater than expected by complete spatial randomness.

Global CCN results were visualised using bubble plots, revealing that cells of similar lineage preferentially formed contact networks. These included interactions among alveolar epithelial cell (AEC) subsets and within lymphocyte populations (Figure 5.3.18).

Within the epithelial compartment, AEC populations were found to be in direct contact with one another; however, interactions between intermediate epithelial states—such as tAT2–ABIa and ABIb–basaloid pairs—exhibited higher contact z-scores, indicating preferential interactions beyond those expected under CSR. These preferential contacts are consistent with the proposed differentiation of transitional epithelial states (Figure 5.3.18), in which neighbouring populations represent progressively differentiated epithelial states.

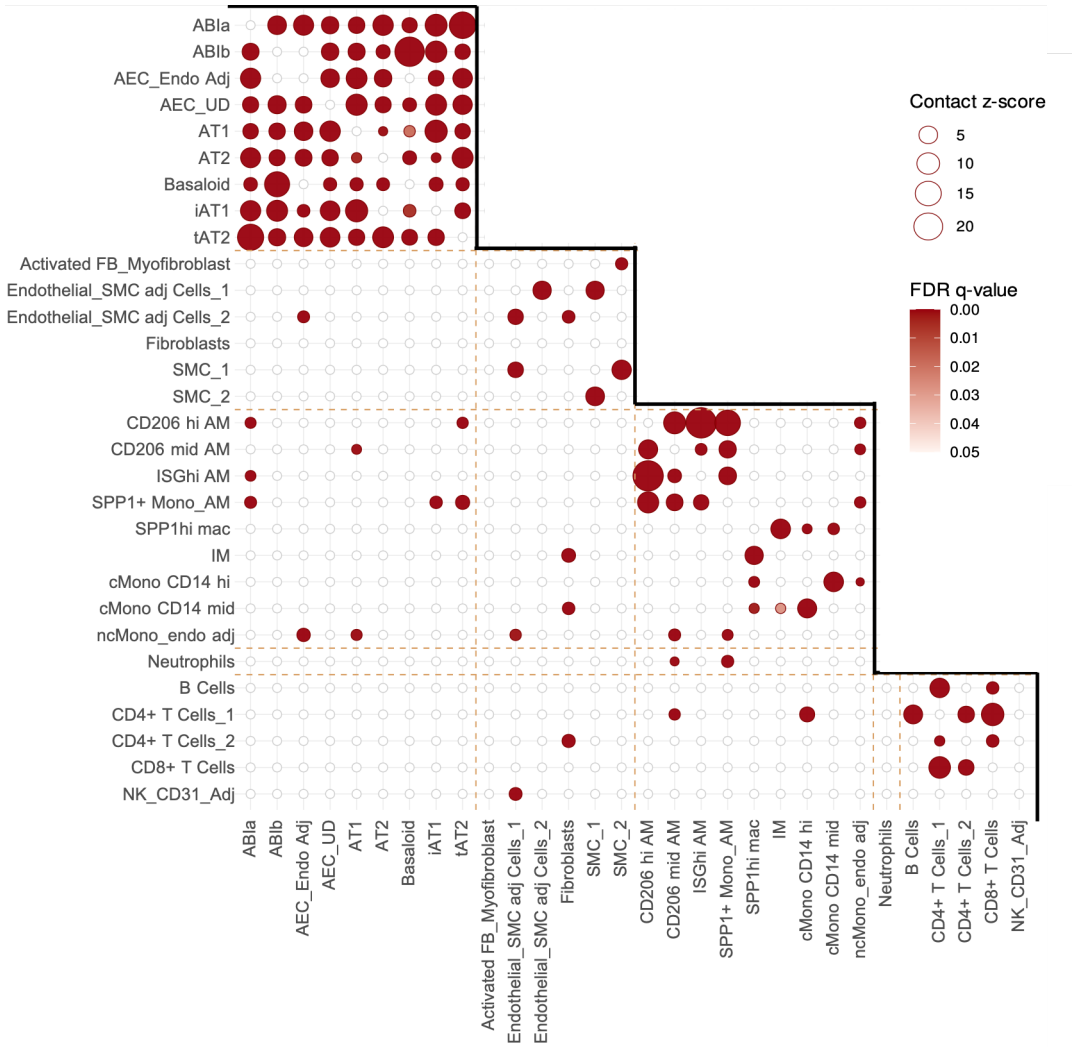


Figure 5.3.18. Global cell contacting network (CCN) analysis. *Bubble plot depicting all pairs of co-locating cells in direct physical contact at a frequency greater than expected under complete spatial randomness (CSR). Only pairs of cells meeting criteria for significance (g(r = 20 µm) > 1, with positive z-scores and false discovery rate (FDR)-adjusted p-values < 0.05 shown (filled bubbles). Bubbles correspond to cell pairs indicated on x and y axis. Size of the bubble represents contact z score a measure of the degree of deviation above CSR. Cells grouped by major cell type (epithelial cells, mesenchymal cells and endothelial cells, monocytes and macrophages, neutrophils and lymphocytes), separated by hatched lines to facilitate interpretation. Abbreviations; endo – endothelial cells, SMC – smooth muscle cells, adj - adjacent.*

Myeloid populations segregated into two distinct contact networks. Alveolar macrophage (AM) populations formed a cohesive network characterised by frequent direct contacts between AM subsets, whereas interstitial macrophages (IMs), SPP1^{hi} macrophages, and monocyte populations formed a separate network. This organisation was consistent with spatial localisation observed in centroid maps, where AMs occupied the alveolar lumen and interstitial populations were distributed within the tissue interstitium (Figure 5.3.18) and (Figures 5.3.16 and 5.3.17 for visual representation). Tissue macrophage subsets, including IMs and SPP1^{hi} macs appear visually dispersed throughout the interstitium (Figure 5.3.17). However, CNN analysis demonstrated that direct contacts between these populations occurred more frequently than expected under CSR indicating that their spatial distribution is organised rather than random.

Unexpectedly, fibroblasts and myofibroblasts were not found to be in direct contact with one another, suggesting that these matrix-producing populations may occupy distinct microenvironments rather than a shared niche. More broadly, interactions between epithelial, mesenchymal, lymphoid, and neutrophil populations were limited, with the exception of a CD4^{+} T cell subset (CD4^{+} T cell_2) that exhibited contact with fibroblasts. No additional statistically significant immune–structural interactions were identified at this level.

Overall, this analysis revealed that direct cell–cell contact occurred predominantly within rather than between cellular lineages, suggesting that the architectural remodelling associated with IPF, cellular organisation remains structured. Among interactions between different cell lineages that majority involved myeloid populations. These interactions were therefore examined in greater detail in the subsequent analysis.

To focus specifically on myeloid interactions, CCN analyses were visualised using contacting network plots with monocyte and macrophage populations designated as anchor nodes (cell type A). In this representation, edges denote statistically significant contacts ($g(r = 20\ \mu m) > 1$, z-score > 0, FDR $p < 0.05$) and are weighted by the frequency of detected interactions above CSR (Figure 5.3.19).

This analysis revealed two distinct interaction networks. AM populations formed a network primarily with epithelial populations at the alveolar barrier, whereas SPP1^{hi} macrophages and IM populations formed a separate network involving classical monocytes, fibroblasts, and CD4^{+} T cells within the interstitium.

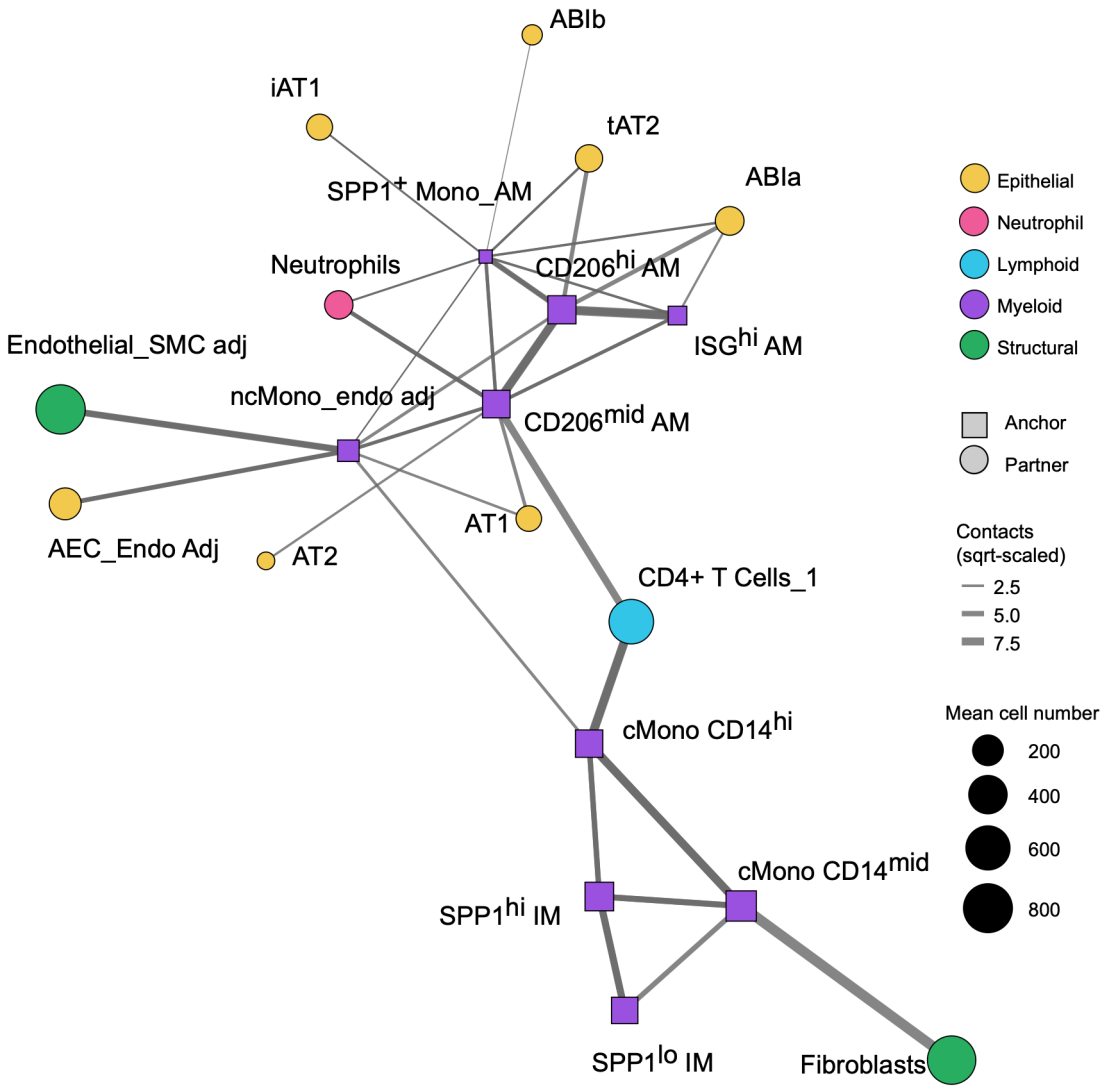


Figure 5.3.19. Cell–cell contact network analysis of monocytes and macrophages.
Network plots depicting spatial interactions between cell populations. Monocyte and macrophage populations are defined as anchor populations (Cell type A) and are represented as square nodes. Circular nodes indicate neighbouring cell populations and are coloured according to cell lineage. Node size reflects the relative abundance of each cell population. Edges (lines) representing contact between the anchor cell population and the neighbouring cell types. Edges weighted by number of contacts between the cell pair. Edges only present when contact between a cell pair occurs more frequently than would be expect under complete spatial randomness and filtered to include cell pairs where (g(r = 20 µm) > 1, z-score > 0, false discovery rate adjusted p < 0.05). Abbreviations; *endo – endothelial cells, SMC – smooth muscle cells, adj – adjacent populations.*

At the alveolar barrier, detailed examination demonstrated that type 1 IFN–activated AM populations (CD206^{hi} AM, ISG^{hi} AM and SPP1^{+} mono_AM) formed direct contacts selectively with intermediate epithelial states. While cross-PCF analysis suggested that CD206^{hi} AMs were co-located with all epithelial populations, CCN analysis refined this observation, demonstrating that these cells were in direct contact specifically with tAT2

and ABIa populations. In addition, whilst ISG^{hi} AM are in *close proximity* to both ABIa and ABIb epithelial populations observed in the cross-PCF analysis, the results from the CCN demonstrate this population is only *direct contact* with ABIa populations relative to CSR (Figure 5.3.20). In contrast, mature AT2 and AT1 cells were found to be in contact predominantly with CD206^{mid} AM populations, which exhibited lower levels of type 1 IFN signalling (Figure 5.3.21).

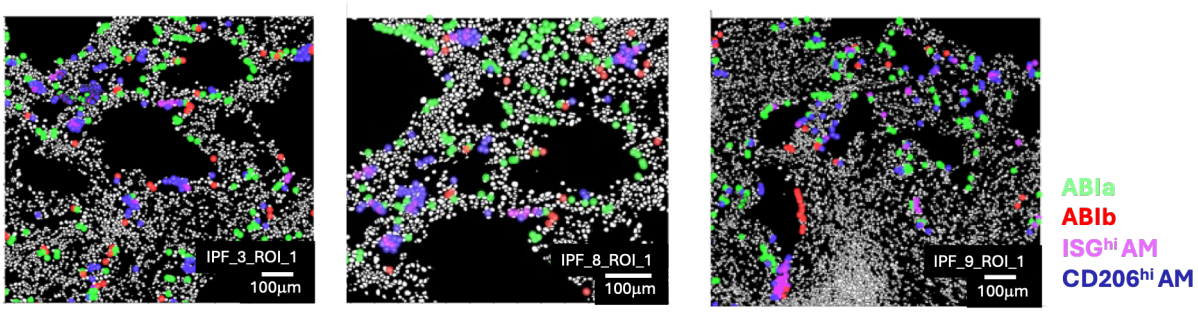


Figure 5.3.20. Representative cell centroid plots illustrating the spatial relationships between ISG^{hi} and CD206^{hi} AMs and ABIa and b epithelial populations identified by CCN analysis. *Representative ROIs demonstrate that both ISG^{hi} AMs (magenta) and CD206^{hi} AMs (blue) are present within regions containing ABIa (green) and ABIb (red) epithelial cells. However, while AMs are frequently observed in direct contact with ABIa cells, they are typically located in close proximity to but not immediately adjacent to ABIb cells. This is consistent with the direct contact network analysis, which did not identify enrichment of direct ISG^{hi} AM–ABIb contacts despite their close spatial proximity. Scale bars = 100 µm.*

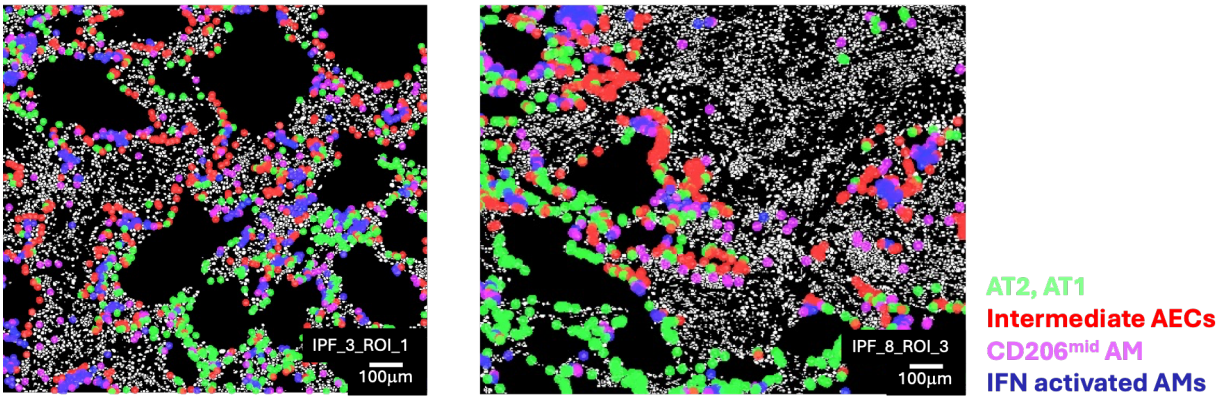


Figure 5.3.21. Spatial distribution and co-localisation of SPP1^{hi} macrophage and IM subsets with immune and structural cell populations. *Representative cell centroid plots illustrating the spatial relationships identified by the quantitative spatial analysis. SPP1^{hi} macs (dark blue) and IMs (light blue) are shown relative to selected immune and structural cell populations. CD4^{+} T cells are shown in yellow in the left panel and fibroblasts in yellow in the right panel. AEC populations (AT2, tAT2 and ABIa/b) are shown in green for spatial reference. Scale bars = 100 µm.*

Together, these findings demonstrate that type 1 IFN–activated alveolar macrophages form direct and selective cellular interactions with intermediate epithelial states at the alveolar barrier. This spatial specificity supports a model in which epithelial dysfunction defines a local niche associated with interferon-driven myeloid activation in IPF.

5.4 Discussion

In this chapter, I profiled and spatially analysed myeloid subsets in IPF lung tissue, identifying discrete type 1 IFN –activated myeloid states localised to the alveolar barrier. These populations showed a consistent enrichment in early and intermediate disease and were spatially associated with intermediate alveolar epithelial cell (AEC) states, including aberrant basaloid intermediates (ABIs), transitional AT2 (tAT2), and inflammatory AT1 (iAT1) cells. These epithelial populations exhibited increased expression of markers of cellular injury (ICAM-1), senescence (p53, p16, TNF-α), pSTING, and cytoplasmic IFN-β compared to homeostatic AT2 and AT1 cells. Spatial analyses demonstrated that type 1 IFN-activated macrophages were not uniformly distributed but instead localised within microenvironments enriched for these intermediate epithelial states, supporting the hypothesis that epithelial dysfunction at the alveolar barrier is associated with local activation of type 1 IFN signalling in neighbouring myeloid cells.

These findings extend the observations described in the previous chapter, in which transcriptomic analyses identified monocyte and macrophage subsets with increased type 1 IFN signalling in IPF. While the prior study demonstrated enrichment of interferon-responsive myeloid populations at the alveolar barrier, the present IMC-based analysis provides spatial resolution, revealing that this activation is not a global feature of all myeloid cells, but is instead restricted to specific subsets within defined tissue niches. In particular, alveolar macrophages exhibited higher type 1 IFN activity compared to interstitial macrophages and circulating monocyte populations. Of note however $CD206^{mid}$ AMs did not exhibit high type 1 IFN protein expression suggesting that local microenvironmental cues, rather than lineage alone, are key determinants of this phenotype.

Consistent with this interpretation, cells with a classical monocyte phenotype were predominantly localised to the interstitium and exhibited relatively low levels of type 1 IFN pathway activation. In contrast, certain IFN-active alveolar macrophage populations, including ISG^{hi} and $SPP1^{+}$ mono_AM subsets, do also express CD14, which may indicate a monocyte-derived origin and suggest that these cells have undergone local reprogramming within the alveolar niche. The relative absence of undifferentiated monocytes within the alveolar space in this study is consistent with the transcriptomic analysis of BAL samples, in which such populations were also infrequent. Together, these findings support a model in which the alveolar microenvironment exert a greater influence on monocyte to AM differentiation compared to the lung interstitium.

Analysis of disease stage further demonstrated that type 1 IFN pathway activation is most prominent in early and intermediate stages of IPF, with reduced expression in advanced fibrosis. This pattern mirrors the regional transcriptomic findings described previously, in which increased type 1 IFN signalling was observed in upper lobe (less

fibrotic) compared to lower lobe (more fibrotic) tissue. Importantly, the use of histologically defined regions of interest in this study addresses a key limitation of regional sampling approaches, namely the spatial heterogeneity of IPF, in which early injury and advanced fibrosis coexist within the same anatomical region. By resolving disease stage at the microscopic level, this analysis demonstrates that type 1 IFN activation is a feature of early pathological niches rather than established fibrotic tissue, suggesting a role in disease initiation or early progression.

High-resolution epithelial clustering identified multiple intermediate AEC states, including tAT2, ABI, and iAT1 populations, consistent with those described in recent transcriptomic studies of IPF and experimental models of lung injury[63, 86, 293, 295, 300]. These populations are increasingly recognised as key features of impaired epithelial repair, characterised by failed AT2-to-AT1 differentiation, activation of stress pathways, and acquisition of senescence-associated phenotypes. While similar transitional states are observed transiently during normal repair[295], they persist and expand in models of chronic injury and in IPF[294, 296, 297], indicating a shift from adaptive to maladaptive regeneration.

Recent experimental studies suggest that these intermediate epithelial states may play a direct role in fibrogenesis. For example, disruption of epithelial proteostasis in murine models results in accumulation of ABI-like populations and the development of fibrosis in the absence of exogenous injury, supporting a causal role for these cells in disease pathogenesis[307]. In the present study, these populations exhibited increased expression of markers associated with cellular stress, DNA damage, and senescence, consistent with prior transcriptomic descriptions[293, 294, 295]. Despite differences in nomenclature across studies, these populations share a conserved transcriptional programme characterised by impaired differentiation and activation of injury-associated pathways[297].

Intermediate AEC populations in this study also showed evidence of pattern recognition receptor activation and inflammatory cytokine production. Although the antibody panel limited comprehensive pathway mapping, increased expression of phosphorylated STING, IFN-β, and TNF-α provides evidence consistent with activation of innate immune sensing pathways, including cGAS–STING signalling[298, 299]. One potential mechanism linking epithelial stress to cytokine production is the senescence-associated secretory phenotype (SASP)[64], through which senescent cells release inflammatory mediators that can modulate the local microenvironment. Increasing evidence suggests that cGAS–STING signalling is activated in senescent cells, potentially through accumulation of cytosolic DNA derived from mitochondrial or nuclear damage[186, 187, 191].

Supporting this, elevated levels of mitochondrial and circulating double-stranded DNA have been reported in patients with IPF[308], particularly in more progressive disease,

providing a potential source of endogenous ligands capable of activating PRR pathways. In this context, the increased expression of pSTING and IFN-β observed in intermediate epithelial populations in this study supports a link between epithelial injury, innate immune activation, and local interferon production. While these observations are associative, they raise the possibility that dysfunctional epithelial cells contribute to the establishment of an interferon-rich microenvironment within the alveolar niche.

Spatial analysis further refined this relationship. Although alveolar macrophages were localised to the alveolar barrier, not all macrophage populations within this compartment exhibited type 1 IFN activation. Specifically, $CD206^{mid}$ alveolar macrophages showed low expression of interferon-related proteins, indicating that localisation alone is insufficient to explain the activated phenotype. Instead, type 1 IFN-activated macrophages were selectively associated with intermediate epithelial states, including ABIs, tAT2, and iAT1 populations. In contrast, mature AT1 and AT2 cells were preferentially associated with macrophage populations exhibiting lower interferon activity.

These findings suggest that type 1 IFN activation is not simply a feature of anatomical localisation but is instead linked to interactions with specific epithelial states associated with injury and dysfunctional repair. This supports a model in which the intermediate epithelial microenvironment provides signals that promote the development of IFN-activated myeloid phenotypes.

One methodological consideration relates to epithelial cell annotation. Annotation in the present study was supported by the combined expression of KRT8, KRT5, SFTPC, SCEL and markers of epithelial dysfunction together with comparison to published transcriptomic and protein-based reference datasets. Ongoing work specifically integrating a complementary IMC antibody panel that includes additional airway epithelial markers but also KRT17, in overlapping regions of interest. This will broaden epithelial cell annotation beyond alveolar epithelial cells and also facilitate closer comparison with published transcriptomic definitions of aberrant basaloid cells.

A key limitation of this study is the reliance on antibody-based imaging, which restricts cell annotation and pathway analysis to predefined markers. However, this targeted approach complements prior transcriptomic analyses and enables hypothesis-driven investigation of specific pathways within their spatial context. In addition, while strong spatial associations were identified, the observational nature of this study does not establish causality. Whether epithelial dysfunction directly drives interferon activation in neighbouring macrophages requires functional validation, which is addressed in the subsequent chapter.

5.5 Conclusion

In summary, this study demonstrates that type 1 IFN–activated macrophages in IPF lung tissue are spatially restricted to the alveolar barrier and are enriched in early stages of disease. These macrophages are selectively associated with intermediate epithelial states, including aberrant basaloid intermediates, transitional AT2, and inflammatory AT1 cells.

Intermediate epithelial populations exhibit features of cellular injury, senescence, and activation of innate immune pathways, including evidence of cGAS–STING signalling and production of inflammatory cytokines such as IFN-β and TNF-α.

Together, these findings support a model in which dysfunctional epithelial states define a local microenvironment associated with type 1 IFN activation in neighbouring myeloid cells. This spatial relationship provides a potential mechanistic link between epithelial injury and immune activation in IPF and highlights interferon signalling as a feature of early disease-associated niches.

Chapter 6 Alveolar epithelial–myeloid interactions using an alveolar spheroid injury model

6.1 Introduction

In this chapter, I aim to develop an in vitro three-dimensional (3D) model of alveolar injury to recapitulate alveolar epithelial dysfunction observed in IPF. This model will be used to investigate epithelial–myeloid cell interactions in early disease.

3D organoid culture systems have emerged as an alternative to conventional monolayer culture since the generation of mouse intestinal enteroids in 2009[309]. These approaches involve culturing stem or progenitor cells within an extracellular matrix (ECM)-based scaffold, enabling self-organisation into structures that partially recapitulate tissue architecture and cellular heterogeneity. Organoids can be derived from either adult tissue–resident progenitor cells or induced pluripotent stem cells (iPSCs).

The in vitro study of alveolar epithelial type 2 (AT2) cells has historically been limited by conventional culture systems, in which cells rapidly lose their cuboidal morphology, surfactant production, and progenitor capacity within days[310, 311]. This restricts investigation of AT2 injury responses, regeneration, and differentiation into alveolar type 1 (AT1) cells. While some differentiation has been demonstrated under defined conditions[73], robust modelling of adult human AT2 cell behaviour in vitro has remained challenging[312].

The application of 3D culture systems to alveolar epithelial cells has enabled significant advances. Early work demonstrated that primary human AT2 cells cultured in ECM with fibroblast support could form long-term, self-renewing alveolar spheroids ("alveospheres") that retain key AT2 features[313]. Subsequent studies established feeder-free systems capable of maintaining AT2 identity, including expression of surfactant-associated markers and partial acquisition of AT1-associated features[228, 229] .

iPSC-derived AT2-like cells provide an alternative approach, offering scalability and experimental flexibility. However, maintenance of AT2 phenotype in these systems typically requires factors such as dexamethasone, cyclic AMP (cAMP), and 3-isobutyl-1-methylxanthine (IBMX), which have immunomodulatory effects that may confound studies of epithelial–immune interactions[314].

Work from Alysandratos et al.,[315] demonstrated that both primary and iPSC-derived AT2 organoids retain core transcriptional features of ex vivo AT2 cells, but primary cells more closely reflected a mature phenotype in contrast to iPSC-derived cells that exhibited increased proliferative capacity. Notably, primary AT2 organoids showed enrichment of

immune and stress-response pathways, suggesting relevance for modelling epithelial injury responses.

Building on these approaches, primary alveolar spheroids were adapted to model AT2 dysfunction and intermediate epithelial states described in IPF. This provides a platform to investigate early epithelial injury and its interaction with immune cells.

The specific objectives of this chapter were to:

1. Establish long-term alveolar spheroids using primary AT2 cells
2. Model AT2 dysfunction and intermediate epithelial states associated with IPF
3. Investigate epithelial–myeloid interactions and type 1 IFN signalling using co-culture systems and pathway inhibition

6.2 Study Design and Methods

6.2.1 Overall Study Design

The schematic workflow used in this section is outlined in Figure 4.2.1 with detailed experimental methods described in sections 2.1.9 – 2.1.21.

6.2.2 Lung Donor selection Criteria and type 2 alveolar epithelial cell isolation

The initial step in this workflow involved the isolation and purification of primary adult AT2 cells. This work was conducted in collaboration with the Oxford Radcliffe Biobank (ORB) under project ID 22/8097. Patients were recruited under a regional ethics committee approved study (13/SC/0420).

Prior to surgery, patients were screened by members of the Oxford Radcliffe Biobank (ORB) for eligibility and provided informed consent if inclusion criteria were met: (i) age 18–75 years; (ii) never-smokers or ex-smokers with a smoking history of <20 pack-years and abstinent for >5 years; (iii) undergoing thoracic surgery for localised malignant or non-malignant lung disease; and (iv) no evidence of diffuse or parenchymal lung disease on pre-surgery CT imaging. Patients were consented that excess lung tissue following surgical resection, not required for clinical histopathological assessment would be used for research purposes. On the day of surgery patients reporting symptoms of respiratory infection were excluded. Members of the research team were anonymised to patient clinical details in line with ORB protocols.

The anatomical location of tissue sampling varied between donors depending on the surgical procedure and site of pathology. In all cases, a senior histopathologist identified macroscopically normal lung parenchyma distant from the primary lesion, from which 1–2 g of tissue was allocated for research.

Lung tissue processing is described in detail in Section 2.1.9. Briefly, lung tissue was stored at 4 °C, transported on ice, and processed immediately to maximise recovery of viable AT2 cells. Tissue was mechanically and chemically digested to generate a single-cell suspension. Cells were incubated with a primary mouse IgM antibody targeting HTII-280, a surface marker specific for AT2 cells, followed by anti-mouse IgM secondary antibodies conjugated to either magnetic beads or fluorescent tags. Positive selection of HTII-280^{+} cells was performed on the same day to preserve cell viability. Characterisation of isolated cells was performed by flow cytometry, and

immunofluorescence staining to assess purity and minimise contamination from other cell populations that could outgrow AT2 cells in culture or impact downstream analyses.

6.2.3 Generation and characterisation of AT2 spheroids

Following positive selection, primary AT2 cells were cultured in extracellular matrix (Matrigel) using serum-free, feeder-free, chemically defined media to minimise variability. Media formulations supplemented with growth factors to support AT2 cell proliferation and expansion have been described in the literature, and two formulations were evaluated in this study[228, 229]. Following in-house comparison, the formulation described by Katsura et al. was selected. This later became commercially available as StemCell Technologies Alveolar Organoid Expansion Medium (AVOE), which was used for all subsequent experiments, including bleomycin titration, THP-1 culture and co-culture studies. During passage colony forming efficiency (CFE) was calculated independently for each passage as the number of viable cells recovered after 2 weeks culture divided by the number of viable cells plated at the start of that passage. Cells allocated for downstream analyses or cryopreservation were excluded from the initial cell count before culture used in this calculation. Expanded AT2 cell populations were characterised using immunohistochemistry, flow cytometry, and quantitative PCR following both early and prolonged culture. Cellular phenotype in culture was assessed and compared with freshly isolated lung tissue.

6.2.4 Development of a lung injury model and co-culture with THP-1 cells

In the third stage of the workflow, an injury–fibrosis model was developed to recapitulate AT2 cell dysfunction observed in intermediate alveolar epithelial states described in the previous chapter, as well as in single-cell transcriptomic studies of IPF patients and experimental models of pulmonary fibrosis. Mature AT2 spheroids were treated with increasing concentrations of bleomycin and harvested at multiple time points for quantitative PCR analysis of transcripts associated with AT2 dysfunction and transitional epithelial states. This experiment was designed to identify the bleomycin concentration and post-injury time point that induced a reproducible injury-associated transcriptional response to inform subsequent co-culture experiments. As the experimental design included two independent variables (bleomycin concentration and time post-injury), gene expression data were analysed using a linear mixed-effects model to account for both the impact of time and bleomycin concentration (treatment) included as fixed effects. The main effects of treatment and time assessed changes in gene expression across bleomycin concentrations and the culture period respectively. A treatment x time interaction term was included to determine whether the effect of bleomycin treatment differed over time. Pre-specified post hoc comparisons were performed between each

bleomycin concentration and the untreated control (0 μg/ml) at each time point, with p values adjusted for multiple testing.

THP-1 a human monocyte-like cell line expressing a functional interferon alpha receptor (IFNAR), along with matched IFNAR$^{-/-}$ counterparts lacking subunit 2, were provided by the Rehwinkel group and used for co-culture experiments to investigate injured AT2 spheroid–myeloid interactions. THP-1 cells were used rather than primary monocytes to provide a reproducible model for investigating monocyte - AT2 interactions while reducing donor-to-donor variability. The availability of matched IFNAR expressing and IFNAR$^{-/-}$ THP-1 cell lines also enabled assessment of the contribution of IFN response signalling on epithelial transcriptomic changes, which was not feasible using primary human monocytes. Although THP-1 cells do not fully recapitulate the phenotype and functional heterogeneity of primary monocytes, they provided a suitable model for these initial mechanistic studies.

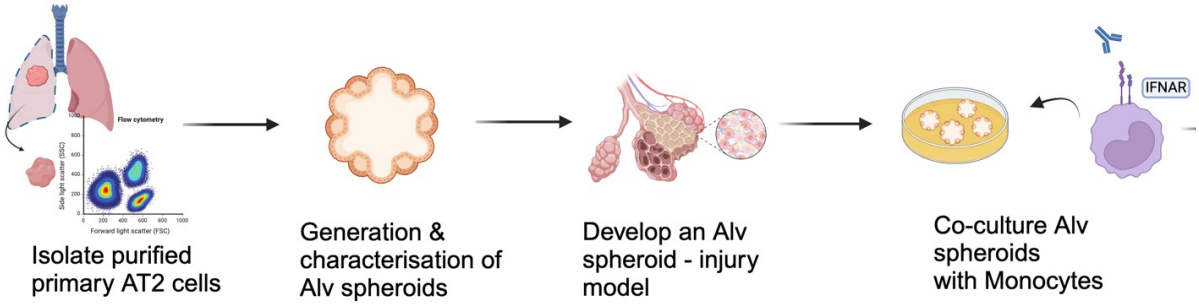


Figure 6.2.1. Experimental workflow. *Schematic outlining the main steps from primary adult AT2 cell isolation established of a long-term in vitro culture system through to coculture of AT2 spheroids and myeloid like THP-1 cells.*

6.3 Results

6.3.1 Isolation of high purity primary human AT2 cells from donor lungs

Primary human AT2 cells were isolated from dissociated distal lung parenchyma using the HTII-280 antibody, which recognises a surface marker specific to AT2 cells[316]. Initial validation by immunohistochemistry demonstrated concordance between HTII-280 labelling and expression of the established AT2 marker, pro-surfactant protein C (ProSPC), confirming specificity for human AT2 cells (Figure 6.3.1). Specificity of staining was assessed using no-staining isotype controls, with low background fluorescence under the same imaging conditions and thresholds. Positive control tissue confirmed expected marker localisation and co-localisation. Given the two-colour widefield design and the use of spectrally distinct fluorophores (HTII-280; Excitation 570nm, Emission 603nm) and ProSPC; Excitation 750nm, Emission 775nm) major channel overlap was not expected.

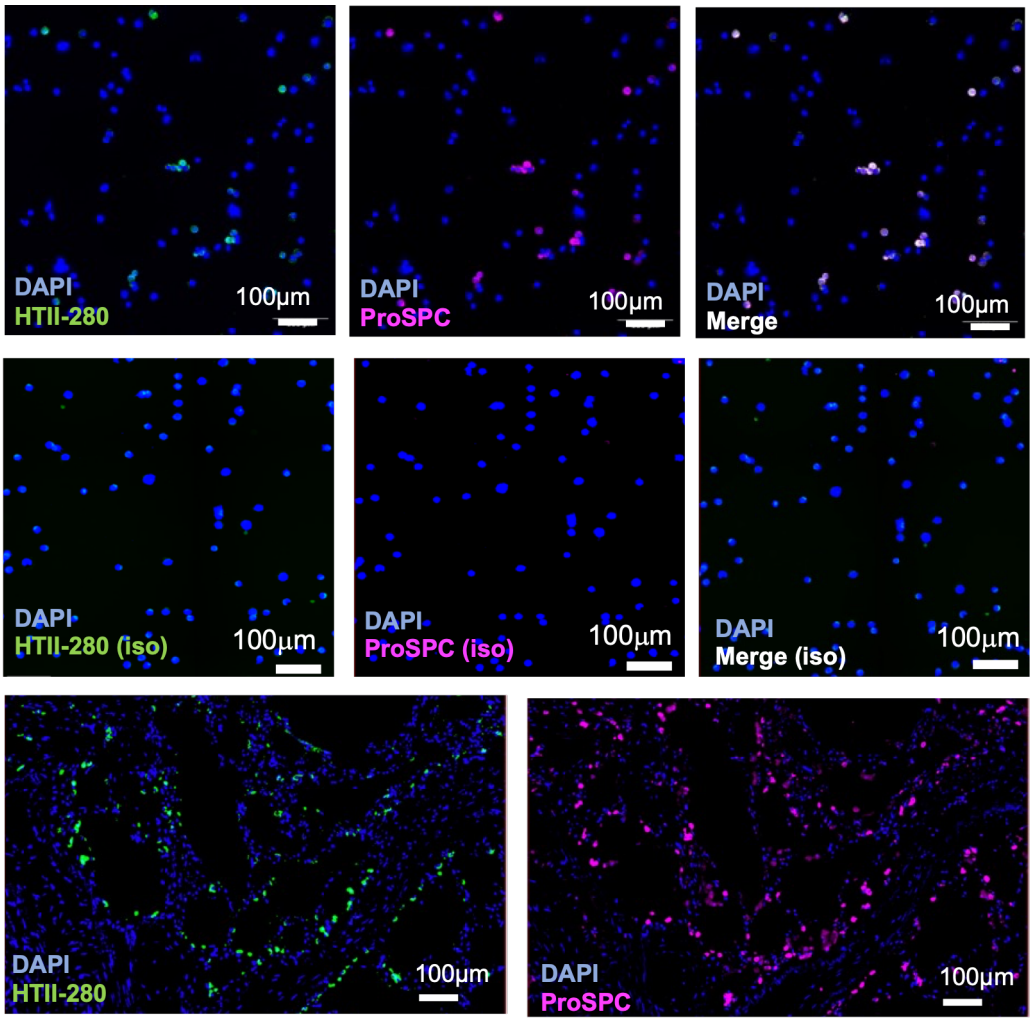


Figure 6.3.1. Co-expression of HTII-280 and pro-SPC confirms specificity to AT2 cells. *Following enzymatic digestion of lung tissue, single-cell suspensions were cytospun and stained for HTII-280 and pro-surfactant protein C (pro-SPC) and counterstained with DAPI. Co-localisation of these markers confirms specificity for alveolar type II epithelial cells. Specificity of staining was assessed using no-staining isotype controls (middle panel), and antibody specificity to type 2 AEC lining alveoli confirmed with positive tissue controls using IPF lung tissue sections (bottom panel).*

A magnetic-activated cell sorting (MACS)–based strategy was initially employed to enable rapid, same-day isolation following tissue collection. However, flow cytometry analysis of MACS-enriched populations revealed persistent contamination by non-epithelial and non-AT2 cell populations, despite optimisation of blocking conditions, antibody concentration, incubation time, and sequential column enrichment (Figure 6.3.2).

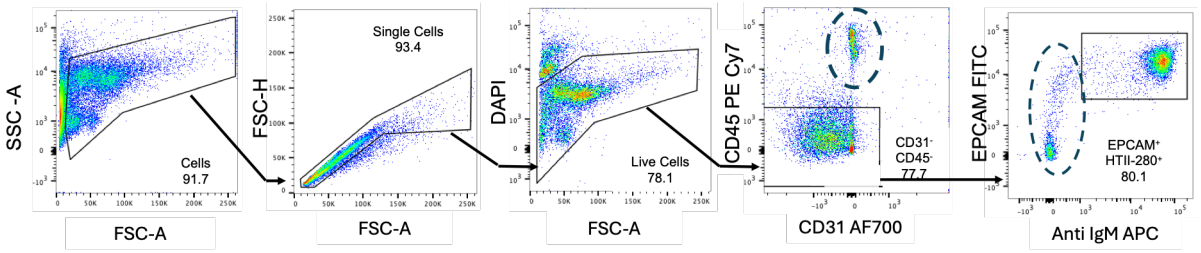


Figure 6.3.2. Magnetic activated cell sorting (MACS) resulted in persistent contamination of non-epithelial cell. *Flow cytometry analysis and representative plots of positively selected population following MACS isolation of lung digests using HTII-280 primary antibody and anti IgM conjugated beads. The positive selection strategy included pretreatment with FC block, a 60 min incubation of primary antibody at 4 degrees and a 2nd column enrichment step. Representative flow cytometry plots are shown and illustrate following exclusion of debris, doublets and dead cells contamination of $CD45^+$ immune cells, $CD31^+$ endothelial cells, $CD45^-CD31^-EPCAM^-$ cells and $EPCAM^+$ $HTII\text{-}280^-$ epithelial cells. Contaminating populations depicted with dashed circles.*

To improve purity, a fluorescence-activated cell sorting (FACS) approach was adopted. Viable epithelial AT2 cells were defined as $EPCAM^+$ $HTII\text{-}280^+$ cells following exclusion of doublets, dead cells, and $CD45^+$ and $CD31^+$ populations (Figure 6.3.3). $HTII\text{-}280^+$ cells comprised approximately 28–30% of the $EPCAM^+$ fraction, consistent with previous reports[228, 317]. Across donors, these cells represented 1–4% of total live single cells, yielding approximately 2–2.5 × 10^5 cells per sample.

FACS isolation consistently achieved >95% purity, as confirmed by flow cytometry and ICC, while preserving cell viability (Figure 6.3.3 and 6.3.4).

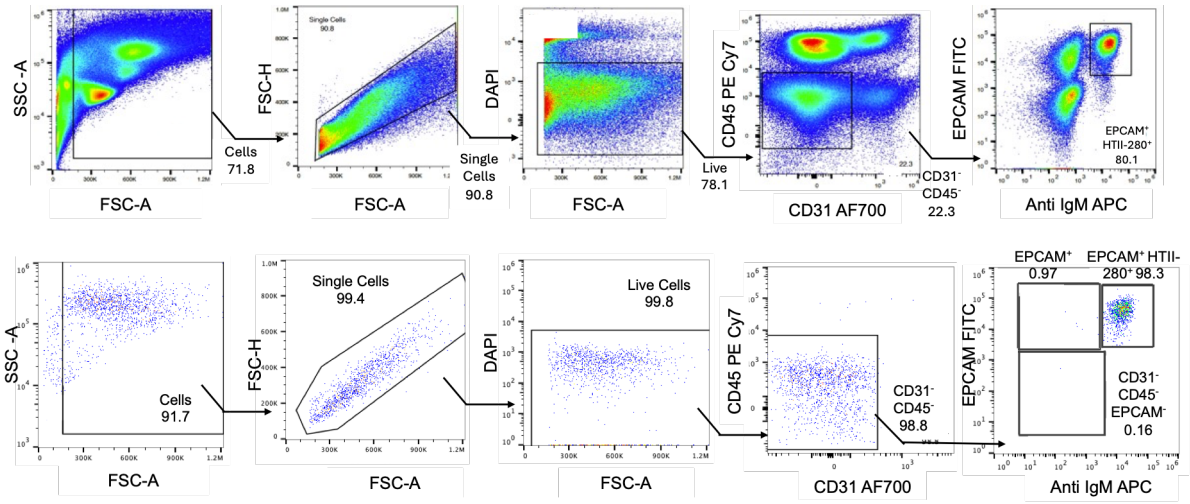


Figure 6.3.3. Fluorescence activated cell sorting (FACS) enabled high purity isolation of HTII-280⁺ cells. *Following enzymatic digestion of lung tissue, single-cell suspensions were stained with primary HTII-280 antibody, followed by a secondary anti-mouse IgM antibody and markers to exclude immune and structural cell populations. Top panel - Gating strategy used for FACS, including exclusion of debris, CD45⁺ and CD31⁺ immune and endothelial cells, doublets and dead cells, prior to positive selection of EPCAM⁺ HTII-280⁺ epithelial cells. Bottom panel: Flow cytometry analysis of the positively selected population demonstrating purity >95%, minimal contaminating populations, and no uptake of DAPI.*

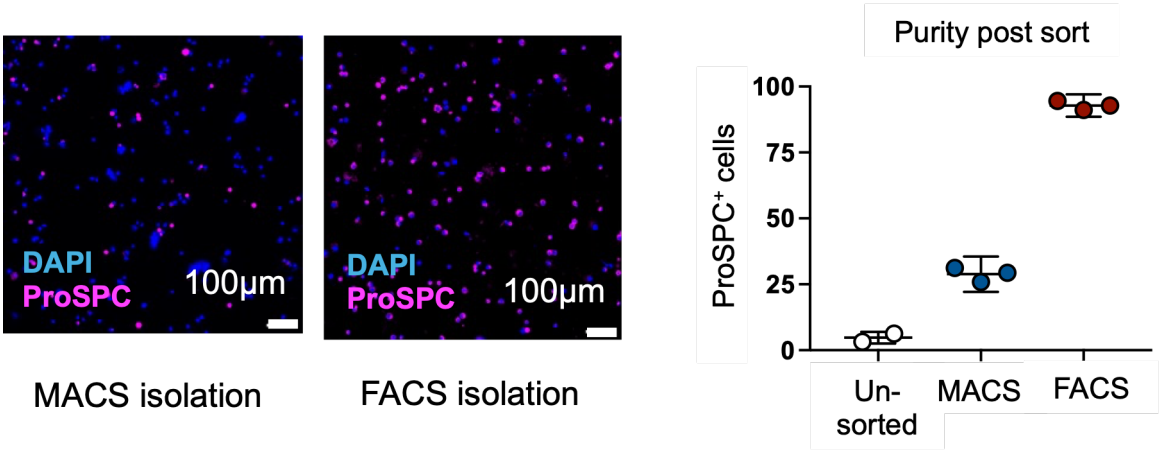


Figure 6.3.4. AT2 cell purity following MACS and FACS assessed by immunocytochemistry. *Representative immunofluorescence images of cytospin preparations from positively selected cells following MACS isolation (left panel) and FACS isolation (middle panel). Cells were stained for the AT2 ProSPC. Right panel: Quantification of AT2 cell purity, expressed as the percentage of pro-SPC⁺ cells relative to total DAPI⁺ nuclei, determined using the cell detection function in QuPath image analysis software. Data are shown for unsorted, MACS-sorted, and FACS-sorted lung samples. Each point represents an independent experiment.*

6.3.2 Primary AT2 cells cultured in extra-cellular matrix (ECM) form 3D spheroid like structures and are capable of long-term expansion

To optimise culture conditions for primary AT2 cells, serum- and feeder-free media formulations described by Youk et al[228]. and Katsura et al[229]. were compared. AT2 cell proliferation and spheroid formation were assessed qualitatively by brightfield

microscopy and semi-quantitatively using the Incucyte Organoid Module®, which enabled longitudinal imaging and measurement of spheroid number, size, and morphology.

Culture in media designed by Katsura et al[229] resulted in a greater increase in both spheroid number and size compared to the formulation by Youk et al[228]. (Figure 6.3.5). Within 14 days, single AT2 cells embedded in ECM domes proliferated and self-organised into multicellular 3D spheroid structures.

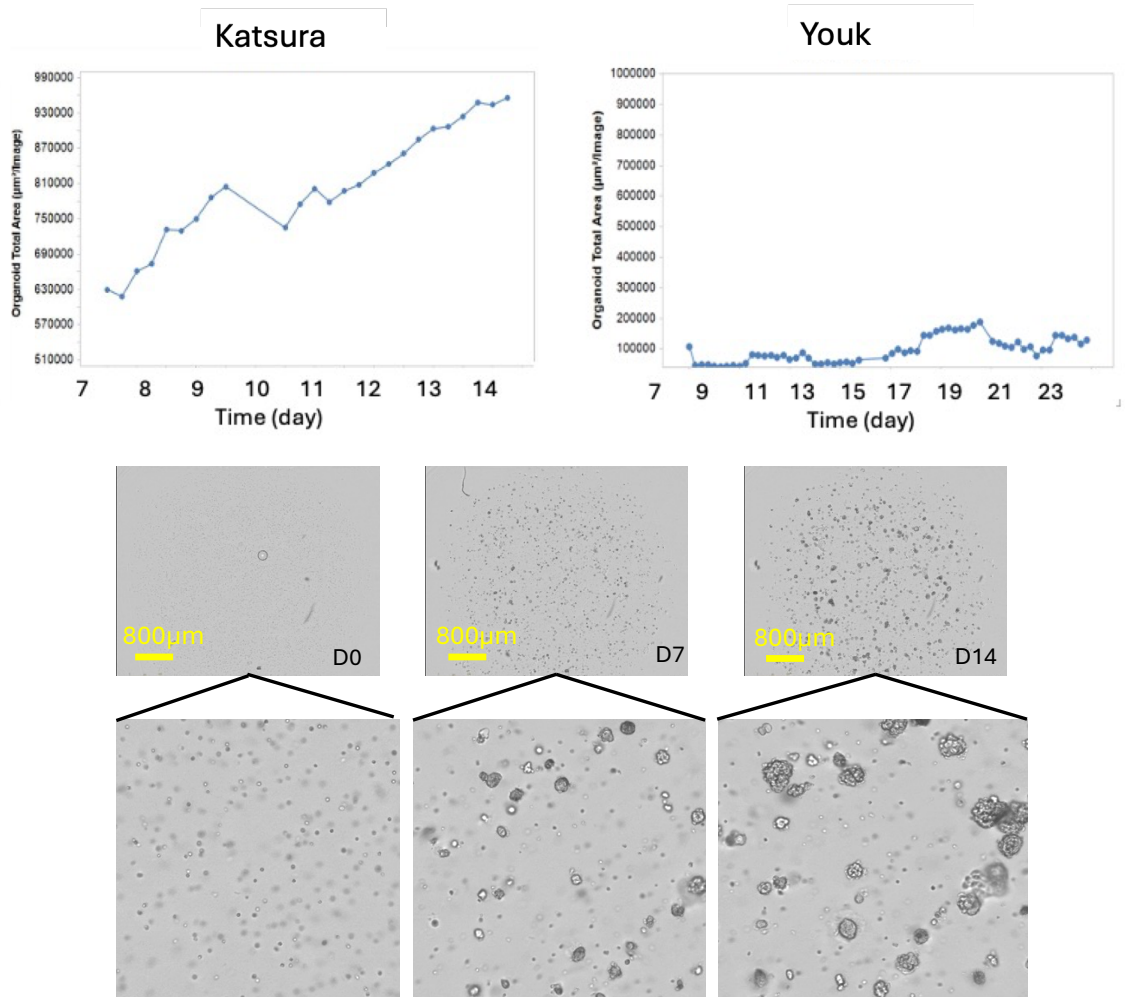


Figure 6.3.5. AT2 cells expand in culture to form spheroid-like structures. *Top panel; assessment of spheroid formation using two published serum-free, feeder-free culture conditions described by Katsura* et al. *(left) and Youk* et al. *(right), analysed using the Incucyte® organoid module. Organoid growth quantified as the total area (µm²) occupied by organoid-like structures relative to the total imaged area in brightfield images. Measurements were derived from serial z-stack imaging followed by label-free detection of cells and organoid structures. Variability in measurements reflects changes in focal plane across z-stacks. Data presented from day 7 onwards due to limited automated detection sensitivity for single cells and small structures at earlier time points. Starting cell number, media replacement frequency and in vitro conditions were identical in both culture systems. Limited AT2 spheroid formation using media described by Youl et al was observed, despite prolonged culture up to 24 day. Bottom panel; representative brightfield images showing alveolar organoid growth in media described by Katsura et al at day 0, 7, and 14, illustrating progression from single cells to three-dimensional spheroid-like structures over time.*

For passaging, spheroids were recovered by ECM digestion with Dispase II and dissociated into single cells using TrypLE Select®, followed by re-embedding in ECM. Under these conditions, EPCAM$^+$ HTII-280$^+$ cells consistently formed expandable AT2 spheroids within two weeks and could be maintained in culture for up to five months. Donor variability in colony-forming efficiency (CFE) was observed, with CFE generally plateauing after approximately six weeks. Optimisation of digestion and dissociation conditions in later experiments improved cell recovery following passage (Figure 6.3.6). As fold expansion was calculated independently for each passage, reductions between successive passages reflect lower expansion efficiency during that passage and should not be interpreted as a reduction in the absolute number of cells maintained in culture.

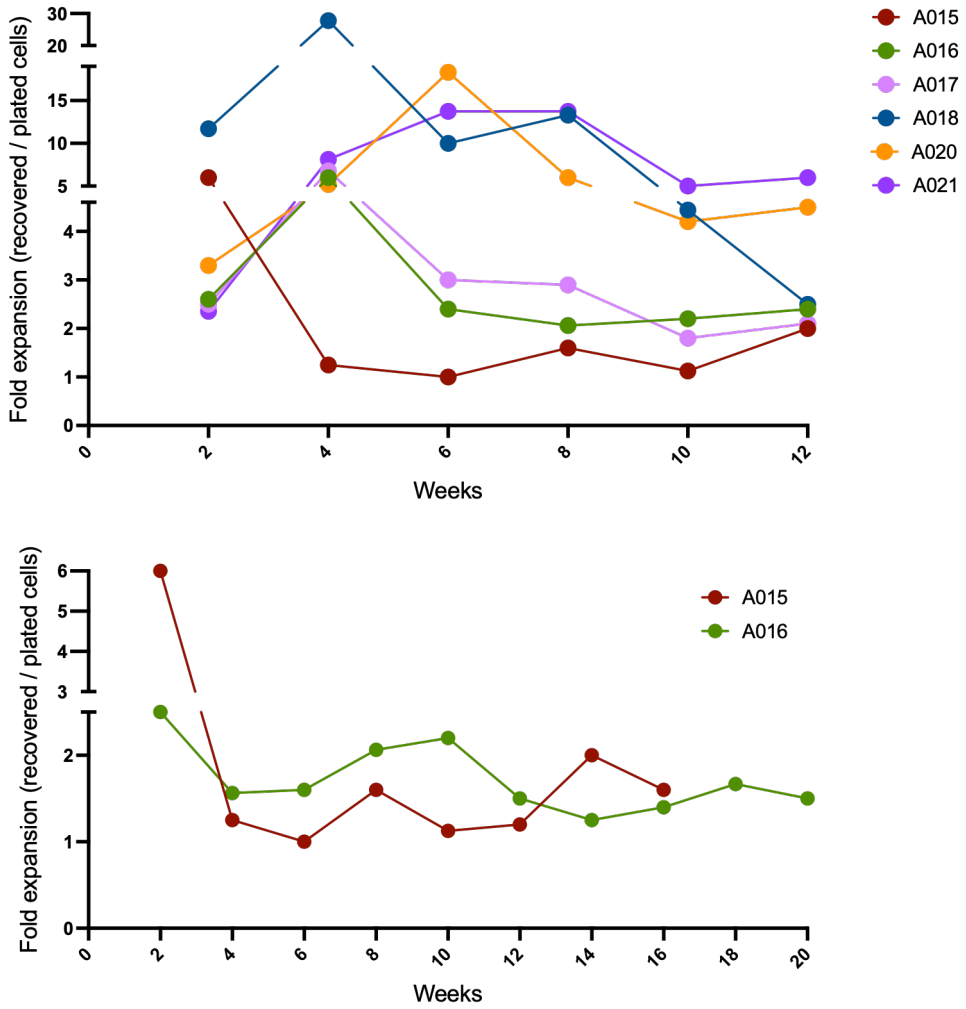


Figure 6.3.6. Colony forming efficiency of AT2 cell derived organoids over serial passage and between donors. *Top panel - Fold expansion of AT2 cell number over a 2-week culture period for six independent donors across serial passage. Fold expansion was calculated independently for each passage as the number of viable cells recovered after 2 weeks divided by the number of viable cells plated at the start of that passage. downstream analysis did not include Each data point represents the expansion efficiency of a single 2-week passage rather than cumulative growth over time. Data demonstrate inter-donor variability in AT2 expansion capacity over serial passage. Bottom panel - Fold expansion during each 2-week passage for two donors maintained in culture for up to 20 weeks. Passaging was performed every 2 weeks, with each data point representing a single passage. Abbreviations: CFE, colony-forming efficiency; AO15 etc., anonymised donor identifiers.*

6.3.3 Primary AT2-derived alveolar spheroids retain expression of canonical AT2 markers and apical–basal polarity

To generate sufficient cell numbers for downstream experiments, HTII-280^{+} EPCAM^{+} AT2 cells were expanded and serially passaged. To minimise phenotypic drift, all downstream analyses were performed at passage 3 (P3; ~2 months in culture), and spheroids were characterised to assess retention of AT2 identity and alveolar structure.

Histological analysis of P3 spheroids demonstrated multicellular structures ranging from 50–100 μm in diameter with cystic or folded morphology, consistent with previous reports. Cells retained a cuboidal epithelial morphology characteristic of AT2 cells (Figure 6.3.7).

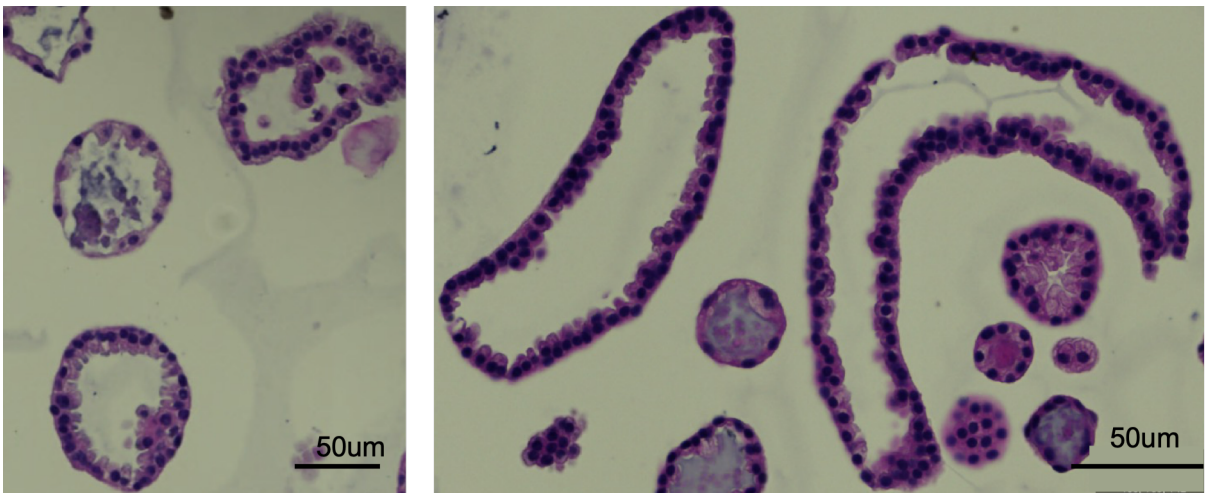


Figure 6.3.7. AT2 spheroid morphology assessed by haematoxylin and eosin (H&E) staining. *Representative brightfield images of formalin-fixed, paraffin-embedded AT2 spheroids following 14 days of culture, stained with haematoxylin and eosin.*

Immunofluorescence staining confirmed expression of canonical AT2 markers. ProSPC localised to the cytoplasm, while HTII-280 expression was restricted to the apical cell surface, consistent with in vivo observations. Spheroids also retained surface expression of HLA-DR, reflecting the recognised antigen-presenting capacity of AT2 cells (Figure 6.3.8).

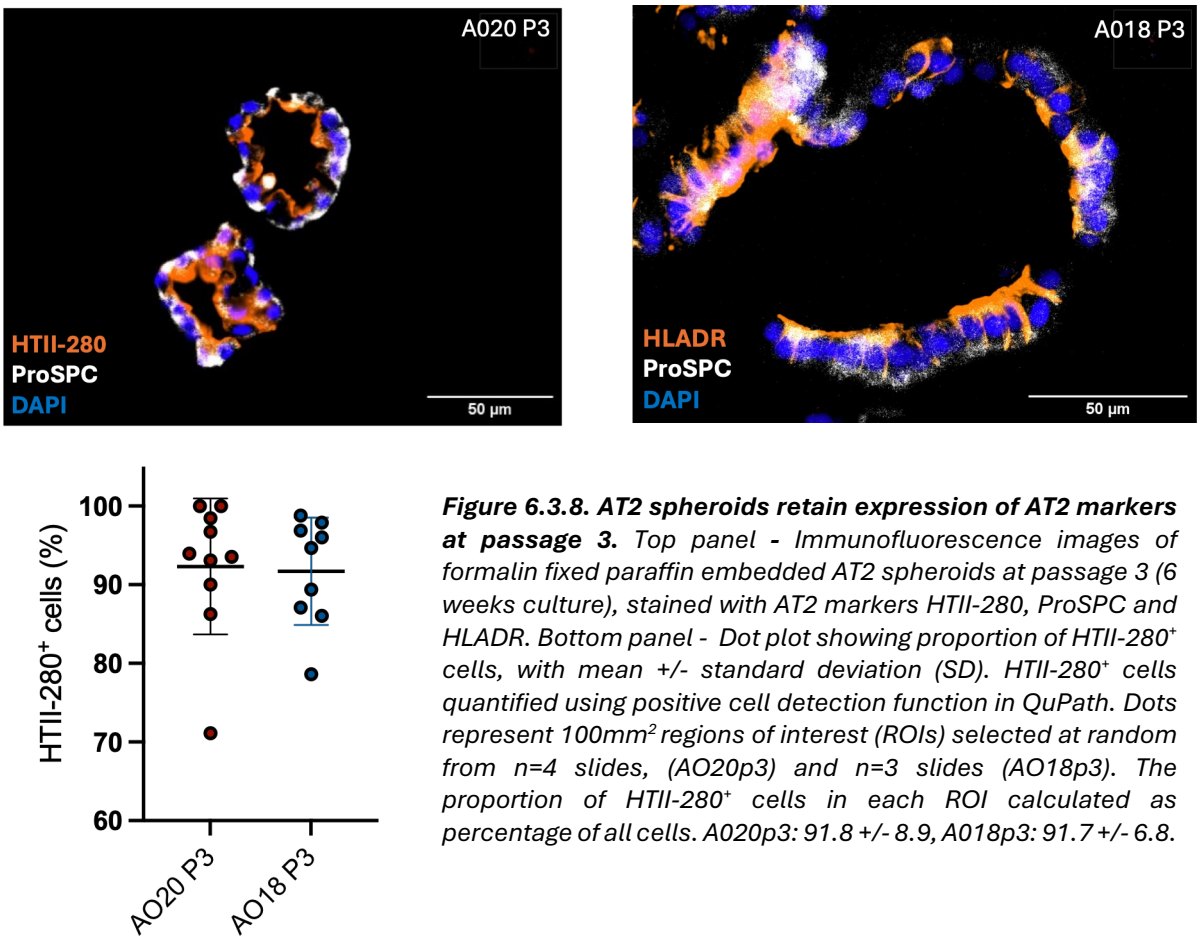


Figure 6.3.8. AT2 spheroids retain expression of AT2 markers at passage 3. *Top panel* ***-*** *Immunofluorescence images of formalin fixed paraffin embedded AT2 spheroids at passage 3 (6 weeks culture), stained with AT2 markers HTII-280, ProSPC and HLADR. Bottom panel - Dot plot showing proportion of HTII-280⁺ cells, with mean +/- standard deviation (SD). HTII-280⁺ cells quantified using positive cell detection function in QuPath. Dots represent 100mm² regions of interest (ROIs) selected at random from n=4 slides, (AO20p3) and n=3 slides (AO18p3). The proportion of HTII-280⁺ cells in each ROI calculated as percentage of all cells. A020p3: 91.8 +/- 8.9, A018p3: 91.7 +/- 6.8.*

Apical–basal polarity was assessed using polarity-associated proteins. HTII-280 and SCRIBBLE localisation to the apico-lateral domain and CRB3 to the basolateral domain demonstrated preserved epithelial polarity, with an inward-facing apical surface forming a central lumen (Figure 6.3.9). In contrast, transfer of spheroids to ECM-free conditions disrupted polarity and spheroid architecture, resulting in “apical-out” structures lacking clear organisation.

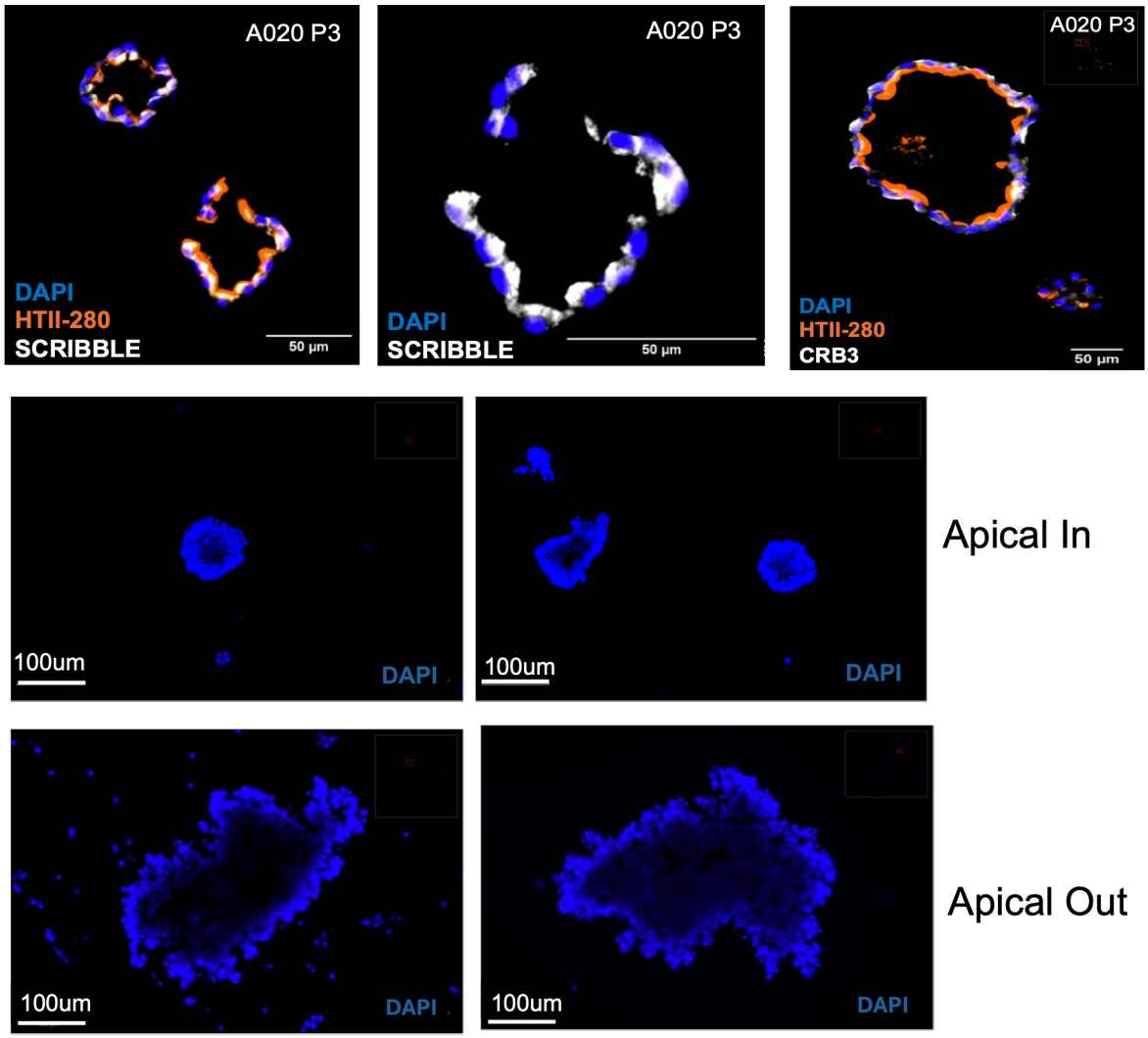


Figure 6.3.9. AT2 spheroids exhibit apical basal polarity in extracellular matrix. *Top panel - Immunofluorescence images of formalin fixed paraffin embedded AT2 spheroids at passage 3, stained apical-lateral markers (SCRIBBLE and HTII-280) and basolateral marker (CRB3). Middle and bottom panels - Immunofluorescence images of whole organoids following cytospin preparation, stained with DAPI. Middle panel shows AT2 spheroids cultured in extra cellular matrix exhibit a spherical morphology. Bottom panel shows AT2 spheroids grown in extra cellular matrix free conditions in ultra-low attachment plates exhibit an outward facing orientation.*

In addition to AT2 markers, spheroids expressed the pan-alveolar epithelial marker PDPN. Low-level expression of SCEL, associated with early AT2-to-AT1 differentiation, was also detected, while expression of mature AT1 markers remained limited. Importantly, markers of airway epithelial contamination, including TP63 and SCGB3A2, were not detected, confirming maintenance of alveolar epithelial identity (Figure 6.3.10).

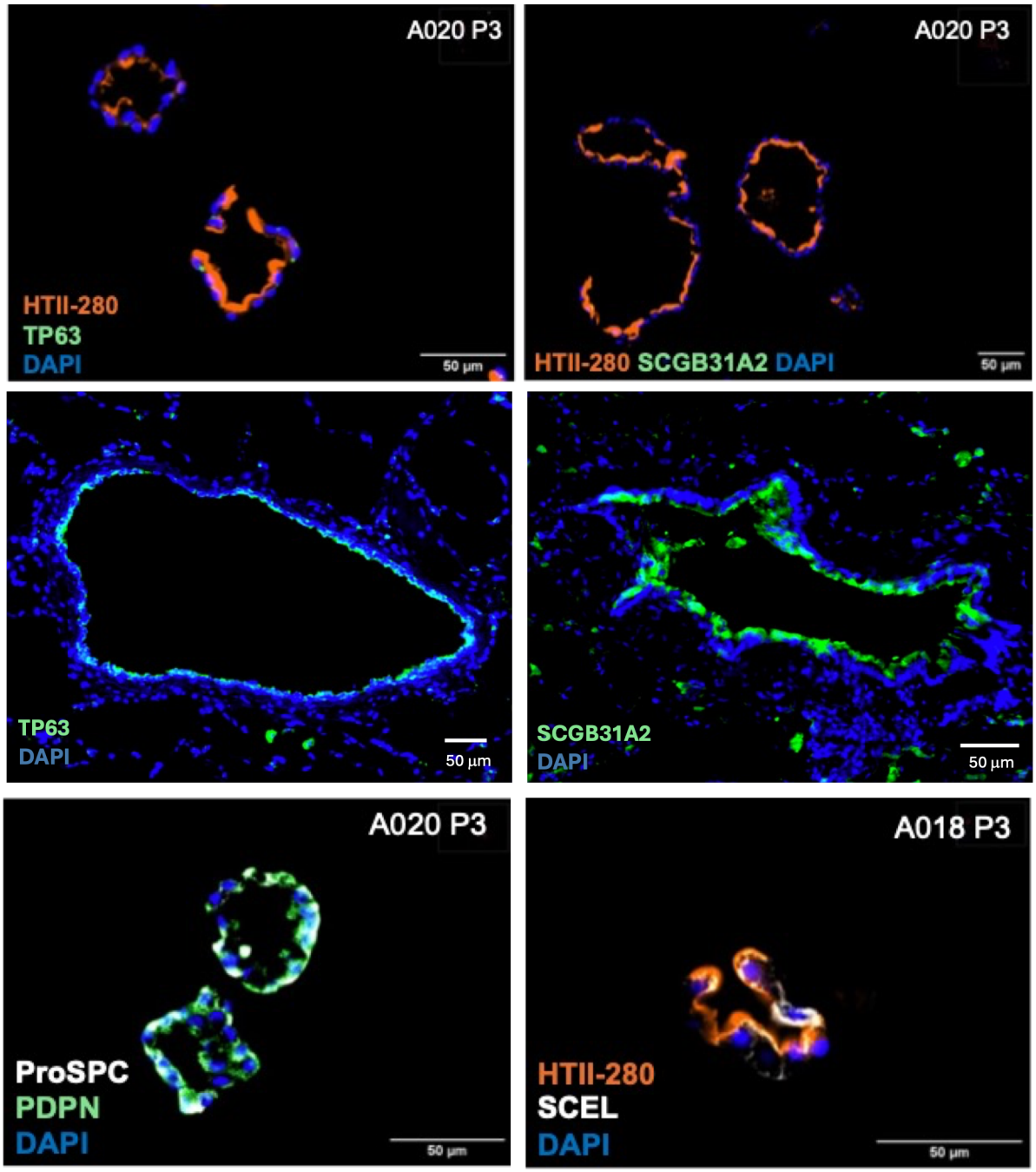


Figure 6.3.10. AT2 spheroids express alveolar but not airway epithelial cell markers. *Immunofluorescence images of formalin fixed paraffin embedded AT2 spheroids at passage 3. Top panel: stained with airway basal cell marker TP63 (top left) and airway secretory cell marker SCGB3A2 (top right) in conjunction with HTII-280. Expression of TP63 and SCGB3A2 equivalent to that observed in no primary antibody controls. Middle panel: regions of interest encompassing large airways from healthy lung tissue stained for TP63 (middle left) and SCGB3A2 (middle right) demonstrating positive tissue staining. Bottom panel: stained with pan alveolar epithelial cell marker PDPN and AT2 marker ProSPC (bottom left) and SCEL and AT2 marker HT2-280 (bottom right)*

RT-qPCR analysis demonstrated stable expression of mature AT2 markers (*SFTPC, ETV5*) between passage 1 and passage 3[318]. SCEL gene expression was detectable but was lower than in lung tissue, while the mature AT1 marker *CAV1* was minimally expressed

and unchanged across passages[294]. These findings indicate preservation of AT2 identity with limited progression toward AT1 differentiation (Figure 6.3.11).

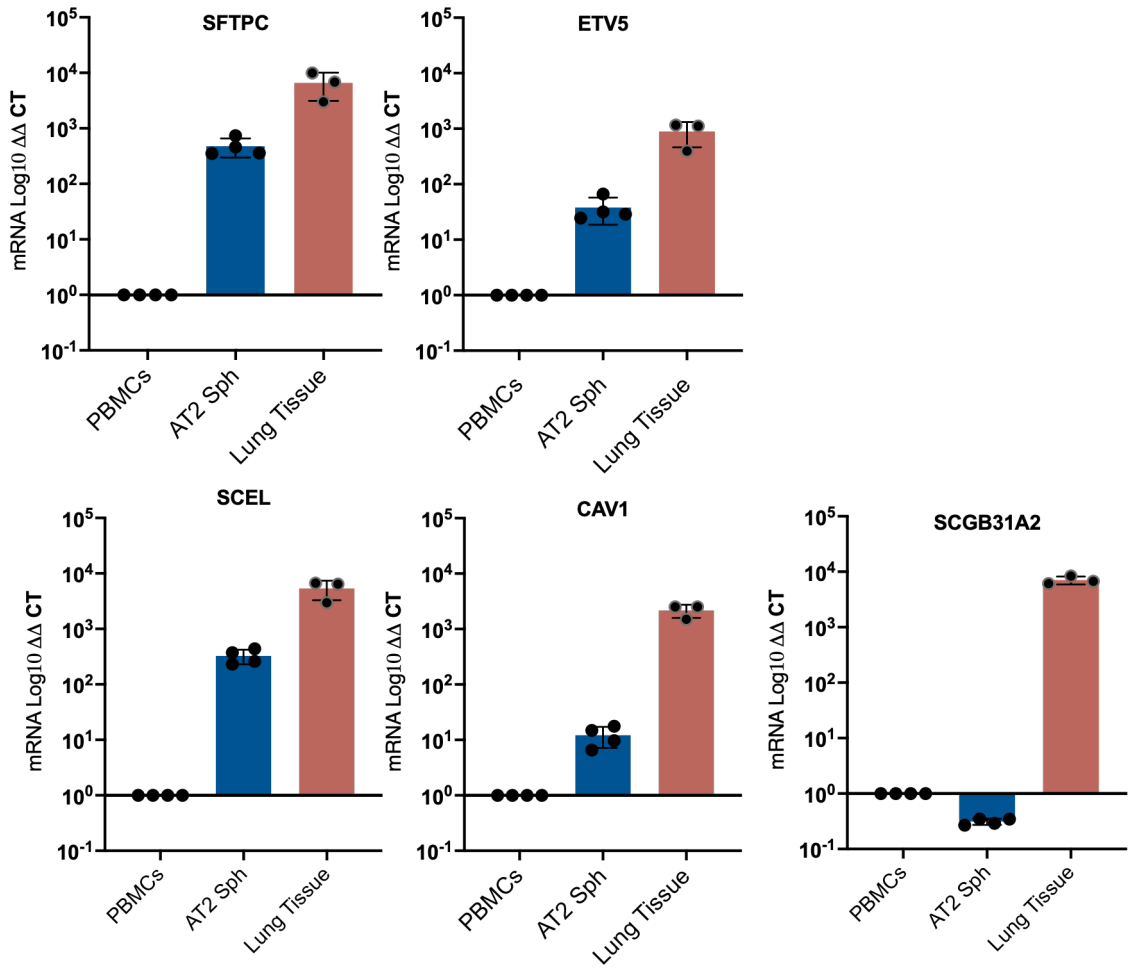


Figure 6.3.11. AT2 spheroids express AT2 and transitional epithelial-associated transcripts. *mRNA expression of genes associated with AT2 cells (SFTPC, ETV5), transitional epithelial states (SCEL), mature AT1 cells (CAV1), and airway secretory cells (SCGB1A1) was assessed by quantitative PCR. Expression was measured in AT2 spheroids, lung tissue (positive control), and peripheral blood mononuclear cells (PBMCs; negative control). Dots represent individual samples analysed across two independent experiments (PBMCs n = 4, AT2 spheroids n = 4, lung tissue n = 3). Data are presented as relative gene expression (ΔΔCt), normalised to PBMCs. Bars represent mean expression and error bars indicate standard deviation.*

Functional assessment using LysoTracker® demonstrated increased fluorescence intensity within $EPCAM^+$ cells compared with $CD3^+$ lymphocytes and $CD14^+$ monocytes, consistent with the presence of acidic lamellar bodies characteristic of mature surfactant-producing AT2 cells[319] (Figure 6.3.12).

Collectively, these data demonstrate that primary AT2-derived spheroids maintain key morphological, molecular, and functional characteristics of AT2 cells, including epithelial polarity, marker expression, and surfactant-associated organelles, while

showing minimal evidence of differentiation toward mature AT1 cells or contamination by airway epithelial populations.

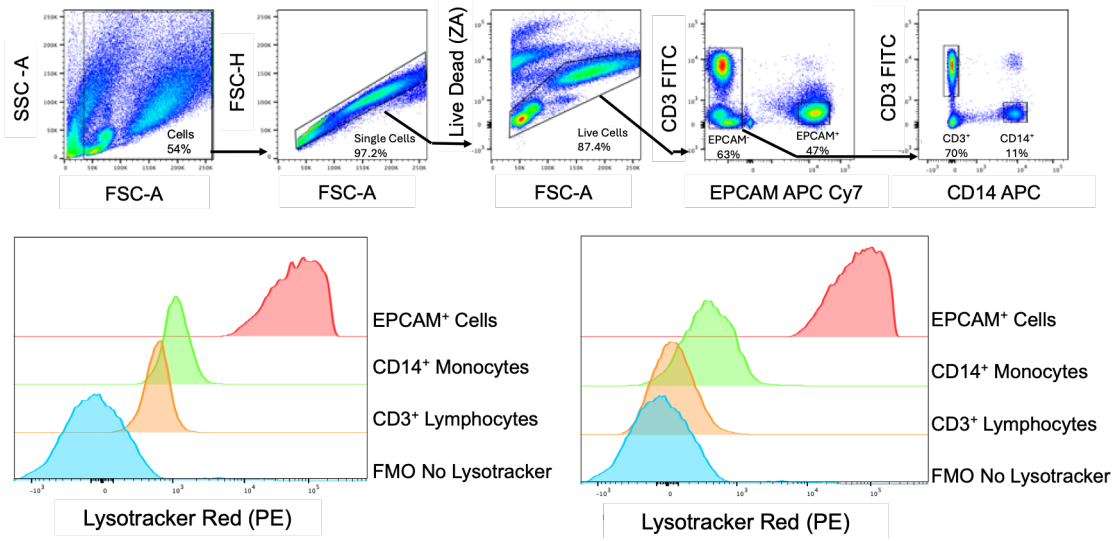


Figure 6.3.12. LysoTracker® expression in alveolar spheroid-derived EPCAM⁺ cells and PBMC populations. *Representative flow cytometry gating strategy showing selection of live single cells followed by identification of EPCAM⁺ AT2 cells from alveolar spheroids and CD3⁺ lymphocytes and CD14⁺ monocytes from PBMCs. Representative histograms demonstrate LysoTracker® Red fluorescence in CD3⁺ lymphocytes (negative control), CD14⁺ monocytes (positive control containing acidic lysosomes) and EPCAM⁺ AT2 cells. LysoTracker® expression was lowest in CD3⁺ lymphocytes, intermediate in CD14⁺ monocytes and highest in EPCAM⁺ alveolar epithelial cells, consistent with the presence of acidic lamellar bodies within AT2 cells.*

6.3.4 Single dose bleomycin induces injury and senescence transcriptional changes consistent with aberrant AEC responses in IPF

To establish an in vitro model of early epithelial injury, primary AT2 spheroids were treated with a single-dose of bleomycin (sdBLM) to recapitulate alveolar epithelial dysfunction observed in IPF. This approach was informed by prior in vitro and in vivo fibrosis models (Table 6.3.1)[294, 300, 320, 321], including murine systems of resolving and non-resolving injury and iPSC-derived AT2 spheroid studies, which have demonstrated induction of aberrant epithelial states following bleomycin exposure.

Author	Agent	Organoid Type	Cell Types reported	Assays
Suezawa 2021 Stem Cell Reports	sd BLM	iSPC feeder dependent	AT2, inflammatory and senescent AT2 cells	qt PCR, bulk RNA seq, FC, IF
Choi 2020 Cell Stem Cell	IL1β	Murine primary AT2	'pAT2', 'DATPs' AT1 cells	sc and bulk RNA seq, qt PCR, IF
Ptasinski 2023 Life science Alliance	'Fibrosis cocktail' (TGFβ, PDGF, TNFα)	iSPC feeder dependent	AT2 –> senescent and inflammatory AT2 and AT1 cells	qt PCR, bulk RNA seq IF,
Kathiriya 2023 Nature Cell Bio	Primary control or IPF fibroblasts	Human primary AT2 and iPSCs	AT2, 'ABI1', 'ABI2' and Basal cells	sc and bulk RNA seq, IF, qt PCR

Table 3.3.1 Overview of AT2 spheroid injury – fibrosis in vitro models. *Summary of published alveolar injury models including organoid/spheroid origin, reported cell populations, and assays used to assess cellular phenotype. Abbreviations; sd BLM – single dose bleomycin, PDGF - platelet derived growth factor, iPSCs – induced pluripotent stem cells, pAT2 – primed AT2, DATP – damage associated transient progenitors, ABI – aberrant basaloid intermediates. FC – flow cytometry, qt PCR – quantitative PCR.*

To define optimal injury conditions, AT2 spheroids were exposed to increasing concentrations of sdBLM and harvested at multiple time points post injury (pi) for transcriptomic analysis, alongside uninjured controls (Figure 6.3.13).

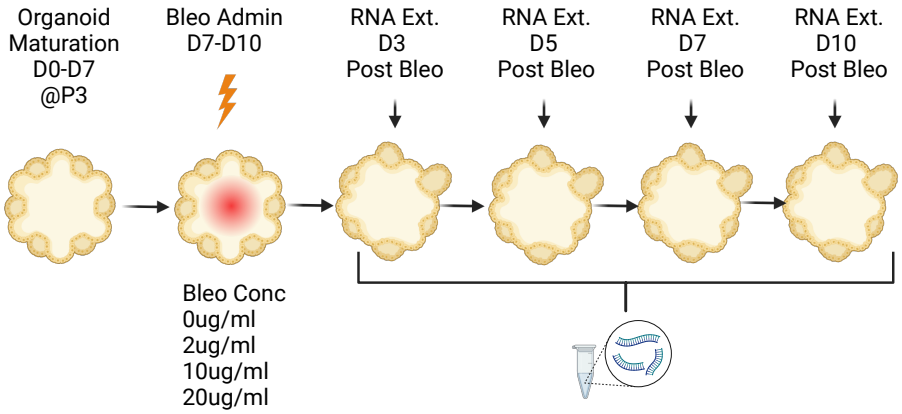


Figure 6.3.13 Experimental overview of single dose bleomycin titration experiment. *Schematic outline of experimental design - AT2 cells were cultured for 7 days to form into spheroids, prior to injury with increasing doses of bleomycin, as indicated. Cells were harvested at multiple time points and RNA extracted for quantitative PCR analysis to measure changes in gene expression. Abbreviations ext. – extraction, bleo – bleomycin, conc – concentration.*

Mixed effects modelling identified a significant main effect of treatment on *CDKN1A* expression and significant main effects of both treatment and time on *TNF-α* expression, whereas no significant time x treatment interactions were observed for either transcript. Visual expression of the marker expression demonstrated the greatest increases in *CDKN1A*, *TNF-α* expression generally occurred at intermediate time points (D5-D7pi) with expression declining by D10pi. Pairwise comparisons at individual time points did not remain significant following correction for multiple testing. *IFN-β* expression showed a similar temporal pattern to *CDKN1A* and *TNF-α* however in some donors but was more variable and did not demonstrate a significant treatment effect. *IL-1β* expression showed inter-donor variability, with increased expression observed visually in one donor at early time points (D3–D5pi) following higher bleomycin concentrations (Figure 6.3.14).

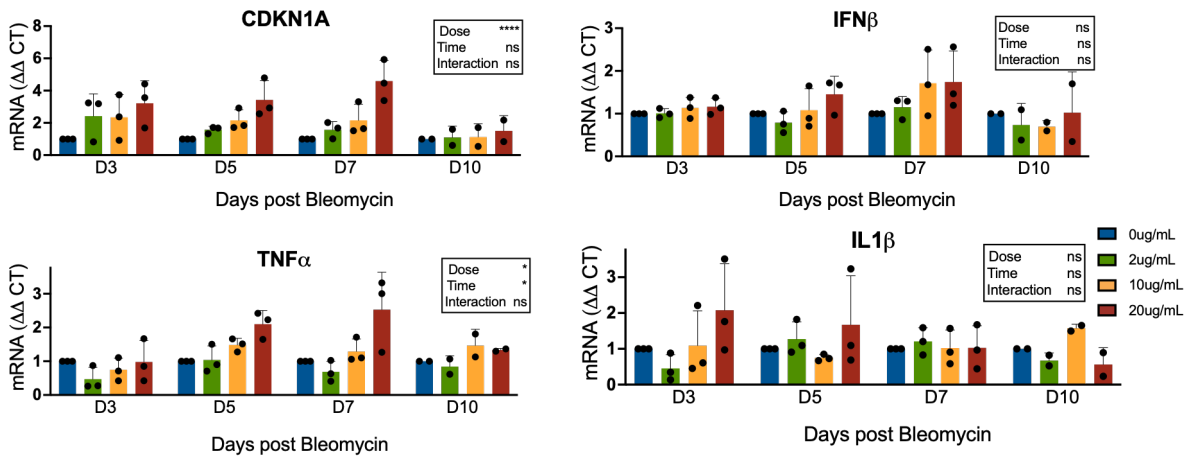


Figure 6.3.14 Expression of inflammatory and senescence associated genes following single dose bleomycin injury. *mRNA expression of genes associated with senescence (CDKN1A) and inflammatory cytokines (TNF-α, IFN-β) was assessed by quantitative PCR. Expression was measured at several time points following injury (x axis) across a range of bleomycin concentrations (coloured bars) Dots represent individual samples from n=3 separate donors with mean and standard deviation. Gene expression presented as relative expression (Log2 ΔΔCt), normalised to uninjured spheroids. Statistical analysis was performed using a linear mixed-effects model with treatment (bleomycin concentration), time and treatment x time interaction included as fixed effects and donor as a random effect. Pairwise comparisons between each bleomycin concentration and the untreated control at each time point were adjusted for multiple testing.*

A broader gene panel was used to assess epithelial transitional states, including markers of mature AT2 (*SFTPC*), AT1 differentiation (*SCEL*), and intermediate aberrant alveolar epithelial cell AEC states described in Chapter 5 and from murine studies. These markers included TMEM173 (coding STING) and LRG1 for 'primed AT2 cells' described by Choi et al in a murine single dose study[294] that is analogous to the transitional AT2 cell state described in human transcriptomic studies[63] and in Chapter 5.

Visual inspection suggested an early transient increase in the mature AT2 marker *SFTPC* at D3pi, followed by progressive decline between D5–D10pi at higher BLM concentrations. Expression of the early AT1 marker *SCEL* appeared to increase at intermediate time points D5 and D7pi at higher concentrations. Markers associated with 'primed' or transitional AT2 states (*LRG1, TMEM173*) also showed apparent increases at earlier time points (D3–D5pi) whereas, markers associated with aberrant basaloid/intermediate states, (*KRT8* and *CDKN1A)*, were also increased at D3pi and remained elevated until D10pi. However, mixed effects modelling did not identify significant effects of treatment, time or treatment x time interactions for the epithelial cell state markers (Figure 6.3.15). Although *SFTPC* showed the strongest treatment-associated trend, this did not reach statistical significance (p = 0.065).

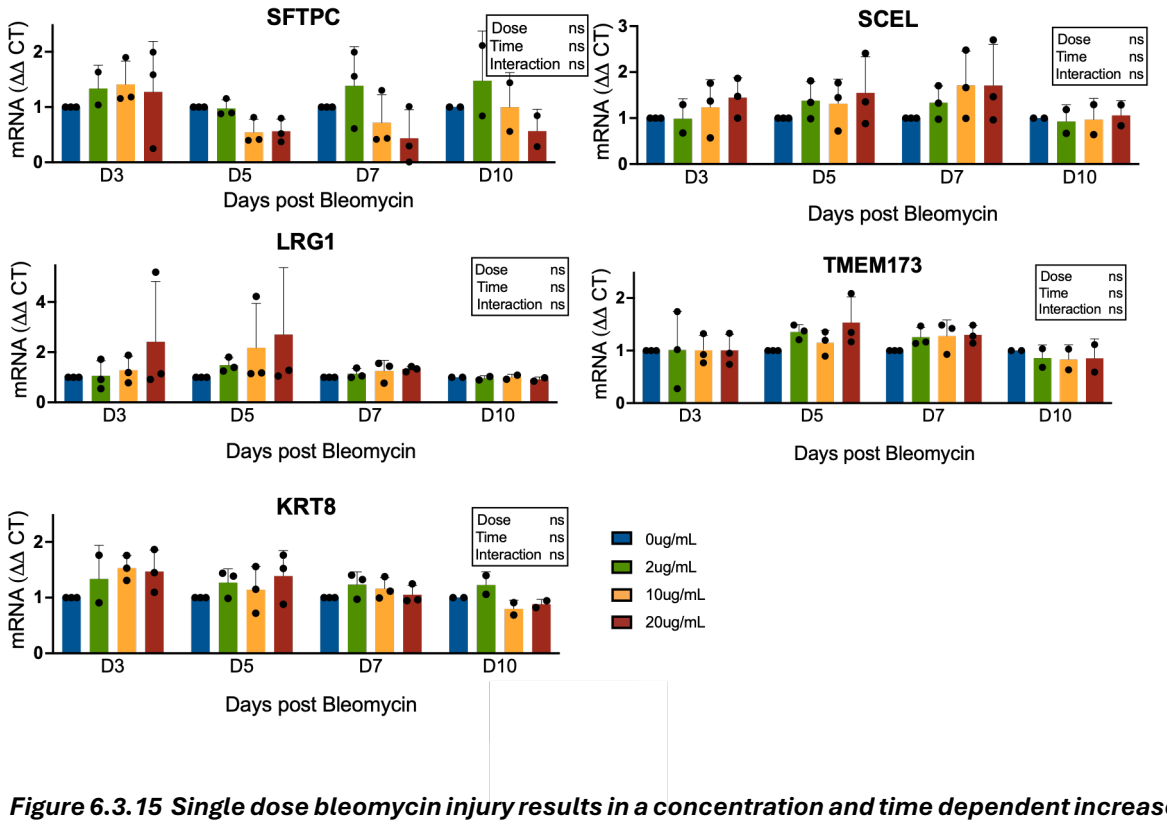


Figure 6.3.15 Single dose bleomycin injury results in a concentration and time dependent increase in expression of intermediate alveolar epithelial cell states. *mRNA expression of genes associated with homeostatic AT2 (SFTPC), transitional and AT1 (SCEL), early transitional AT2 cells (LRG1, TMEM 173), and intermediate ABIs (KRT8) was assessed by quantitative PCR. Expression measured at several time points following injury (x axis) across a range of bleomycin concentrations (coloured bars) Dots represent individual samples from n=3 separate donors with mean and standard deviation. Gene expression presented as relative expression (Log2 ΔΔCt), normalised to uninjured spheroids. Statistical analysis was performed using a linear mixed-effects model with treatment (bleomycin concentration), time and treatment x time interaction included as fixed effects and donor as a random effect. Pairwise comparisons between each bleomycin concentration and the untreated control at each time point were adjusted for multiple testing.*

Collectively, these findings demonstrate that sdBLM induces a reproducible inflammatory and stress-associated transcriptional response in primary AT2 spheroids characterised by CDKN1A and TNF-α expression. Although visual inspection suggests temporally emerging epithelial transitional states following injury, these responses were variable between donors and were not supported by significant treatment or time effects in the mixed-effects analysis. Together, these findings guided selection of sdBLM dose and the timing of subsequent THP-1 co-culture experiments to capture the peak injury-associated transcriptional response.

6.3.5 THP-1 cells retain cell surface expression and functional responses to LPS and IFN-β when co-cultured with AT2 cells in serum free AVOE media

To investigate epithelial–myeloid interactions following sdBLM-induced injury, co-culture experiments were performed using THP-1 monocyte-like cells and AT2 spheroids. IFNAR$^{-/-}$ THP-1 cells, generated by the Rehwinkel group, were used in parallel functional assays to assess type 1 IFN dependency.

Initial experiments assessed THP-1 cell viability, localisation, and compatibility with serum-free AVOE media. AT2 spheroids and THP-1 cells were fluorescently labelled (LysoTracker and CFSE, respectively) and co-cultured within ECM domes. Both populations remained viable over 7 days, as confirmed by live/dead flow cytometry and FACS-based separation using CD45 and EPCAM expression (Figures 6.3.16–6.3.17). THP-1 cells formed small clusters within the ECM but showed no evidence of directed migration toward AT2 spheroids.

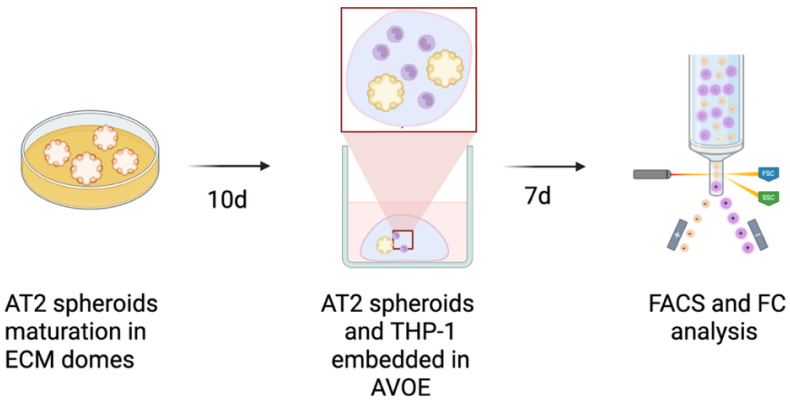


Figure 6.3.16 Uninjured AT2 spheroid-THP-1 coculture. *Schematic outlining the experimental design. AT2 cells were cultured for 10 days to form spheroids, then extracted from extracellular matrix (ECM), co-cultured with THP-1 cells, and re-embedded in ECM domes in alveolar organoid expansion medium (AVOE). Prior to co-culture, AT2 spheroids were labelled with Lysotracker and THP-1 cells with CFSE. Co-cultures were monitored over 7 days using live-cell imaging (Incucyte®) and interval brightfield assessment. Following co-culture, cell populations were separated by fluorescence-activated cell sorting (FACS).*

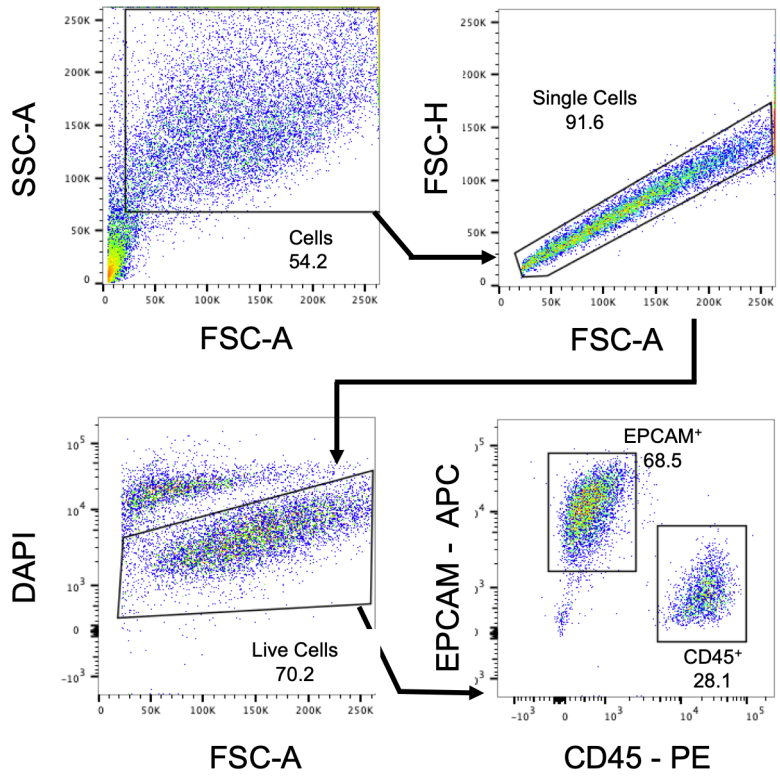


Figure 6.3.17 AT2 spheroids and THP-1 cells can be separated by FACS. *Representative plots outlining gating strategy used for fluorescence activated cell sorting of AT2 spheroids and THP-1 cells following 7 days co-culture, following exclusion of debris doublets and dead cells, AT2 cell and THP-1 cells were identified by expression of EPCAM and CD45 respectively. Viability assessment with live dead dye illustrates that 70% cell populations were viable with no uptake of DAPI.*

To assess the impact of culture conditions on myeloid phenotype, THP-1 cells were cultured in standard RPMI (R10), AT2 spheroid alveolar media (AVOE), or co-cultured with uninjured AT2 spheroids in AVOE. Compared to R10, both AVOE culture and co-culture conditions resulted in increased expression of CD14, CD64, and HLA-DR, as well as enhanced LysoTracker uptake, indicating a more activated or differentiated-like phenotype (Figure 6.3.18).

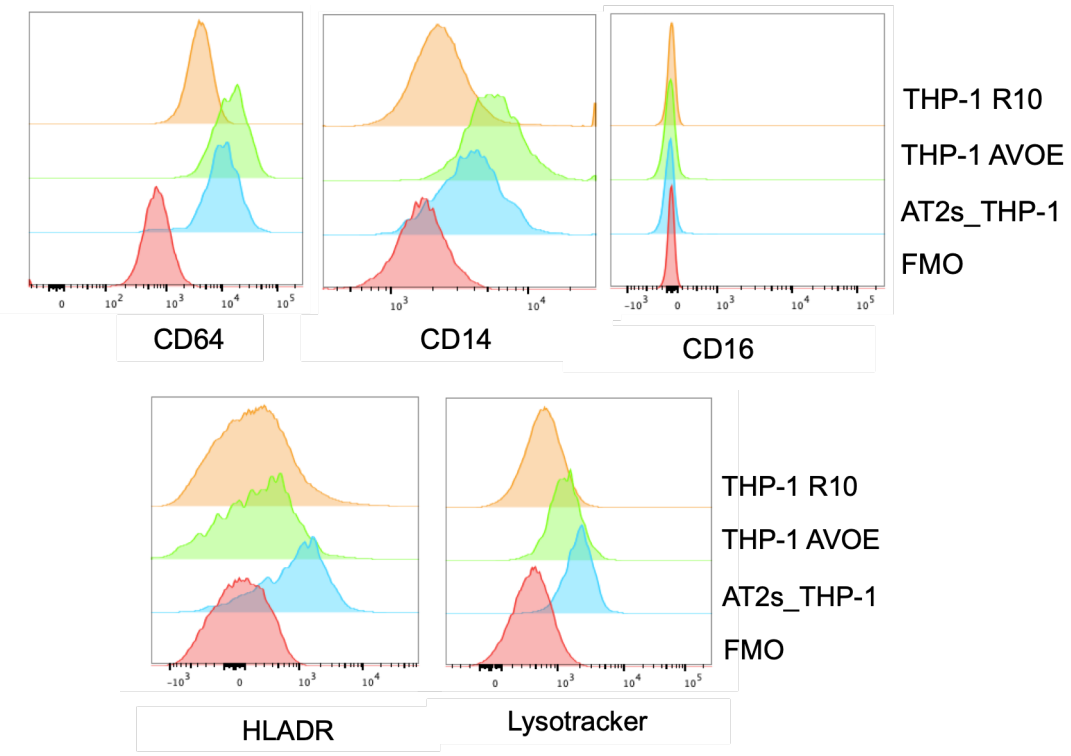


Figure 6.3.18 Characterisation of changes in cell surface marker expression of THP-1 cells . *Flow cytometry staining of cell surface markers (CD64, CD14, CD16 and HLADR) and lysotracker uptake in THP-1 cells cultured in standard media R10 (Orange,) AVOE (Green) and AVOE with AT2 spheroids (Blue) for 7 days.. THP-1 cells do not express CD16 in any conditions as is reported. Culture in AVOE with or without AT2 resulted in increased CD64, CD14 expression and lysotracker uptake. HLADR expression increased only when THP-1 cells were cultured with AT2 spheroids. Abbreviations; R10 – RMPI with 10% fetal calf serum)*

Baseline cytokine expression was also elevated in THP-1 cells cultured in AVOE or co-culture conditions relative to R10 (Figure 6.3.19). To determine whether THP-1 cells retained functional responsiveness under the altered culture conditions, cells were stimulated with LPS, a well-established activator of THP-1 inflammatory responses. THP-1 cells across all culture conditions retained responsiveness to LPS stimulation and demonstrating increased intracellular TNF-α expression whereas IFNγ and IL-6 intracellular expression remained largely unchanged in all experimental conditions.

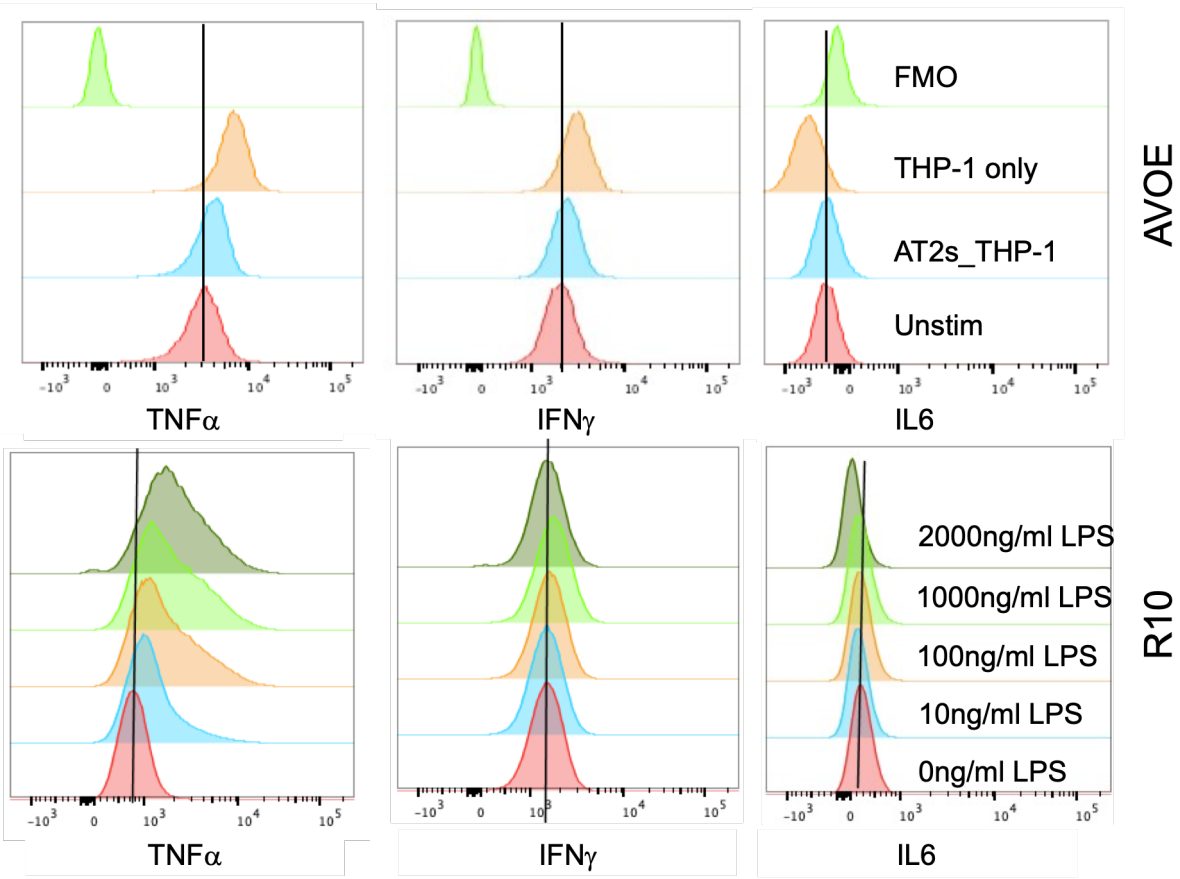


Figure 6.3.19 Characterisation of THP-1 responses to LPS under different culture conditions. *Flow cytometry analysis of intracellular cytokine expression (TNF-α, IFN-γ, IL-6) in THP-1 cells following stimulation with lipopolysaccharide (100 ng/mL) for 6 hours in the presence of brefeldin A. THP-1 cells were cultured for 7 days in R10 (orange), AVOE (green), or AVOE supplemented with AT2 spheroids (blue). Culture in AVOE and AVOE with AT2 spheroids was associated with increased TNF-α and IFN-γ production compared to R10. Abbreviations: R10, RPMI with 10% fetal calf serum; AVOE, alveolar organoid expansion medium; LPS, lipopolysaccharide. Unstim. – unstimulated cells.*

To assess type 1 IFN signalling capacity, WT and IFNAR$^{-/-}$ THP-1 cells were stimulated with IFN-β in suspension culture in AVOE medium. IFN-β stimulation induced robust STAT1 phosphorylation in WT cells cultured in AVOE, whereas no pSTAT1 signal was detected in IFNAR$^{-/-}$ cells confirming pathway specificity. (Section 5.3.2, Figure 5.3.3)

6.3.6 Injured alveolar spheroids upregulate ISGs and TNF-α in THP-1 cells

Following establishment of THP-1–AT2 co-culture conditions, subsequent experiments examined whether injured AT2 spheroids induce a type 1 IFN–associated response in myeloid cells, and whether this is dependent on IFNAR signalling. In parallel, the impact of myeloid cells on epithelial injury-associated transcriptional programmes was also assessed.

AT2 spheroids (n = 3 donors) were generated over 7 days and subsequently exposed to sdBLM (20 ng/ml) for 72 hours. Following removal of BLM, ECM digestion was performed to additionally remove additional BLM within ECM domes, injured or uninjured spheroids were co-cultured with THP-1 cells in ECM-free ultra-low attachment (ULA) plates for 48 hours to enable direct cell–cell interaction, confirmed by imaging (Figure 6.3.20).

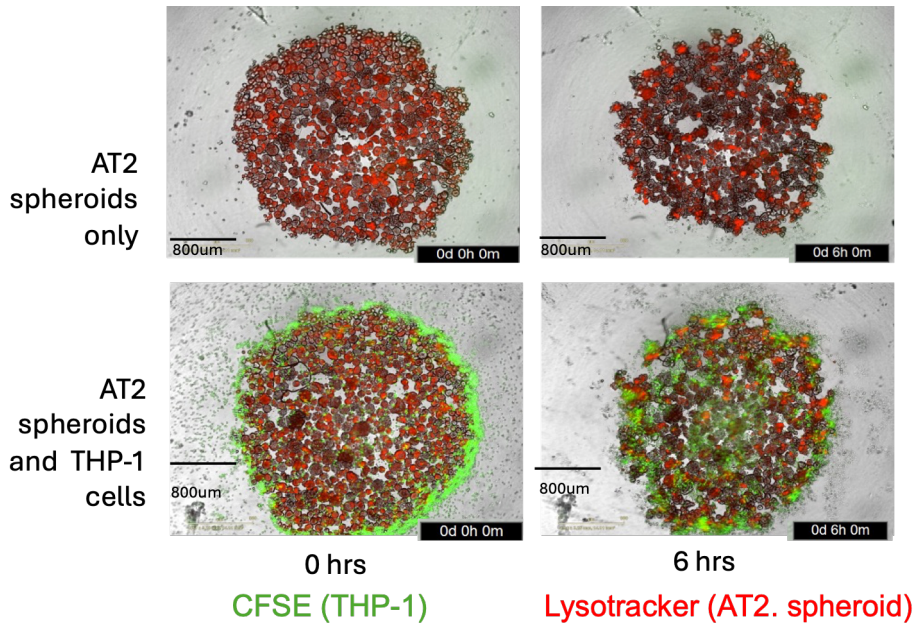


Figure 6.3.20 Direct cell contact following co-culture of AT2 spheroids and THP-1 cells in ECM free conditions. *Representative live-cell imaging using the IncuCyte S3 live cell imaging system showing lysotracker stained AT2 spheroids and CFSE - labelled THP-1 cells cultured without ECM in ultra-low attachment plates. Images demonstrate migration of THP-1 cells towards AT2 spheroids and direct cell to cell contact within 6 hours of co-culture. Abbreviations; AVOE – alveolar organoids expansion media, ECM – extracellular matrix.*

Five experimental conditions were analysed (Figure 6.3.21), and both epithelial and myeloid populations were recovered by FACS for downstream qPCR analysis. The myeloid gene panel included interferon-stimulated genes (*MX1, ISG15, STAT1*), *IFN-β,* and inflammatory markers *TNF-α* and *CD36*.

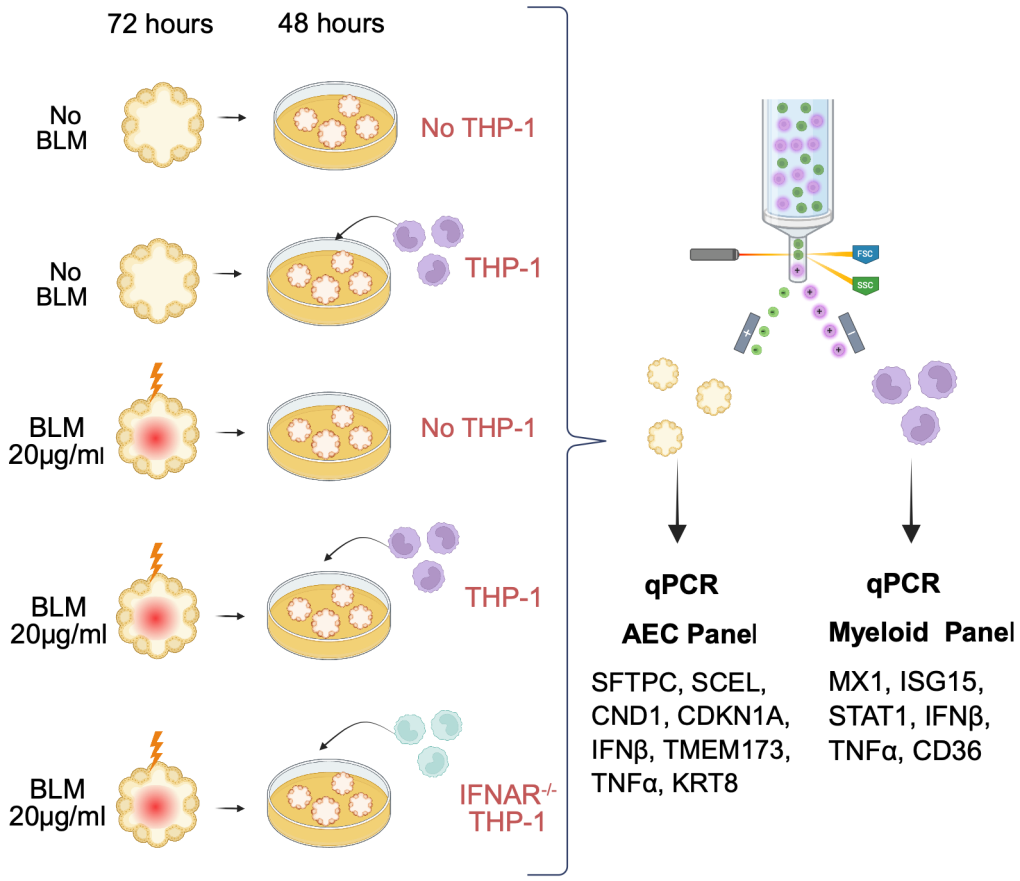


Figure 6.3.21. Experimental overview of co-culture of uninjured and injured AT2 spheroids with THP-1 cells. *Schematic outlining the experimental design. AT2 spheroids were cultured for 7 days and then either left uninjured or treated with bleomycin (20 µg) for 72 hours. THP-1 cells or IFNAR-/- THP-1 cells were subsequently co-cultured with AT2 spheroids for 48 hours in ultra-low attachment plates. Cell populations were then separated by fluorescence-activated cell sorting (FACS), followed by RNA extraction and quantitative PCR analysis. Experiments were performed using three independent donors. Abbreviations BLM – bleomycin, AEC panel - alveolar epithelial cells panel.*

To validate pathway specificity and impaired IFNAR signalling, WT and IFNAR$^{-/-}$ THP-1 cells were stimulated with IFN-β as a positive control. As expected, IFN-β stimulation increased expression of ISGs in WT cells, whereas IFNAR$^{-/-}$ cells exhibited markedly reduced *MX1* expression and complete suppression of *ISG15* and *STAT1* indicating impaired IFNAR signalling. IFN-β stimulation also reduced *TNF-α* and *IFN-β* transcript expression in WT cells, consistent with established negative feedback regulation of type 1 IFN signalling (Figure 6.3.22).

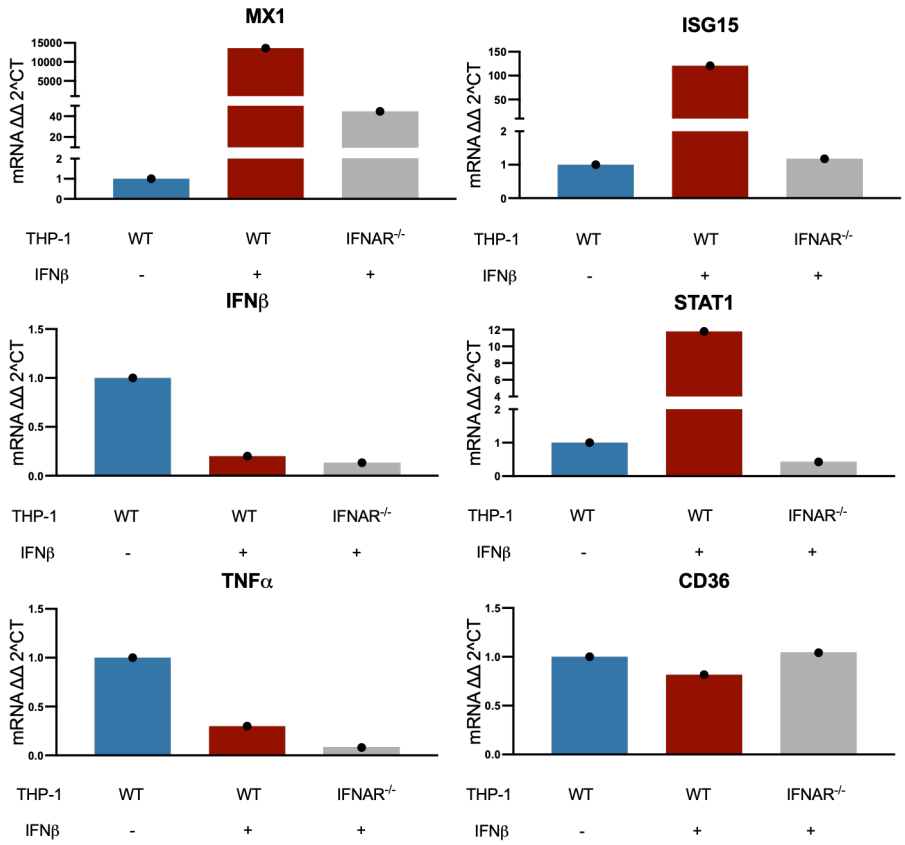


Figure 6.3.22. Validation of IFNAR signalling in WT and IFNAR$^{-/-}$ THP-1 following stimulation with IFN-β. *Representative qPCR analysis from a single experiment showing mRNA expression of interferon stimulated genes (MX1, ISG15, STAT1) and TNF-α, IFN-β and CD36. Expression was measured in unstimulated THP-1 cells (blue) and both WT (red) and IFNAR$^{-/-}$ THP-1 cells (grey bars) following stimulation with IFN-β 250u/mL. Dots represent individual samples, Data are presented as relative gene expression (Log 2 ΔΔCt), normalised to unstimulated THP-1 cells. Abbreviations; WT – wildtype.*

Co-culture experiments demonstrated that injured AT2 spheroids induced a significant increase in ISG expression in WT THP-1 cells, but not in IFNAR^{-}/$^{-}$ cells, confirming dependence on type 1 IFN signalling (Figure 6.3.23). In contrast, *TNF-α* and *CD36* expression were not significantly altered under these conditions. Together with the increase in ISG expression, these findings suggest that co-culture with injured AT2 cells preferentially induced a type 1 IFN associated transcriptional response rather than increasing expression of the inflammatory markers examined. *IFN-β* transcript expression was reduced in WT but not IFNAR$^{-/-}$ THP-1 co-cultured with injured AT2 cells. These findings indicate that increased ISG expression in WT THP-1 cells is likely driven by IFN-β produced by injured AT2 spheroids rather than autonomous IFN-β production by THP-1 cells. Taken together with the increase in ISG expression in WT THP-1 cells, the reduction in IFN-β expression observed in WT THP-1 cells may reflect activation of regulatory mechanisms that limit sustained type 1 IFN signalling and further supress

THP-1 IFN-β transcription. However, these regulatory mechanisms were not directly investigated in the present study.

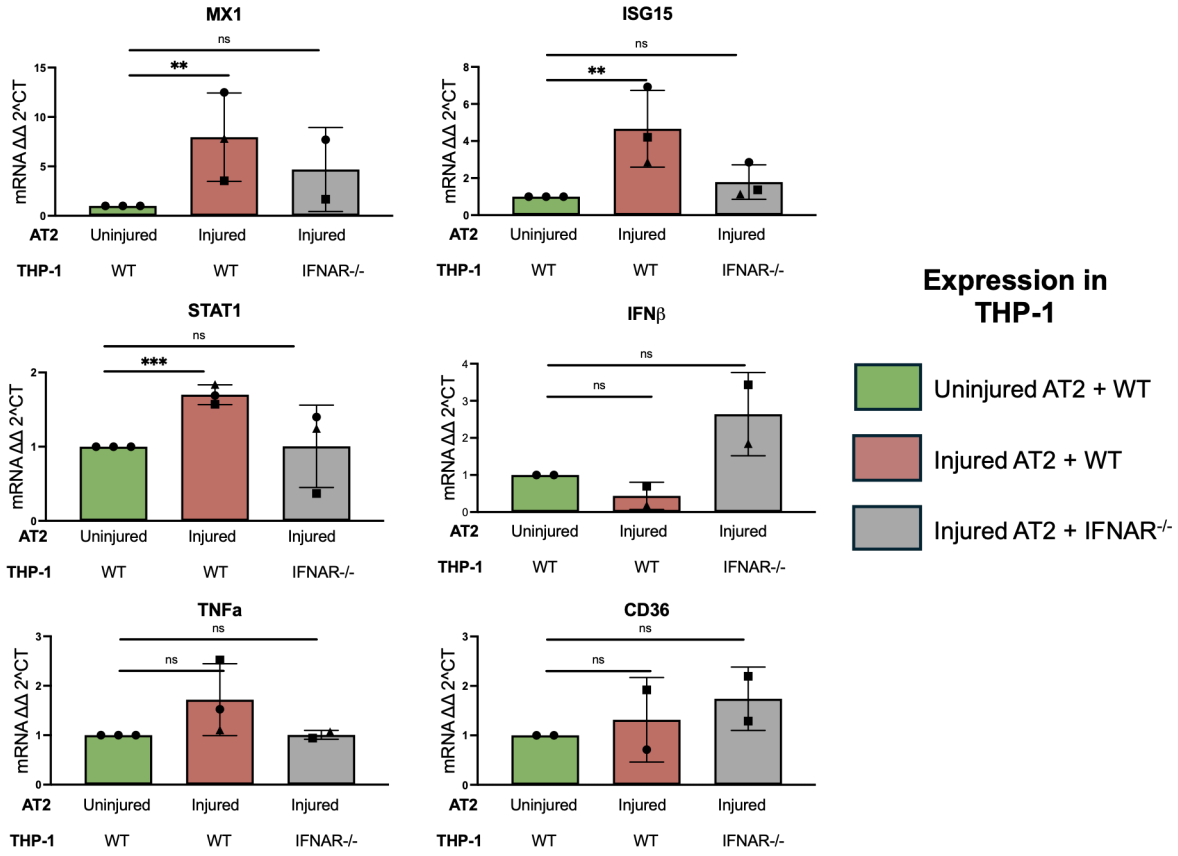


Figure 6.3.23. Injured AT2 spheroids induce ISG expression in THP-1 cells. *mRNA expression of interferon stimulated genes (MX1, ISG15, STAT1) and TNF-α, IFN-β and CD36 assessed by quantitative PCR. Expression measured in THP-1 cells co-cultured with uninjured AT2 spheroids (blue), and in WT (red) and IFNAR$^{-/-}$ THP-1 cells (green) cocultured with injured AT2 spheroids. Dots represent individual samples, Data are presented as relative gene expression (ΔΔCt), normalised to THP-1 cells in culture with uninjured AT2 spheroids. Statistical comparisons between pre-specified donor matched groups were performed using paired t-test on ΔΔCt values. Asterisks denote statistical significance as follows: *p< 0.05, **p < 0.01, ***p< 0.001, ns, not significant (P ≥ 0.05).*

To determine specificity of this response, THP-1 gene expression across all co-culture conditions was compared to unstimulated WT THP-1 controls. ISG induction was observed only in WT THP-1 cells co-cultured with injured AT2 spheroids, confirming that epithelial injury is required to drive this response. Interestingly, co-culture with uninjured AT2 spheroids resulted in reduced expression of *MX1* and *ISG15* compared to unstimulated controls, while *STAT1* expression was modestly increased (Figure 6.3.24).

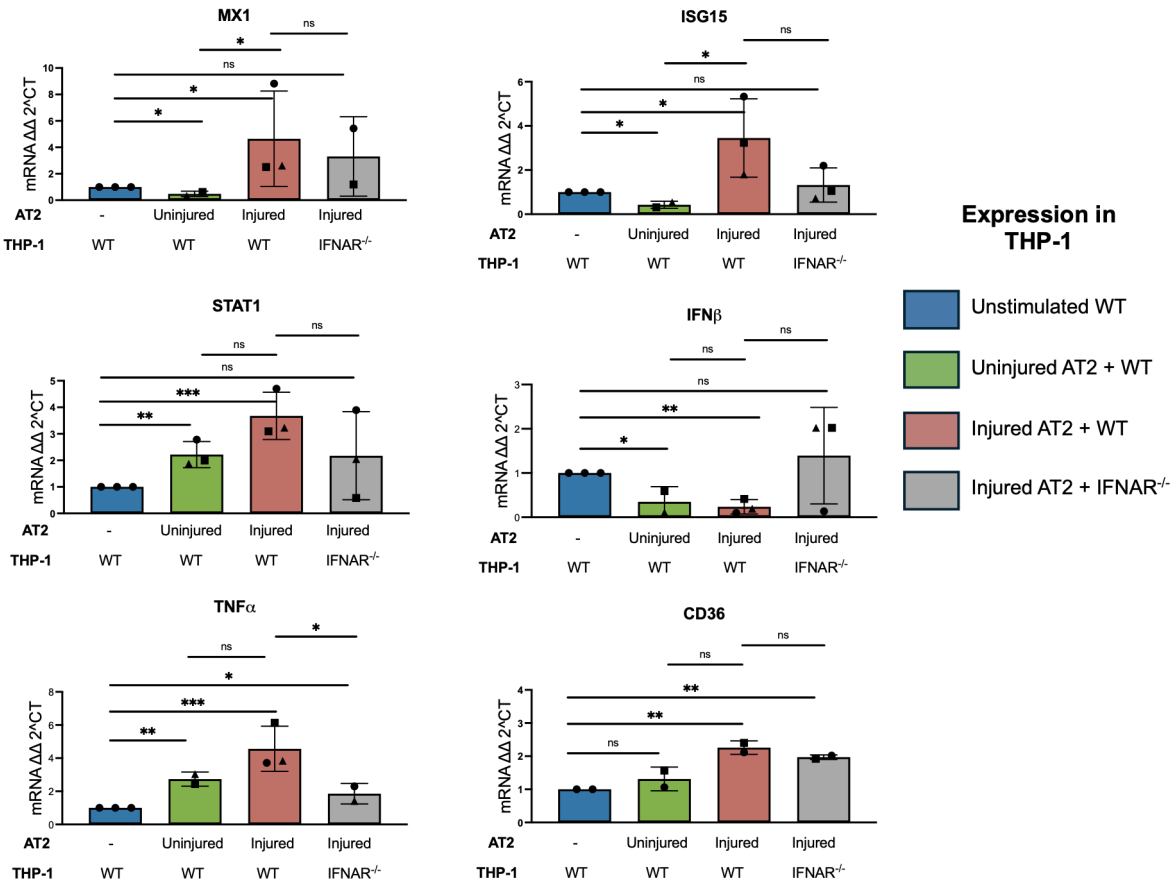


Figure 6.3.24. Co-culture with uninjured AT2 spheroid causes a reduction in THP-1 ISG transcription compared to unstimulated controls. *mRNA expression of interferon stimulated genes (MX1, ISG15, STAT1) and TNF-α, IFNβ and CD36 assessed by quantitative PCR. Expression measured in unstimulated THP1 cells (blue), THP-1 cells co-cultured with uninjured AT2 spheroids (green), and both type (red) and IFNAR$^{-/-}$ THP-1 cells (grey) cultured with injured AT2 spheroids. Dots represent individual samples, Data are presented as relative gene expression (ΔΔCt), normalised to unstimulated THP-1 cells. Statistical comparisons between pre-specified donor matched groups were performed using paired t-test on ΔΔCt values. Asterisks denote statistical significance as follows:* *p< 0.05, **p < 0.01, ***p< 0.001, ns, not significant (P ≥ 0.05).*

In addition, *TNF-α* expression was increased in THP-1 cells following co-culture with both injured and uninjured AT2 spheroids compared to unstimulated controls consistent with intracellular cytokine flow cytometry data (Section 6.3.5). This effect was observed in only WT but not IFNAR$^{-/-}$ cells, indicating the increased TNFα response in co-culture with injured AT2 cells, is dependent on IFNAR signalling. (Figure 6.3.24)

6.3.7 THP-1 cells influence expression of injury -related transcripts in injured alveolar spheroids

To investigate the effects of sdBLM injury and co-culture with THP-1 cells, gene expression in AT2 spheroids under conditions outlined in (Figure 6.3.21) were compared to uninjured AT2 spheroids alone. The gene panel included markers of mature AT2 cells

(*SFTPC*), intermediate or aberrant epithelial states (*KRT8, LRG1, CDKN1A*), and AT1 cells (*SCEL*). In addition, markers associated with epithelial dysfunction were assessed, including injury (*LRG1*), senescence (*CCND1, CDKN1A*), inflammation (*TNF-α),* and type 1 interferon signalling (*TMEM173* [STING] and *IFN-β*).

Co-culture of uninjured AT2 spheroids with THP-1 monocytes resulted in increased *SCEL* expression in AT2 cells (Figure 6.3.25). However, markers associated with epithelial injury or activation (*LRG1, CCND1, CDKN1A, KRT8*) were not increased, indicating that THP-1 co-culture alone without injury does not induce a broader injury associated or transitional epithelial state seen with bleomycin injury (Figure 6.3.25).

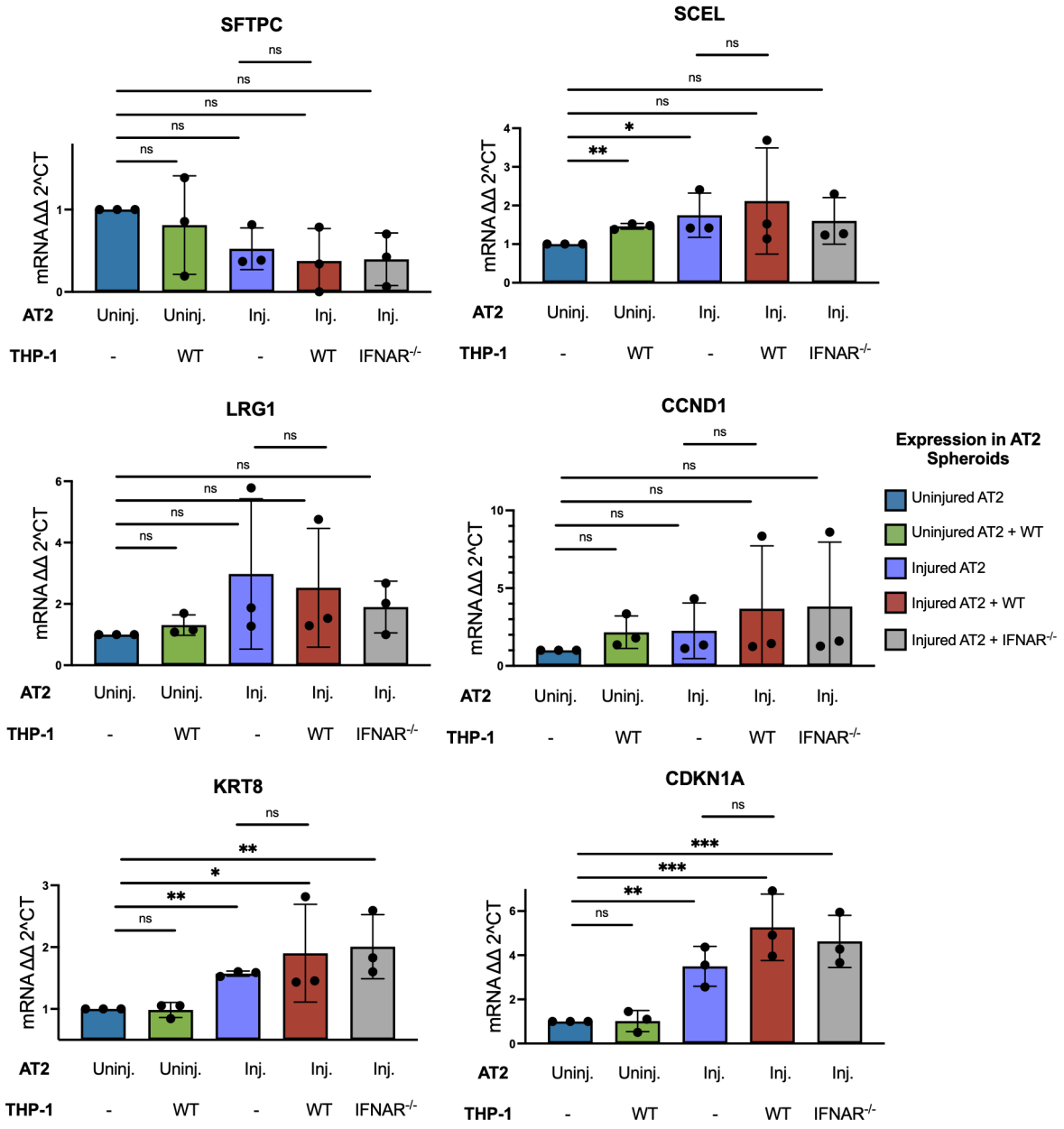


Figure 6.3.25. Coculture with THP-1 cells results in increased SCEL and TNF-α expression in AT2 spheroids. *mRNA expression of mature AT2 cells (SFTPC), intermediate or aberrant epithelial states (KRT8, LRG1, CCND1 CDKN1A), and AT1 cells (SCEL) was assessed by quantitative PCR. Expression measured in uninjured AT2 spheroids in monoculture (blue), with THP-1 cells (green), bleomycin injury only (purple) and injury with coculture of WT THP-1 (red) or IFNAR $^{-/-}$ (grey). Dots represent individual samples, Data are presented as relative gene expression (ΔΔCt), normalised to uninjured AT2 spheroids. Statistical comparisons between pre-specified donor matched groups were performed using paired t-test on ΔΔCt values. Asterisks denote statistical significance as follows:* p< *0.05, ** p < 0.01, *** p< 0.001, ns, not significant (P ≥ 0.05).*

In contrast, AT2 spheroids exposed to BLM (20 ng/ml) demonstrated an injury-associated transcriptional profile (Figure 6.3.25) with increased expression of senescence (*CDKN1A*) and inflammatory (*TNF-α)* markers (Figure 6.3.25). Transcripts associated with aberrant or transitional epithelial states (*KRT8, SCEL*) were also upregulated following bleomycin. These findings are consistent with observations described previously (Section 6.3.4).

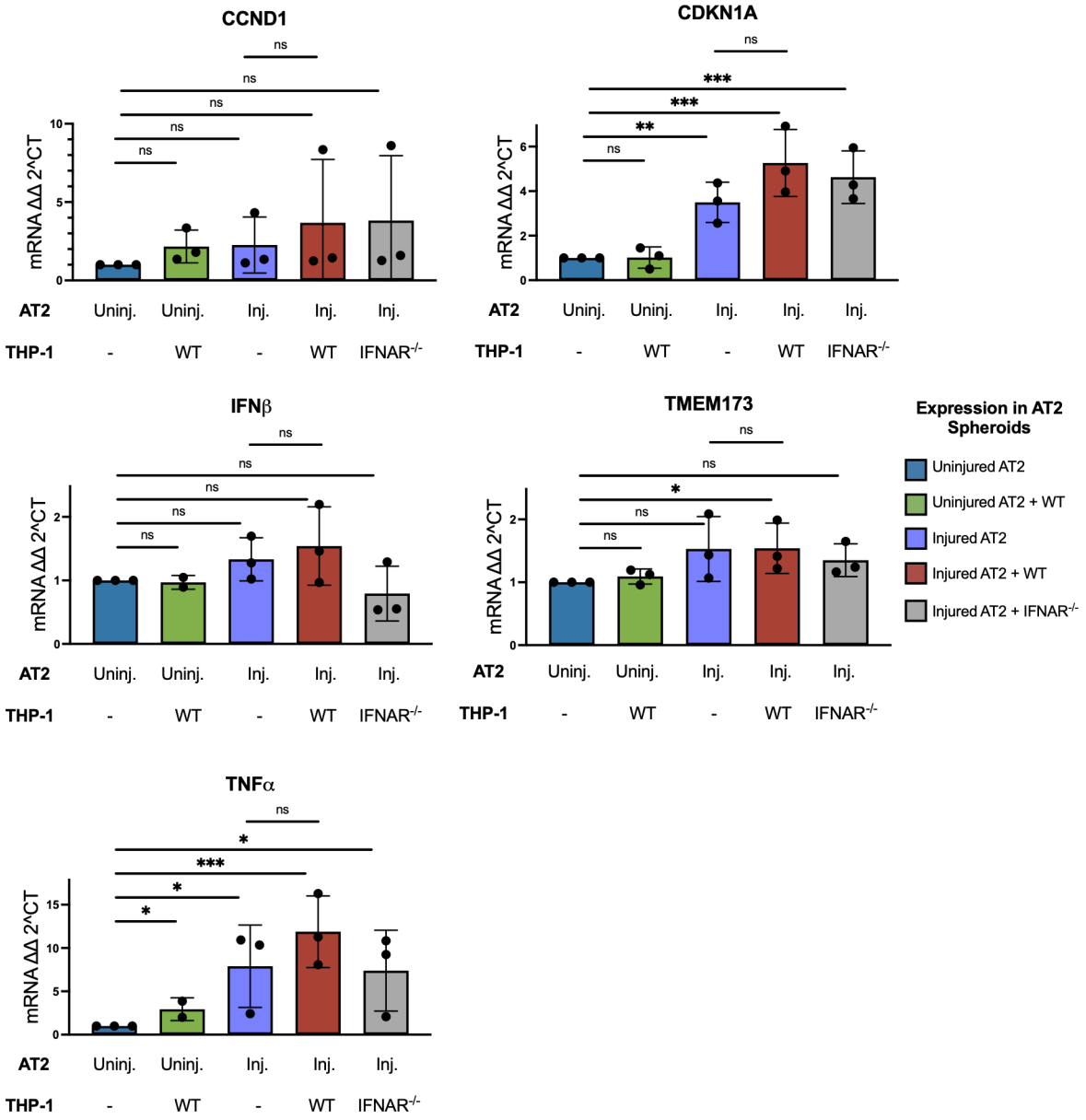


Figure 6.3.26. Co-culture with THP-1 cells does not result in statistically significant changes in expression of AT2 injury or senescence-associated genes. *mRNA expression of AT2 injury or senescence markers measured by quantitative PCR. Expression measured in uninjured AT2 spheroids in monoculture (blue), with THP-1 cells (green), bleomycin injury only (purple), injury with coculture of WT THP-1 (red) or IFNAR $^{-/-}$ THP-1 cells (grey). Dots represent individual samples. Data are presented as relative gene expression (ΔΔCt), normalised to uninjured AT2 spheroids. Statistical comparisons between pre-specified donor matched groups were performed using paired t-test on ΔΔCt values. Asterisks denote statistical significance as follows:* *p< *0.05, **p < 0.01, ***p< 0.001, ns, not significant (P ≥ 0.05).*

Co-culture of BLM injured AT2 spheroids with wild-type THP-1 cells was associated with modest increases in *CDKN1A* and *TNF-α* expression compared to injured spheroids cultured alone. This effect was not observed when AT2 spheroids were co-cultured with IFNAR^{-}/$^{-}$ THP-1 cells. Although these differences did not reach statistical significance across donors (Figure 6.3.26), donor matched responses demonstrated a consistent direction of effect. In all three donors, co-culture with WT THP-1 cells increased *CDKN1A* and *TNF-α* expression relative to injured spheroids cultured alone, whereas this increase was attenuated following co-culture with IFNAR$^{-/-}$ THP-1 cells (Figure 6.3.27). The magnitude of these responses varied substantially between donors, contributing to the absence of a statistically significant overall effect.

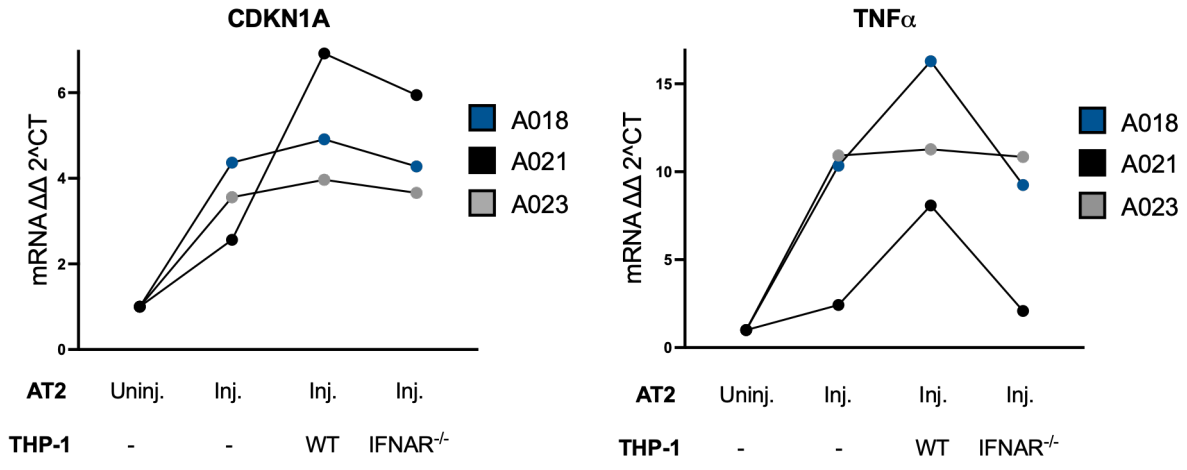


Figure 6.3.27. Co-culture with THP-1 cells reveal consistent effects on CDKN1A and TNF-α expression in injured AT2 spheroids across donors. *Line graph of mRNA expression of CDKN1A (left) and TNF-α (right) across experimental conditions (x axis). Each line linking coloured points represents an individual donor. Figure illustrates the consistent direction of donor responses following co-culture with WT THP-1 cells despite variation in the magnitude of response between donors.*

Together, these findings suggest that co-culture with WT THP-1 cells may contribute to injury-associated epithelial transcriptional responses following bleomycin injury, although these effects were variable between donors and did not reach statistical significance across the cohort.

6.4 Discussion

In this study, primary human AT2 cells cultured in ECM formed 3D spheroids that retained key morphological, phenotypic, and functional characteristics of AT2 cells, including surfactant protein expression, lysotracker uptake consistent with lamellar bodies, and HLA-DR expression. These cells demonstrated sustained proliferative capacity and the ability to transition into injury-associated epithelial states. Structurally, AT2 cells self-organised into polarised spheroids with a central lumen, recapitulating key features of alveolar architecture. This organisation was dependent on ECM, as cells cultured without ECM failed to establish polarity or spheroid structure. These findings are consistent with established primary AT2 organoid systems and support the physiological relevance of this model.

Although AT2 spheroids expressed some AT1-associated markers (e.g., *PDPN*, *HOPX*), they retained AT2 identity and did not acquire the flattened morphology of mature AT1 cells, suggesting an early or transitional differentiation state. This is in line with previous reports[314, 315, 317] and reflects the absence of differentiation-promoting conditions such as serum exposure, which were not applied here in order to preserve AT2 identity and model injury responses.

AT2 spheroid injury with BLM was associated with a transient, concentration dependent downregulation of AT2 gene expression (*SFTPC*), an increase in transcripts seen in AT2 transitional states and those associated with senescence and inflammatory signalling. These *in vitro* findings replicate features of AT2 dysfunction observed in intermediate AEC states that co-locate with IFN activated myeloid populations (Chapter 5.3.8 and Chapter 5.3.9). These findings as also consistent with AT2 cell aberrant states in murine BLM models *in vivo*[293, 294, 295] and sc RNA seq studies of alveolar epithelial cells from IPF patients[63, 86]. Notably, BLM treatment induced expression of TNF-α and IFN-β, consistent with prior in vitro models[68] and in vivo studies[68, 293, 295].

Mechanistically, these responses may be driven by DNA damage and mitochondrial dysfunction induced by BLM, leading to accumulation of cytoplasmic nuclear and mitochondrial DNA[59, 322, 323, 324, 325]. These damage-associated molecular patterns can activate innate immune pathways, including cGAS–STING signalling, promoting type 1 IFN and NF-κB–mediated inflammatory responses. BLM mediated activation of cGAS-STING was not shown here however other groups have demonstrated that BLM treated epithelial cell lines or cultured precision cut murine lung slices exhibited increased cytoplasmic mtDNA, reduced mitochondrial membrane integrity and increased cGAS activity [59, 308, 323].

Compared to alternative injury models (e.g., IL-1β stimulation[294] or fibroblast co-culture[300]), BLM uniquely induced both epithelial injury states and inflammatory/IFN

responses, suggesting that direct cellular damage and DAMP release are key drivers of the inflammatory phenotype observed in IPF-associated epithelial cells.

A central finding of this study is that injured AT2 cells promote type 1 IFN–dependent activation of myeloid cells. In co-culture, THP-1 cells exhibited increased expression of interferon-stimulated genes (*MX1, ISG15, STAT1*), which was dependent on IFNAR signalling. BLM injured AT2 cells exhibited increased IFN-β expression, whilst in THP-1 cells *IFN-β* was supressed, indicating the increased ISG expression seen in co-cultured THP-1 cells appears to be mediated via paracrine IFN-β arising from injured AT2 cells.

Increased *IFN-β* expression in injured AT2 cells supports a model in which epithelial-derived IFN-β acts in a paracrine manner to drive myeloid activation. This mirrors the IFN-activated myeloid populations observed at the alveolar barrier in IPF, Section 4.3.3 and Chapter 5.3.6.

In addition to ISG induction, THP-1 cells demonstrated increased *TNF-α* expression in co-culture. The effect of type 1 IFN on TNF-α appeared context-dependent: IFN-β alone suppressed *TNF-α,* whereas in the presence of epithelial injury signals, IFNAR signalling enhanced *TNF-α* expression. This is consistent with established models in which type 1 IFNs can both suppress and amplify inflammatory responses depending on signalling context[201, 242, 255], reflecting cross-talk between IFN and NF-κB pathways[195, 199, 326].

This study also provided initial insight into how IFN activated monocytes and macrophages influence AT2 cell gene expression. One issue encountered was donor variability in AT2 gene expression in response to BLM and coculture. Despite this variability, some consistent trends were observed. Co-culture with IFN-responsive THP-1 cells was associated with increased epithelial expression of *CDKN1A* and *TNF-α*, which was reduced when IFNAR signalling was abrogated. Although these findings did not reach statistical significance, the consistent direction of donor responses suggests that myeloid IFN signalling may influence epithelial stress and senescence programmes and warrants further investigation.

In line with this finding, increased IFN signalling has been shown to promote cellular senescence. Patients with Hutchinson-Gilford progeria syndrome (HGPS) and telomerase RNA component deficient ($TERC^{-/-}$) mice are predisposed to early senescence due to telomere shortening and exhibit increased IFN signalling. Treatment of cells from HGPS patients in vitro with IFN-β neutralising antibodies and $TERC^{-/-}$ $IFNAR^{-/-}$ mice have reduced features of senescence and cell cycle arrest[327]. Blockade of IFN-β signalling was also associated with a reduction in expression of senescence markers *CDKN1A*, *CDKN2A* and *p53*. In a separate study, inhibition of cGAS in AECs from patients with IPF or etoposide injured A549 epithelial cells was associated with reduced *IFN-β,*

CDKN1A and reduced SA-β-GAL staining[59]. In both studies type 1 IFN mediated senescence was also associated with increase proinflammatory marker expression.

To develop these findings, the study is currently being repeated using additional donor derived AT2 spheroids to reduce the influence of inter-donor variability and assess the reproducibility of the donor specific responses. This experiment will also include a time course analysis where additional samples will be collected at multiple time points to determine whether co-culture with THP-1 cells influences the magnitude of AEC responses but also persistence of injury associated transcriptional responses, including senescent or aberrant AEC phenotypes characteristic of IPF. Additional samples retained from these experiments will facilitate subsequent bulk transcriptomic analysis, proteomic analysis of culture supernatants, and immunofluorescence assessment of senescence protein expression, including SA-β-Gal, p53 and p16 in paraffin embedded AT2 spheroids and THP-1 cocultures. Together, these complementary analyses will provide additional measures of epithelial stress responses beyond targeted qPCR.

Future co-culture studies using primary human monocytes isolated from PBMCs and alveolar macrophages obtained from BAL samples will enable validation of these findings in physiologically relevant myeloid populations and determine whether the responses observed using THP-1 cells are recapitulated in primary cells.

6.5 Conclusion

In this study, an in vitro model of AT2 dysfunction was developed using primary human AT2 cells, which recapitulated key ytanscriptional features of aberrant alveolar epithelial states described in IPF. Within this system, injured AT2 cells exhibited transcriptional signatures consistent with senescence, inflammatory activation, and IFN-β production, reflecting intermediate and aberrant epithelial cell states identified in tissue-based and transcriptomic analyses.

Co-culture experiments demonstrated that injured AT2 cells induce a type 1 interferon–associated response in THP-1 myeloid cells, evidenced by increased ISG expression. This provides functional evidence that epithelial injury contributes to the IFN-activated myeloid phenotype observed in IPF.

These findings are consistent with spatial studies showing co-localisation of dysfunctional epithelial states and IFN-activated macrophages within the diseased lung. In addition, IFN-responsive myeloid cells may influence epithelial stress and senescence markers, suggesting bidirectional epithelial–myeloid crosstalk that warrants further investigation in primary human myeloid cells and more physiologically relevant co-culture systems.

Chapter 7 - General Discussion and Future Directions

7.1 Discussion

In this thesis, I investigated type 1 IFN signalling across circulating, alveolar barrier (BAL), and lung-resident monocyte and macrophage populations in IPF, with the aim of defining how this pathway relates to disease stage, tissue context, and epithelial dysfunction. By integrating single-cell, spatial, and functional approaches, my findings support a model in which type 1 IFN signalling links epithelial injury to myeloid activation in the early IPF disease process.

In the first part of the thesis, I showed that circulating monocytes in IPF exhibit enhanced responsiveness to IFN-β stimulation, characterised by increased activation of canonical JAK-STAT signalling pathways, alongside increased type 1 IFN regulatory activity ex vivo. This primed phenotype extends prior observations of elevated interferon-stimulated gene expression in IPF monocytes and suggests that circulating monocytes are either pre-conditioned to respond to interferon signals before entering the lung, or reflect prior priming within the lung environment.

Within the lung, single-cell transcriptomic analysis revealed substantial heterogeneity across monocyte and macrophage populations. Five discrete alveolar macrophage subsets were identified in BAL samples, and fourteen monocyte and macrophage subsets in lung digests, each with distinct transcriptomic profiles. Some of these likely represent activation, homeostatic, or metabolic states rather than fixed lineages. While some of these populations have been described in other contexts[142, 156, 263] , macrophage heterogeneity has not been fully characterised in IPF, where the compartment has often been treated as homogeneous[63] or divided into a small number of subsets[62, 86, 185].

This analysis highlights two key aspects of macrophage biology in IPF that have not been previously reported. First, despite marked heterogeneity, macrophages in lung tissue converge on a shared transcriptional programme characterised by upregulation of extracellular matrix remodelling genes, likely reflecting adaptation to the fibrotic environment. SPP1^{hi} macrophages, the most consistently described subset in IPF, likely represent an example of this state. This has potential therapeutic implications, suggesting that targeting environmental cues driving this convergent phenotype may be more effective than targeting individual subsets.

Second, when upper (earlier) and lower (advanced disease) lobe lung digests were analysed, type 1 IFN activation was found to be enhanced in discrete myeloid populations in the upper lobe. Alveolar macrophage subsets at the alveolar barrier,

representing an early point in disease-notably CXCL10^{+}, FABP4^{hi}, IGF1^{+}, and CD206^{hi} AM populations-also exhibited a type 1 IFN–activated transcriptional phenotype associated with inflammatory signalling. In contrast, interstitial macrophages, including SPP1^{+} populations, and monocytes within fibrotic regions showed lower interferon pathway activation. These findings indicate that local microenvironmental context, rather than lineage alone, is a key determinant of macrophage phenotype.

Spatial profiling at single cell level provided further insight into this microenvironment. Using imaging mass cytometry and the SpOOx v2.0 analytical pipeline, I demonstrated that type 1 IFN - activated alveolar macrophages were selectively enriched in proximity to intermediate epithelial cell states, including transitional AT2 cells, aberrant basaloid intermediates (ABIs), and inflammatory AT1 populations. These epithelial states are recognised as hallmarks of impaired epithelial repair in IPF and may represent critical decision points between normal and aberrant regeneration[225]. Here, I show that intermediate epithelial populations exhibited increased expression of markers associated with DNA damage and senescence as previously described in transcriptomic studies[294, 295, 300]. In this study these cells were found to also show evidence of innate immune activation, including evidence of cGAS–STING pathway engagement and production of IFN-β and TNF-α. Cell contact network analysis using SpOOx v2.0 further showed that these spatial relationships reflect direct physical cellular associations. Type 1 IFN - activated macrophage subsets formed contacts selectively with transitional and aberrant epithelial populations, whereas normal AT1 and AT2 cells were associated with macrophages exhibiting lower IFN activity. This finding refines the alveolar epithelial- myeloid cell spatial relationship, localising it to specific epithelial cell states. Whilst this spatial study supported a model in which dysfunctional epithelial cells may act as a local source of signals that promote the interferon-activated myeloid phenotype in IPF.

Moving beyond observational associations, an in vitro model of epithelial injury was developed using primary human AT2-derived spheroids. Bleomycin-induced injury recapitulated key features of intermediate epithelial states, including increased TNF-α, senescence, and type 1 interferon signalling. Co-culture with monocyte-like cells (THP-1) induced ISG expression in the myeloid compartment, providing functional support for a link between epithelial injury or alveolar epithelial cell dysfunction and myeloid type 1 IFN activation.

Taken together, these findings support a model in which type 1 IFN signalling emerges as a spatially restricted axis linking aberrant epithelial states to myeloid activation in early IPF. In regions of intact epithelial integrity, interactions with normal AT2 and AT1 cells are associated with macrophage states exhibiting low IFN activity. In contrast, within niches of epithelial dysfunction characterised by transitional AT2, ABI, and inflammatory AT1

states, exhibited cellular senescence and were associated with local production of type 1 IFN and presence of type 1 IFN-activated macrophage states. This specific epithelial-myeloid coupling is most prominent in early and intermediate stages of disease and appears to diminish as macrophages transition toward matrix-remodelling phenotypes in advanced fibrosis.

The spatial association between dysfunctional epithelial states and IFN-activated myeloid populations also provides insight into the mechanism linking epithelial injury with local innate immune activation. One potential mechanism linking these observations is the induction of cellular stress pathways within dysfunctional alveolar epithelial cells. Cellular senescence and mitochondrial dysfunction are associated with the release of damage-associated molecular patterns (DAMPs), including cytoplasmic mitochondrial and nuclear DNA, which activate innate immune sensing pathways such as cGAS-STING and promote type 1 IFN production. Consistent with this mechanism, transitional epithelial populations identified by imaging mass cytometry demonstrated increased phosphorylated STING together with expression of IFN-β and TNF-α. Furthermore, increased extracellular mitochondrial DNA has been reported in BAL fluid and serum from patients with IPF[328], supporting activation of this pathway during epithelial injury. As IPF is associated with advancing age, this mechanism also aligns with emerging concepts of inflammaging whereby cellular dysfunction, senescence and persistent cell stress promote chronic activation of innate immune pathways and age-related diseases.

Together, these observations provide a potential mechanism through which epithelial injury may initiate local type 1 IFN activation in neighbouring myeloid cells. The organoid co-culture studies further suggest that IFN-responsive monocytes and macrophages may not simply respond to epithelial injury but could also influence epithelial stress responses, consistent with bidirectional epithelial–myeloid communication. Whether these IFN activated cells contribute directly to disease progression in IPF, however, remains uncertain.

Inflammatory diseases characterised by dysregulated type 1 IFN signalling, including SLE and SSc, may provide insight into the potential functional consequences of IFN-activated myeloid populations in IPF. In SSc, a fibrosing disease characterised by dermal and often pulmonary fibrosis, blockade of IFNAR in preclinical models has been shown to reduce dermal fibrosis, accompanied by decreased expression of TGF-β[223]. Similarly, SLE is frequently complicated by lupus nephritis which can result in renal fibrosis. Anifrolumab, an IFNAR blocking antibody, has been licenced for use in SLE and has been associated with reduced markers of renal inflammation and fibrosis and has been shown in a recent study investigating its mechanism of action to reduce urinary CD163 a marker of interstitial renal macrophages, together with CCL2, a key mediator of $CCR2^{+}$

monocyte recruitment[329]. Separate studies have also demonstrated reduced monocyte infiltration in renal tissue following IFNAR blockade[330].

Together, these findings highlight the relevance of type 1 IFN signalling in immune-mediated fibrotic diseases and support further investigation into whether IFN-activated myeloid populations contribute directly to disease pathogenesis in IPF.

Within IPF, these observations should also be considered alongside $SPP1^{+/hi}$ macrophages, which are consistently expanded in advanced disease. There is growing evidence supporting a pro-fibrotic role for $SPP1^{+}$ macrophages across multiple organ systems. Hoeft et al. identified $SPP1^{+}$ macrophages in cardiac and renal fibrosis models and demonstrated that platelet-derived CXCL4 promotes this phenotype *in vitro*. Notably, $CXCL4^{-/-}$ mice exhibited reduced numbers of $SPP1^{+}$ macrophages and reduced fibrosis[289]. Similarly, Fabre et al. described 'scar-associated macrophages' (SAMs) in liver and lung fibrosis, where IL-17, GM-CSF, and TGF-β drive monocyte differentiation into this phenotype, and blockade of these pathways reduces collagen deposition and attenuated both hepatic and pulmonary fibrosis[290]. In the lung specific model described in this study, asbestos exposure induced a monocyte derived $SPP1^{+}$ macrophage population expressing TIMP2, arginase 1, and matrix metalloproteinases, comparable to those observed in IPF[290].

Within this context, type 1 IFN activation may represent an additional, non-mutually exclusive pathway through which monocytes and macrophages influence disease pathophysiology. Notably, the association of IFN signalling with epithelial injury and its enrichment in earlier disease stages suggests that targeting this pathway may offer an opportunity to intervene prior to the development of irreversible fibrosis, in contrast to $SPP1^{+}$ macrophage populations, which predominate in later disease.

Collectively, these findings support the integrated model presented in Figure 7.1.1, in which genetically susceptible and ageing alveolar epithelial cells undergo chronic low-level repetitive injury, leading to the emergence of intermediate epithelial states characterised by cellular stress, activation of innate immune sensing pathways including cGAS–STING, and production of type 1 IFNs and inflammatory cytokines. These signals are proposed to promote activation of neighbouring monocytes and macrophages, resulting in local activation of type 1 IFN-responsive monocytes and macrophages at the alveolar barrier. Recruitment and differentiation of IFN-responsive monocytes may further amplify this response, establishing a feed-forward loop of epithelial injury, innate immune activation and the initiation of tissue remodelling.

The proposed model should, however, be interpreted within the context of several limitations. First, although spatial and in vitro findings are consistent with a directional relationship between epithelial dysfunction and myeloid activation, causality cannot be

definitively established. Second, antibody-based spatial profiling (single cell tissue imaging mass cytometry) restricts analysis to predefined markers and may not capture the full complexity of signalling pathways involved. Finally, the organoid model simplifies the in vivo microenvironment and does not incorporate the full range of stromal and immune interactions present in IPF lung tissue.

Furthermore, although much of this work focused on signalling downstream of IFNAR and utilised IFN-β stimulation, some interferon-stimulated genes and transcriptional regulators identified through transcriptomic and regulon analyses are shared between type 1 and type 2 IFN signalling pathways. Consequently, where direct evidence of IFNAR activation was unavailable, these findings should be interpreted cautiously and discussed in the context of broader interferon signalling.

Finally, this work focused on a specific hypothesis and did not address several additional ways in which myeloid type 1 IFN activation may influence alveolar epithelial cell dysfunction. In particular, it remains unclear whether epithelial-myeloid type 1 IFN interactions contribute to the persistence of epithelial senescence and dysfunction, rather than simply influencing the transient injury response. Similarly, the current alveolar organoid model recapitulates epithelial injury and early repair but does not extend to persistent epithelial dysfunction, failed regeneration or fibrosis development.

The present work intentionally focused on epithelial-myeloid interactions to investigate a specific mechanistic hypothesis. Future application of spatial transcriptomic technologies will enable this model to be extended by examining additional stromal, vascular and lymphoid populations within the broader fibrotic niche and facilitate interrogation of type 1 IFN responses within the context of additional signalling pathways. Although advances in spatial transcriptomic technologies will enable more comprehensive molecular characterisation of epithelial-myeloid interactions, these approaches remain fundamentally observational. Establishing causality will require complementary functional models that permit direct interrogation of epithelial-myeloid signalling pathways.

Therefore, the priority for future work, building on the organoid co-culture platform established here will be to further develop the organoid model to better recapitulate chronic epithelial injury in IPF. This includes the development of repeated low-dose bleomycin injury models, incorporation of additional stromal cell populations, and investigation of epithelial-myeloid interactions using primary human monocytes and macrophages. These approaches will enable assessment of whether IFN activated myeloid cells contribute to the persistence of epithelial dysfunction and fibrogenesis directly and will be the next step in determining whether this pathway represents a potential therapeutic target during the early stages of disease.

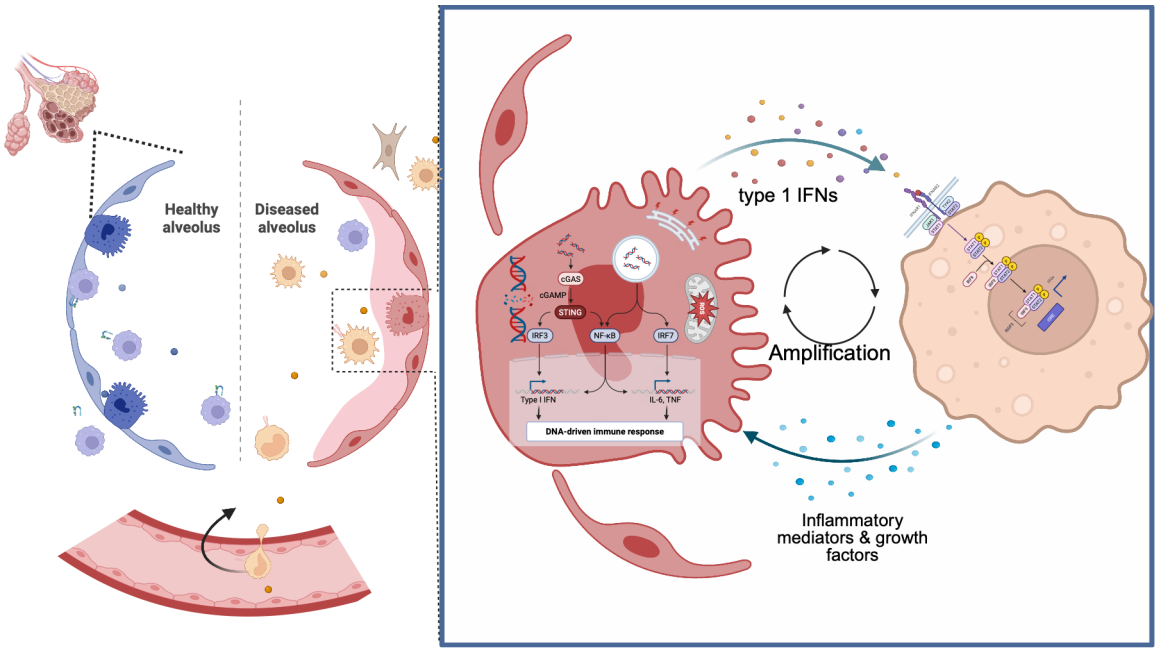


Figure 7.1 Proposed model linking alveolar epithelial cell dysfunction to a type 1 interferon activated monocyte and macrophage state

7.2 Conclusion

In summary, this study demonstrates that type 1 IFN-activated macrophages in IPF lung tissue are spatially restricted to the alveolar barrier and enriched in earlier stages of the disease process. These macrophages are selectively associated with intermediate epithelial states, including aberrant basaloid intermediates, transitional AT2, and inflammatory AT1 populations. In vitro studies indicate that these epithelial states can induce type 1 interferon responses in myeloid cells.

Overall, this thesis supports a model in which epithelial dysfunction and aberrant repair define a local microenvironment associated with myeloid type 1 IFN activation at sites of early fibrogenesis, preceding established fibrosis.

Bibliography

1. Raghu, G. *et al*. Idiopathic pulmonary fibrosis in US Medicare beneficiaries aged 65 years and older: incidence, prevalence, and survival, 2001–11. *The Lancet Respiratory Medicine* **2**, 566-572 (2014).

2. Khor, Y.H. *et al*. Prognosis of idiopathic pulmonary fibrosis without anti-fibrotic therapy: a systematic review. *Eur Respir Rev* **29** (2020).

3. Spagnolo, P. *et al*. Global epidemiology and burden of interstitial lung disease. *The Lancet Respiratory Medicine* **13**, 739-755 (2025).

4. Navaratnam, V. *et al*. The rising incidence of idiopathic pulmonary fibrosis in the U.K. *Thorax* **66**, 462-467 (2011).

5. Gupta, R., Morgan, A.D., George, P.M. & Quint, J.K. Incidence, prevalence and mortality of idiopathic pulmonary fibrosis in England from 2008 to 2018: a cohort study. *Thorax* **79**, 624 (2024).

6. Hutchinson, J., Fogarty, A., Hubbard, R. & McKeever, T. Global incidence and mortality of idiopathic pulmonary fibrosis: a systematic review. *European Respiratory Journal* **46**, 795-806 (2015).

7. Collard, H.R. *et al*. Health Care Utilization and Costs of Idiopathic Pulmonary Fibrosis in U.S. Medicare Beneficiaries Aged 65 Years and Older. *Annals of the American Thoracic Society* **12**, 981-987 (2015).

8. Ley, B. & Collard, H.R. Epidemiology of idiopathic pulmonary fibrosis. *Clin Epidemiol* **5**, 483-492 (2013).

9. Fletcher, S.V. *et al*. Safety and tolerability of nintedanib for the treatment of idiopathic pulmonary fibrosis in routine UK clinical practice. *ERJ Open Res* **4** (2018).

10. Tran, T. *et al*. The European MultiPartner IPF registry (EMPIRE): validating long-term prognostic factors in idiopathic pulmonary fibrosis. *Respir Res* **21**, 11 (2020).

11. Lamas, D.J. *et al*. Delayed Access and Survival in Idiopathic Pulmonary Fibrosis: A Cohort Study. *American Journal of Respiratory and Critical Care Medicine* **184**, 842-847 (2011).

12. Mooney, J. *et al*. Potential Delays in Diagnosis of Idiopathic Pulmonary Fibrosis in Medicare Beneficiaries. *Annals of the American Thoracic Society* **16**, 393-396 (2019).

13. Lee, R.W. *et al*. Implementation of the NHS England Lung Cancer Screening Programme over 5 years. *Nature Medicine* (2026).

14. Achaiah, A. *et al*. Monocyte and neutrophil levels are potentially linked to progression to IPF for patients with indeterminate UIP CT pattern. *BMJ Open Respiratory Research* **8**, e000899 (2021).

15. Rose, J.A. *et al*. Development, Progression, and Mortality of Suspected Interstitial Lung Disease in COPDGene. *American Journal of Respiratory and Critical Care Medicine* **210**, 1453-1460 (2024).

16. Ley, B. *et al*. A Multidimensional Index and Staging System for Idiopathic Pulmonary Fibrosis. *Annals of Internal Medicine* **156**, 684-691 (2012).

17. Lee, S.H. *et al*. Predicting survival of patients with idiopathic pulmonary fibrosis using GAP score: a nationwide cohort study. *Respiratory Research* **17**, 131 (2016).

18. van Manen, M.J.G. *et al*. Clubbing in patients with fibrotic interstitial lung diseases. *Respiratory Medicine* **132**, 226-231 (2017).

19. Raghu, G. *et al*. Diagnosis of Idiopathic Pulmonary Fibrosis. An Official ATS/ERS/JRS/ALAT Clinical Practice Guideline. *Am J Respir Crit Care Med* **198**, e44-e68 (2018).

20. Raghu, G. *et al*. Diagnosis of Idiopathic Pulmonary Fibrosis. An Official ATS/ERS/JRS/ALAT Clinical Practice Guideline. *American Journal of Respiratory and Critical Care Medicine* **198**, e44-e68 (2018).

21. Collard, H.R. *et al*. Acute Exacerbation of Idiopathic Pulmonary Fibrosis. An International Working Group Report. *American Journal of Respiratory and Critical Care Medicine* **194**, 265-275 (2016).

22. Song, J.W., Hong, S.-B., Lim, C.-M., Koh, Y. & Kim, D.S. Acute exacerbation of idiopathic pulmonary fibrosis: incidence, risk factors and outcome. *European Respiratory Journal* **37**, 356-363 (2010).

23. Schupp, J.C. *et al*. Macrophage Activation in Acute Exacerbation of Idiopathic Pulmonary Fibrosis. *PLOS ONE* **10**, e0116775 (2015).

24. Johannson, K.A. *et al*. Acute exacerbation of idiopathic pulmonary fibrosis associated with air pollution exposure. *European Respiratory Journal* **43**, 1124-1131 (2013).

25. Ghatol, A., Ruhl, A.P. & Danoff, S.K. Exacerbations in Idiopathic Pulmonary Fibrosis Triggered by Pulmonary and Nonpulmonary Surgery: A Case Series and Comprehensive Review of the Literature. *Lung* **190**, 373-380 (2012).

26. Oda, K. *et al*. Autopsy analyses in acute exacerbation of idiopathic pulmonary fibrosis. *Respiratory Research* **15**, 109 (2014).

27. Fujita, H. *et al*. Effects of Doxycycline on Production of Growth Factors and Matrix Metalloproteinases in Pulmonary Fibrosis. *Respiration* **81**, 420-430 (2011).

28. Krempaska, K. *et al*. Azithromycin has enhanced effects on lung fibroblasts from idiopathic pulmonary fibrosis (IPF) patients compared to controls. *Respiratory Research* **21**, 25 (2020).

29. Tong, X. *et al*. Azithromycin Attenuates Bleomycin-Induced Pulmonary Fibrosis Partly by Inhibiting the Expression of LOX and LOXL-2. *Frontiers in Pharmacology* **Volume 12 - 2021** (2021).

30. Chen, C.-Y. *et al*. The effect of additional antimicrobial therapy on the outcomes of patients with idiopathic pulmonary fibrosis: a systematic review and meta-analysis. *Respiratory Research* **22**, 243 (2021).

31. Richeldi, L. *et al*. Efficacy and safety of nintedanib in idiopathic pulmonary fibrosis. *N Engl J Med* **370**, 2071-2082 (2014).

32. Noble, P.W. *et al*. Pirfenidone in patients with idiopathic pulmonary fibrosis (CAPACITY): two randomised trials. *Lancet* **377**, 1760-1769 (2011).

33. Nathan, S.D. *et al*. Effect of pirfenidone on mortality: pooled analyses and meta-analyses of clinical trials in idiopathic pulmonary fibrosis. *The Lancet Respiratory Medicine* **5**, 33-41 (2017).

34. Lancaster, L. *et al*. Safety and survival data in patients with idiopathic pulmonary fibrosis treated with nintedanib: pooled data from six clinical trials. *BMJ Open Respiratory Research* **6**, e000397 (2019).

35. Petnak, T., Lertjitbanjong, P., Thongprayoon, C. & Moua, T. Impact of Antifibrotic Therapy on Mortality and Acute Exacerbation in Idiopathic Pulmonary Fibrosis: A Systematic Review and Meta-Analysis. *Chest* **160**, 1751-1763 (2021).

36. Hozumi, H. *et al*. Antifibrotics and mortality in idiopathic pulmonary fibrosis: external validity and avoidance of immortal time bias. *Respiratory Research* **25**, 293 (2024).

37. Zhao, R. *et al*. The tolerability and efficacy of antifibrotic therapy in patients with idiopathic pulmonary fibrosis: Results from a real-world study. *Pulmonary Pharmacology & Therapeutics* **84**, 102287 (2024).

38. Sugino, K., Ono, H., Saito, M., Ando, M. & Tsuboi, E. Tolerability and efficacy of switching anti-fibrotic treatment from nintedanib to pirfenidone for idiopathic pulmonary fibrosis. *PLOS ONE* **19**, e0305429 (2024).

39. Ruwanpura, S.M., Thomas, B.J. & Bardin, P.G. Pirfenidone: Molecular Mechanisms and Potential Clinical Applications in Lung Disease. *American Journal of Respiratory Cell and Molecular Biology* **62**, 413-422 (2020).

40. Wollin, L. *et al*. Mode of action of nintedanib in the treatment of idiopathic pulmonary fibrosis. *European Respiratory Journal* **45**, 1434-1445 (2015).

41. Bellamri, N. *et al*. Alteration of human macrophage phenotypes by the anti-fibrotic drug nintedanib. *International Immunopharmacology* **72**, 112-123 (2019).

42. Farooq, H. *et al*. Molecular imaging in experimental pulmonary fibrosis reveals that nintedanib unexpectedly modulates CCR2 immune cell infiltration. *eBioMedicine* **110** (2024).

43. Joshi, N. *et al*. A spatially restricted fibrotic niche in pulmonary fibrosis is sustained by M-CSF/M-CSFR signalling in monocyte-derived alveolar macrophages. *Eur Respir J* **55** (2020).

44. Seibold Max, A. *et al*. A Common MUC5B Promoter Polymorphism and Pulmonary Fibrosis. *New England Journal of Medicine* **364**, 1503-1512.

45. Hancock, L.A. *et al*. Muc5b overexpression causes mucociliary dysfunction and enhances lung fibrosis in mice. *Nature Communications* **9**, 5363 (2018).

46. Armanios Mary, Y. *et al*. Telomerase Mutations in Families with Idiopathic Pulmonary Fibrosis. *New England Journal of Medicine* **356**, 1317-1326.

47. Alder, J.K. *et al*. Short telomeres are a risk factor for idiopathic pulmonary fibrosis. *Proceedings of the National Academy of Sciences* **105**, 13051-13056 (2008).

48. Thomas, A.Q. *et al*. Heterozygosity for a surfactant protein C gene mutation associated with usual interstitial pneumonitis and cellular nonspecific interstitial pneumonitis in one kindred. *American journal of respiratory and critical care medicine* **165 9**, 1322-1328 (2002).

49. Wang, Y. *et al*. Genetic Defects in Surfactant Protein A2 Are Associated with Pulmonary Fibrosis and Lung Cancer. *The American Journal of Human Genetics* **84**, 52-59 (2009).

50. Katzen, J. *et al*. An SFTPC BRICHOS mutant links epithelial ER stress and spontaneous lung fibrosis. *JCI Insight* **4** (2019).

51. Wolters, P.J., Collard, H.R. & Jones, K.D. Pathogenesis of Idiopathic Pulmonary Fibrosis. *Annual Review of Pathology: Mechanisms of Disease* **9**, 157-179 (2014).

52. Lawson, W.E. *et al*. Endoplasmic reticulum stress in alveolar epithelial cells is prominent in IPF: association with altered surfactant protein processing and herpesvirus infection. *American Journal of Physiology-Lung Cellular and Molecular Physiology* **294**, L1119-L1126 (2008).

53. Tobin, R.W. *et al*. Increased Prevalence of Gastroesophageal Reflux in Patients with Idiopathic Pulmonary Fibrosis. *American Journal of Respiratory and Critical Care Medicine* **158**, 1804-1808 (1998).

54. Steele, M.P. *et al*. Clinical and Pathologic Features of Familial Interstitial Pneumonia. *American Journal of Respiratory and Critical Care Medicine* **172**, 1146-1152 (2005).

55. Scott, J., Johnston, I. & Britton, J. What causes cryptogenic fibrosing alveolitis? A case-control study of environmental exposure to dust. *British Medical Journal* **301**, 1015 (1990).

56. Invernizzi, R. & Molyneaux, P.L. The contribution of infection and the respiratory microbiome in acute exacerbations of idiopathic pulmonary fibrosis. *European Respiratory Review* **28**, 190045 (2019).

57. Moss, B.J., Ryter, S.W. & Rosas, I.O. Pathogenic Mechanisms Underlying Idiopathic Pulmonary Fibrosis. *Annual Review of Pathology: Mechanisms of Disease* **17**, 515-546 (2022).

58. Raghu, G. *et al*. Idiopathic pulmonary fibrosis in US Medicare beneficiaries aged 65 years and older: incidence, prevalence, and survival, 2001-11. *Lancet Respir Med* **2**, 566-572 (2014).

59. Schuliga, M., Read, J. & Knight, D.A. Ageing mechanisms that contribute to tissue remodeling in lung disease. *Ageing Research Reviews* **70**, 101405 (2021).

60. Katzen, J. & Beers, M.F. Contributions of alveolar epithelial cell quality control to pulmonary fibrosis. *The Journal of Clinical Investigation* **130**, 5088-5099 (2020).

61. Schafer, M.J. *et al*. Cellular senescence mediates fibrotic pulmonary disease. *Nat Commun* **8**, 14532 (2017).

62. Reyfman, P.A. *et al*. Single-Cell Transcriptomic Analysis of Human Lung Provides Insights into the Pathobiology of Pulmonary Fibrosis. *American Journal of Respiratory and Critical Care Medicine* **199**, 1517-1536 (2019).

63. Habermann, A.C. *et al*. Single-cell RNA sequencing reveals profibrotic roles of distinct epithelial and mesenchymal lineages in pulmonary fibrosis. *Science Advances* **6**, eaba1972.

64. Yao, C. *et al*. Senescence of Alveolar Type 2 Cells Drives Progressive Pulmonary Fibrosis. *American Journal of Respiratory and Critical Care Medicine* **203**, 707-717 (2021).

65. Herbig, U., Jobling, W.A., Chen, B.P.C., Chen, D.J. & Sedivy, J.M. Telomere Shortening Triggers Senescence of Human Cells through a Pathway Involving ATM, p53, and p21CIP1, but Not p16INK4a. *Molecular Cell* **14**, 501-513 (2004).

66. Naikawadi, R.P. *et al*. Telomere dysfunction in alveolar epithelial cells causes lung remodeling and fibrosis. *JCI Insight* **1** (2016).

67. Zhang, Y. *et al*. Cigarette smoke-inactivated SIRT1 promotes autophagy-dependent senescence of alveolar epithelial type 2 cells to induce pulmonary fibrosis. *Free Radical Biology and Medicine* **166**, 116-127 (2021).

68. Aoshiba, K. & Nagai, A. Oxidative Stress, Cell Death, and Other Damage to Alveolar Epithelial Cells Induced by Cigarette Smoke. *Tob. Induc. Dis.* **1** (2003).

69. Jablonski, R.P. *et al*. SIRT3 deficiency promotes lung fibrosis by augmenting alveolar epithelial cell mitochondrial DNA damage and apoptosis. *The FASEB Journal* **31**, 2520-2532 (2017).

70. Bueno, M. *et al*. PINK1 deficiency impairs mitochondrial homeostasis and promotes lung fibrosis. *The Journal of Clinical Investigation* **125**, 521-538 (2014).

71. Patel, A.S. *et al*. Autophagy in Idiopathic Pulmonary Fibrosis. *PLOS ONE* **7**, e41394 (2012).

72. Korfei, M. *et al*. Epithelial Endoplasmic Reticulum Stress and Apoptosis in Sporadic Idiopathic Pulmonary Fibrosis. *American Journal of Respiratory and Critical Care Medicine* **178**, 838-846 (2008).

73. Borok, Z. *et al*. Grp78 Loss in Epithelial Progenitors Reveals an Age-linked Role for Endoplasmic Reticulum Stress in Pulmonary Fibrosis. *American Journal of Respiratory and Critical Care Medicine* **201**, 198-211 (2020).

74. Khalil, N., O'Connor, R.N., Flanders, K.C. & Unruh, H. TGF-β1, but Not TGF-β2 or TGF-β3, is Differentially Present in Epithelial Cells of Advanced Pulmonary Fibrosis: An Immunohistochemical Study. *American Journal of Respiratory Cell and Molecular Biology* **14**, 131-138 (1996).

75. Hewlett, J.C., Kropski, J.A. & Blackwell, T.S. Idiopathic pulmonary fibrosis: Epithelial-mesenchymal interactions and emerging therapeutic targets. *Matrix Biology* **71-72**, 112-127 (2018).

76. Sheppard, D. Transforming Growth Factor β: A Central Modulator of Pulmonary and Airway Inflammation and Fibrosis. *Proceedings of the American Thoracic Society* **3**, 413-417 (2006).

77. Sime, P.J., Xing, Z., Graham, F.L., Csaky, K.G. & Gauldie, J. Adenovector-mediated gene transfer of active transforming growth factor-beta1 induces prolonged severe fibrosis in rat lung. *The Journal of Clinical Investigation* **100**, 768-776 (1997).

78. Munger, J.S. *et al*. A Mechanism for Regulating Pulmonary Inflammation and Fibrosis: The Integrin αvβ6 Binds and Activates Latent TGF β1. *Cell* **96**, 319-328 (1999).

79. Kendall, R.T. & Feghali-Bostwick, C.A. Fibroblasts in fibrosis: novel roles and mediators. *Frontiers in Pharmacology* **Volume 5 - 2014** (2014).

80. Redente, E.F. *et al*. Loss of Fas signaling in fibroblasts impairs homeostatic fibrosis resolution and promotes persistent pulmonary fibrosis. *JCI Insight* **6** (2020).

81. Maher, T.M. *et al*. Diminished Prostaglandin E2 Contributes to the Apoptosis Paradox in Idiopathic Pulmonary Fibrosis. *American Journal of Respiratory and Critical Care Medicine* **182**, 73-82 (2010).

82. Garrison, G. *et al*. Reversal of Myofibroblast Differentiation by Prostaglandin E2. *American Journal of Respiratory Cell and Molecular Biology* **48**, 550-558 (2013).

83. Booth, A.J. *et al*. Acellular Normal and Fibrotic Human Lung Matrices as a Culture System for In Vitro Investigation. *American Journal of Respiratory and Critical Care Medicine* **186**, 866-876 (2012).

84. Liu, F. *et al*. Mechanosignaling through YAP and TAZ drives fibroblast activation and fibrosis. *American Journal of Physiology-Lung Cellular and Molecular Physiology* **308**, L344-L357 (2014).

85. Song, J.Y. *et al*. YAP/TAZ activity in PDGFRα-expressing alveolar fibroblasts modulates AT2 proliferation through Wnt4. *Cell Reports* **44** (2025).

86. Adams, T.S. *et al*. Single-cell RNA-seq reveals ectopic and aberrant lung-resident cell populations in idiopathic pulmonary fibrosis. *Science Advances* **6**, eaba1983 (2020).

87. Jin, C. *et al*. Single-cell RNA sequencing reveals special basal cells and fibroblasts in idiopathic pulmonary fibrosis. *Scientific Reports* **14**, 15778 (2024).

88. null, n. Prednisone, Azathioprine, and N-Acetylcysteine for Pulmonary Fibrosis. *New England Journal of Medicine* **366**, 1968-1977.

89. Kinder, B.W. *et al*. Baseline BAL Neutrophilia Predicts Early Mortality in Idiopathic Pulmonary Fibrosis. *CHEST* **133**, 226-232 (2008).

90. Achaiah, A. *et al*. Neutrophil lymphocyte ratio as an indicator for disease progression in Idiopathic Pulmonary Fibrosis. *BMJ Open Respiratory Research* **9**, e001202 (2022).

91. Chua, F. *et al*. Mice Lacking Neutrophil Elastase Are Resistant to Bleomycin-Induced Pulmonary Fibrosis. *The American Journal of Pathology* **170**, 65-74 (2007).

92. Gregory, A.D. *et al*. Neutrophil elastase promotes myofibroblast differentiation in lung fibrosis. *Journal of Leukocyte Biology* **98**, 143-152 (2015).

93. Manoury, B., Nénan, S., Guénon, I., Lagente, V. & Boichot, E. Influence of early neutrophil depletion on MMPs/TIMP-1 balance in bleomycin-induced lung fibrosis. *International Immunopharmacology* **7**, 900-911 (2007).

94. Chrysanthopoulou, A. *et al*. Neutrophil extracellular traps promote differentiation and function of fibroblasts. *The Journal of Pathology* **233**, 294-307 (2014).

95. Hams, E. *et al*. IL-25 and type 2 innate lymphoid cells induce pulmonary fibrosis. *Proceedings of the National Academy of Sciences* **111**, 367-372 (2014).

96. Luzina, I.G. *et al*. Interleukin-33 Potentiates Bleomycin-Induced Lung Injury. *American Journal of Respiratory Cell and Molecular Biology* **49**, 999-1008 (2013).

97. Lee, J.-U. *et al*. Upregulation of interleukin-33 and thymic stromal lymphopoietin levels in the lungs of idiopathic pulmonary fibrosis. *BMC Pulmonary Medicine* **17**, 39 (2017).

98. Saito, A., Okazaki, H., Sugawara, I., Yamamoto, K. & Takizawa, H. Potential Action of IL-4 and IL-13 as Fibrogenic Factors on Lung Fibroblasts in vitro. *International Archives of Allergy and Immunology* **132**, 168-176 (2003).

99. Murray, L.A. *et al*. Targeting Interleukin-13 with Tralokinumab Attenuates Lung Fibrosis and Epithelial Damage in a Humanized SCID Idiopathic Pulmonary Fibrosis Model. *American Journal of Respiratory Cell and Molecular Biology* **50**, 985-994 (2014).

100. Parker, J.M. *et al*. A Phase 2 Randomized Controlled Study of Tralokinumab in Subjects with Idiopathic Pulmonary Fibrosis. *American Journal of Respiratory and Critical Care Medicine* **197**, 94-103 (2018).

101. Wilson, M.S. *et al*. Bleomycin and IL-1β–mediated pulmonary fibrosis is IL-17A dependent. *Journal of Experimental Medicine* **207**, 535-552 (2010).

102. Zhang, J. *et al*. Profibrotic effect of IL-17A and elevated IL-17RA in idiopathic pulmonary fibrosis and rheumatoid arthritis-associated lung disease support a direct role for IL-17A/IL-17RA in human fibrotic interstitial lung disease. *American Journal of Physiology-Lung Cellular and Molecular Physiology* **316**, L487-L497 (2019).

103. Cipolla, E. *et al*. IL-17A deficiency mitigates bleomycin-induced complement activation during lung fibrosis. *The FASEB Journal* **31**, 5543-5556 (2017).

104. Paun, A., Bergeron, M.-E. & Haston, C.K. The Th1/Th17 balance dictates the fibrosis response in murine radiation-induced lung disease. *Scientific Reports* **7**, 11586 (2017).

105. Konieczny, P. *et al*. Interleukin-17 governs hypoxic adaptation of injured epithelium. *Science* **377**, eabg9302.

106. Kotsianidis, I. *et al*. Global Impairment of CD4+CD25+FOXP3+ Regulatory T Cells in Idiopathic Pulmonary Fibrosis. *American Journal of Respiratory and Critical Care Medicine* **179**, 1121-1130 (2009).

107. Galati, D. *et al*. Peripheral depletion of NK cells and imbalance of the Treg/Th17 axis in idiopathic pulmonary fibrosis patients. *Cytokine* **66**, 119-126 (2014).

108. Unterman, A. *et al*. Single-Cell Profiling Reveals Immune Aberrations in Progressive Idiopathic Pulmonary Fibrosis. *American Journal of Respiratory and Critical Care Medicine* **210**, 484-496 (2024).

109. Xiong, S. *et al*. Treg depletion attenuates irradiation-induced pulmonary fibrosis by reducing fibrocyte accumulation, inducing Th17 response, and shifting IFN-γ, IL-12/IL-4, IL-5 balance. *Immunobiology* **220**, 1284-1291 (2015).

110. Birjandi, S.Z. *et al*. CD4⁺CD25^{hi}Foxp3⁺ Cells Exacerbate Bleomycin-Induced Pulmonary Fibrosis. *The American Journal of Pathology* **186**, 2008-2020 (2016).

111. Boveda-Ruiz, D. *et al*. Differential role of regulatory T cells in early and late stages of pulmonary fibrosis. *Immunobiology* **218**, 245-254 (2013).

112. Todd, N.W. *et al*. Lymphocyte aggregates persist and accumulate in the lungs of patients with idiopathic pulmonary fibrosis. *Journal of Inflammation Research* **6**, 63-70 (2013).

113. Wallace, W.A. *et al*. Circulating antibodies to lung protein(s) in patients with cryptogenic fibrosing alveolitis. *Thorax* **49**, 218 (1994).

114. Yang, Y. *et al*. Detection of antivimentin antibody in sera of patients with idiopathic pulmonary fibrosis and non-specific interstitial pneumonia. *Clinical and Experimental Immunology* **128**, 169-174 (2002).

115. Li, F.J. *et al*. Autoimmunity to Vimentin Is Associated with Outcomes of Patients with Idiopathic Pulmonary Fibrosis. *The Journal of Immunology* **199**, 1596-1605 (2017).

116. François, A. *et al*. B cell activating factor is central to bleomycin- and IL-17-mediated experimental pulmonary fibrosis. *Journal of Autoimmunity* **56**, 1-11 (2015).

117. Shenderov, K., Collins, S.L., Powell, J.D. & Horton, M.R. Immune dysregulation as a driver of idiopathic pulmonary fibrosis. *The Journal of Clinical Investigation* **131** (2021).

118. Desai, O., Winkler, J., Minasyan, M. & Herzog, E.L. The Role of Immune and Inflammatory Cells in Idiopathic Pulmonary Fibrosis. *Frontiers in Medicine* **Volume 5 - 2018** (2018).

119. Wynn, T.A. Integrating mechanisms of pulmonary fibrosis. *Journal of Experimental Medicine* **208**, 1339-1350 (2011).

120. Ziegler-Heitbrock, L. *et al*. Nomenclature of monocytes and dendritic cells in blood. *Blood* **116**, e74-e80 (2010).

121. Guilliams, M., Mildner, A. & Yona, S. Developmental and Functional Heterogeneity of Monocytes. *Immunity* **49**, 595-613 (2018).

122. Geissmann, F., Jung, S. & Littman, D.R. Blood Monocytes Consist of Two Principal Subsets with Distinct Migratory Properties. *Immunity* **19**, 71-82 (2003).

123. Ingersoll, M.A. *et al*. Comparison of gene expression profiles between human and mouse monocyte subsets. *Blood* **115**, e10-e19 (2010).

124. Yona, S. *et al*. Fate Mapping Reveals Origins and Dynamics of Monocytes and Tissue Macrophages under Homeostasis. *Immunity* **38**, 79-91 (2013).

125. Lavin, Y. *et al*. Tissue-Resident Macrophage Enhancer Landscapes Are Shaped by the Local Microenvironment. *Cell* **159**, 1312-1326 (2014).

126. Scott, C.L. *et al*. Bone marrow-derived monocytes give rise to self-renewing and fully differentiated Kupffer cells. *Nature Communications* **7**, 10321 (2016).

127. van de Laar, L. *et al*. Yolk Sac Macrophages, Fetal Liver, and Adult Monocytes Can Colonize an Empty Niche and Develop into Functional Tissue-Resident Macrophages. *Immunity* **44**, 755-768 (2016).

128. Cronk, J.C. *et al*. Peripherally derived macrophages can engraft the brain independent of irradiation and maintain an identity distinct from microglia. *Journal of Experimental Medicine* **215**, 1627-1647 (2018).

129. Shi, C. & Pamer, E.G. Monocyte recruitment during infection and inflammation. *Nature Reviews Immunology* **11**, 762-774 (2011).

130. Serbina, N.V., Salazar-Mather, T.P., Biron, C.A., Kuziel, W.A. & Pamer, E.G. TNF/iNOS-Producing Dendritic Cells Mediate Innate Immune Defense against Bacterial Infection. *Immunity* **19**, 59-70 (2003).

131. Jakubzick, C.V., Randolph, G.J. & Henson, P.M. Monocyte differentiation and antigen-presenting functions. *Nature Reviews Immunology* **17**, 349-362 (2017).

132. Hanna, R.N. *et al*. The transcription factor NR4A1 (Nur77) controls bone marrow differentiation and the survival of Ly6C− monocytes. *Nature Immunology* **12**, 778-785 (2011).

133. Auffray, C. *et al*. Monitoring of Blood Vessels and Tissues by a Population of Monocytes with Patrolling Behavior. *Science* **317**, 666-670 (2007).

134. Cros, J. *et al*. Human CD14^{dim} Monocytes Patrol and Sense Nucleic Acids and Viruses via TLR7 and TLR8 Receptors. *Immunity* **33**, 375-386 (2010).

135. Carlin, Leo M. *et al*. Nr4a1-Dependent Ly6C^{low} Monocytes Monitor Endothelial Cells and Orchestrate Their Disposal. *Cell* **153**, 362-375 (2013).

136. Belge, K.-U. *et al*. The Proinflammatory CD14+CD16+DR++ Monocytes Are a Major Source of TNF1. *The Journal of Immunology* **168**, 3536-3542 (2002).

137. Fingerle, G. *et al*. The novel subset of CD14+/CD16+ blood monocytes is expanded in sepsis patients. *Blood* **82**, 3170-3176 (1993).

138. Rogacev, K.S. *et al*. CD14++CD16+ Monocytes Independently Predict Cardiovascular Events: A Cohort Study of 951 Patients Referred for Elective Coronary Angiography. *Journal of the American College of Cardiology* **60**, 1512-1520 (2012).

139. Tsukamoto, M. *et al*. CD14brightCD16+ intermediate monocytes are induced by interleukin-10 and positively correlate with disease activity in rheumatoid arthritis. *Arthritis Research & Therapy* **19**, 28 (2017).

140. Bain, C.C. & MacDonald, A.S. The impact of the lung environment on macrophage development, activation and function: diversity in the face of adversity. *Mucosal Immunol* **15**, 223-234 (2022).

141. Aegerter, H., Lambrecht, B.N. & Jakubzick, C.V. Biology of lung macrophages in health and disease. *Immunity* **55**, 1564-1580 (2022).

142. Mulder, K. *et al*. Cross-tissue single-cell landscape of human monocytes and macrophages in health and disease. *Immunity* **54**, 1883-1900.e1885 (2021).

143. Hume, P.S. *et al*. Localization of Macrophages in the Human Lung via Design-based Stereology. *American Journal of Respiratory and Critical Care Medicine* **201**, 1209-1217 (2020).

144. Svedberg, F.R. *et al*. The lung environment controls alveolar macrophage metabolism and responsiveness in type 2 inflammation. *Nature Immunology* **20**, 571-580 (2019).

145. Subramanian, S. *et al*. Long-term culture-expanded alveolar macrophages restore their full epigenetic identity after transfer in vivo. *Nature Immunology* **23**, 458-468 (2022).

146. Gschwend, J. *et al*. Alveolar macrophages rely on GM-CSF from alveolar epithelial type 2 cells before and after birth. *Journal of Experimental Medicine* **218**, e20210745 (2021).

147. Shibata, Y. *et al*. GM-CSF Regulates Alveolar Macrophage Differentiation and Innate Immunity in the Lung through PU.1. *Immunity* **15**, 557-567 (2001).

148. Guilliams, M. *et al*. Alveolar macrophages develop from fetal monocytes that differentiate into long-lived cells in the first week of life via GM-CSF. *J Exp Med* **210**, 1977-1992 (2013).

149. Bosteels, C. *et al*. Loss of GM-CSF-dependent instruction of alveolar macrophages in COVID-19 provides a rationale for inhaled GM-CSF treatment. *Cell Reports Medicine* **3** (2022).

150. Ural, B.B. *et al*. Identification of a nerve-associated, lung-resident interstitial macrophage subset with distinct localization and immunoregulatory properties. *Science Immunology* **5**, eaax8756 (2020).

151. Yu, Y.-R.A. *et al*. Flow Cytometric Analysis of Myeloid Cells in Human Blood, Bronchoalveolar Lavage, and Lung Tissues. *American Journal of Respiratory Cell and Molecular Biology* **54**, 13-24 (2016).

152. Bharat, A. *et al*. Flow Cytometry Reveals Similarities Between Lung Macrophages in Humans and Mice. *American Journal of Respiratory Cell and Molecular Biology* **54**, 147-149 (2016).

153. Desch, A.N. *et al*. Flow Cytometric Analysis of Mononuclear Phagocytes in Nondiseased Human Lung and Lung-Draining Lymph Nodes. *American Journal of Respiratory and Critical Care Medicine* **193**, 614-626 (2016).

154. Leach, S.M. *et al*. Human and Mouse Transcriptome Profiling Identifies Cross-Species Homology in Pulmonary and Lymph Node Mononuclear Phagocytes. *Cell Reports* **33** (2020).

155. Li, X. *et al*. ScRNA-seq expression of IFI27 and APOC2; identifies four alveolar macrophage superclusters in healthy BALF. *Life Science Alliance* **5**, e202201458 (2022).

156. Mould, K.J. *et al*. Airspace Macrophages and Monocytes Exist in Transcriptionally Distinct Subsets in Healthy Adults. *Am J Respir Crit Care Med* **203**, 946-956 (2021).

157. Roberts, A.W. *et al*. Tissue-Resident Macrophages Are Locally Programmed for Silent Clearance of Apoptotic Cells. *Immunity* **47**, 913-927.e916 (2017).

158. Fujimori, T. *et al*. The Axl receptor tyrosine kinase is a discriminator of macrophage function in the inflamed lung. *Mucosal Immunology* **8**, 1021-1030 (2015).

159. Branchett, W.J. *et al*. Airway macrophage-intrinsic TGF-β1 regulates pulmonary immunity during early-life allergen exposure. *Journal of Allergy and Clinical Immunology* **147**, 1892-1906 (2021).

160. Suzuki, T. *et al*. Familial pulmonary alveolar proteinosis caused by mutations in CSF2RA. *Journal of Experimental Medicine* **205**, 2703-2710 (2008).

161. Robb, L. *et al*. Hematopoietic and lung abnormalities in mice with a null mutation of the common beta subunit of the receptors for granulocyte-macrophage colony-stimulating factor and interleukins 3 and 5. *Proceedings of the National Academy of Sciences* **92**, 9565-9569 (1995).

162. Kawano, H. *et al*. IL-10-producing lung interstitial macrophages prevent neutrophilic asthma. *International Immunology* **28**, 489-501 (2016).

163. Sabatel, C. *et al*. Exposure to Bacterial CpG DNA Protects from Airway Allergic Inflammation by Expanding Regulatory Lung Interstitial Macrophages. *Immunity* **46**, 457-473 (2017).

164. Gibbings, S.L. *et al*. Three Unique Interstitial Macrophages in the Murine Lung at Steady State. *Am J Respir Cell Mol Biol* **57**, 66-76 (2017).

165. Brody, A.R. *et al*. Interstitial pulmonary macrophages produce platelet-derived growth factor that stimulates rat lung fibroblast proliferation in vitro. *Journal of Leukocyte Biology* **51**, 640-648 (1992).

166. Chakarov, S. *et al*. Two distinct interstitial macrophage populations coexist across tissues in specific subtissular niches. *Science* **363** (2019).

167. Hashimoto, D. *et al*. Tissue-resident macrophages self-maintain locally throughout adult life with minimal contribution from circulating monocytes. *Immunity* **38**, 792-804 (2013).

168. Bain, C.C. *et al*. Constant replenishment from circulating monocytes maintains the macrophage pool in the intestine of adult mice. *Nature Immunology* **15**, 929-937 (2014).

169. Eguiluz-Gracia, I. *et al*. Long-term persistence of human donor alveolar macrophages in lung transplant recipients. *Thorax* **71**, 1006-1011 (2016).

170. Nayak, D.K. *et al*. Long-Term Persistence of Donor Alveolar Macrophages in Human Lung Transplant Recipients That Influences Donor-Specific Immune Responses. *Am J Transplant* **16**, 2300-2311 (2016).

171. Byrne, A.J. *et al*. Dynamics of human monocytes and airway macrophages during healthy aging and after transplant. *J Exp Med* **217** (2020).

172. Misharin, A.V. *et al*. Monocyte-derived alveolar macrophages drive lung fibrosis and persist in the lung over the life span. *Journal of Experimental Medicine* **214**, 2387-2404 (2017).

173. Aegerter, H. *et al*. Influenza-induced monocyte-derived alveolar macrophages confer prolonged antibacterial protection. *Nature Immunology* **21**, 145-157 (2020).

174. Mata, E. *et al*. Pulmonary BCG induces lung-resident macrophage activation and confers long-term protection against tuberculosis. *Science Immunology* **6**, eabc2934 (2021).

175. Chen, F. *et al*. Helminth resistance is mediated by differential activation of recruited monocyte-derived alveolar macrophages and arginine depletion. *Cell Reports* **38** (2022).

176. Scott, M.K.D. *et al*. Increased monocyte count as a cellular biomarker for poor outcomes in fibrotic diseases: a retrospective, multicentre cohort study. *The Lancet Respiratory Medicine* **7**, 497-508 (2019).

177. Kreuter, M. *et al*. Monocyte Count as a Prognostic Biomarker in Patients with Idiopathic Pulmonary Fibrosis. *American Journal of Respiratory and Critical Care Medicine* **204**, 74-81 (2021).

178. Gibbons, M.A. *et al*. Ly6Chi Monocytes Direct Alternatively Activated Profibrotic Macrophage Regulation of Lung Fibrosis. *American Journal of Respiratory and Critical Care Medicine* **184**, 569-581 (2011).

179. Osterholzer, J.J. *et al*. Implicating Exudate Macrophages and Ly-6Chigh Monocytes in CCR2-Dependent Lung Fibrosis following Gene-Targeted Alveolar Injury. *The Journal of Immunology* **190**, 3447-3457 (2013).

180. Satoh, T. *et al*. Identification of an atypical monocyte and committed progenitor involved in fibrosis. *Nature* **541**, 96-101 (2017).

181. Fraser, E. *et al*. Multi-Modal Characterization of Monocytes in Idiopathic Pulmonary Fibrosis Reveals a Primed Type I Interferon Immune Phenotype. *Frontiers in Immunology* **Volume 12 - 2021** (2021).

182. McCubbrey, A.L. *et al*. Deletion of c-FLIP from CD11bhi Macrophages Prevents Development of Bleomycin-induced Lung Fibrosis. *American Journal of Respiratory Cell and Molecular Biology* **58**, 66-78 (2018).

183. Brody, S.L. *et al*. Chemokine Receptor 2–targeted Molecular Imaging in Pulmonary Fibrosis. A Clinical Trial. *American Journal of Respiratory and Critical Care Medicine* **203**, 78-89 (2020).

184. Ayaub, E.A. *et al*. Single Cell RNA-seq and Mass Cytometry Reveals a Novel and a Targetable Population of Macrophages in Idiopathic Pulmonary Fibrosis. *bioRxiv*, 2021.2001.2004.425268 (2021).

185. Morse, C. *et al*. Proliferating SPP1/MERTK-expressing macrophages in idiopathic pulmonary fibrosis. *European Respiratory Journal* **54**, 1802441 (2019).

186. Barrat, F.J., Elkon, K.B. & Fitzgerald, K.A. Importance of Nucleic Acid Recognition in Inflammation and Autoimmunity. *Annual Review of Medicine* **67**, 323-336 (2016).

187. Chen, R. *et al*. Pattern recognition receptors: function, regulation and therapeutic potential. *Signal Transduction and Targeted Therapy* **10**, 216 (2025).

188. Rehwinkel, J. & Gack, M.U. RIG-I-like receptors: their regulation and roles in RNA sensing. *Nature Reviews Immunology* **20**, 537-551 (2020).

189. Hopfner, K.-P. & Hornung, V. Molecular mechanisms and cellular functions of cGAS–STING signalling. *Nature Reviews Molecular Cell Biology* **21**, 501-521 (2020).

190. Kurt-Jones, E.A. *et al*. Pattern recognition receptors TLR4 and CD14 mediate response to respiratory syncytial virus. *Nature Immunology* **1**, 398-401 (2000).

191. West, A.P. *et al.* Mitochondrial DNA stress primes the antiviral innate immune response. *Nature* **520**, 553-557 (2015).

192. Zhang, Q. *et al.* Circulating mitochondrial DAMPs cause inflammatory responses to injury. *Nature* **464**, 104-107 (2010).

193. Härtlova, A. *et al.* DNA Damage Primes the Type I Interferon System via the Cytosolic DNA Sensor STING to Promote Anti-Microbial Innate Immunity. *Immunity* **42**, 332-343 (2015).

194. Platanias, L.C. Mechanisms of type-I- and type-II-interferon-mediated signalling. *Nature Reviews Immunology* **5**, 375-386 (2005).

195. Ivashkiv, L.B. Type I Interferon Modulation of Cellular Responses to Cytokines and Infectious Pathogens: Potential Role in SLE Pathogenesis. *Autoimmunity* **36**, 473-479 (2003).

196. Van Boxel-Dezaire, A.H.H., Rani, M.R.S. & Stark, G.R. Complex Modulation of Cell Type-Specific Signaling in Response to Type I Interferons. *Immunity* **25**, 361-372 (2006).

197. Wang, W.-B., Levy, D.E. & Lee, C.-K. STAT3 Negatively Regulates Type I IFN-Mediated Antiviral Response. *The Journal of Immunology* **187**, 2578-2585 (2011).

198. González-Navajas, J.M., Lee, J., David, M. & Raz, E. Immunomodulatory functions of type I interferons. *Nature Reviews Immunology* **12**, 125-135 (2012).

199. Ivashkiv, L.B. & Donlin, L.T. Regulation of type I interferon responses. *Nature Reviews Immunology* **14**, 36-49 (2014).

200. Montoya, M. *et al.* Type I interferons produced by dendritic cells promote their phenotypic and functional activation. *Blood* **99**, 3263-3271 (2002).

201. McNab, F., Mayer-Barber, K., Sher, A., Wack, A. & O'Garra, A. Type I interferons in infectious disease. *Nature Reviews Immunology* **15**, 87-103 (2015).

202. Liew, F.Y., Millott, S., Parkinson, C., Palmer, R.M.J. & Moncada, S. Macrophage killing of Leishmania parasite in vivo is mediated by nitric oxide from l-arginine. *The Journal of Immunology* **144**, 4794-4797 (1990).

203. Herold, S. *et al.* Lung epithelial apoptosis in influenza virus pneumonia: the role of macrophage-expressed TNF-related apoptosis-inducing ligand. *Journal of Experimental Medicine* **205**, 3065-3077 (2008).

204. Högner, K. *et al.* Macrophage-expressed IFN-β Contributes to Apoptotic Alveolar Epithelial Cell Injury in Severe Influenza Virus Pneumonia. *PLOS Pathogens* **9**, e1003188 (2013).

205. Davidson, S., Crotta, S., McCabe, T.M. & Wack, A. Pathogenic potential of interferon αβ in acute influenza infection. *Nature Communications* **5**, 3864 (2014).

206. Sefik, E. *et al*. Inflammasome activation in infected macrophages drives COVID-19 pathology. *Nature* **606**, 585-593 (2022).

207. Channappanavar, R. *et al*. Dysregulated Type I Interferon and Inflammatory Monocyte-Macrophage Responses Cause Lethal Pneumonia in SARS-CoV-Infected Mice. *Cell Host & Microbe* **19**, 181-193 (2016).

208. Wilson, Elizabeth B. *et al*. Emergence of Distinct Multiarmed Immunoregulatory Antigen-Presenting Cells during Persistent Viral Infection. *Cell Host & Microbe* **11**, 481-491 (2012).

209. Wilson, E.B. *et al*. Blockade of Chronic Type I Interferon Signaling to Control Persistent LCMV Infection. *Science* **340**, 202-207 (2013).

210. Teijaro, J.R. *et al*. Persistent LCMV Infection Is Controlled by Blockade of Type I Interferon Signaling. *Science* **340**, 207-211 (2013).

211. Crow, M.K., Olferiev, M. & Kirou, K.A. Type I Interferons in Autoimmune Disease. *Annual Review of Pathology: Mechanisms of Disease* **14**, 369-393 (2019).

212. Mavragani, C.P. *et al*. Expression of Long Interspersed Nuclear Element 1 Retroelements and Induction of Type I Interferon in Patients With Systemic Autoimmune Disease. *Arthritis & Rheumatology* **68**, 2686-2696 (2016).

213. Vermi, W. *et al*. Cutaneous distribution of plasmacytoid dendritic cells in lupus erythematosus. Selective tropism at the site of epithelial apoptotic damage. *Immunobiology* **214**, 877-886 (2009).

214. Rowland, S.L. *et al*. Early, transient depletion of plasmacytoid dendritic cells ameliorates autoimmunity in a lupus model. *Journal of Experimental Medicine* **211**, 1977-1991 (2014).

215. Caielli, S. *et al*. Type I IFN drives unconventional IL-1β secretion in lupus monocytes. *Immunity* **57**, 2497-2513.e2412 (2024).

216. Liu, Z. *et al*. Interferon-α accelerates murine systemic lupus erythematosus in a T cell–dependent manner. *Arthritis & Rheumatism* **63**, 219-229 (2011).

217. Flaherty Kevin, R. *et al*. Nintedanib in Progressive Fibrosing Interstitial Lung Diseases. *New England Journal of Medicine* **381**, 1718-1727 (2019).

218. Kakkar, V. *et al*. Type 1 interferon activation in systemic sclerosis: a biomarker, a target or the culprit. *Current Opinion in Rheumatology* **34** (2022).

219. Szabo, I. *et al*. Enhanced Innate and Acquired Immune Responses in Systemic Sclerosis Primary Peripheral Blood Mononuclear Cells (PBMCs). *International Journal of Molecular Sciences*; 2023. p. 14438.

220. Ah Kioon, M.D. *et al*. Plasmacytoid dendritic cells promote systemic sclerosis with a key role for TLR8. *Science Translational Medicine* **10**, eaam8458 (2018).

221. Christmann, R.B. *et al*. Association of Interferon- and Transforming Growth Factor β–Regulated Genes and Macrophage Activation With Systemic Sclerosis–Related Progressive Lung Fibrosis. *Arthritis & Rheumatology* **66**, 714-725 (2014).

222. Brkic, Z. *et al*. The interferon type I signature is present in systemic sclerosis before overt fibrosis and might contribute to its pathogenesis through high BAFF gene expression and high collagen synthesis. *Annals of the Rheumatic Diseases* **75**, 1567-1573 (2016).

223. Delaney, T.A. *et al*. Type I IFNs Regulate Inflammation, Vasculopathy, and Fibrosis in Chronic Cutaneous Graft-versus-Host Disease. *The Journal of Immunology* **197**, 42-50 (2016).

224. Rigby, R.E., Rue-Albrecht, K., Fedorov, A., Sims, D. & Rehwinkel, J. Single-cell analysis of signalling and transcriptional responses to type I interferons. *EMBO Reports* **27**, 2491-2513 (2026).

225. Weeratunga, P. *et al*. Temporo-spatial cellular atlas of the regenerating alveolar niche in idiopathic pulmonary fibrosis. *Nature Communications* **16**, 7150 (2025).

226. Hunter, B. *et al*. OPTIMAL: An OPTimized Imaging Mass cytometry AnaLysis framework for benchmarking segmentation and data exploration. *Cytometry Part A* **105**, 36-53 (2024).

227. Ijsselsteijn, M.E., van der Breggen, R., Farina Sarasqueta, A., Koning, F. & de Miranda, N.F.C.C. A 40-Marker Panel for High Dimensional Characterization of Cancer Immune Microenvironments by Imaging Mass Cytometry. *Frontiers in Immunology* **Volume 10 - 2019** (2019).

228. Youk, J. *et al*. Three-Dimensional Human Alveolar Stem Cell Culture Models Reveal Infection Response to SARS-CoV-2. *Cell Stem Cell* **27**, 905-919.e910 (2020).

229. Katsura, H. *et al*. Human Lung Stem Cell-Based Alveolospheres Provide Insights into SARS-CoV-2-Mediated Interferon Responses and Pneumocyte Dysfunction. *Cell Stem Cell* **27**, 890-904.e898 (2020).

230. Groves, A.M., Johnston, C.J., Williams, J.P. & Finkelstein, J.N. Role of Infiltrating Monocytes in the Development of Radiation-Induced Pulmonary Fibrosis. *Radiation Research* **189**, 300-311 (2018).

231. Pedersen, C.B. *et al*. cyCombine allows for robust integration of single-cell cytometry datasets within and across technologies. *Nature Communications* **13**, 1698 (2022).

232. Nowicka, M. *et al*. CyTOF workflow: differential discovery in high-throughput high-dimensional cytometry datasets [version 3; peer review: 2 approved]. *F1000Research* **6** (2019).

233. Aibar, S. *et al*. SCENIC: single-cell regulatory network inference and clustering. *Nature Methods* **14**, 1083-1086 (2017).

234. Cooper, M.A. *et al*. Human natural killer cells: a unique innate immunoregulatory role for the CD56bright subset. *Blood* **97**, 3146-3151 (2001).

235. Freud, A.G. & Caligiuri, M.A. Human natural killer cell development. *Immunological Reviews* **214**, 56-72 (2006).

236. Ahern, D.J. *et al*. A blood atlas of COVID-19 defines hallmarks of disease severity and specificity. *Cell* **185**, 916-938.e958 (2022).

237. Rigby, R.E., Rue-Albrecht, K., Sims, D. & Rehwinkel, J. Single-cell analysis of signalling and transcriptional responses to type I interferons. *bioRxiv*, 2023.2007.2003.547491 (2023).

238. Uddin, S. *et al*. Role of Stat5 in Type I interferon-signaling and transcriptional regulation. *Biochemical and Biophysical Research Communications* **308**, 325-330 (2003).

239. Matikainen, S. *et al*. Interferon-□ Activates Multiple STAT Proteins and Upregulates Proliferation-Associated IL-2R□, c-myc, and pim-1 Genes in Human T Cells. *Blood* **93**, 1980-1991 (1999).

240. Gupta, S., Jiang M Fau - Pernis, A.B. & Pernis, A.B. IFN-alpha activates Stat6 and leads to the formation of Stat2:Stat6 complexes in B cells. *Journal of Immunology* **163**, 3834-3841 (1999).

241. Ho, H.H. & Ivashkiv, L.B. Role of STAT3 in Type I Interferon Responses: NEGATIVE REGULATION OF STAT1-DEPENDENT INFLAMMATORY GENE ACTIVATION*. *Journal of Biological Chemistry* **281**, 14111-14118 (2006).

242. Yarilina, A., Park-Min, K.-H., Antoniv, T., Hu, X. & Ivashkiv, L.B. TNF activates an IRF1-dependent autocrine loop leading to sustained expression of chemokines

and STAT1-dependent type I interferon–response genes. *Nature Immunology* **9**, 378-387 (2008).

243. Venkatesh, D. *et al*. Endothelial TNF Receptor 2 Induces IRF1 Transcription Factor-Dependent Interferon-β Autocrine Signaling to Promote Monocyte Recruitment. *Immunity* **38**, 1025-1037 (2013).

244. Nehar-Belaid, D. *et al*. Mapping systemic lupus erythematosus heterogeneity at the single-cell level. *Nature Immunology* **21**, 1094-1106 (2020).

245. Wong, L.H., Hatzinisiriou, I., Devenish, R.J. & Ralph, S.J. IFN-γ Priming Up-Regulates IFN-Stimulated Gene Factor 3 (ISGF3) Components, Augmenting Responsiveness of IFN-Resistant Melanoma Cells to Type I IFNs. *The Journal of Immunology* **160**, 5475-5484 (1998).

246. Hu, X. *et al*. Sensitization of IFN-γ Jak-STAT signaling during macrophage activation. *Nature Immunology* **3**, 859-866 (2002).

247. Tanabe, Y. *et al*. Cutting Edge: Role of STAT1, STAT3, and STAT5 in IFN-αβ Responses in T Lymphocytes. *The Journal of Immunology* **174**, 609-613 (2005).

248. Gimeno, R., Lee, C.-K., Schindler, C. & Levy, D.E. Stat1 and Stat2 but Not Stat3 Arbitrate Contradictory Growth Signals Elicited by Alpha/Beta Interferon in T Lymphocytes. *Molecular and Cellular Biology* **25**, 5456-5465 (2005).

249. Erickson, S. *et al*. Interferon-alpha inhibits Stat5 DNA-binding in IL-2 stimulated primary T-lymphocytes. *European Journal of Biochemistry* **269**, 29-37 (2002).

250. Wang, B., Han, J., Elisseeff, J.H. & Demaria, M. The senescence-associated secretory phenotype and its physiological and pathological implications. *Nature Reviews Molecular Cell Biology* **25**, 958-978 (2024).

251. Manfredi, M. *et al*. Circulating Calprotectin (cCLP) in autoimmune diseases. *Autoimmunity Reviews* **22**, 103295 (2023).

252. Jakobsson, G. *et al*. Therapeutic S100A8/A9 blockade inhibits myocardial and systemic inflammation and mitigates sepsis-induced myocardial dysfunction. *Critical Care* **27**, 374 (2023).

253. Machahua, C. *et al*. Serum calprotectin as new biomarker for disease severity in idiopathic pulmonary fibrosis: a cross-sectional study in two independent cohorts. *BMJ Open Respiratory Research* **8**, e000827 (2021).

254. Averill, M.M., Kerkhoff, C. & Bornfeldt, K.E. S100A8 and S100A9 in Cardiovascular Biology and Disease. *Arteriosclerosis, Thrombosis, and Vascular Biology* **32**, 223-229 (2012).

255. Takaoka, A. *et al.* Integral role of IRF-5 in the gene induction programme activated by Toll-like receptors. *Nature* **434**, 243-249 (2005).

256. Lazarov, T., Juarez-Carreno, S., Cox, N. & Geissmann, F. Physiology and diseases of tissue-resident macrophages. *Nature* **618**, 698-707 (2023).

257. Wang, J. *et al.* Integrated analysis of single-cell and bulk RNA sequencing reveals pro-fibrotic PLA2G7high macrophages in pulmonary fibrosis. *Pharmacological Research* **182**, 106286 (2022).

258. Ding, H. *et al.* Kidney fibrosis molecular mechanisms Spp1 influences fibroblast activity through transforming growth factor beta smad signaling. *iScience* **27**, 109839 (2024).

259. Dong, J. & Ma, Q. Osteopontin enhances multi-walled carbon nanotube-triggered lung fibrosis by promoting TGF-β1 activation and myofibroblast differentiation. *Particle and Fibre Toxicology* **14**, 18 (2017).

260. Zhao, J. *et al.* Single-cell RNA sequencing reveals the heterogeneity of liver-resident immune cells in human. *Cell Discovery* **6**, 22 (2020).

261. MacParland, S.A. *et al.* Single cell RNA sequencing of human liver reveals distinct intrahepatic macrophage populations. *Nature Communications* **9**, 4383 (2018).

262. Mangiola, S. *et al.* sccomp: Robust differential composition and variability analysis for single-cell data. *Proceedings of the National Academy of Sciences* **120**, e2203828120 (2023).

263. Morrell, E.D. *et al.* The transcriptional and phenotypic characteristics that define alveolar macrophage subsets in acute hypoxemic respiratory failure. *Nature Communications* **14**, 7443 (2023).

264. Sikkema, L. *et al.* An integrated cell atlas of the lung in health and disease. *Nat Med* **29**, 1563-1577 (2023).

265. Zhang, F. *et al.* IFN-γ and TNF-α drive a CXCL10+ CCL2+ macrophage phenotype expanded in severe COVID-19 lungs and inflammatory diseases with tissue inflammation. *Genome Medicine* **13**, 64 (2021).

266. Mulder, K. *et al.* Cross-tissue single-cell landscape of human monocytes and macrophages in health and disease. *Immunity* **54**, 1883-1900 e1885 (2021).

267. Morse, C. *et al.* Proliferating SPP1/MERTK-expressing macrophages in idiopathic pulmonary fibrosis. *Eur Respir J* **54** (2019).

268. Rennard, S.I., Hunninghake, G.W., Bitterman, P.B. & Crystal, R.G. Production of fibronectin by the human alveolar macrophage: mechanism for the recruitment

of fibroblasts to sites of tissue injury in interstitial lung diseases. *Proceedings of the National Academy of Sciences* **78**, 7147-7151 (1981).

269. Jiang, C., Ting, A.T. & Seed, B. PPAR-γ agonists inhibit production of monocyte inflammatory cytokines. *Nature* **391**, 82-86 (1998).

270. Gallardo-Soler, A. *et al*. Arginase I Induction by Modified Lipoproteins in Macrophages: A Peroxisome Proliferator-Activated Receptor-γ/δ-Mediated Effect that Links Lipid Metabolism and Immunity. *Molecular Endocrinology* **22**, 1394-1402 (2008).

271. Busillo, J.M., Azzam, K.M. & Cidlowski, J.A. Glucocorticoids Sensitize the Innate Immune System through Regulation of the NLRP3 Inflammasome *. *Journal of Biological Chemistry* **286**, 38703-38713 (2011).

272. Kajimura, Y. *et al*. E4BP4 in macrophages induces an anti-inflammatory phenotype that ameliorates the severity of colitis. *Communications Biology* **7**, 527 (2024).

273. Zhu, B. *et al*. Uncoupling of macrophage inflammation from self-renewal modulates host recovery from respiratory viral infection. *Immunity* **54**, 1200-1218.e1209 (2021).

274. Iwata, A. *et al*. Egr2 drives the differentiation of Ly6Chi monocytes into fibrosis-promoting macrophages in metabolic dysfunction-associated steatohepatitis in mice. *Communications Biology* **7**, 681 (2024).

275. Kuwata, H. *et al*. IL-10-inducible Bcl-3 negatively regulates LPS-induced TNF-α production in macrophages. *Blood* **102**, 4123-4129 (2003).

276. Matsumoto, H. *et al*. HIVEP1 Is a Negative Regulator of NF-κB That Inhibits Systemic Inflammation in Sepsis. *Frontiers in Immunology* **Volume 12 - 2021** (2021).

277. Lee, J. *et al*. Bronchoalveolar lavage (BAL) cells in idiopathic pulmonary fibrosis express a complex pro-inflammatory, pro-repair, angiogenic activation pattern, likely associated with macrophage iron accumulation. *PLOS ONE* **13**, e0194803 (2018).

278. Prasse, A. *et al*. CCL18 as an indicator of pulmonary fibrotic activity in idiopathic interstitial pneumonias and systemic sclerosis. *Arthritis & Rheumatism* **56**, 1685-1693 (2007).

279. Liberzon, A. *et al*. The Molecular Signatures Database Hallmark Gene Set Collection. *Cell Systems* **1**, 417-425 (2015).

280. Grabner, R. & Meerbach, W. Phagocytosis of surfactant by alveolar macrophages in vitro. *American Journal of Physiology-Lung Cellular and Molecular Physiology* **261**, L472-L477 (1991).

281. Wright, J.R. & Youmans, D.C. Degradation of surfactant lipids and surfactant protein A by alveolar macrophages in vitro. *American Journal of Physiology-Lung Cellular and Molecular Physiology* **268**, L772-L780 (1995).

282. Mostafavi, S. *et al*. Parsing the Interferon Transcriptional Network and Its Disease Associations. *Cell* **164**, 564-578 (2016).

283. Larsen, S., Kawamoto, S., Tanuma, S.-i. & Uchiumi, F. The hematopoietic regulator, ELF-1, enhances the transcriptional response to Interferon-β of the OAS1 anti-viral gene. *Scientific Reports* **5**, 17497 (2015).

284. Milacic, M. *et al*. The Reactome Pathway Knowledgebase 2024. *Nucleic Acids Research* **52**, D672-D678 (2024).

285. Henderson, N.C. *et al*. Targeting of αv integrin identifies a core molecular pathway that regulates fibrosis in several organs. *Nature Medicine* **19**, 1617-1624 (2013).

286. Ezzo, M. *et al*. Acute contact with profibrotic macrophages mechanically activates fibroblasts via αvβ3 integrin–mediated engagement of Piezo1. *Science Advances* **10**, eadp4726.

287. Parimon, T. *et al*. Syndecan-1 promotes lung fibrosis by regulating epithelial reprogramming through extracellular vesicles. *JCI Insight* **4** (2019).

288. Tanino, Y. *et al*. Syndecan-4 Inhibits the Development of Pulmonary Fibrosis by Attenuating TGF-β Signaling. *International Journal of Molecular Sciences*; 2019. p. 4989.

289. Hoeft, K. *et al*. Platelet-instructed SPP1⁺ macrophages drive myofibroblast activation in fibrosis in a CXCL4-dependent manner. *Cell Reports* **42** (2023).

290. Fabre, T. *et al*. Identification of a broadly fibrogenic macrophage subset induced by type 3 inflammation. *Science Immunology* **8**, eadd8945.

291. Kotliar, D. *et al*. Identifying gene expression programs of cell-type identity and cellular activity with single-cell RNA-Seq. *eLife* **8**, e43803 (2019).

292. Kunes, R.Z., Walle, T., Land, M., Nawy, T. & Pe'er, D. Supervised discovery of interpretable gene programs from single-cell data. *Nature Biotechnology* **42**, 1084-1095 (2024).

293. Strunz, M. *et al*. Alveolar regeneration through a Krt8+ transitional stem cell state that persists in human lung fibrosis. *Nature Communications* **11**, 3559 (2020).

294. Choi, J. *et al*. Inflammatory Signals Induce AT2 Cell-Derived Damage-Associated Transient Progenitors that Mediate Alveolar Regeneration. *Cell Stem Cell* **27**, 366-382.e367 (2020).

295. Kobayashi, Y. *et al*. Persistence of a regeneration-associated, transitional alveolar epithelial cell state in pulmonary fibrosis. *Nature Cell Biology* **22**, 934-946 (2020).

296. Jiang, P. *et al*. Ineffectual Type 2–to–Type 1 Alveolar Epithelial Cell Differentiation in Idiopathic Pulmonary Fibrosis: Persistence of the KRT8hi Transitional State. *American Journal of Respiratory and Critical Care Medicine* **201**, 1443-1447 (2020).

297. Wang, F. *et al*. Regulation of epithelial transitional states in murine and human pulmonary fibrosis. *The Journal of Clinical Investigation* **133** (2023).

298. Dvorkin, S., Cambier, S., Volkman, H.E. & Stetson, D.B. New frontiers in the cGAS-STING intracellular DNA-sensing pathway. *Immunity* **57**, 718-730 (2024).

299. Gulen, M.F. *et al*. cGAS–STING drives ageing-related inflammation and neurodegeneration. *Nature* **620**, 374-380 (2023).

300. Kathiriya, J.J. *et al*. Human alveolar type 2 epithelium transdifferentiates into metaplastic KRT5+ basal cells. *Nature Cell Biology* **24**, 10-23 (2022).

301. Weeratunga, P. *et al*. Single cell spatial analysis reveals inflammatory foci of immature neutrophil and CD8 T cells in COVID-19 lungs. *Nature Communications* **14**, 7216 (2023).

302. Greenwald, N.F. *et al*. Whole-cell segmentation of tissue images with human-level performance using large-scale data annotation and deep learning. *Nature Biotechnology* **40**, 555-565 (2022).

303. Vannan, A. *et al*. Spatial transcriptomics identifies molecular niche dysregulation associated with distal lung remodeling in pulmonary fibrosis. *Nature Genetics* **57**, 647-658 (2025).

304. Neumark, N., Cosme, C., Rose, K.-A. & Kaminski, N. The Idiopathic Pulmonary Fibrosis Cell Atlas. *American Journal of Physiology-Lung Cellular and Molecular Physiology* **319**, L887-L892 (2020).

305. Misharin, A.V., Morales-Nebreda, L., Mutlu, G.M., Budinger, G.R.S. & Perlman, H. Flow Cytometric Analysis of Macrophages and Dendritic Cell Subsets in the

Mouse Lung. *American Journal of Respiratory Cell and Molecular Biology* **49**, 503-510 (2013).

306. Mayr, C.H. *et al*. Spatial transcriptomic characterization of pathologic niches in IPF. *Science Advances* **10**, eadl5473 (2024).

307. Hoffman, E.T. *et al*. Aberrant intermediate alveolar epithelial cells promote pathogenic activation of lung fibroblasts in preclinical fibrosis models. *Nature Communications* **16**, 8710 (2025).

308. Ryu, C. *et al*. Bioactive Plasma Mitochondrial DNA Is Associated With Disease Progression in Scleroderma-Associated Interstitial Lung Disease. *Arthritis & Rheumatology* **72**, 1905-1915 (2020).

309. Sato, T. *et al*. Single Lgr5 stem cells build crypt-villus structures in vitro without a mesenchymal niche. *Nature* **459**, 262-265 (2009).

310. Dobbs, L.G. Isolation and culture of alveolar type II cells. *American Journal of Physiology-Lung Cellular and Molecular Physiology* **258**, L134-L147 (1990).

311. Sucre, J.M.S. *et al*. Successful Establishment of Primary Type II Alveolar Epithelium with 3D Organotypic Coculture. *American Journal of Respiratory Cell and Molecular Biology* **59**, 158-166 (2018).

312. Isakson, B.E., Seedorf, G.J., Lubman, R.L., Evans, W.H. & Boitano, S. Cell–Cell Communication in Heterocellular Cultures of Alveolar Epithelial Cells. *American Journal of Respiratory Cell and Molecular Biology* **29**, 552-561 (2003).

313. Barkauskas, C.E. *et al*. Type 2 alveolar cells are stem cells in adult lung. *The Journal of Clinical Investigation* **123**, 3025-3036 (2013).

314. Jacob, A. *et al*. Derivation of self-renewing lung alveolar epithelial type II cells from human pluripotent stem cells. *Nature Protocols* **14**, 3303-3332 (2019).

315. Alysandratos, K.-D. *et al*. Culture impact on the transcriptomic programs of primary and iPSC-derived human alveolar type 2 cells. *JCI Insight* **8** (2022).

316. Gonzalez, R.F., Allen, L., Gonzales, L., Ballard, P.L. & Dobbs, L.G. HTII-280, a Biomarker Specific to the Apical Plasma Membrane of Human Lung Alveolar Type II Cells. *Journal of Histochemistry & Cytochemistry* **58**, 891-901 (2010).

317. Zacharias, W.J. *et al*. Regeneration of the lung alveolus by an evolutionarily conserved epithelial progenitor. *Nature* **555**, 251-255 (2018).

318. Zhang, Z. *et al*. Transcription factor Etv5 is essential for the maintenance of alveolar type II cells. *Proceedings of the National Academy of Sciences* **114**, 3903-3908 (2017).

319. Van der Velden, J.L., Bertoncello, I. & McQualter, J.L. LysoTracker is a marker of differentiated alveolar type II cells. *Respiratory Research* **14**, 123 (2013).

320. Suezawa, T. *et al*. Disease modeling of pulmonary fibrosis using human pluripotent stem cell-derived alveolar organoids. *Stem Cell Reports* **16**, 2973-2987 (2021).

321. Ptasinski, V. *et al*. Modeling fibrotic alveolar transitional cells with pluripotent stem cell-derived alveolar organoids. *Life Science Alliance* **6**, e202201853 (2023).

322. Aoshiba, K. *et al*. Senescence-associated secretory phenotype in a mouse model of bleomycin-induced lung injury. *Experimental and Toxicologic Pathology* **65**, 1053-1062 (2013).

323. Miura, Y., Lam, M., Bourke, J.E. & Kanazawa, S. Bimodal fibrosis in a novel mouse model of bleomycin-induced usual interstitial pneumonia. *Life Science Alliance* **5**, e202101059 (2022).

324. Wallach-Dayan, S.B. *et al*. Bleomycin initiates apoptosis of lung epithelial cells by ROS but not by Fas/FasL pathway. *American Journal of Physiology-Lung Cellular and Molecular Physiology* **290**, L790-L796 (2006).

325. Lee, V.Y. *et al*. Bleomycin induces alveolar epithelial cell death through JNK-dependent activation of the mitochondrial death pathway. *American Journal of Physiology-Lung Cellular and Molecular Physiology* **289**, L521-L528 (2005).

326. Taniguchi, T. & Takaoka, A. A weak signal for strong responses: interferon-alpha/beta revisited. *Nature Reviews Molecular Cell Biology* **2**, 378-386 (2001).

327. Yu, Q. *et al*. DNA-Damage-Induced Type I Interferon Promotes Senescence and Inhibits Stem Cell Function. *Cell Reports* **11**, 785-797 (2015).

328. Ryu, C. *et al*. Extracellular Mitochondrial DNA Is Generated by Fibroblasts and Predicts Death in Idiopathic Pulmonary Fibrosis. *American Journal of Respiratory and Critical Care Medicine* **196**, 1571-1581 (2017).

329. Fava, A. *et al*. Anifrolumab Treatment Leads to Rapid Reduction in Urinary Biomarkers of Intrarenal Inflammation in Lupus Nephritis: Results From the Phase 2 Randomized Trial. *Arthritis & Rheumatology* **78**, 1692-1699 (2026).

330. Baker, T. *et al*. Type I interferon blockade with anifrolumab in patients with systemic lupus erythematosus modulates key immunopathological pathways in a gene expression and proteomic analysis of two phase 3 trials. *Annals of the Rheumatic Diseases* **83**, 1018-1027 (2024).